

2013 SUMMER RESEARCH PROGRAM FOR HIGH SCHOOL JUNIORS
AT THE
UNIVERSITY OF ROCHESTER'S
LABORATORY FOR LASER ENERGETICS

STUDENT RESEARCH REPORTS

PROGRAM COORDINATOR

Dr. R. Stephen Craxton

June 2014

Laboratory Report 379

2013 SUMMER RESEARCH PROGRAM FOR HIGH SCHOOL JUNIORS

AT THE

UNIVERSITY OF ROCHESTER'S

LABORATORY FOR LASER ENERGETICS

STUDENT RESEARCH REPORTS

PROGRAM COORDINATOR

Dr. R. Stephen Craxton

LABORATORY FOR LASER ENERGETICS

University of Rochester

250 East River Road

Rochester, NY 14623-1299

During the summer of 2013, 15 students from Rochester-area high schools participated in the Laboratory for Laser Energetics' Summer High School Research Program. The goal of this program is to excite a group of high school students about careers in the areas of science and technology by exposing them to research in a state-of-the-art environment. Too often, students are exposed to "research" only through classroom laboratories, which have prescribed procedures and predictable results. In LLE's summer program, the students experience many of the trials, tribulations, and rewards of scientific research. By participating in research in a real

environment, the students often become more excited about careers in science and technology. In addition, LLE gains from the contributions of the many highly talented students who are attracted to the program.

The students spent most of their time working on their individual research projects with members of LLE's scientific staff. The projects were related to current research activities at LLE and covered a broad range of areas of interest including laser physics, computational modeling of implosion physics, experimental diagnostic development, spectroscopy, cryogenic deuterium properties, liquid crystal devices, tritium detection and capture, ballistic deflection transistors, positioning systems, and 3-D virtual modeling. The students, their high schools, their LLE supervisors, and their project titles are listed in the table. Their written reports are collected in this volume.

The students attended weekly seminars on technical topics associated with LLE's research. Topics this year included laser physics, fusion, holography, nonlinear optics, atomic force microscopy, electronic paper, and scientific ethics. The students also received safety training, learned how to give scientific presentations, and were introduced to LLE's resources, especially the computational facilities.

The program culminated on 28 August with the "High School Student Summer Research Symposium," at which the students presented the results of their research to an audience including parents, teachers, and LLE staff. Each student spoke for approximately ten minutes and answered questions. At the symposium LLE presented its 17th annual William D. Ryan Inspirational Teacher Award. The recipient this year was Mrs. Eugenie Foster, a mathematics teacher from Brighton High School. This award honors a teacher, nominated by alumni of the LLE program, who has inspired outstanding students in the areas of science, mathematics, and

technology. Mrs. Foster was nominated by Mitch Perry, Julia Tucker, and Jack Valinsky, participants in the 2012 Summer Program.

A total of 312 high school students have participated in the program since it began in 1989. The students this year were selected from nearly 80 applicants. Each applicant submitted an essay describing their interests in science and technology, a copy of their transcript, and a letter of recommendation from a science or math teacher.

In the past, several participants of this program have gone on to become semifinalists and finalists in the prestigious, nationwide Intel Science Talent Search. This tradition of success continued this year with the selection of Yifan Kong as one of the 300 semifinalists nationwide in this competition.

LLE plans to continue this program in future years. The program is strictly for students from Rochester-area high schools who have just completed their junior year. Application information is mailed to schools and placed on the LLE website in early February with an application deadline near the middle of March. For more information about the program, please contact Dr. R. Stephen Craxton at LLE.

This program was supported by the U.S. Department of Energy Office of Inertial Confinement Fusion under Cooperative Agreement No. DE-NA0001944.

High school students and projects—Summer 2013.

Name	High School	Supervisor	Project Title
Aaron Appelle	Brighton	R. Sobolewski and Y. Akbas	Drift-to-Ballistic Electron Transport for Operation of Ballistic Deflection Transistors
Alexander Frenett	Allendale Columbia	F. J. Marshall	Integration of X-Ray Microscope Elements to a High-Speed Framing Camera Format
Sara Gnolek	Webster Thomas	W. T. Shmayda	Catalytic Oxidation of Hydrogen in Air Streams
Samuel Goodman	Pittsford Mendon	W. T. Shmayda	Detecting Hydrogen in Helium Streams
Michael Hartman	Pittsford Sutherland	R. W. Kidder	Emulating Laser Facility Operations Through a Real-Time Collaborative Network
Eric Hwang	Penfield	R. Boni and W. R. Donaldson	The Development and Testing of a Signal Processing Algorithm to Improve OMEGA Beam Timing
Katherine James	Honeoye Falls-Lima	K. L. Marshall	Rewriteable Photoalignment of Liquid Crystals as a Route to High-Laser-Damage-Threshold Active Beam Shapers
John Jamieson	Allendale Columbia	M. J. Guardalben	Modeling the Effects of Deformable Mirror Location in the OMEGA EP Pulse Compression System
Yifan Kong	Webster Schroeder	R. S. Craxton	Beam-Pointing Optimization for Proton Backlighting on the NIF
Nathaniel Rogalskyj	McQuaid	G. Brent and D. Lonobile	A Radiation and Cryogenic Tolerant Encoder
Ben Saltzman	Brighton	P. M. Nilson	Determining Plasma Temperature Using K-Line Shifts in Rapidly Heated Matter
Adeeb Sheikh	Pittsford Sutherland	R. Epstein	Controlling Laser Beam Speckle with Optimized Illumination of Zooming Phase Plates
Logan Toops	Webster Thomas	R. Sobolewski and Y. Akbas	Modeling and Controlling Electron Movement in a Ballistic Deflection Transistor
Erin Wang	Brighton	D. R. Harding	Thermodynamics of the Solid-Liquid Phase Boundary of Deuterium
Cameron Ziegler	Canandaigua Academy	S.-W. Bahk	Alignment of an Offner Triplet Radial Group Delay Compensator

Drift-to-Ballistic Electron Transport for Operation of Ballistic Deflection Transistors

Aaron Appelle
Brighton High School
Rochester, NY

Advisors: Dr. Roman Sobolewski and Yunus Akbas

Laboratory for Laser Energetics
University of Rochester
Rochester, NY
December 2013

Abstract

The program *ETCHD* (Electron Trajectory & CHannel Deflection) was created in MATLAB to simulate electron motion, drift or ballistic, through a ballistic deflection transistor (BDT) or conducting nanochannel of any shape. Each electron's velocity is continuously monitored and changed in *ETCHD* simulations. By calculating the angle of incidence between the transistor's walls and the electron's velocity, new electron velocities are output for ballistic collisions. Electron drift is modeled by creating a nearly uniform field of scatter points. Electric fields are also applied to the motion of electrons. Simulations were run to measure electron velocities and directions with varied electric fields and scatter densities. It was found that the BDT efficiency increases dramatically as electron motion changes from drift to ballistic. A working BDT is unrealistic with a scatter density that is very high, such as 0.1 pts/nm². Increasing the gate width to strengthen the lateral electric field increases electron lateral displacement in the ideal BDT. However, it has a negligible effect with scatter densities that are too high. These *ETCHD* results provided valuable information about the feasibility of a real, working BDT.

Introduction

A key function of transistors in contemporary electronics is to act as a switch, producing outputs of "one" or "zero" by turning on or off, respectively. Conventional field-effect transistors work by amplifying electrical inputs and moving electrons on and off a capacitor. When electrons collect on the capacitor, the memory bit element of the transistor registers as "on" and produces a "one." When the electrons are removed, it registers as "off" and produces a "zero." The memory capacitor must be repeatedly filled and emptied, starting and stopping the flow of electrons, so the speed of the transistor is limited [1]. Emptying the capacitor also produces large quantities of heat, allowing electrical "leaks" to form in the transistor's ultra-thin

walls. The drawbacks of conventional transistors are amplified as transistors are scaled down, and they will eventually prevent further progress. The ballistic deflection transistor (BDT) aims to alleviate these drawbacks by discarding the capacitor in favor of a ballistic design, bouncing individual electrons off deflectors to different directions [2].

A simplified BDT schematic is shown in Figure 1. Electrons move in uninterrupted pathways and, due to their inertia, bounce off the walls of the transistor. The BDT also produces “one”s and “zero”s, but does so by changing the direction of electrical current instead of starting and stopping it.

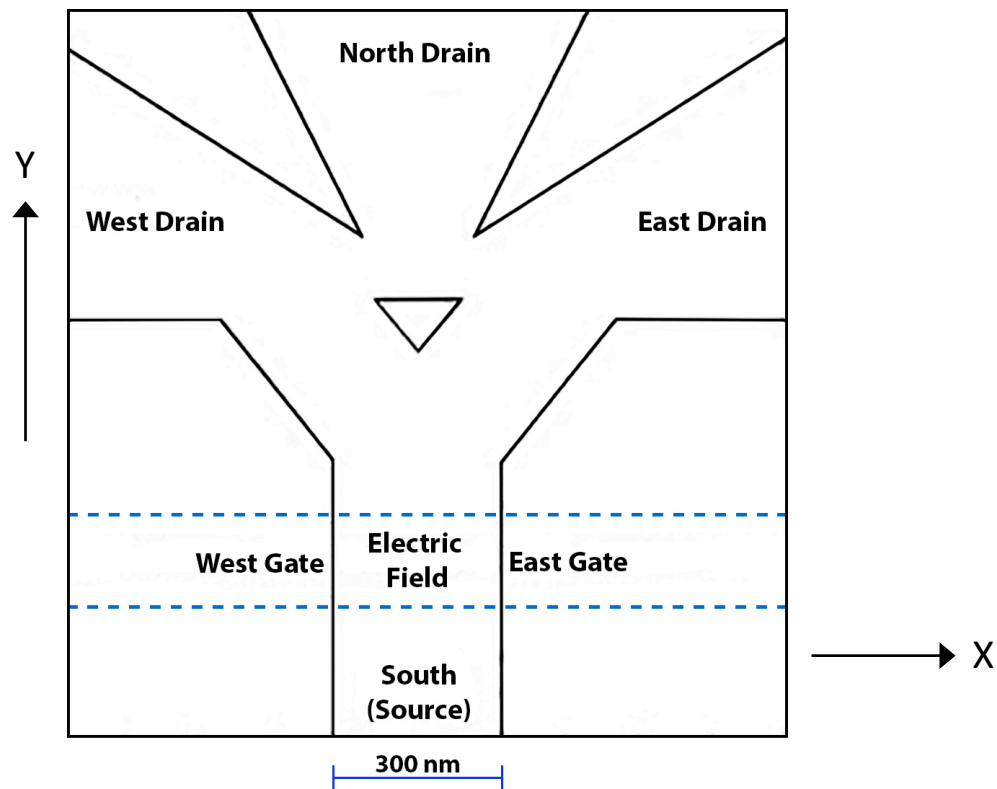


Figure 1: Schematic of a ballistic deflection transistor generated by the program ETCHD.

From the “South” end of the BDT called the source, electrons enter the transistor. As they move upwards under the action of an electric field applied in the vertical direction (not shown), they pass through an electrical field between the East and West gates that pushes them east or west depending on the charge applied. The electrons then bounce off a central triangular

platform to the desired direction. If the electrons bounce “East” and exit in the east drain, the BDT will produce an output of “zero”. If the electrons bounce “West” and exit through the west drain, the BDT will produce an output of “one”.

If manufactured correctly, the BDT will have numerous advantages over conventional transistors. Because electrons move ballistically via inertia, the BDT uses less energy [3]. Their ballistic motion also reduces electrical noise generated by the random thermal movement of electrons, producing less heat [3]. Because less heat is produced, BDTs do not have problems with electrical “leakage” as do conventional transistors [2, 3]. The BDT runs at speeds measured as high as terahertz frequencies [1], a thousand times faster than conventional transistors, because it does not stop and start the flow of electrons.

BDTs can be manufactured using current nanoscale fabrication technologies and existing materials. The conducting medium of the transistor is typically a two-dimensional electron gas (2DEG), instead of the silicon present in conventional transistors. A 2DEG is a gas composed of electrons that is very thin in a third dimension and thus appears as nearly two-dimensional. When electrons move in 2DEGs, their paths are nearly uninterrupted and thus ballistic. However, the manufacturing process is not perfect, which can result in an imperfect conducting medium. When electrons hit imperfections in the BDT, they scatter randomly, leading to electron drift. Electron drift hinders the performance of BDTs.

BDTs are highly adjustable, from their basic shape to the size and location of the applied electric field. These varying aspects have not yet been tested, so the optimal configuration has not yet been recognized. In this project, a program titled Electron Transport and Channel Deflection (*ETCHD*) was created to realistically simulate electrons traveling through a BDT. The program can simulate electron movement whether the motion is drift or ballistic, and the user is able to define the amount that electrons drift. *ETCHD* has been used to determine the degree to which electrons must be ballistic, as opposed to drift, for a BDT to function effectively. *ETCHD*

results also provide valuable information about the feasibility of the BDT in varying sizes and strengths depending on the prevalence of electron drift. As electron motion is changed from drift to ballistic, electrons behave differently inside the BDT and require different transistor configurations for optimization.

Electron motion

When traveling through conducting media, electrons hit impurities that interrupt their pathways. The average path length that an electron moves through a material between collisions is called its mean-free path (ℓ). ℓ is dependent on a variety of factors. First and foremost is the medium in which the electrons are moving [4]. Depending on the atomic packing and density of the medium, electrons can have longer or shorter ℓ s. The next important factor that affects ℓ is the temperature of the medium [4]: when the medium is hot, atoms vibrate with more energy and thus electrons more frequently hit imperfections, shortening ℓ . In some cases, ℓ is dependent on the physical size of the conducting medium: if the conductor is relatively large, there is a high chance that the electron will scatter before traveling the full length of the conductor [3].

If the conductor is at nanoscale, it is possible that the electron will hit the edges of the medium before travelling the complete length of ℓ . In such an ideal BDT, electrons are “ballistic”. These ballistic electrons move rapidly in relatively long, uninterrupted pathways, much like bullets. When electrons move ballistically through the BDT, the only time their trajectories change is when they collide with the transistors’ walls or are influenced by an electric field; they do not bounce in unpredictable manners, because they do not complete their ℓ before hitting a transistor wall [3]. Thus, in order for electrons to move ballistically, the BDT must be manufactured at nanoscale. If the BDT is too large, electrons will be able to travel their full ℓ before hitting the walls of the channel, and they will randomly scatter. Scattering in a conducting

channel is illustrated in Figure 2. On a scale larger than nanoscale, electron motion is determined predominantly by scattering in a Brownian manner.

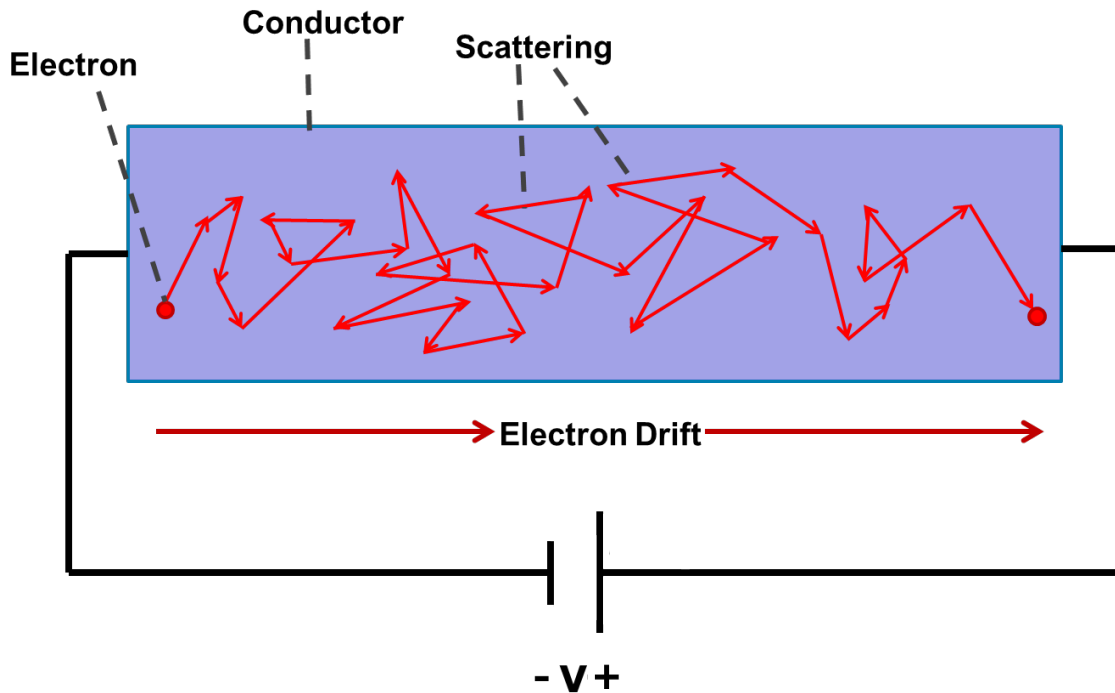


Figure 2: Path of an electron in a conducting channel. The electron is pulled in a net direction because of an applied voltage but scatters through collisions in the conducting medium.

Even though electrons bounce randomly, they are still impacted by electric and magnetic fields. When a voltage is applied to a conducting medium in which electrons are scattering, the electrons are affected by the field in between scatters as they travel ℓ . Because of this, even though the electrons bounce randomly, as a whole they move more in the direction that the field is pulling them. This motion is known as electron drift.

Both electron drift and ballistic electron motion can be used to move electrons in one direction. When electrons are drifting, many electrons all drift in one direction as a cloud at low velocities. This happens at a large scale. When electrons are ballistic, they move in one direction individually, bouncing at high velocities. This happens at a very small scale.

Program *ETCHD*

The program *ETCHD* was coded in MATLAB. It consists of three main components which work in sequence to produce a visual display of electrons moving through a BDT as well as a collection of the results for each electron. These three components are entitled *Geometry*, *Calculate*, and *Plot_e*.

Geometry allows the user to define the precise, coordinate-based geometry of the BDT. The function takes in parameters that allow the user to define the shape of the BDT, the scatter point field, and electric field. Vectors are provided that contain the start points and endpoints of each transistor wall in the BDT's shape. *Geometry* uses these coordinates to output a list of equations that define the walls of the transistor (the shape). This data is carried onto the next file, *Calculate*. *Geometry* also draws out each line on-screen to create a visual setup of the BDT, as shown in Figure 1. Other parameters draw scatter points and dotted lines to visually represent nonuniformities and the applied electric field.

Calculate is an extensive iterative and algorithm-based file that uses the linear, piecewise equations outputted from *Geometry* to determine an electron's trajectory through the BDT. Every physical property of the transistor and the electron is programmed in *Calculate*. The coordinates of the electron's path are generated entirely by this file. Four numbers determine each electron's existence: its x-coordinate, y-coordinate, x-velocity component, and y-velocity component. The coordinates represent the electron's location in the BDT, and the velocity components represent the direction that the electron is travelling. In all *ETCHD* simulations in the BDT, the electrons enter the source channel with a random x-coordinate, a fixed positive velocity magnitude, and a random direction between 0 and 180°. In all nanochannel simulations, the electrons enter the source channel centered and travelling due north. Unaltered, each electron would continue in a straight line forever with constant velocity. However, a number of factors within the channel can alter the electron's velocity and, consequently, its trajectory. If an electron hits a channel wall,

encounters an electric field, or scatters due to nonuniformities its velocity must change.

Calculate functions by checking continuously whether the electron is encountering any of these events and by changing its position and velocity appropriately.

The first factor that frequently modifies an electron's trajectory is a collision with a channel wall (Figure 4). *ETCHD* assumes that collisions are elastic, which means that the angle of incidence between an electron and a wall is the same as the angle of reflection and that the electron loses no energy in the collision; thus, the magnitude of its velocity remains the same. Because the electron's final direction is dependent entirely on angular geometry, *ETCHD* considers every possible orientation.

β : Angle of the wall relative to the +x axis

θ_A : Angle of electron before collision relative to +x axis

θ_C : Angle of the electron relative to the wall

θ_D : Angle of the electron after collision relative to +x axis

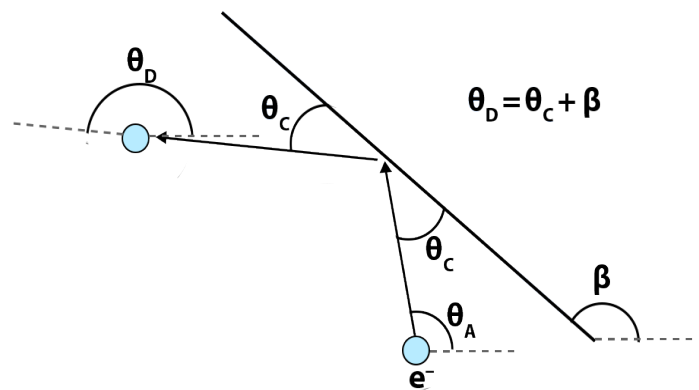


Figure 4: The geometry and important angles in an electron-wall collision. The wall is represented by the thick black line positioned β away from the horizontal. The light blue circle represents the electron.

For each case, θ_D is calculated from the other three angles according to the geometry. *Calculate* continuously monitors whether an electron is hitting a wall and determines which case it is by identifying the angle of the wall and the incoming electron. In order to determine which wall the electron will hit, *Calculate* references the equations matrix generated in *Geometry* to identify the nearest wall's β angle and start and end coordinates.

The next factor that modifies the position and velocity of electrons is the presence of electric fields in the BDT. Because the transistor works on the basis of a central voltage pull upwards, the electron is always being affected by an electric field in the y-direction of Figure 1.

Additionally, as the electron enters the region between the East and West gates, the applied electric field of the transistor pulls the electron towards one side by changing the x-velocity.

Lastly, the electron's trajectory can be changed by colliding with a scatter point. *ETCHD* continuously detects whether the electron is colliding with any of the thousands of scatter points that may be simulated at any moment. A collision is defined as a distance of less than or equal to 1 nm between the electron and scatter point. When the electron does scatter, it is randomly assigned a new velocity of the same magnitude but with a new direction between 0 and 180° (this is an approximation to the true unpredictable behavior).

ETCHD's Calculate file must monitor each of these factors every time it moves the electron. Upon completion, it outputs a list of 1000 coordinate points in sequence that track the electron's trajectory through the transistor. The program takes different amounts of time depending on the simulation. For example, running three tests of 100 electrons through the nanochannel at 10 different scatter point densities (3000 electrons total) took about 30 seconds. Animating more than 100 electrons at once caused MATLAB to lag or freeze, so the algorithm should be optimized for any future testing to improve performance.

The third and last major component of *ETCHD* is *Plot_e*, which serves the purpose of visually displaying the results of *Calculate* for quick, qualitative results. It is able to draw a line tracing the electron's trajectory or animate a (much enlarged) image of an electron moving through the transistor. *Plot_e* also serves as a log-file creator. It tracks the number of electrons that are outputted in each drain of the BDT as well as each electron's average velocity. It can combine data from thousands of electrons into a cumulative data set. The end result of these three comprehensive files is an easy-to-use system to track any electron moving through any BDT. The user may enter a BDT's shape, calculate the trajectories of any number of electrons moving through it, then plot the calculated coordinates and observe the results.

ETCHD Simulations

ETCHD has been used to carry out a variety of simulations. *Geometry* has been used to set up both a nanochannel (two walls) and the entire BDT (the thirteen walls of Fig. 1). Four main types of simulations were run in a nanochannel whose width was 1300 nm and length 2200 nm. An electric field was applied to the nanochannel near the source to deflect electrons towards the East or West drains. The first simulation (Fig. 5) allowed electrons to flow through the nanochannel without interruption, moving ballistically. In a nanochannel, the lateral displacement seen in Figure 5 can serve as an indicator of how easy it is to physically move an electron in the BDT.

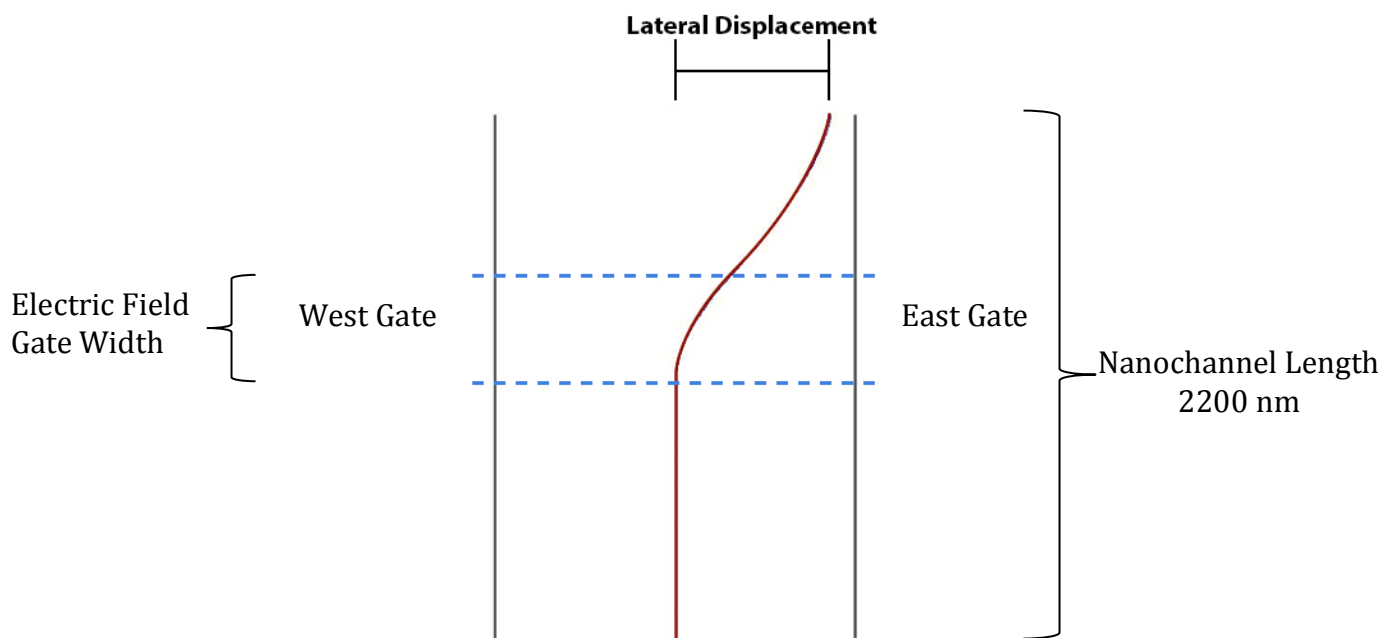


Figure 5: An electron's path through a nanochannel traced with a solid line. It enters from the South, moves upward through the channel, and is laterally displaced some amount East by an electric field within the East and West gates. There is also a uniform electric field in the vertical direction.

The goal was to determine the relationship between the physical extent of the electric field and the lateral electron displacement. Theoretically, the larger the width of the electric field, the farther each electron should be displaced as it moves through the source channel. Since there were no scatter points in the conducting medium for the first simulation, the electrons' lateral

displacements were undisturbed by scattering. The width of the electric field in the simulation was increased from 0 nm to 800 nm to 1540 nm while the MATLAB file *Plot_e* recorded the lateral displacement, in nanometers, of each electron that was sent through the nanochannel. This simulation was repeated for five different applied voltages (1-5 V). The corresponding applied electric field was 3.3×10^6 to 1.7×10^7 V/m. As seen in Figure 6, as the electric field's gate width increased, the lateral displacement of an electron moving through the nanochannel increased. The stronger the applied voltage, the larger the displacement of the electron for a given gate width.

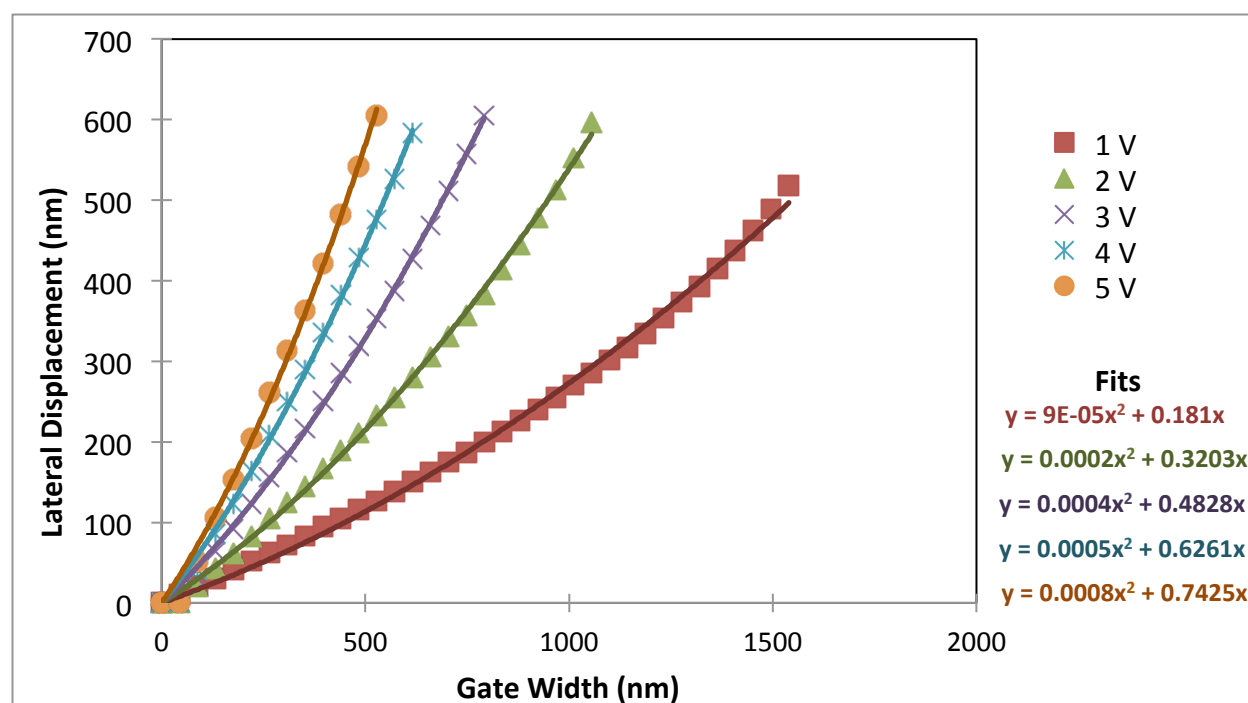


Figure 6: Electron displacement as a function of gate width for several applied lateral voltages. Lateral voltages push West to East, and a central voltage of 1 V pushes North.

A second simulation conducted in a nanochannel measured lateral displacement as in the first simulation but included the possibility of electron scattering. In this second simulation, electrons were sent through the nanochannel with varying electric field gate widths from 0 to 1540 nm, with varying voltages from 1 to 10 V, and with an applied scatter point density of 0.05

pts/nm². The magnitude of the electric field remained in the range between 3.3×10^6 and 1.7×10^7 V/m. Figure 7 displays these results.

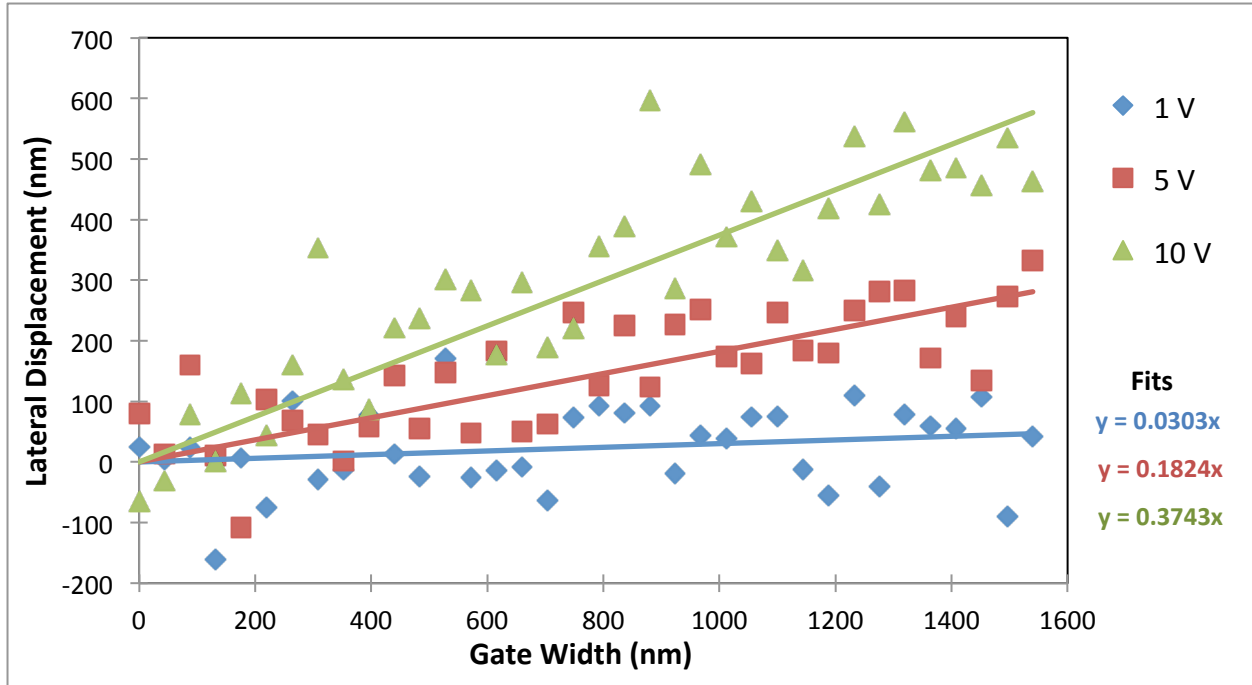


Figure 7: Lateral displacement as a function of gate width for varying lateral voltages with a scatter density of .05 pts/nm². Lateral voltages push West to East, and a central voltage of 1V pushes North. Straight line fits for each voltage are shown in corresponding colors.

As in the previous simulation, as gate width increases, so does lateral displacement. However, in this case a constantly increasing gate width leads to a constantly increasing lateral displacement. Because scatter points hinder an electron's displacement, it can also be seen that larger voltages are required to move an electron by the same amount as it moved while travelling ballistically. For instance, it takes a field width of approximately 1500 nm and a voltage of 10 V to move an electron just 500 nm laterally. In the previous experiment, it took a field width of 1500 nm and a voltage of only 1V to move an electron the same amount.

A third simulation examined the density of scatter points in the nanochannel's conducting medium. In this simulation, electrons were run through the nanochannel of width 1300 nm and *Plot_e* plotted each electron's lateral displacement (just as in the previous two experiments).

However, the electric gate width was fixed at 800 nm, while the scatter point density was raised from 0 pts/nm² to 0.1 pts/nm². Each scatter density was tested with voltages of 0 V through 10 V applied. The data for this simulation are recorded in Figure 8. This graph must be interpreted differently because there now exist negative lateral displacements, indicating that the electron was pushed West of normal. This is illustrated in Figure 9.

When the density is low, the electron is pushed so far East that it bounces against the wall of the nanochannel and is sent travelling West. When the density is high, the electron travels mostly in the vertical direction. The slight motion West in the case of no voltage between the gates is just the random result of scattering and is insignificant. That being said, Figure 8 clearly illustrates that higher scatter point densities approaching 0.1 pts/nm² stop the electron from being displaced laterally in either direction. At scatter densities higher than 0.1 pts/nm², the BDT would be ineffective, and the transistor would never register as “on” or “off.” With a density this high, it is nearly impossible to control the direction of electrons moving through the transistor.

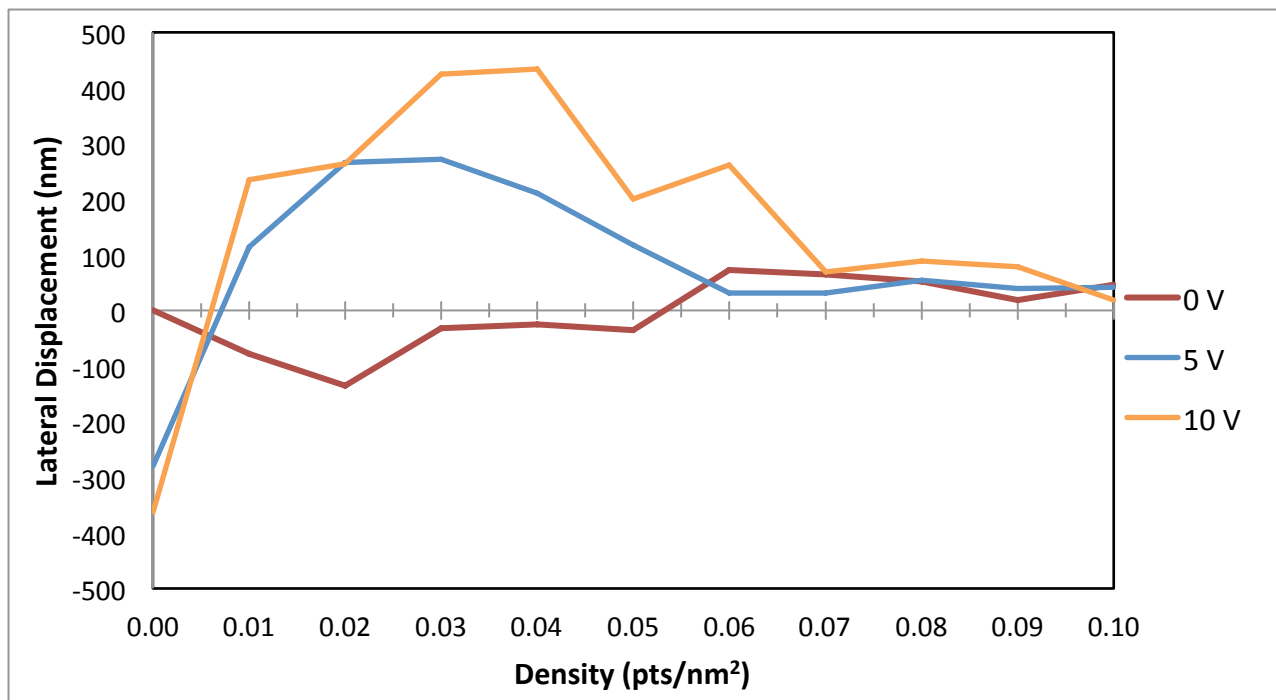


Figure 8: Lateral displacement as a function of scatter point density for varied voltages and a fixed gate width of 800 nm. When density increases, electrons cannot be laterally displaced by an applied electric field.

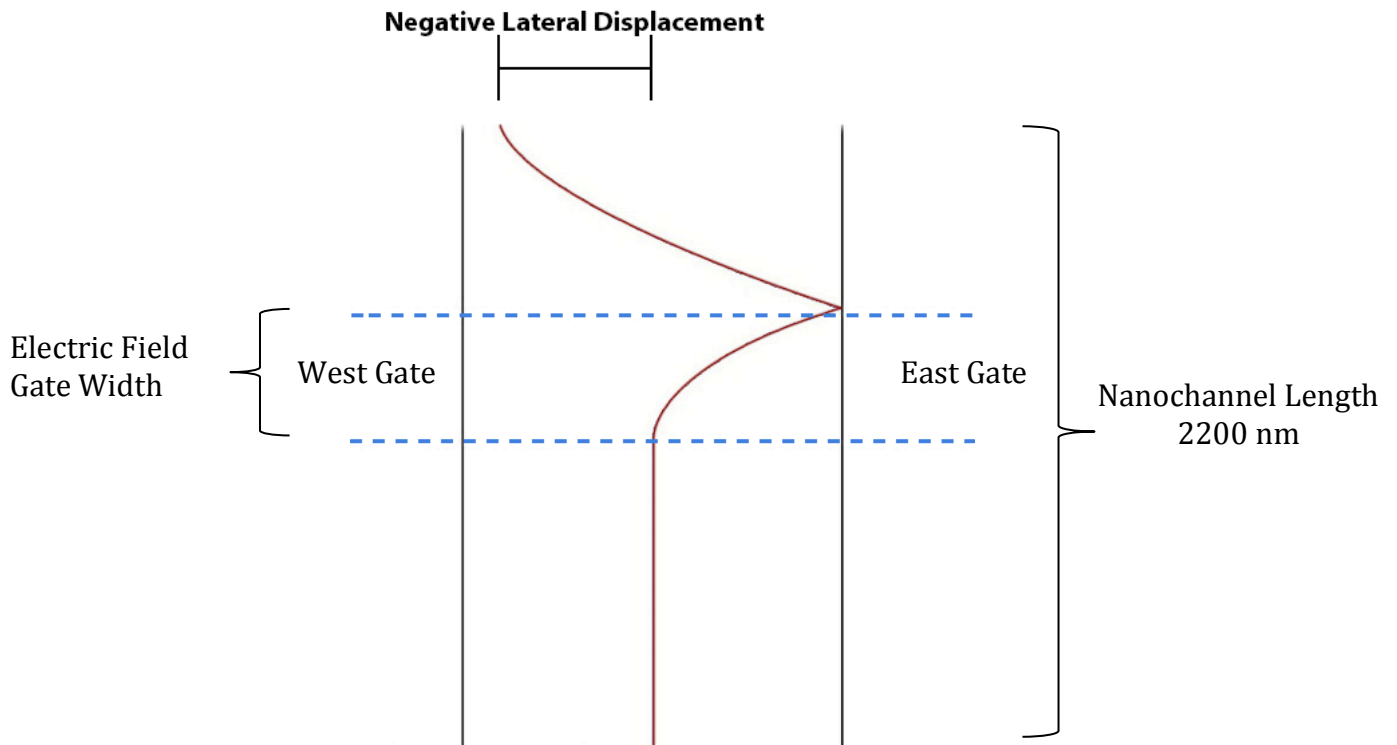


Figure 9: An electron's path through a nanochannel traced with a solid line. It enters from the South, moves upward through the channel, and is laterally displaced by an electric field between the East and West gates. It is pulled enough that it collides with the channel wall and is displaced West of vertical (negative displacement).

The last major simulation run in the nanochannel digresses from the study of electron lateral displacements and focuses on the velocity of the electron. When the scatter density becomes close to zero, the electron becomes more and more ballistic. Ballistic electrons move much faster than electrons that drift, due to fewer interruptions in velocity. *ETCHD* simulated the velocity of electrons in a nanochannel with the approximate true length of a BDT (2200 nm). In this simulation, electrons are sent through the nanochannel at densities from 0.1 to 0 pts/nm², simulating drift-to-ballistic transport. Results are shown in Figure 10.

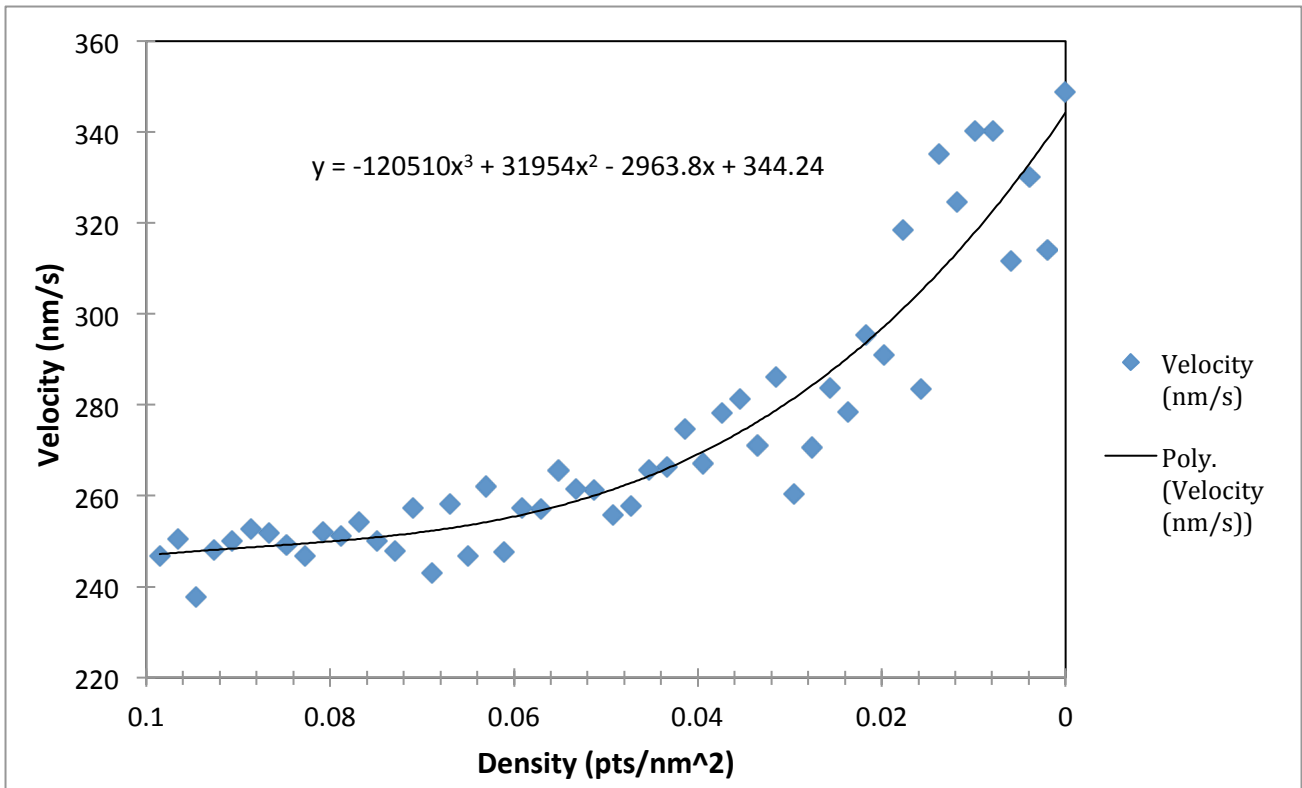


Figure 10: Electron velocity at the end of the nanochannel as a function of scatter point density. Density is shown from high to low to illustrate the trend of a drifting electron becoming ballistic. A polynomial fit is shown with a black line to model the observed pattern; it does not extrapolate past the domain shown.

From Figure 10 it can be seen that the fastest velocity for an electron at the end of the nanochannel is about 350 nm/s. Once the scatter density approaches 0.1 pts/nm², the electrons jitter and slowly move north. The velocity of the electrons in *ETCHD* plateaus with a high scatter point density. This is a phenomenon caused by the way *ETCHD* was coded. Because each scatter point actually affects a 1 nm radius surrounding it, the electrons are always scattering when the scatter point density is high. In a real BDT, the velocity of the electrons would be inversely proportional to the number of scatter points per unit area, thus the velocity graph would not plateau. Figure 10 serves as a proof of concept but not an accurate predictor of the velocity of electrons in a manufactured BDT. It illustrates that a BDT becomes unrealistic with scatter point densities that are too high. Electrons scatter and slow down, so they are unable to travel ballistically.

When considering the entire BDT of Fig. 1, the program *ETCHD* shows that an ideal BDT with no scatter points in the conducting medium is extremely efficient. This is seen in Figure 11, which shows the directional data of electrons that were pushed with varying voltages. A negative voltage indicates that there was a positive charge applied to the left wall of the BDT source channel and a negative charge applied to the right wall of the channel, causing the electron to be pushed West. A positive voltage indicates that there was a negative charge applied to the left wall and a positive charge applied to the right wall, pushing the electron to the East.

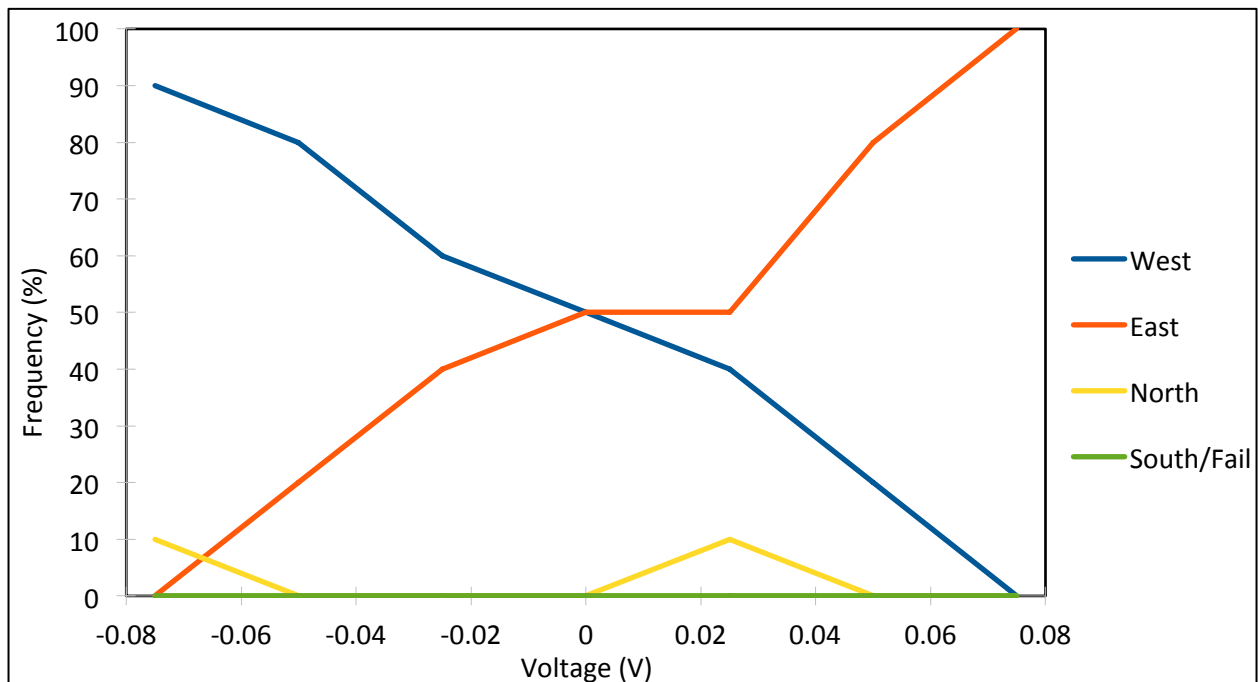


Figure 11: Percentages of electrons exiting the four gates of the BDT with different applied lateral voltages, for the case of no scatter points. The gate width was 300 nm.

It can be seen that, with positive voltages, electrons drain mostly in the East drain, which is the desired outcome as the electrons have been pushed east in the BDT source channel due to the applied electric field. Likewise, with negative voltages, a majority of electrons drain in the West drain after being pushed West. Furthermore, the larger the magnitude of the applied voltage, the greater percentage of electrons drain in the desired direction. Thus, an ideal BDT with

completely ballistic electrons can be very efficient. The frequencies recorded in Fig. 11 are recorded from individual sample simulations; they are examples but they are not absolute.

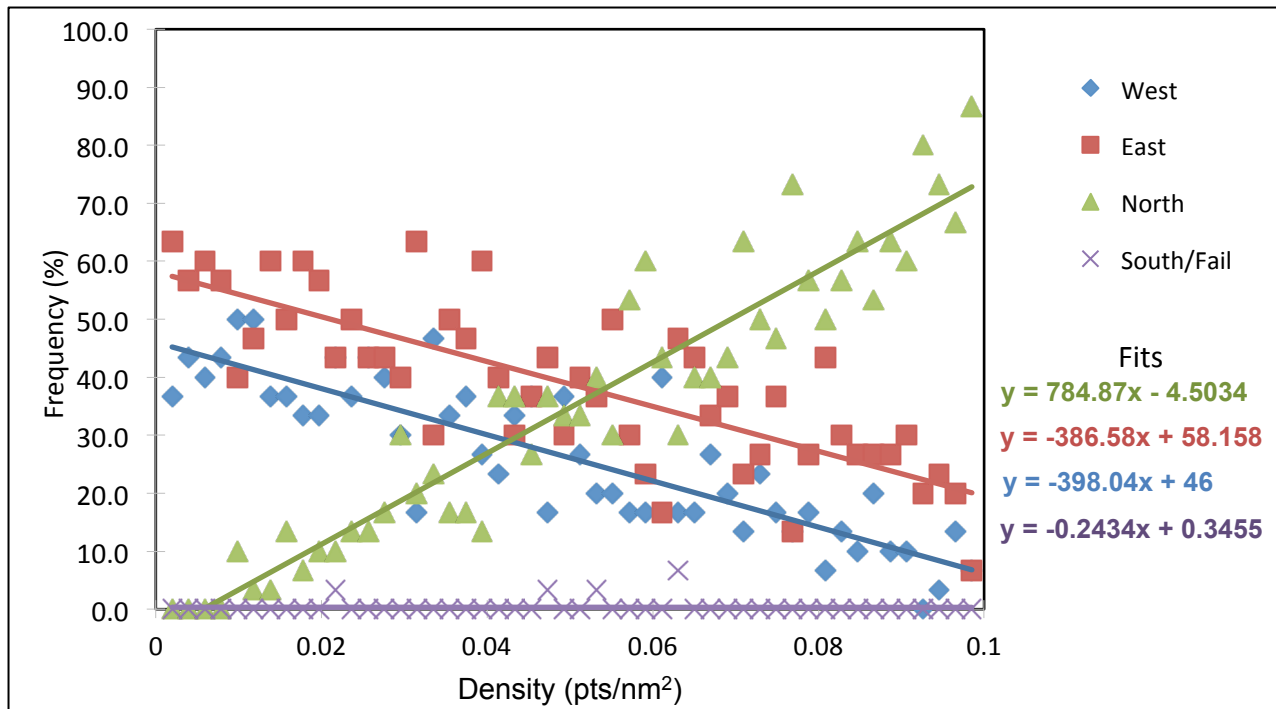


Figure 12: The proportion of electrons that exit through each gate for scatter densities between 0 and 0.1 pts/nm². Electrons were pushed East. When electrons drift, a higher proportion exit through the North drain and a lower proportion exit through the East drain. The lateral voltage was 0.1 V. The gate width was 500 nm.

Another simulation was run in *ETCHD* that recorded electron directional data across the spectrum of possible scatter densities. Figure 12 shows how the frequency of exit directions changes as the scatter density increases and electrons drift more. In this simulation, two electric fields were applied. The main electric field pulled electrons North and had a magnitude of 1 V, which applied throughout the source channel and North drain. The lateral electric field had a magnitude of 3.3×10^5 V/m. An applied voltage of 0.1 V pushed electrons to the East, as a result of positive charge applied to the right gate wall and negative charge to the left wall. Figure 12 shows different frequency results than Figure 11 due to a larger gate width and due to random chance. The East-to-West difference is smaller for low scatter point densities because the larger

gate width and lateral voltage caused electrons to bounce against the source channel walls (as in Fig. 9) and exit west.

As the density of scatter points increases (and electron motion transitions from ballistic to drift), a number of important trends can be seen. First, as the density increases, the number of electrons that exit in the East drain (the forced direction) decreases. Second, the number of electrons that exit in the West drain (the non-desired direction) also decreases. Third, the number of electrons that drain north increases at a faster rate than the other two trends. As the scatter density increases, the electrons only drift in the direction of the net voltage, which is North, and are not displaced laterally. Most electrons reach the central triangle of the BDT (see Fig. 1) but they flow around it continuing northwards instead of catching the walls of the East and West drains. Very few electrons ever drain South or fail to reach a drain.

Conclusion

In conclusion, a program entitled *ETCHD* was created to realistically simulate a BDT for the purpose of determining optimum conditions for future manufacturing processes. Results indicate that a BDT would be most effective when electrons are ballistic or near ballistic. In this scenario, the required voltage and the required electric gate width are minimal, which is the most energy efficient. A BDT is also feasible with small levels of electron drift. In this scenario, the required voltage is much higher that would be required when electrons are ballistic. This is less energy efficient, but still consistent and effective. In an ideal BDT, over three-quarters of the electrons can consistently be forced in the desired direction, which is a clear enough difference to indicate “on” or “off”. However, when electrons drift to a large degree, the BDT will not work. The electrons are only able to move in their net direction, which is upwards (North) due to the central voltage of the BDT. As a result the BDT cannot be turned “on” or “off”.

Acknowledgements

I will be forever grateful for the opportunity to work at the Laboratory for Laser Energetics. I would like to thank Dr. R. Stephen Craxton for running the high-school intern program and greatly helping me with this paper. Thank you to my advisors, Dr. Roman Sobolewski and Yunus Akbas, for providing me with an interesting project in the field of electrical engineering. My gratitude goes to Logan Toops, my partner, who worked together with me on a similar project. Without our teamwork, we would not have been able to complete this program. In addition, the other interns in Room 2650 deserve mention for helping me debug when I became frustrated; thanks especially to Ian Gabalski, who was kindly invested in this project just due to personal interest. Last but certainly not least, I would like to thank my family for inspiring and always supporting me.

References

1. Irie, Hiroshi. *Ballistic Electron Transport in Nanoscale Three-Branch Junctions*. Thesis. University of Rochester, 2010. N.p.: n.p., n.d. Print.
2. Sherwood, Jonathan. "Radical 'Ballistic Computing' Chip Bounces Electrons like Billiards." *Rochester News*. University of Rochester, 16 August 2006. Web. 10 March 2014.
3. "Ballistic Deflection Transistor and Ballistic Deflection Transistor Based Logic Circuits." *University of Rochester*. N.p., n.d. Web. 11 March 2014.
4. "Mean Free Path." *Georgia State University HyperPhysics*. GSU Department of Physics and Astronomy, n.d. Web. 11 March 2014.

Integration of X-ray Microscope Elements to a High-Speed Framing Camera Format

Laboratory for Laser Energetics

Summer High School Research Program 2013

Alexander Frenett
Allendale Columbia School
LLE Advisor: Frederic J. Marshall

Integration of X-Ray Microscope Elements to a High-Speed Framing Camera Format

Abstract

Compact x-ray mirrors have been positioned so as to form multiple images in a high-speed framing camera format. The angles at which the mirrors lie are altered by glass shims. The image offsets are set by positioning the mirrors using a multiple stepper-motor table positioning system. The mirror assembly has been tested in the x-ray diagnostic laboratory using electron-beam-generated x rays. Successful alignment of the images will allow for use of high-speed framing cameras in conjunction with the microscope elements to diagnose plasmas formed by the OMEGA laser system.

Introduction

Inertial confinement fusion (ICF) attempts to produce an ignited plasma by compression of a deuterium-tritium target using high-intensity laser beams. The OMEGA [1] laser system at the University of Rochester's Laboratory for Laser Energetics (LLE) is used to create high temperature plasmas (> 1 keV) via ICF. The plasma conditions of the compressed target, such as the density, shape, and size, can be assessed through imaging.

X rays in the energy range from ~ 0.1 to ~ 10 keV are emitted by the laser-heated plasma. X-ray imaging systems are used in the OMEGA target chamber to space resolve the emission from the plasma.

The principle means of imaging in use at LLE consist of either pinhole arrays [2] or Kirkpatrick-Baez (KB) [3] microscopes. When combined with a framing camera [4] the x-ray emission is also time resolved. The pinhole arrays and KB microscopes serve to magnify the

image, while the framing camera serves to record time-resolved images. Time resolution of ~ 30 ps is achievable with framing cameras. Framing cameras usually are used with pinhole arrays, though development of KB image arrays is desired.

X-ray Imaging

Figure 1 shows a KB mirror pair and an assembled pinhole camera. The pinhole camera is the simpler of the two, and is modeled similarly to a visible-light pinhole camera, although on a much smaller scale. Figure 1 shows a single pinhole used for imaging on OMEGA, whereas framing cameras use an array of ~ 10 μm laser-drilled holes. The resulting inverted image from the x rays passing through the holes is recorded on the opposite side, using either a framing camera as mentioned above, or an x-ray sensitive detector. Due to the simplicity of the pinhole array, this method is relatively inexpensive and can produce images with moderate resolution (~ 15 μm for a 10 μm pinhole). However, this resolution limits the ability to distinguish smaller features in the plasma. As an example, the center of a target imploded by OMEGA is ~ 30 μm in diameter. This is only 2 resolution elements if the resolution is 15 μm .

KB microscopes can improve on pinhole camera resolution with resolution as high as ~ 3 μm . The KB x-ray microscope consists of mirror pairs each of which produces a single image. One design uses sixteen pairs, providing sixteen images of the plasma emission [5]. When coupled with a framing camera these KB mirror pairs can provide time-separated images.

KB X-Ray Microscopes

The Kirkpatrick-Baez x-ray microscope was developed by Kirkpatrick and Baez in 1948 [3]. KB microscopes have been used at LLE to image laser-generated plasma x-ray emission

since the 1980's, originally on the 24-beam OMEGA laser system and more recently on the 60-beam OMEGA laser [6]. A Kirkpatrick-Baez microscope consists of perpendicular, spherical, concave mirror pairs (Figure 2) designed so that the planes of focus for each mirror are combined. When x rays reflect off both mirrors a two-dimensional image is formed.

As shown in Figure 2, only x rays that reflect off the mirror pairs will contribute to the two-dimensional image. To prevent other x rays that reflect off one or none of the mirrors in a pair from reaching the image plane, a baffle is used in conjunction with the mirror pairs. With the baffle in place, only x rays that reflect off both mirrors in the pair create the image.

Each mirror in the pair obeys the focus equation

$$\frac{1}{p} + \frac{1}{q} = \frac{2}{R \sin(i)}, \quad (1)$$

where p is the source-to-mirror distance, q is the mirror-to-image distance, R is the radius of curvature of the mirror, and i is the angle of incidence of the x rays (Figure 3). The image is magnified by an amount $M=q/p$. As i becomes small, $\sin(i)$ approaches $\tan(i)$, which is equivalent to $\Delta x/p$, where Δx is the perpendicular distance from a mirror to the optical axis.

When p is assumed a fixed quantity (~ 180 mm on OMEGA) and q is rewritten as Mp (for a magnification M), it is possible to verify R . R was verified to be between 25 and 30 m for the mirrors in use. The angle i on the mirrors is ~ 0.7 degrees, which is necessarily small, since x rays in the energy range of interest will not reflect unless the angle is small [7].

A schematic of a KB mirror pair is seen in Figure 4. A mirror in a mirror pair on the 16-image KB microscope measures 17 mm long (if the triangle is extended) and 4.5 mm thick. The

pair subtends an angle of 22.5 degrees, or 1/16 of a complete circle. The top ~3 mm of a mirror are cut to a 45 degree angle, so that the two mirror surfaces in the pair are perpendicular. To increase the reflectivity of the mirrors, metallic coatings are used on each individual mirror, on the perpendicular face. It is used, as it provides the best reflectivity of x rays at the highest energies. Each mirror departs from a perfect flat by 97 nm (0.1 μm) in the curved direction.

The mirror pairs in one 16-image KB optic design are assembled in a 16-mirror-pair arrangement, with all pairs touching [Figure 5(a)], so as to make a spherical arrangement in the center [8]. This uniform distribution of mirrors, when combined with a circular framing camera design, can produce circular sets of 16 images, separated by ~100 ps, with a temporal resolution of ~80 ps [8]. These times are limited by the unusual design of the circular framing design, as the speed of the pulse (which captures the image) running through the strip ($\sim c/2$) and the diameter of the image (76 mm) determine the time frame in which images can be taken.

A new design of KB microscope has been proposed [Figure 5(b)], such that it continues to take 16 images at a time, but instead of focusing on a circular framing camera, the mirrors are spaced such that they focus on a rectangular array. The image points are 9 mm apart, and located on four framing camera strips, each 5.6 mm wide. These camera strips allow for much more closely spaced time-gated images (60 ps), and these strips can have up to a 30 ps time resolution. Figure 5(b) only shows 12 of the 16 mirrors of the new design, as two-plane tilts will have to be implemented for the final four mirrors, as four more mirror pairs will not fit in this design on the optical base.

Figure 6 shows the array of points and the framing camera strips. It also shows, as an overlay, the image circle that the 16-image KB microscope would produce without shifts to the

mirror pairs. Four mirror pairs need to be shifted onto the outermost circle, eight to the middle circle, and four to the innermost circle, to create the 4 by 4 grid of images.

Figure 7 shows the shift necessary for a mirror pair on the existing 16-image optic design to result in the desired layout. If the image needs to be moved by a distance $\delta x'$ on the image plane (from the unshifted circle to the appropriate new circle), and the image plane is treated as a concave surface with a large radius of curvature, the angle that the mirror needs to be tilted is determined by

$$\Delta\theta = \delta x' / (p + q). \quad (2)$$

For the mirror pairs on the proposed model [5], operating at $M=9.2$ to function properly on the OMEGA laser system, the values of $\Delta\theta$ are 0.596, 0.352, and 0.200 degrees for the outer, middle, and inner circle tilts, respectively. Furthermore, the mirrors would have to be moved outward from the center by an amount

$$\delta x'' = \frac{\delta x'}{(M + 1)}, \quad (3)$$

or 1.88 mm, 1.10 mm, and 0.63 mm respectively.

This is made difficult, however, by the aberrations caused by the movement and tilt of the mirrors. As seen in Figure 8, the resolution drops off dramatically when the mirrors are off focus by even 0.4 mm. Further aberration occurs due to mis-tilting because the error in tilt of the mirror is doubled in the image placement error.

Experiments

To create a 16-image KB microscope such that the images fall onto four image strips, the mirrors must be tilted and placed with precision. The x-ray microscope chassis available in the x-ray laboratory was configured to operate at a magnification of 12.85 which is different than the case of $M=9.2$ given in ref. [5]. Only four mirror pairs (two outer, two middle) were included on the test assembly, to test that one row of images could be produced. Small wedges were used to produce the tilts (Figure 9). The wedges were made by using Huntsman Araldite 1253 Epoxy [9] to hold two glass slides together over a pre-measured distance of 50 mm, with plastic shims on one end of the slides to create the correct angle. The wedges were measured by taking the inverse tangent of the difference of the height of the slides at the thin end and the 50 mm mark divided by 50 mm (see brown triangle in Figure 9). The angles of the wedges produced measured 0.401 and 0.516 degrees, while the angles calculated for the outer and middle circles for $M=12.85$ are 0.408 and 0.520 degrees. The differences between the desired and measured angles are 0.007 and 0.004 deg respectively.

The mirror assembly apparatus can be seen in Figure 10. To center and appropriately move the optical base, three stepper-motor tables were assembled on top of each other. A micropositioner stage was also used. Two tables were set up to move perpendicularly to each other in the horizontal plane, and the third was a rotary stage. All three stepper tables were combined with stepping motors, giving a precision of 1/10,000th of an inch (2.54 microns) and 1/100 of a degree on the flat and rotating tables, respectively. To hold the optical base in place, a metal plate was constructed that allowed the base to rest securely on the assembly stage. To view the assembly at a magnification, a Panasonic Video Camera was held above the stage using an apparatus comprising aluminum rods and 90-degree clamps. The camera lens was fitted with a

correction lens ~20 mm away from the top of the optic, and provided an image of the assembly at a magnification of 153 resulting in a ~10 micron resolution on a connected display. A sliding positioner was set up on one side of the stage, with two aluminum rods holding a rod with a three-axis micropositioner stage. The sliding stage acted as a rough positioner, while the micropositioner stages were used for precise movements when close.

To assemble the mirror pairs, a fence was made out of a glass base and glass slides; one slide was used to line up the mirror bases, and a stack of glass slides acted to insure the mirrors were also at the correct angle when assembled. UV cured epoxy was used to bond the mirrors. Curing was accomplished by exposing the epoxy to UV light for ~10 sec. The tilted wedges were attached to the mirror pairs in this fashion as well.

Vacuum grease was then used to hold the mirror pairs (with wedges) to an aluminum plate that attached to the micrometer stages at the end of the rough slider. The stepper-motor tables were then rotated and displaced such that the crosshairs of the viewing camera was directly above the point at which the mirror pair was desired. The rough slide was moved until the mirror pair was visible on the viewing screen. Then, the micrometer stages were used to center the mirrors in place directly to the crosshairs, such that the mirror pair was then in the correct place. A precisely placed mirror pair can be seen in Figure 10. UV epoxy was used to attach the mirrors to the base. The micropositioner was then backed away from the optic. The stepper motor tables were then rotated to the correct angle and displaced to the correct radius for the next mirror pair, and the process was repeated for the remaining mirrors. The vacuum grease was then cleaned from the top of the mirror pairs using acetone. The final test optic is seen in Figure 11.

Results

The assembled KB microscope mirror pairs were tested in the LLE X-Ray Laboratory. Figure 12 shows a schematic of the x-ray testing device. Five exposures of a Cu 25 μm mesh were taken. Figure 13 shows one sample exposure. The three images seen are not in a straight line as desired. One mirror-pair image is not visible on the images, likely due to a large tilt error introduced in the assembly process. Table 1 shows the placement error of the mirror pairs on the base. These numbers, when multiplied by the magnification 12.85, result in the error in the image due to the misplacement. Small placement errors during assembly demonstrate that only ~ 1 mm of image error is due to misplacement. Angle error thus accounts for the majority of the image error. If the error due to misplacement is assumed to be 1 mm, then the remaining error is contributed by wedge construction error. The angle error can be calculated using the following formula,

$$\Delta i = \frac{\delta x'}{2pM}, \quad (4)$$

where (See Figures 3 and 7) Δi is the angle error, $\delta x'$ is the distance the image is away from where the ideal image would be, p is the distance from the object to the mirror, and M is the magnification (12.85) for this experiment. Given the image positions as seen in Fig. 13, the inferred shim errors are between 0.06 and 0.02 degrees. This additional error (compared to 0.007 and 0.004 deg) was likely made during assembly, and was likely due to misalignment of the mirror pairs with the optic base. As the micropositioner was a flat surface and the mirrors had a

tilted shim on them, it is likely that the mirror pairs were not placed flat on the optic base, thus contributing to the error of the images.

Conclusions

KB mirror pairs were assembled in a high-speed framing camera format, such that a single column of images was to appear when exposed to x rays. Accurate wedges were built using glass slides and epoxy to better than the desired angular accuracy (~ 0.01 deg). A test assembly with these glass wedges was performed to measure the relative placement of the images produced by the tilted KB mirror pairs. The images were found to be mislocated with respect to the desired positions by much greater than 1 mm (~ 10 mm) indicating a very large tilt error. Since the wedges were accurately manufactured it is likely that an error in tilt was introduced in assembly. This error may have also been introduced by radial placement errors. The tilt error needs to be lower than 0.01 degrees to assure properly placed images. Once the alignment problem is solved, high-speed framing cameras coupled to KB optics promise to provide a significant enhancement to LLE capabilities.

Acknowledgements

I would like to thank my advisor, Dr. F. J. Marshall, for allowing me this opportunity to work with him, as well as for his patience when I needed assistance; Dr. R. S. Craxton for hosting the Summer High School Program which gave me the chance to work at LLE. I would also like to thank the numerous scientists and engineers who facilitated the completion of the project around LLE, as well as my fellow high school participants. The experience I gained from the aforementioned people will continue to be of value to me throughout university, and onward in my scientific endeavors.

References

1. Laboratory for Laser Energetics, *About OMEGA*,
<http://www.lle.rochester.edu/omega_facility/omega/>, 27 August 2013
2. G. H. McCall, SPIE, Bellingham WA, Vol. 106 *X-Ray Imaging*, 2 (1977)
3. P. Kirkpatrick, A. V. Baez, J. Opt. Soc. Am. **38**, 766 (1948)
4. D. K. Bradley, P. M. Bell, O. L. Landen, and J. Oertel, Rev. Sci. Instrum. **66**, 716 (1995)
5. F. J. Marshall, Rev. Sci. Instrum. 83, 10E518-1 (2012).
6. F. J. Marshall, Q. Su, Rev. Sci. Instrum., **725**, 66 (1), 1995
7. B. D. Cullity, S. R. Stock. Elements of X-ray Diffraction, Third Edition. (Prentice Hall, Inc., Upper Saddle River, NJ, 2001)
8. F. J. Marshall, J. A. Oertel, and P. J. Walsh, Rev. Sci. Instrum. 75 (10), 4045-4047 (2004).
9. *Advanced Materials: Araldite 1253 Resin*,
<<http://www.freemansupply.com/datasheets/Araldite/1253.pdf>>, 15 September 2013

Table 1. Table showing the mirror pair locations, ideal tilt angles, as-built angles, and as-measured angles of the four mirror pairs. Also included is the angle and radius where each pair was placed, as well as the placement error of each pair.

		Tilt Angle (degrees)			Optical Base Placement		Placement Error
Mirror pair	Assignment	Ideal	As Built	Measured	θ (degrees)	R (mm)	δR (mm)
1	Outer	0.408	0.393	0.401	45.00	4.39	0.131
2	Middle	0.520	0.509	0.516	18.43	4.74	0.013
3	Middle	0.520	0.509	0.516	-18.43	4.74	0.033
4	Outer	0.408	0.393	0.401	-45.00	4.39	0.098

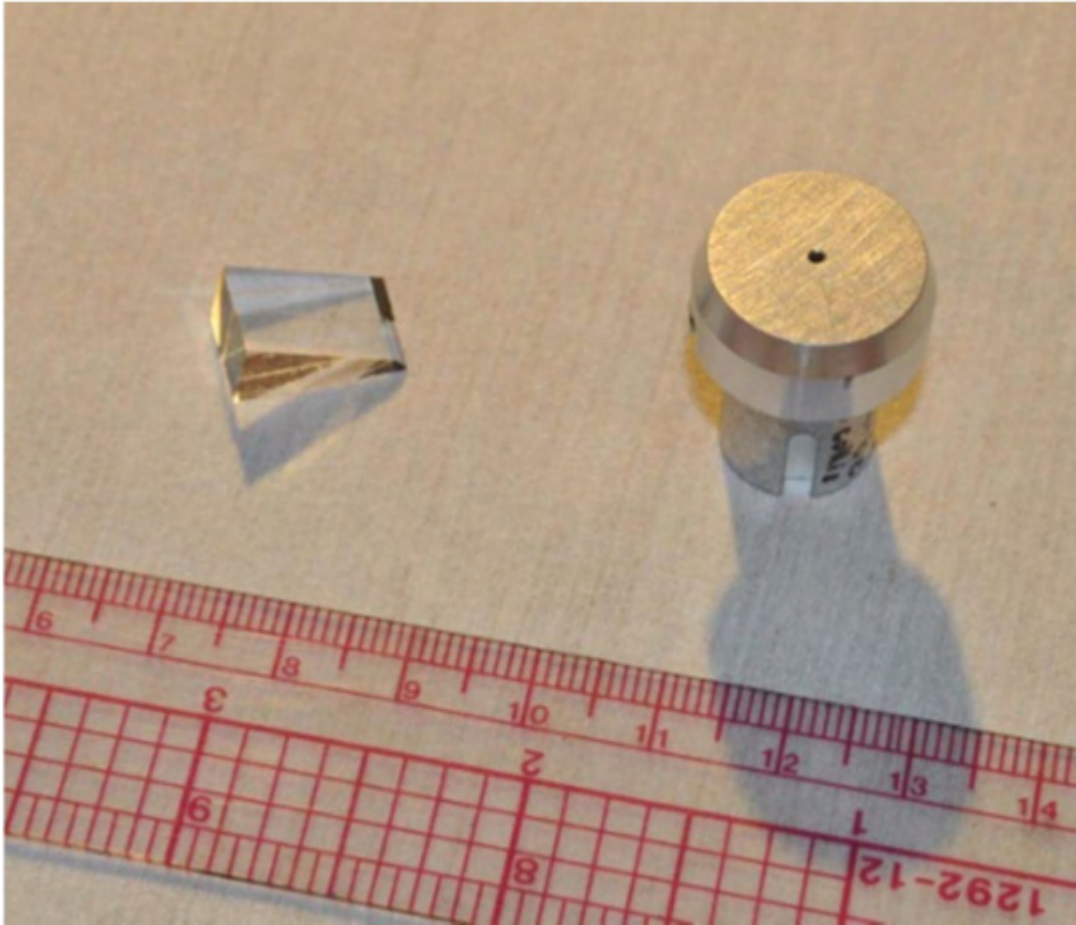
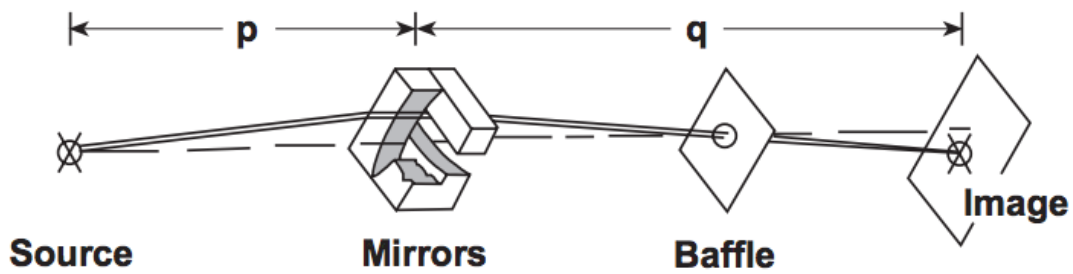


Figure 1. Photograph showing a KB mirror pair (left) and a pinhole camera (right). The two x-ray reflecting surfaces are located on the right of the mirror pair, at the tip of the wedge, and are mutually orthogonal.



E8640

Figure 2. Schematic of a combination of two KB mirror pairs, perpendicularly arranged such that the image is in focus, such that the mirrors are the correct distance from the source p and distance from image q . A baffle is also in place to prevent unfocused x rays from appearing on the image plane. (This figure appears as Fig. 1 in ref. [8]).

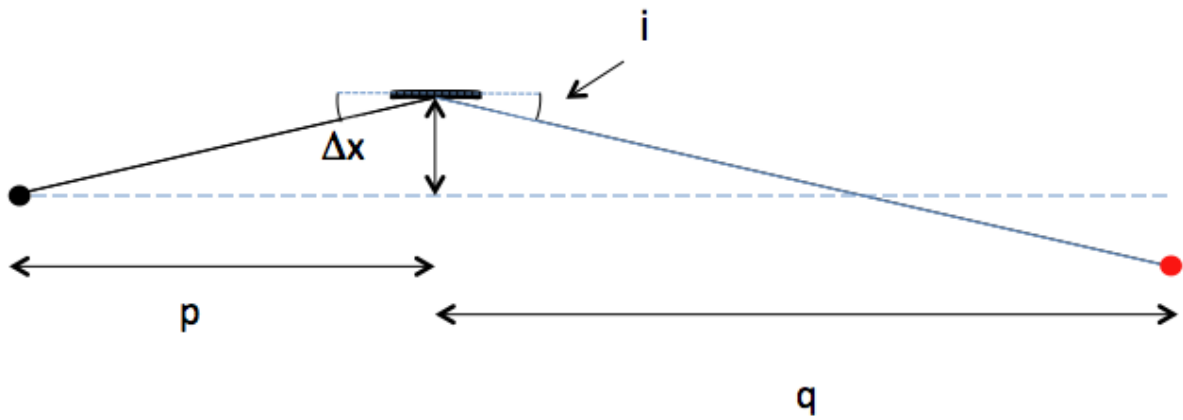


Figure 3. Side view of x rays reflecting off a focused KB mirror. Δx is the distance from point of reflection to optical axis, p is the distance from object to point of reflection, q is the distance from point of reflection to image, and i is the angle of incidence of the x rays off the mirror.

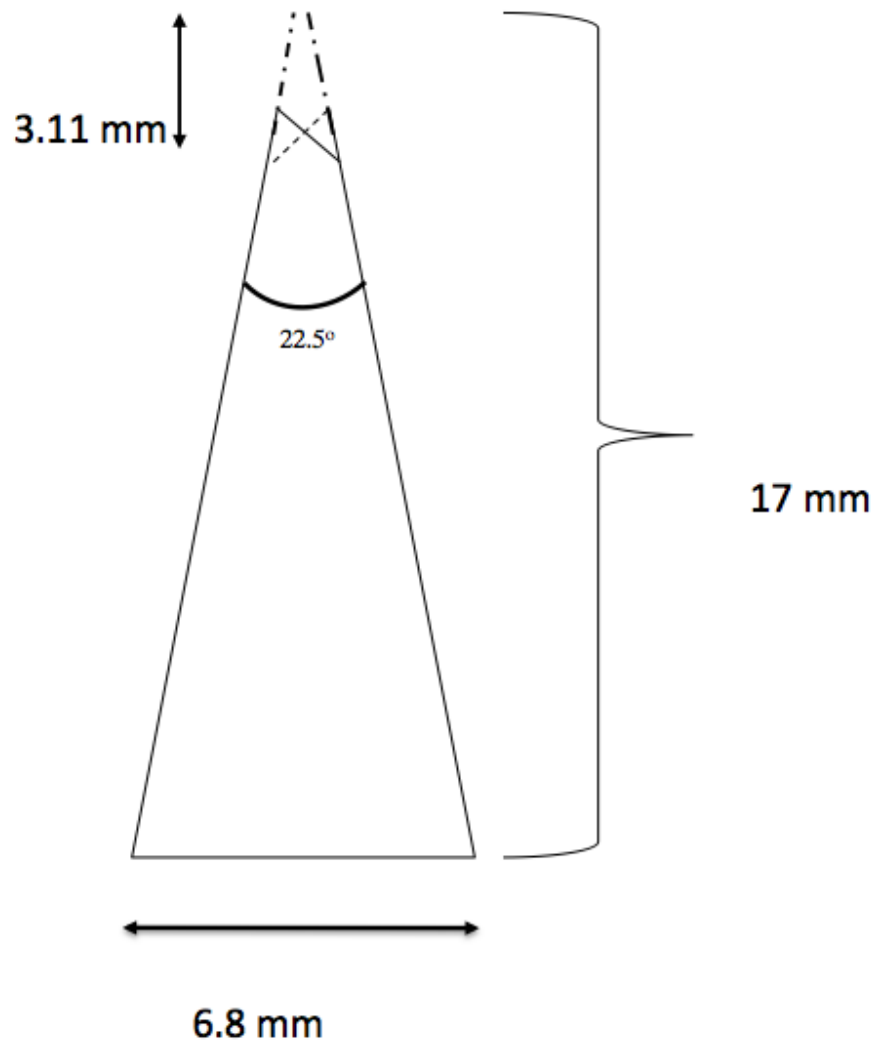


Figure 4. Diagram of a single KB mirror pair viewed edge on, with a continuation of the triangle (dash-dot) after it has been cut, to demonstrate the original length of 17 mm.

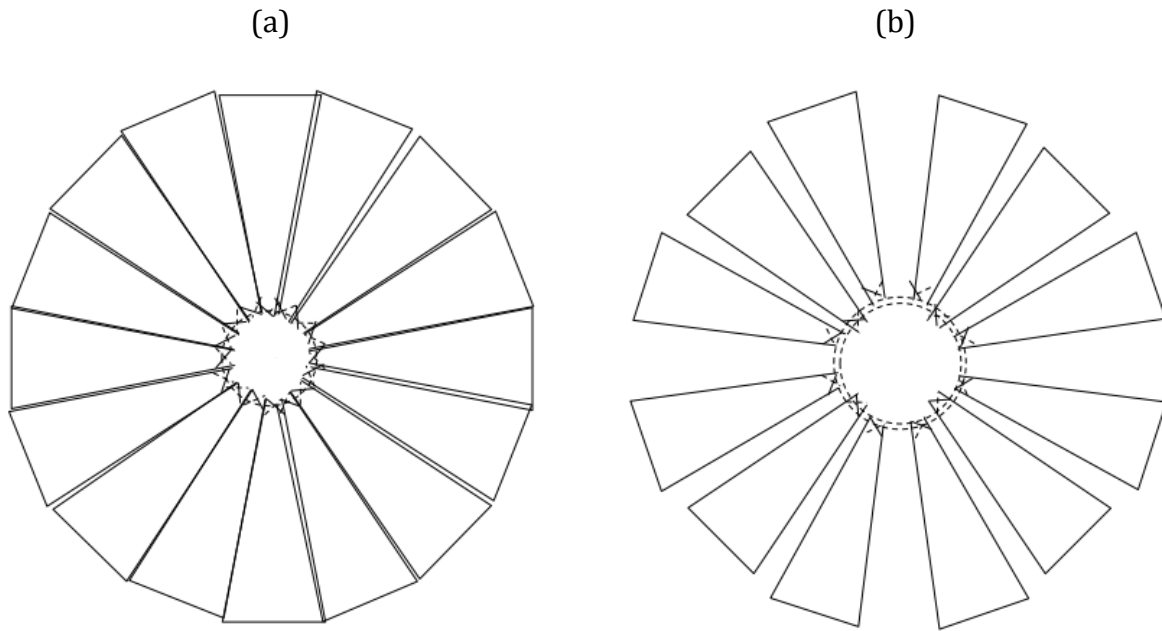


Figure 5. Schematic of two arrangements of KB mirror pairs on an optical base. (a) 16 uniformly spaced mirror pairs that produce a ring of 16 images; (b) 12 out of a set of 16 mirror pairs proposed to produce a rectangular array of images.

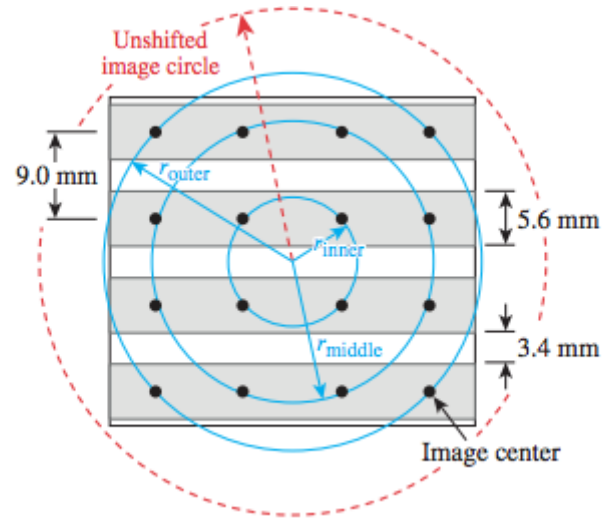


Figure 6. Schematic of a 4-strip framing camera, with three concentric circles overlaid to show how images would be arranged. (This figure appears as Fig. 6 in ref. [5]).

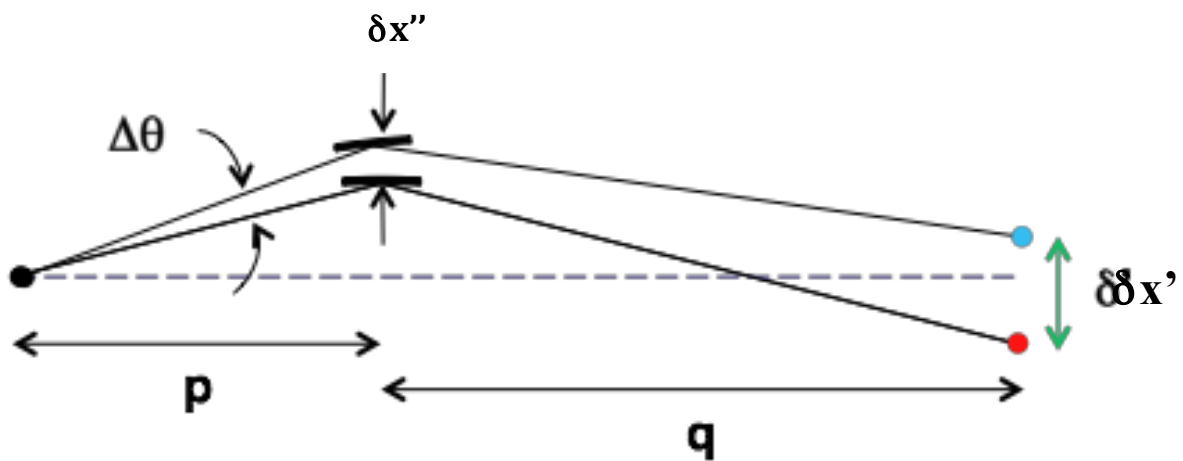
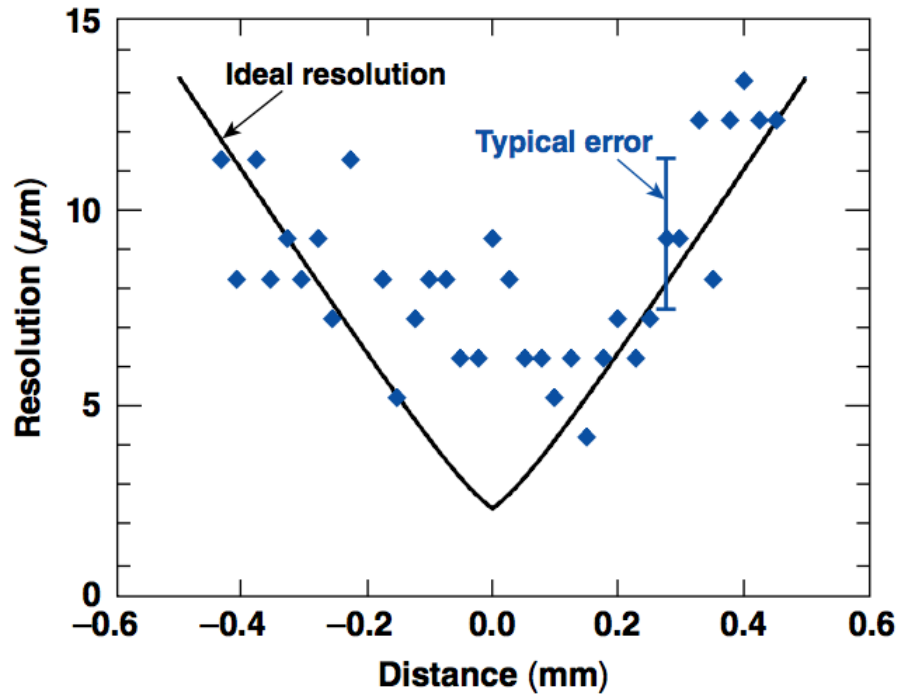


Figure 7. Side view of a tilted mirror and the effect on the image location. $\Delta\theta$ is the change in angle, p is the distance from object to mirror, q is the distance from mirror to image, $\delta x''$ is the mirror's change in distance away from the optical axis, and $\delta x'$ is the resulting change in the image location.



E8626b

Figure 8. Chart showing the decrease of resolution as distance error increases from the ideal case. (This figure appears as Fig. 4 in ref. [5]).

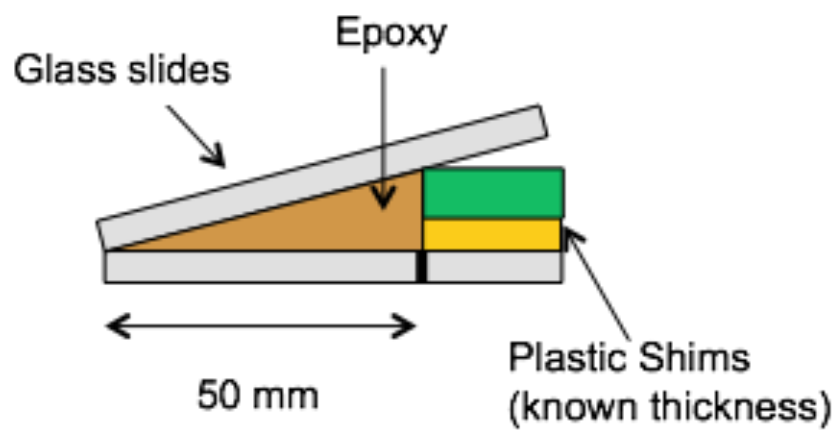


Figure 9. Diagram showing an exaggeration of the wedge assembly. The shims are typically ~15 mm thick.

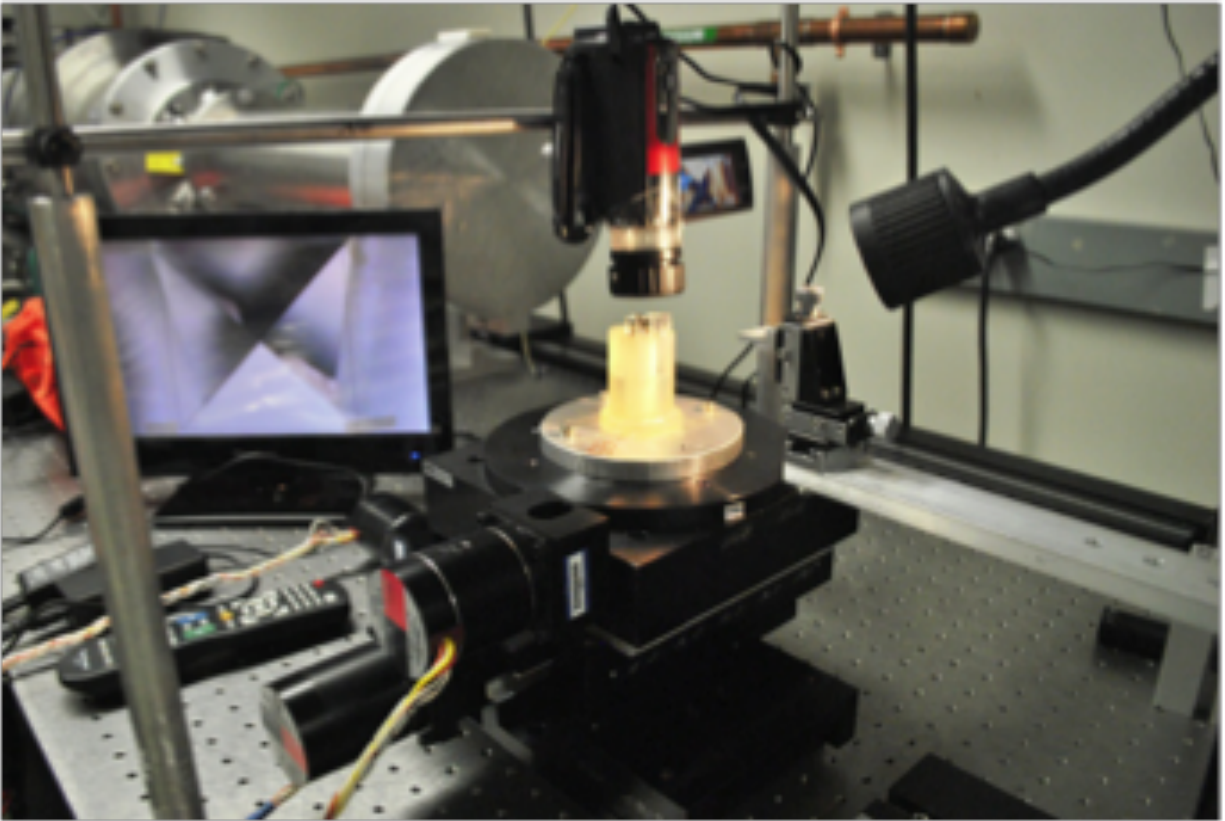


Figure 10. Photograph of the experimental set up. The sliding stage can be seen in the lower right, the light source in the upper right. The viewing screen, with the mirror pair at the crosshairs, can be seen far left. The optical base is seated on the stepper-motor tables in the middle, and the video camera sits above it, with the attached magnifying lens.

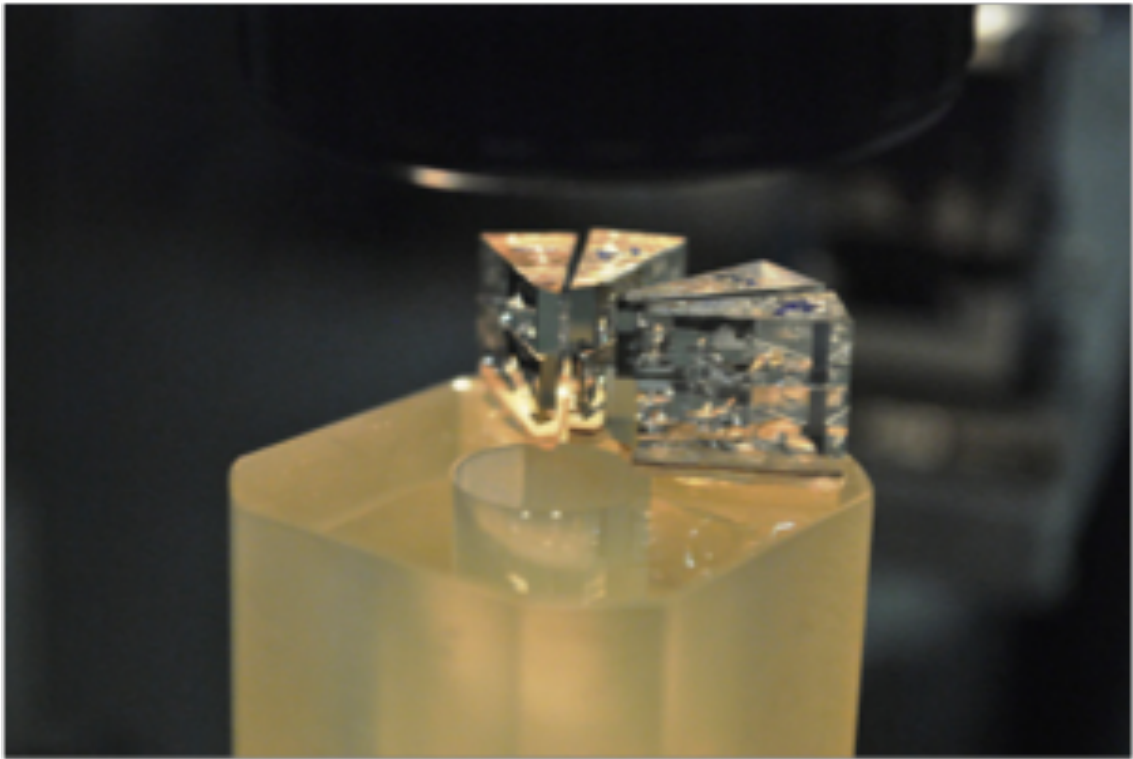
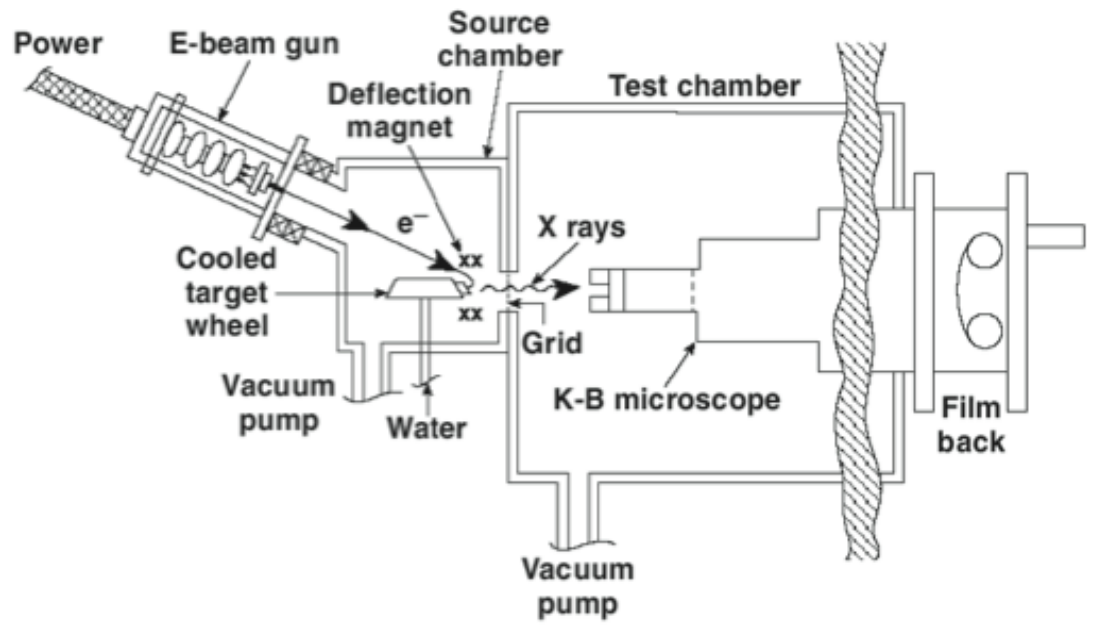


Figure 11. Photograph showing the final test optic. The mirror pairs are fastened to the optical base using UV-cured epoxy.



E14829

Figure 12. Schematic of the X-ray testing chamber. The e-beam from the upper left hits a copper target (middle left), and the resulting x-rays are aimed into the test chamber.

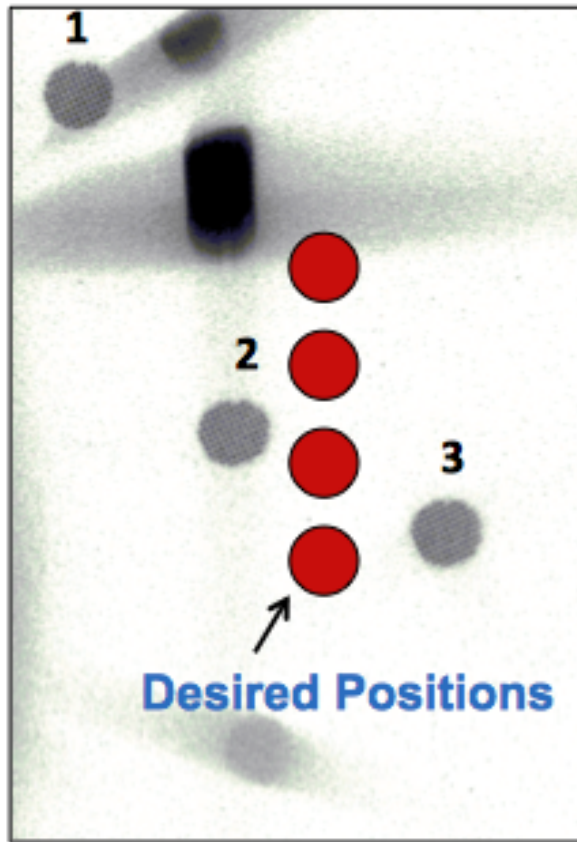


Image plate x-ray exposure

Figure 13. Image from the test x-ray exposure film pack. The ideal locations are overlaid in red, showing the significant error in the locations of the resulting images (1, 2, and 3). The desired positions' centers are separated by 9 mm.

Catalytic Oxidation of Hydrogen in Air Streams

Sara Gnolek

Webster Thomas High School

LLE Adviser: Walter Shmayda

Laboratory for Laser Energetics

University of Rochester

Summer High School Research Program 2013

November 2013

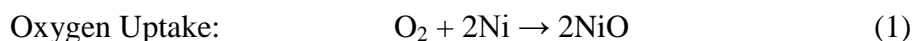
Abstract

At LLE, a zirconium-iron (ZrFe) alloy recovers tritium that has escaped from process systems. Tritium in air streams cannot be captured with ZrFe alloy because oxygen retards the alloy's function to remove tritium and consumes the alloy. A copper/zinc (Cu/Zn) alloy bed was tested as an alternative method for capturing hydrogen. Helium, oxygen, and hydrogen were all flowed through a Cu/Zn bed pre-loaded with oxygen at the same time, and the hydrogen concentration was not elevated in the outlet stream; it was captured and formed water. The alloy was determined to have the ability to function as a catalyst. To increase the efficiency of the catalytic function, tests were performed analyzing oxygen gettering and oxidation of hydrogen. Increasing the temperature of the alloy bed increases the time it takes to fill the bed to full capacity, along with the amount of oxygen that can be absorbed by the Cu/Zn alloy. Hydrogen oxidation improves when the flow rate of the carrier gas (helium) is increased and when the temperature is also increased.

1. Introduction

Tritium is usually contained in gloveboxes to decrease its escape to the environment. The inert gas helium is used in process equipment because elemental hydrogen (T_2) can be recaptured in a zirconium-iron alloy (ZrFe) bed. Minute amounts of nitrogen, oxygen and water (N_2 , O_2 , H_2O) seep into the glove box along with the tritium. These gases contaminate the helium gas. The ZrFe bed can be consumed by oxygen and hydrogen in water molecules which decreases the effectiveness of the ZrFe bed and retards its ability to capture tritium.¹ These contaminant gases are currently cycled through a drier to capture the water, and an oxygen getter to remove the oxygen.

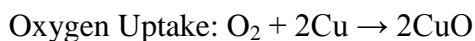
Upstream of the ZrFe bed, a molecular sieve bed is placed to remove water from the air stream. Currently at LLE, a nickel bed is placed after the molecular sieve to remove oxygen.² Once the bed is consumed, the bed can be regenerated with hydrogen.³ The equations for the nickel bed are:



The oxygen is being absorbed by the bed, and then the bed is regenerated and water is formed.

In this experiment, a copper/zinc alloy (Cu/Zn) was tested for its ability to remove oxygen from an air stream and be regenerated with hydrogen. The purpose of this experiment was to test the Cu/Zn alloy's oxygen getting and hydrogen regeneration capacity and to understand how conditions such as temperature, flow rate and pellet size affected the efficiency.

The equations for this process are:



The alloy's ability to function as a catalyst when both air and tritium were flown through the bed, where the tritium was captured by the bed and then removed by bonding with the oxygen to form tritiated water, was also tested. The parameters which affected the ability of the alloy to capture tritium and convert it into tritiated water were tested. This could be used in situations other than in the glovebox, where air has been contaminated by tritium.

2.Experimental

A system was built to test how oxygen gettering by Cu/Zn alloy is affected by temperature and flow rates. As seen in Figure 1, there are three cylinders containing He, 1% O₂ in He, and H₂.

The gases flow either through the bed or through the bypass. The gases are monitored after the bed by the atmospheric sampling system. An RGA (residual gas analyzer) measures the partial pressures of gases in the system. Oxygen, nitrogen, helium, hydrogen and water were monitored.

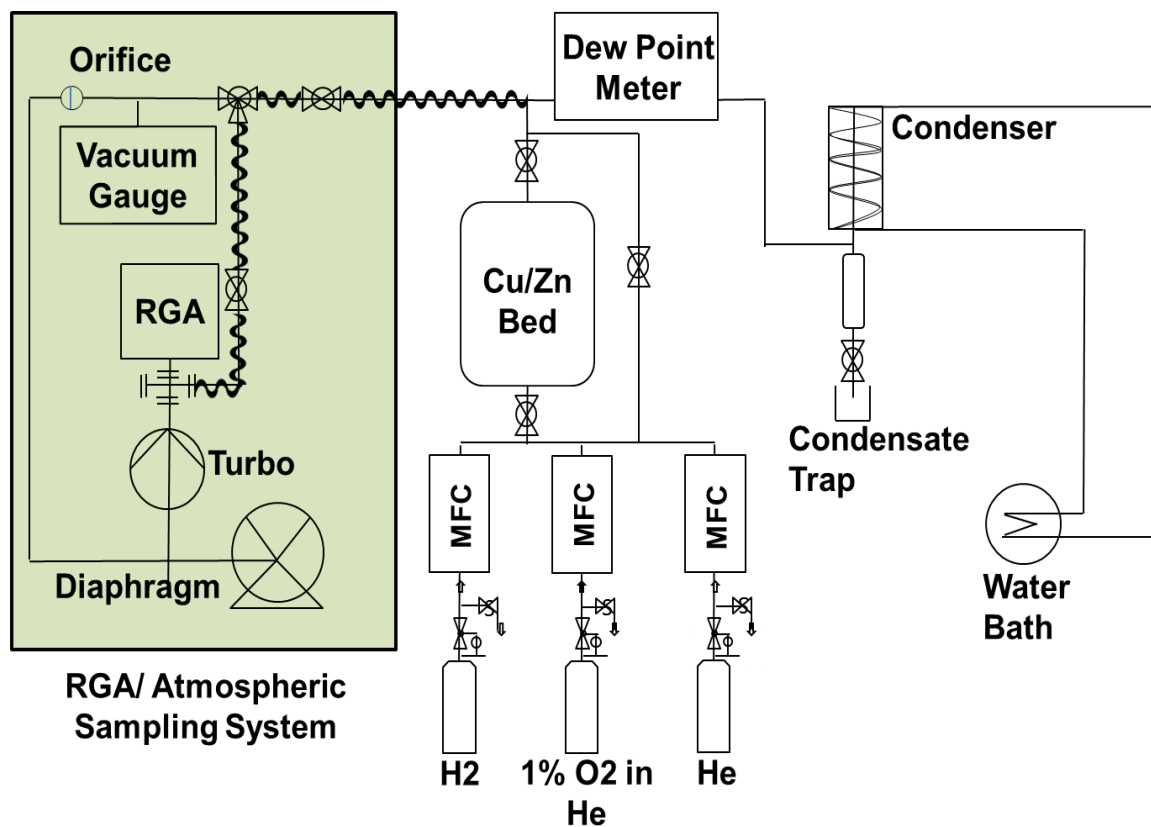


Figure 1. Schematic of experimental system

Nitrogen was measured to ensure that no air leaked into the system. The total pressure could also be measured. Thermocouples were located on the inlet and outlet streams, as well as on the bed and were monitored using a National Instruments data acquisition system. A dew point meter was placed after the bed and was recorded with the National Instruments system.

The catalyst bed and the capillary tubing were heated. The capillary tubing heated the gases from the outlet of the bed to the RGA. The alloy's temperature ranged from room temperature to 200°C. The capillary tubing was set to 120°C.

The Cu/Zn catalyst used for this experiment is 40% copper and 40% zinc, with alumina for balance. Two size pellets were used, 3mm (width) x 3mm (diameter) and 3mm x 5mm cylinders. The surface area was about 100 m²/g for both sizes.

Three gases were used to test the Cu/Zn alloy bed. Mass flow controllers (MFC's) regulate the flow rates of these gases. Helium was flowed at the rate of 5 L/min as a carrier gas and to purge the system of air or previous gases. Helium flowed at rates between 1 L/min and 2 L/min. 1% oxygen in helium was used to load the bed with oxygen, for both oxygen getting testing and catalytic experiments. Hydrogen was used to regenerate the bed and in the catalytic experiment. H₂ was flowed at rates of 10 sccm-100 sccm (standard cubic centimeters per minute). Gases were flowed through the bypass for calibration.

While the bed is being loaded with oxygen, breakthrough is defined when the O₂ concentration reaches 0.01% in the outlet stream, which is monitored using the RGA. During the oxygen gettering capacity tests, the partial pressure of the oxygen gas in the outlet stream during the loading phase is less than the inlet stream because oxygen is being removed from the stream by the alloy bed. The alloy bed is no longer absorbing all of the oxygen from the inlet stream when breakthrough occurs, and its ability to effectively remove oxygen deteriorates at breakthrough.

3. Results and Discussion

3.1 Oxygen Uptake

The Cu/Zn alloy bed's capacity for "gettering", or removing oxygen from air streams, was tested at 30°C, 100°C and 200°C. 1% O₂ in He was flown at 5 L/min through the bypass in

order to get a reference reading of the inlet partial pressure of the oxygen. Then the Cu/Zn alloy bed's valve was opened and the bypass was shut off, and the partial pressure of oxygen in the outlet stream was measured as a function of time. Breakthrough was defined to occur when the O₂ concentration in the outlet stream reached 0.01%. The results can be seen in Figure 3.1 and Table 3.1. The two curves at each temperature corresponds to the two different particle sizes, with the color code given in Table 3.1.

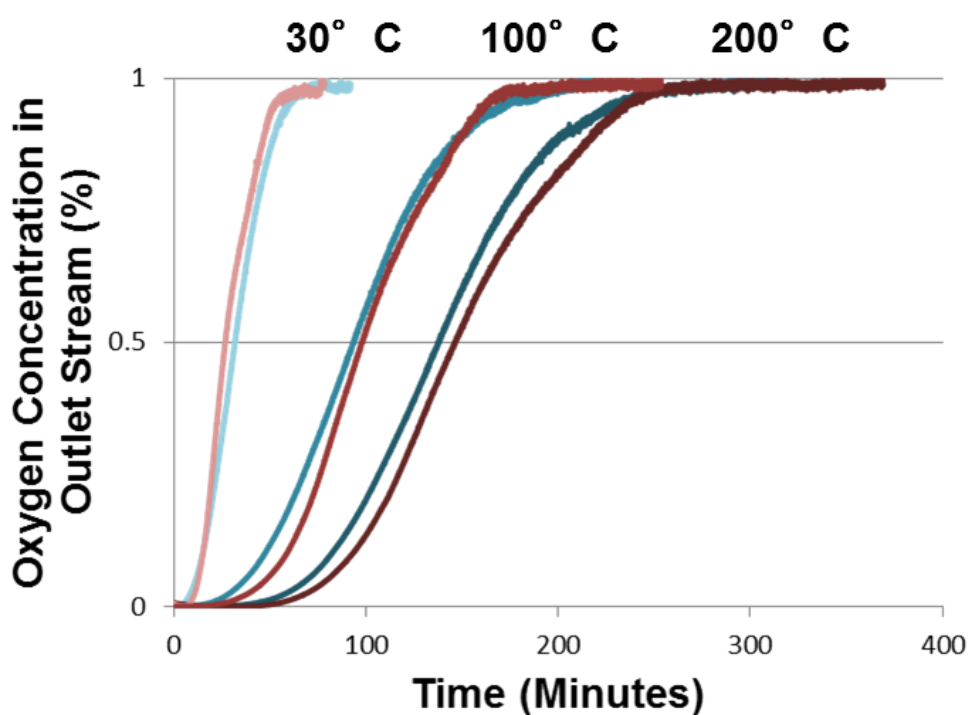


Figure 3.1 The concentration of oxygen in the outlet stream over time for different temperatures.

	3mm x 3mm				3mm x 5mm		
Temperature (° C)	30	100	200		30	100	200
Time to *Break-through (Minutes)	9.1	29.4	58.2		6.2	21.3	46.7
Time to 90% Capacity (Minutes)	37.2	114.8	165.1		41.2	144.5	154.5
Capacity (% Cu consumed)	11.3	38.7	57.6		13.2	38.7	55.9

Table 3.1 Breakthrough times and capacity of Cu/Zn beds

It was found that as temperature increases, the time to reach breakthrough increased. This can be seen in Table 3.1. The time until breakthrough increased with the 3mm x 3mm particle bed because there is less gas channeling around the particles on the side of the bed container.

The fraction of the Cu/Zn bed consumed as a function of time was also examined for each temperature and presented in Figure 3.2, which has the same color code as Table 3.1. The time until 90% capacity can be seen in Table 3.1. At 200°C, 57.6% of the bed was consumed by oxygen, compared to 11.3% consumed at 30°C. The bulk of the alloy is being consumed at the higher temperature whereas only surface copper is oxidized at room temperature. At the higher temperature, both the time to breakthrough and the capacity of the Cu/Zn alloy to consume oxygen increase.

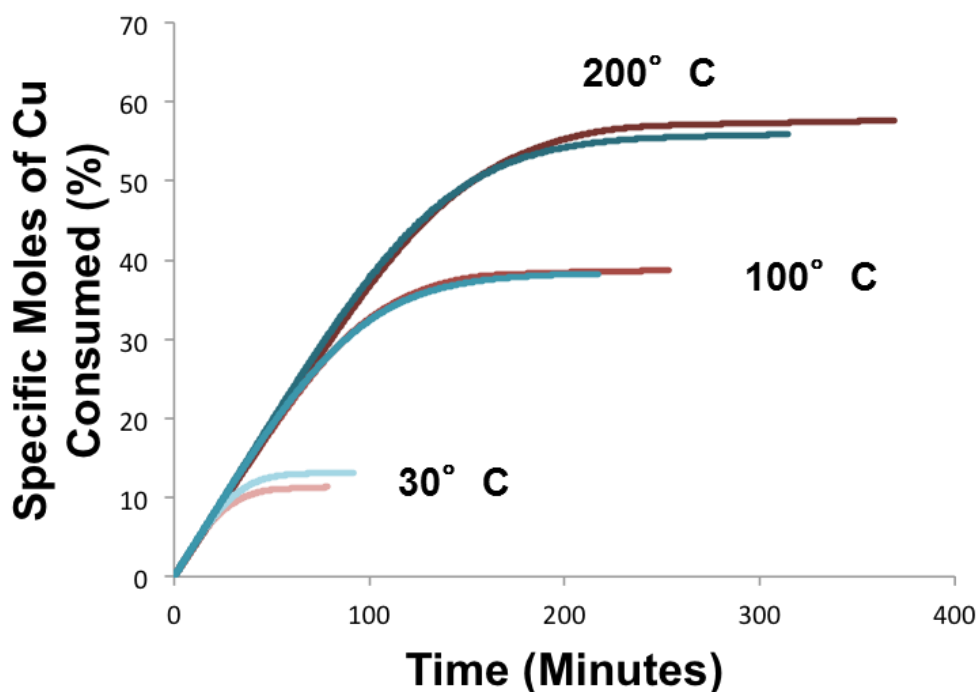


Figure 3.2 Consumption of CuZn bed over time

3.2 Copper Regeneration using Hydrogen

The cupric oxide formed by oxygen gettering can be reduced back to copper using hydrogen. The bed can then be re-used for additional oxygen gettering. Hydrogen was flown at 100 sccm for all tests. The ability to regenerate the oxidized alloy was tested at 100°C, 150°C, and 200°C, and at helium purge gas flow rates of 1 L/min, 1.5 L/min, and 2 L/min. The hydrogen partial pressure and water partial pressure were measured. The effect of varying the carrier (Helium) gas concentration can be seen in Figure 3.3. Starting with 1 L/min, the concentration of hydrogen in the outlet stream decreased with each increase in carrier gas concentration. This is because the efficiency of the regeneration process improved with increased purge rate. As the copper oxide is reduced, water vapor is formed and must be removed from the vicinity of the alloy in order for more copper oxide to be reduced. The increased flow rate decreases the amount

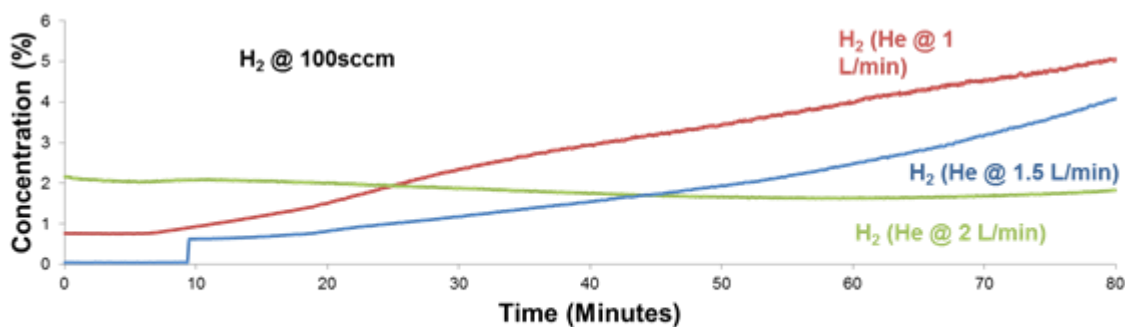


Figure 3.3 Concentration of hydrogen in outlet stream over time

of water vapor present around the alloy and allows more hydrogen to be used, thereby decreasing the outlet concentration of hydrogen.

Increasing the temperature also affected the regeneration, as can be seen in Figure 3.4, which shows the concentrations of hydrogen and water as a percent of their total possible concentrations in the outlet stream, or the concentrations of the gases compared to their total

bypass of the alloy bed concentrations (100%). As the temperature increased over time, the regeneration increased until the bed was completely regenerated. With each increase in temperature, more hydrogen was consumed for copper oxide reduction, and more water was produced. In the beginning of the run, the low temperature allows almost no capture of hydrogen,

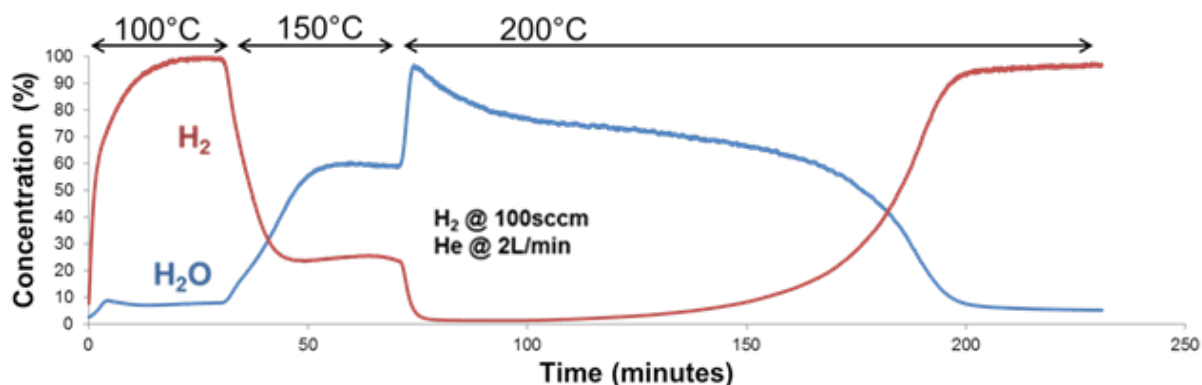


Figure 3.4 Concentrations of hydrogen and water in outlet stream over time with increasing temperature

so most of it passes through the bed and the concentration is very high. Towards the end of the run, the alloy is nearly regenerated and the amount of copper oxide available to be reduced drops. Consequently the water concentration in the outlet drops. Increasing the temperature decreases the time needed to regenerate the bed.

3.3 Catalytic Ability

The ability of the Cu/Zn alloy to function as a catalyst was tested. A catalytic bed would use oxygen from an air stream to transform elemental hydrogen into water without altering the alloy. In this case, the Cu/Zn functions as a pseudo-catalyst in that hydrogen can remove oxygen from the alloy but oxygen in the carrier will replace the missing oxygen on the alloy.

In the first test to determine if catalytic function was possible, hydrogen was flown at 100 sccm, and 1% oxygen in helium was flown at 5 L/min. The alloy temperature was set at 200°C because the efficiency for both oxygen getting and hydrogen regeneration improved with increased temperature. The results can be seen in Figure 3.5. Concentrations of hydrogen,

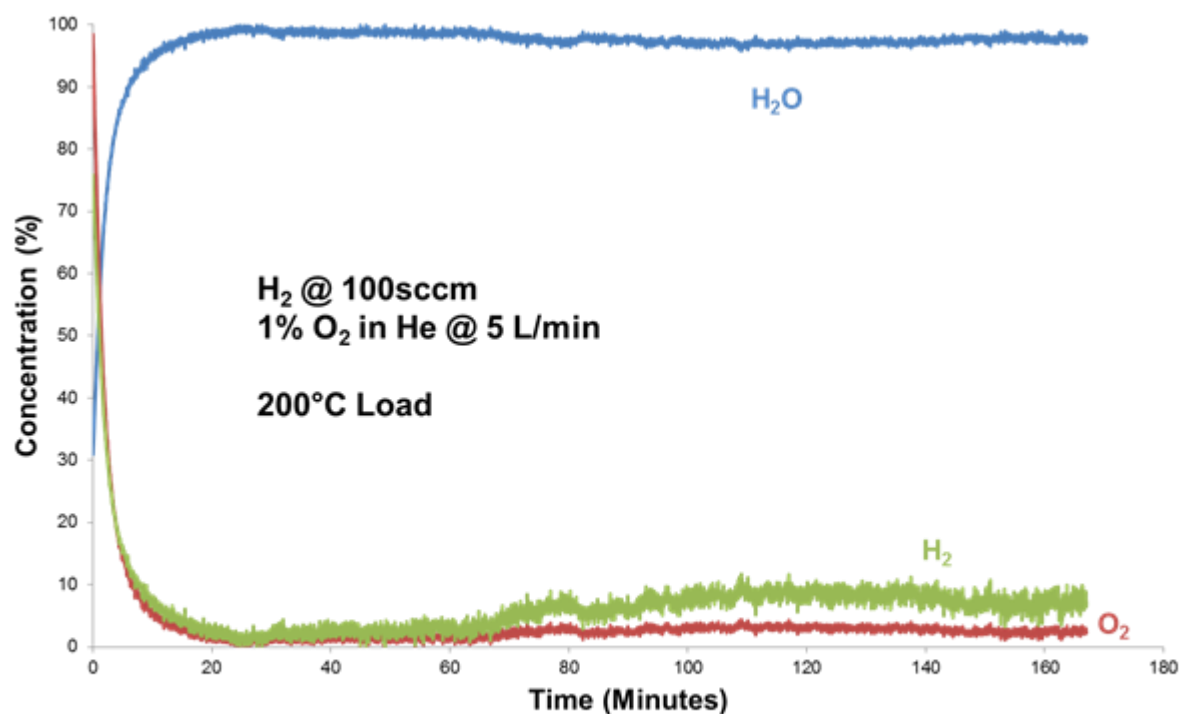


Figure 3.5 Catalytic function of Cu/Zn alloy

oxygen and water compared to their individual complete bypass concentrations are shown. Hydrogen was only seen with very small concentrations in the outlet stream, and oxygen breakthrough did not occur even though the experiment ran beyond when breakthrough would normally occur for the 200°C case. This indicates that the oxygen was being removed from the bed while the oxygen entrained in the carrier oxidized the alloy. Catalytic function is shown to be possible.

Since slight concentrations of hydrogen were seen in the outlet stream, it seems that the conversion efficiency was less than 100% in this case. The amount of hydrogen in the air stream overwhelmed the alloy's ability to convert the hydrogen to water. As H_2O is formed, there is twice as much hydrogen as oxygen in the air stream. It appears that it is necessary to operate in a condition where excess oxygen is present for complete oxidation of the hydrogen to occur.

In the second catalytic test the oxygen concentration was increased so that the ratio of hydrogen to oxygen was 1:5, but since the molecular formula for water contains twice as many hydrogens as oxygens, the ratio for the amount of possible water formation is 1:10. This is a more realistic approach, as there will be at least 5 times more oxygen in the carrier as there would be in any conceivable tritium release to the air, as much as $1:10^9$. The hydrogen flow was decreased to 10 sccm for this experiment. The results can be seen in Figure 3.6. H_2 was flown at

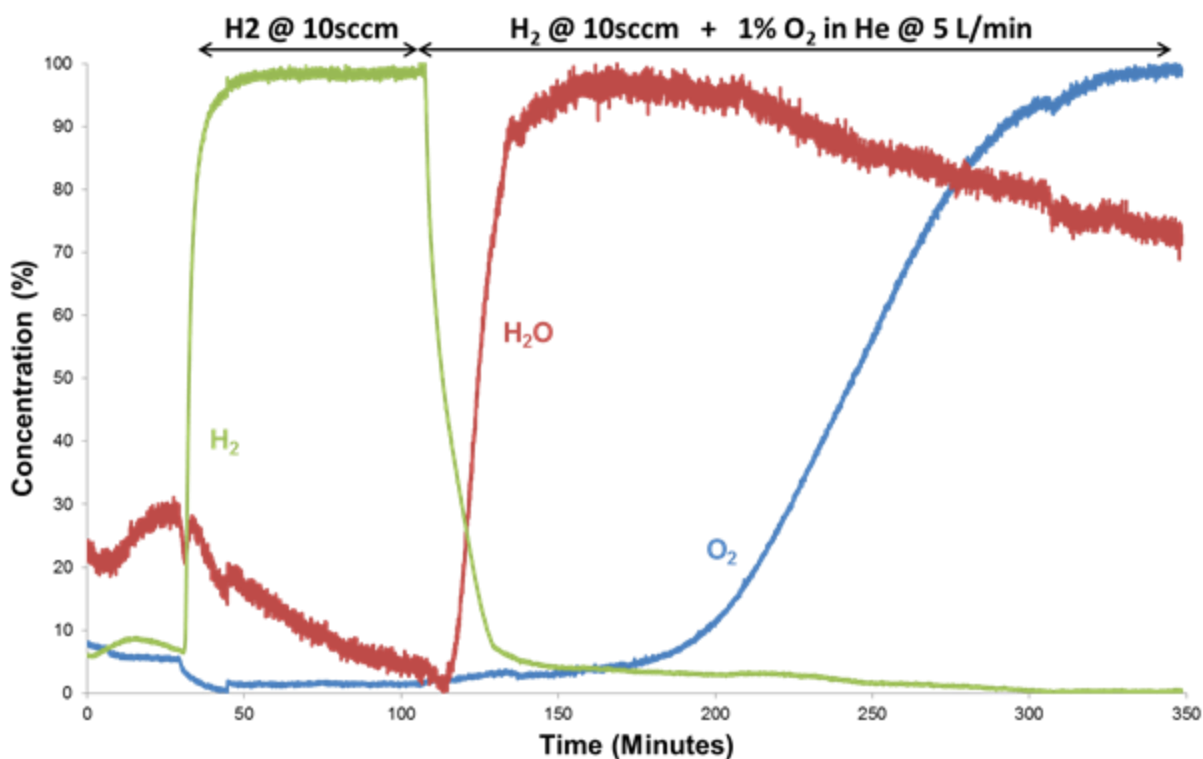


Figure 3.6 Catalytic function with 10:1 oxygen to hydrogen ratio

10 sccm until approximately 100 minutes, and then 1% O₂ in helium was flown at 5 L/min. When oxygen was introduced, the hydrogen concentration dropped to zero over the next 100 minutes. The addition of oxygen captures the hydrogen from the air and bonds into water, which is why the water concentration suddenly increases when oxygen is added. Oxygen overwhelms the hydrogen as there is much more than needed to fully capture the hydrogen so its concentration rises, as expected, when the alloy becomes fully oxidized. This experiment indicates that the Cu/Zn alloy has the ability to function as a catalyst for tritium removal at realistic ratios of hydrogen to oxygen.

The temperature of the alloy bed was varied in the third catalytic experiment to try and find

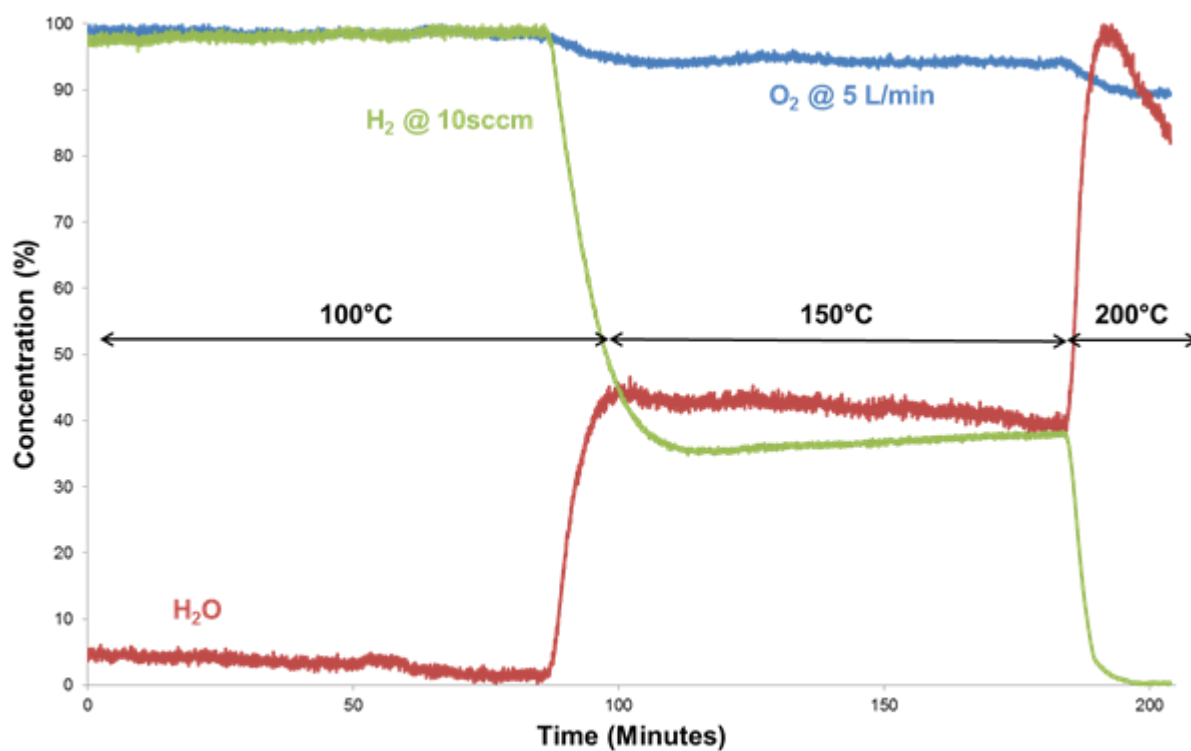


Figure 3.7 Catalytic function with increasing temperature over time

the optimal temperature for continuous catalytic function. The alloy bed was started at a low

temperature, with 0.01% O₂ in He at 5 L/min, and H₂ at 10 sccm, or the same ratios and setup as the previous experiment, beside temperature. Alloy temperatures of 100°C, 150°C and 200°C were used. The results can be seen in Figure 3.7. Each time the temperature was increased, less hydrogen was seen in the outlet stream. At the final temperature, 200°C, the hydrogen concentration at the bed outlet dropped to background values. This test reveals that higher temperatures improve catalytic function significantly. Operating the bed at 200°C ensures that hydrogen is being captured fully.

Conclusion

Experiments were performed to find optimal conditions for Cu/Zn oxygen gettering, hydrogen regeneration, and catalytic function. Increasing the bed temperature from 30°C to 200°C improves oxygen gettering capacity and increases the time until oxygen breakthrough. Regeneration is more efficient as flow rate of the carrier gas and temperature increase. Catalytic function is possible with the Cu/Zn alloy. Conversion efficiency improves with higher ratios of oxygen to hydrogen and increasing temperature. Higher temperatures are preferred for oxygen gettering, hydrogen regeneration and catalytic function.

Discovering that the Cu/Zn has the ability to be a catalyst is very beneficial to LLE. It can be operated at much lower temperatures than other catalyst options, and it would eliminate the need for an oxygen getter and its frequent regeneration. This is a very efficient solution to tritium removal from air streams.

Acknowledgements

I would like to thank Dr. Craxton for allowing me to be a part of the internship program. It has been such a valuable experience. I also would like to thank my advisor Dr. Shmayda, and Neil Redden, for the knowledge and advice they have given me. My lab partners Sam Goodman, Aaron Jo, Andrew Boyce, and the other high school interns for their help and support.

References

1. W. T. Shmayda, N. P. Kherani, and A. G. Heics, "Tritium removal from noble gas streams," *Journal of Vacuum Science & Technology A: Vacuum, Surfaces, and Films* 6 (3), 1259-1262 (1988).
2. MaryKate Hanchett, *Oxygen Uptake Using a Nickel Catalyst*. LLE High School Program Project Report (2012).
3. W. T. Shmayda, N. P. Kherani, B. Wallace, and F. Mazza, *Fusion Technol.* 21, 616 (1992).

Detecting Hydrogen in Helium Streams

Samuel Goodman

Pittsford Mendon High School

Rochester, New York

Advisor: Dr. Walter Shmayda

Laboratory for Laser Energetics

University of Rochester

Rochester, New York

September 2013

Abstract

Three different approaches to detecting hydrogen in helium streams were assessed: thermal conductivity, atmospheric sampling using a mass spectrometer, and permeation through a palladium/silver membrane. The thermal conductivity detection system utilized an assembly of four cells fitted with filaments wired to make a Wheatstone bridge. Pure helium flowed through two of the cells. Helium containing hydrogen passed through the remaining two cells. The filament temperature, which is determined by the thermal conductivity of the gas surrounding the filaments, depends on the hydrogen concentration in the helium carrier. In the atmospheric sampling approach, a slip-stream is drawn from the carrier via two differentially pumped orifices and injected into a vacuum system. The vacuum system is fitted with a mass spectrometer tuned to hydrogen. In the permeation approach, the helium stream is passed over a hot palladium/silver (Pd/Ag) membrane. Hydrogen permeates through the membrane to increase the pressure in a vacuum system. The change in the vacuum pressure is directly related to the hydrogen concentration in the carrier on the upstream side of the membrane. The Pd/Ag permeation approach proved to be the most sensitive hydrogen detection technique. This approach was used to investigate the performance of a cryotrap. Several interesting phenomena were detected when evaluating the cryotrap. A large but brief breakthrough occurs when the column reaches capacity, and hydrogen elution can occur when the full, cold column is purged with helium.

Introduction

The University of Rochester Laboratory for Laser Energetics (LLE), whilst carrying out internal confinement fusion experiments, utilizes tritium gas, one of the reactants required for the fusion process, in the fabrication of its cryogenic targets. Tritium processing equipment is

typically encased in a glovebox to prevent the release of the tritium to the environment. Helium is used as a purge gas in the glovebox. Any tritium that has been released from process equipment is swept out of the glovebox and collected by zirconium-iron (ZrFe) alloy. Annually, the ZrFe alloy is removed from the box circulation loop to recover the tritium. Tritium is released from the alloy into a helium carrier stream by heating the ZrFe to 450° C. One proposed method for recovering the tritium from this inert gas stream is a cryotrap.⁽¹⁾

The cryotrap is a specialized coil of stainless steel tubing filled with a molecular sieve. The helium containing tritium is flown through the cryotrap. When cooled to liquid nitrogen temperatures (77 K), the molecular sieve extracts tritium from the carrier stream, while helium flows out the other end of the cryotrap. When the temperature of the molecular sieve is raised above liquid nitrogen temperatures, tritium is released back into the carrier stream and exits the cryotrap. This way, tritium can be concentrated and recovered, minimizing risk and emissions.

To evaluate the cryotrap's ability to collect, store and release tritium, three systems for detecting hydrogen in a helium stream were proposed, constructed, and calibrated. For the sake of safety and convenience, tritium was replaced with hydrogen for all experiments, as its behavior is almost identical when interacting with the molecular sieve, the vacuum-backed membrane, and various detectors. The most sensitive system was then used to investigate the performance of the cryotrap.

System 1

The first detection system relied on a thermal conductivity detector (TCD). The TCD consists of four cells: two are used as reference, while the other two are used for the sample itself. These cells are aligned in a Wheatstone bridge configuration (figure 1). Hydrogen gas

flows through the sample cells in a helium carrier, while the reference cells are exposed to pure helium gas. When the concentration of hydrogen in helium changes through the sample cells, the thermal conductivity of the gas stream changes, causing a change in temperature of the cell's filament.⁽²⁾ This temperature change results in a changed resistance in the circuit shown in figure 1. The resistance change results in a different voltage output from the TCD. The Wheatstone bridge is balanced when gas compositions across all reference and sample cells are the same. When this occurs, the voltage output is zero.

This hydrogen detection system proved problematic. The thermal conductivities of hydrogen and helium are very similar, $0.1805 \text{ W}\cdot\text{m}^{-1}\cdot\text{K}^{-1}$ for hydrogen compared to $0.1513 \text{ W}\cdot\text{m}^{-1}\cdot\text{K}^{-1}$ for helium. Because the sample gas stream was primarily composed of helium, with the hydrogen concentration often less than 2% of the helium concentration, the signal-to-noise ratio of the TCD voltage output was low, regardless of the differences in gas flow rate and hydrogen concentration. The TCD was operated at temperatures ranging from 80°C to 200°C in an attempt to enhance the TCD's response relative to the helium carrier, but no significant difference in the signal-to-noise ratio was produced. Shielded cabling also failed to significantly reduce noise.

Options to improve hydrogen detectability include a more sensitive TCD, the implementation of a lock-in amplifier, or the use of an inert carrier gas with a thermal conductivity more remote from that of hydrogen.

System 2

The second proposed system relies on an atmospheric sampling system with an RF-quadrupole mass spectrometer. The schematic for this system can be found in figure 2. Gas flow

is initially regulated by two mass flow controllers (MFCs). The slip stream of the carrier gas is pumped through a precision micro-orifice. The delivery pressure of the hydrogen/helium slip stream is measured by the first ion gauge P_1 . From there, a sample stream passes through a second precision micro-orifice (leftward of P_1 in figure 2) and into the vacuum chamber created by the turbomolecular pump. The pressure of the sample stream is measured by the second ion gauge P_2 , and the pressures of the individual molecular components of the sample stream are measured by the RF-quadrupole within the residual gas analyzer (RGA). The flow rate through the second micro-orifice can be increased by increasing the upstream pressure measured by P_1 . All gas that is taken in with the slip stream, but is not part of the sample stream, is pumped out by the scroll pump. For the following tests, the carrier gas passed through the cryotrap bypass.

The effect of delivery pressure through the precision micro-orifice and changes in the flow rate were evaluated in order to characterize the RGA hydrogen detection system.

For the test in figure 3, 1% hydrogen in helium gas was flown in the carrier stream. The linear relationship between delivery pressure and hydrogen detector response in figure 3 shows that the pressure on the upstream side of the precision micro-orifice determines the gas flow into the vacuum. A four fold increase in the delivery pressure yielded a 28% increase in detected hydrogen. To first order, the detected signal was insensitive to the helium gas flow rate.

For the test summarized in table 1, only helium was flown in the sample stream. The hydrogen partial pressure detected by the RGA did not change with delivery pressure, but it did change slightly when the helium flow rate set by the MFCs increased. The very small hydrogen partial pressures indicate that the vacuum system is remarkably efficient at pumping out hydrogen.

Figure 4 illustrates the ratio between the partial pressures in figure 3 (with hydrogen flow) and table 1 (without hydrogen flow), and that ratio's dependence on flow rate and delivery pressure. This shows the system's ability to distinguish different hydrogen concentrations under varying delivery pressures and flow rates. The system can differentiate between an absence of hydrogen and the presence of very small quantities of hydrogen. Also of note is that the ratio becomes less dependent on delivery pressure at higher flow rates. Operating at 150 sccm eliminates the detector's dependence on delivery pressure.

While this system allowed for predictable and precise measurements of hydrogen pressure, it took a very long time for all hydrogen to be pumped out the system once introduced, and the flow rate through the micro-orifices had to be recalculated every time the upstream pressure was changed. It also proved to be less sensitive than system 3.

System 3

The third system relies on permeation through a palladium/silver membrane. A schematic for this sampling approach can be seen in figure 5. In this system, a membrane separates the vacuum chamber from the carrier stream. The vacuum chamber draws gas from the carrier stream through the membrane, but the membrane is only permeable to atomic hydrogen. Molecular hydrogen dissociates on the membrane surface into atomic hydrogen which readily passes through the membrane and reforms as molecular hydrogen on the downstream side.⁽³⁾ Most hydrogen in the carrier stream passes through the membrane. Helium and some hydrogen in the carrier stream leave through the exhaust system. Molecular hydrogen within the vacuum chamber on the downstream side is detected by ion gauge P. When heated above 180° C, the membrane diffusivity for hydrogen increases noticeably. In the present work, the membrane

temperature was maintained between 250°C and 400°C. Temperatures below 400°C were used to ensure that the amount of hydrogen permeating into the vacuum system did not swamp the turbomolecular pump.

Figure 6 shows the relationship between hydrogen flow on the upstream side and the rate at which that hydrogen permeates into the vacuum chamber at various permeator temperatures.

In figure 6, hydrogen mass throughput on the downstream side was calculated using the equation

$$\Phi_v = \frac{P}{\sum_{i=1}^n \frac{1}{C_i}} = PC_{net}$$

where Φ_v is the mass throughput, P is the hydrogen partial pressure within the vacuum chamber in torr, n is the number of straight-tube sections (in series) connecting the membrane housing to the turbomolecular pump, C_i is the conductance of individual straight-tube sections (longer tubes have lower conductance), and C_{net} is the effective conductance of the entire vacuum system. For figure 6, the net conductance was simply the combined conductance of the turbomolecular and scroll pumps, 50 liters per second. As the temperature of the membrane increases, more hydrogen appears on the downstream side of the membrane. Not all hydrogen introduced to the membrane permeates through, indicating that the membrane is limiting hydrogen detection.

To determine how limiting the permeator is, the efficiency of the permeator at various temperatures was calculated and displayed in figure 7. The net conductance was found to be 26.1 liters per second. The hydrogen partial pressure was measured by a mass spectrometer and an ion gauge. At 400°C the Pd/Ag membrane transfers about 78% of the hydrogen available on the

upstream side of the membrane, as shown in figure 7. Using this figure, the hydrogen flow in the system can be measured, even though some of it does not pass through the Pd/Ag membrane.

Characterization of the Cryotrap

Because system 3 (the permeation approach) had the highest sensitivity to hydrogen and was the most user friendly, it was chosen to detect hydrogen flowing through the cryotrap. The schematic for these tests is illustrated in figure 5.

The cryotrap was cooled with liquid nitrogen. The liquid nitrogen was flown through a stainless steel coil which was brazed to the stainless steel column containing the molecular sieve. The assembly was insulated to reduce heat loss to the surroundings. The column was cooled by thermal conduction once the cooling coil was filled with liquid nitrogen. The temperature of the cryotrap was monitored by thermocouples. Once the cryotrap reached temperatures around -180°C , helium gas was flown through the cryotrap bypass to establish a baseline reading on the mass spectrometer hydrogen detector. Once this baseline was established, the bypass was closed, the cryotrap was opened, and a hydrogen/helium carrier stream was flown through. This change in gas composition produced no change in the baseline, indicating that the molecular sieve was extracting all the hydrogen from the carrier stream. Once the column was filled to capacity, hydrogen would break through to the downstream side. At this point the hydrogen/helium flow was stopped and a pure helium stream initiated. The column was unloaded by raising the temperature of the column.

Figure 8 provides the partial pressure of hydrogen present downstream of the cryotrap as a function of time during the loading and unloading cycle of the cryotrap. Helium flowing at 150 sccm is co-mixed with hydrogen flowing at 40 sccm and introduced into the inlet of the cryotrap

held at 93 K. Initially all the hydrogen is adsorbed on the cold molecular sieve. No hydrogen is detected downstream of the cryotrap, and the hydrogen partial pressure at the exhaust end of the cryotrap is at a background value. At 146 minutes hydrogen breaks through the cryotrap. A spike in the hydrogen partial pressure is observed followed by a steady although slightly declining hydrogen partial pressure. This curve suggests that initially a puff of hydrogen is released into the helium stream followed by a gradual release of hydrogen into the helium discharge approximately two orders of magnitude lower. The capacity of the column to hold hydrogen at 93 K before hydrogen appears at the outlet is 5.86 sL or equivalently 108.7 scc per gram of molecular sieve at 93 K (-180°C).

At 209 minutes, the injection of hydrogen into the cryotrap inlet is stopped but the helium purge stream continues to flow at 150 sccm. Within a few seconds the hydrogen partial pressure in the exhaust stream is observed to decrease towards the original baseline value and remain at the low value until the cryotrap begins to warm up. Clearly the column can retain the captured hydrogen without releasing its contents to the helium purge stream provided the column remains cold.

At 210 minutes, the liquid nitrogen cooling to the coil is turned off but the coil does not warm up noticeably for an additional 13 minutes. At 233 minutes, the coil temperature reaches 127 K (-156°C) and the hydrogen partial pressure is observed to increase above the baseline value. The majority of the hydrogen is released once the column reaches approximately 130 K (-140°C). The remainder of the gas is released as the coil warms up beyond 170 K (-100°C).

To understand if the initial spike observed at minute 146 in Figure 8 was an artifact of filling the coil to capacity, a second test was carried out in which the coil was filled to half capacity using the same loading conditions. The results are provided in Figure 9. At 85 min both

the hydrogen and the liquid nitrogen flows were stopped. A spike similar to that observed in Figure 8 is observed moments after the hydrogen flow is turned off before the hydrogen partial pressure in the coil exhaust returns towards background. As the coil starts to warm up, the hydrogen partial pressure is observed to rise above its background value. This test establishes that the hydrogen partial pressure spike in the coil effluent is not a result of the cryotrap being charged to capacity.

Deuterium is naturally present in hydrogen gas at a concentration on the order of 150 ppm. To determine if D_2 is responsible for the spike observed in the two preceding tests, the experiment described in Figure 8 was repeated. However, in this test the residual gas analyzer (RGA) was set to measure the concentrations of three hydrogen isotopes: H_2 , HD and D_2 . The results are illustrated in Figure 10. At 146 minutes hydrogen breaks through the column as before, once the column is fully loaded, and the characteristic spike is observed. However, increases in both HD and D_2 are also observed. The HD contribution is most likely a result of isotope scrambling of H_2 and D_2 to form HD as the two species permeate through the Pd/Ag membrane in the hydrogen detector. The D_2 partial pressure increase continues for an additional 30 minutes and then begins to decrease with time even after the hydrogen flow has been re-initiated at 319 minutes. The H_2 partial pressure increases to approximately the peak value of the initial spike and remains at that value even though hydrogen is being added at the coil entrance. Both H_2 and D_2 are being eluted from the coil at concentrations that do not depend on the inlet hydrogen/deuterium concentrations.

At 428 minutes the LN_2 cooling to the coil is turned off. Four minutes later, at 432 minutes, D_2 release from the coil increases rapidly to reach an approximate steady state value until the column is emptied of D_2 . The hydrogen concentration in the effluent drops, and at 428

minutes the coil has heated sufficiently to start the release of H₂ from the coil. All the D₂ is released in about 58 minutes. The bulk of the H₂ is released after 400 minutes. The details of this behavior will be the subject of future work.

Conclusions

Of the three hydrogen detection systems proposed for evaluating the performance of the cryotrap, the permeation system proved to be the most effective and feasible. It had a high degree of sensitivity and efficiency. The thermal conductivity detection system was difficult to implement due to the similar thermal conductivities of helium and 1% hydrogen in helium. The atmospheric sampling system, while workable, lacked the sensitivity of the permeation system.

Evaluation of the cryotrap with the permeation system revealed several interesting phenomena. Breakthrough is sudden and significant once the column reaches capacity. Hydrogen can be eluted from a full, cold column by continuously purging the column with helium. Deuterium can be separated from hydrogen by warming the column.

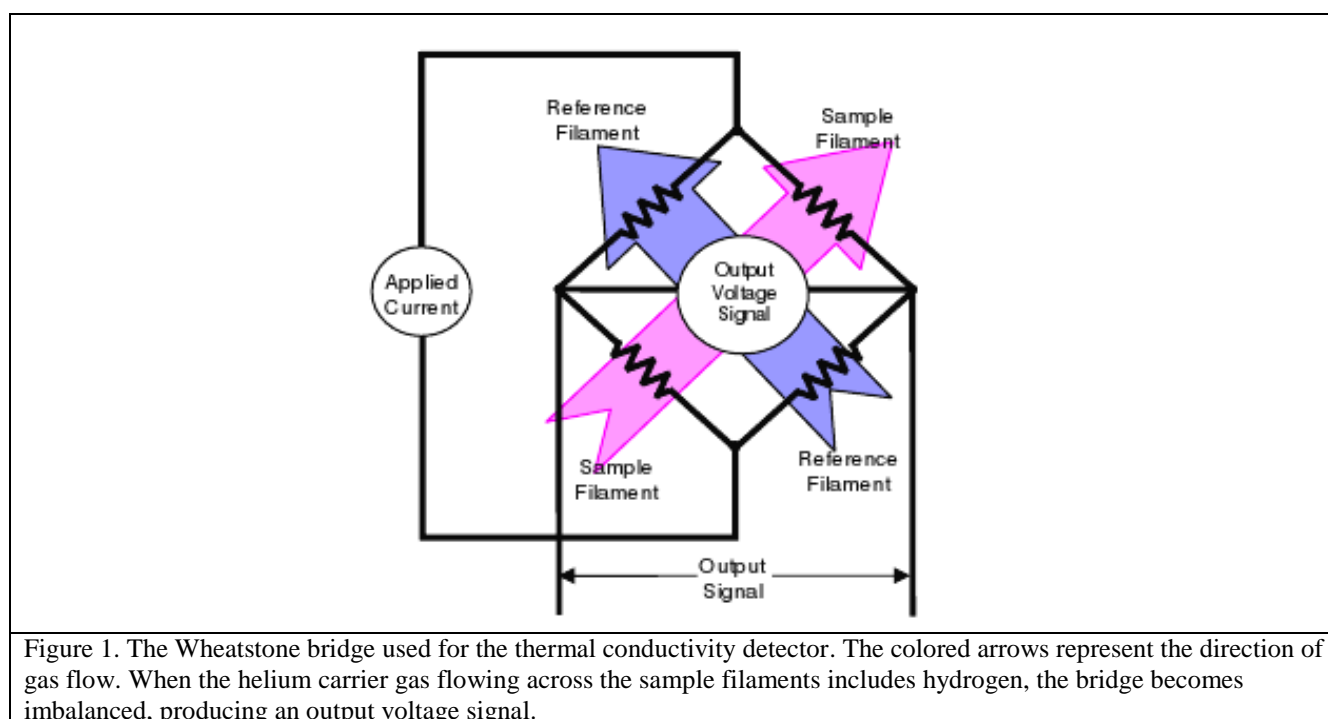
References

1. Shmayda, Walter. *Evaluation of Tritium Capture Systems*. 25th Symposium on Fusion Engineering. San Francisco, CA, USA. June 10-14 2013.
2. Jo, Aaron. *Hydrogen Isotope Separation Using Gas Chromatography*. 2012 Summer Research Program at the University of Rochester's Laboratory for Laser Energetics.
3. Yokogawa Corporation of America. *Hydrogen Permeation*. January 11, 2012

Acknowledgements

I would like to thank Dr. R.S. Craxton for allowing me to participate in this program. I would also like to thank Dr. Shmayda and Neil Redden for the incredible support they gave me, along with Andrew Boyce and Aaron Jo for the guidance they provided.

Figures



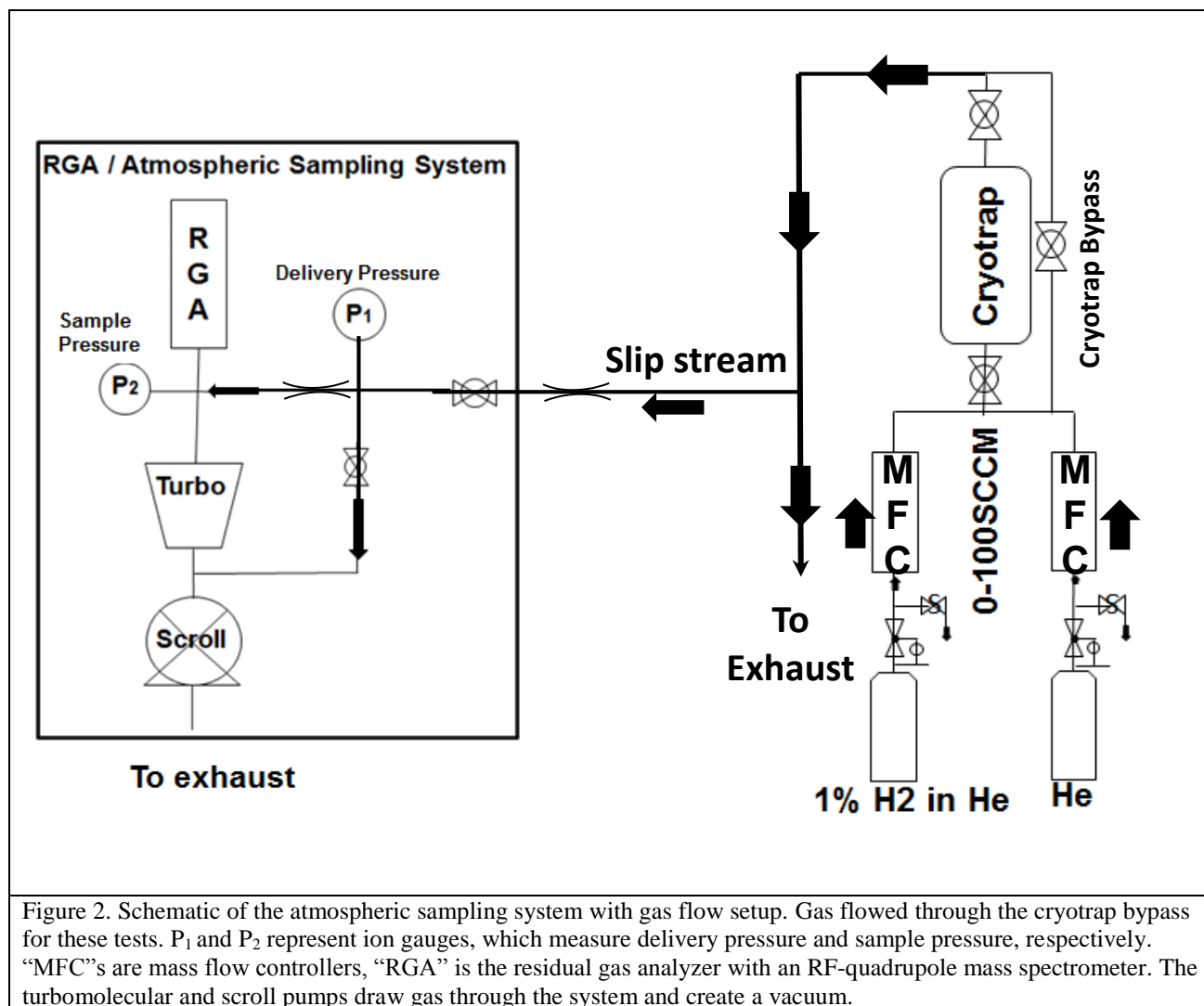


Figure 2. Schematic of the atmospheric sampling system with gas flow setup. Gas flowed through the cryotrap bypass for these tests. P₁ and P₂ represent ion gauges, which measure delivery pressure and sample pressure, respectively. “MFC”s are mass flow controllers, “RGA” is the residual gas analyzer with an RF-quadrupole mass spectrometer. The turbomolecular and scroll pumps draw gas through the system and create a vacuum.

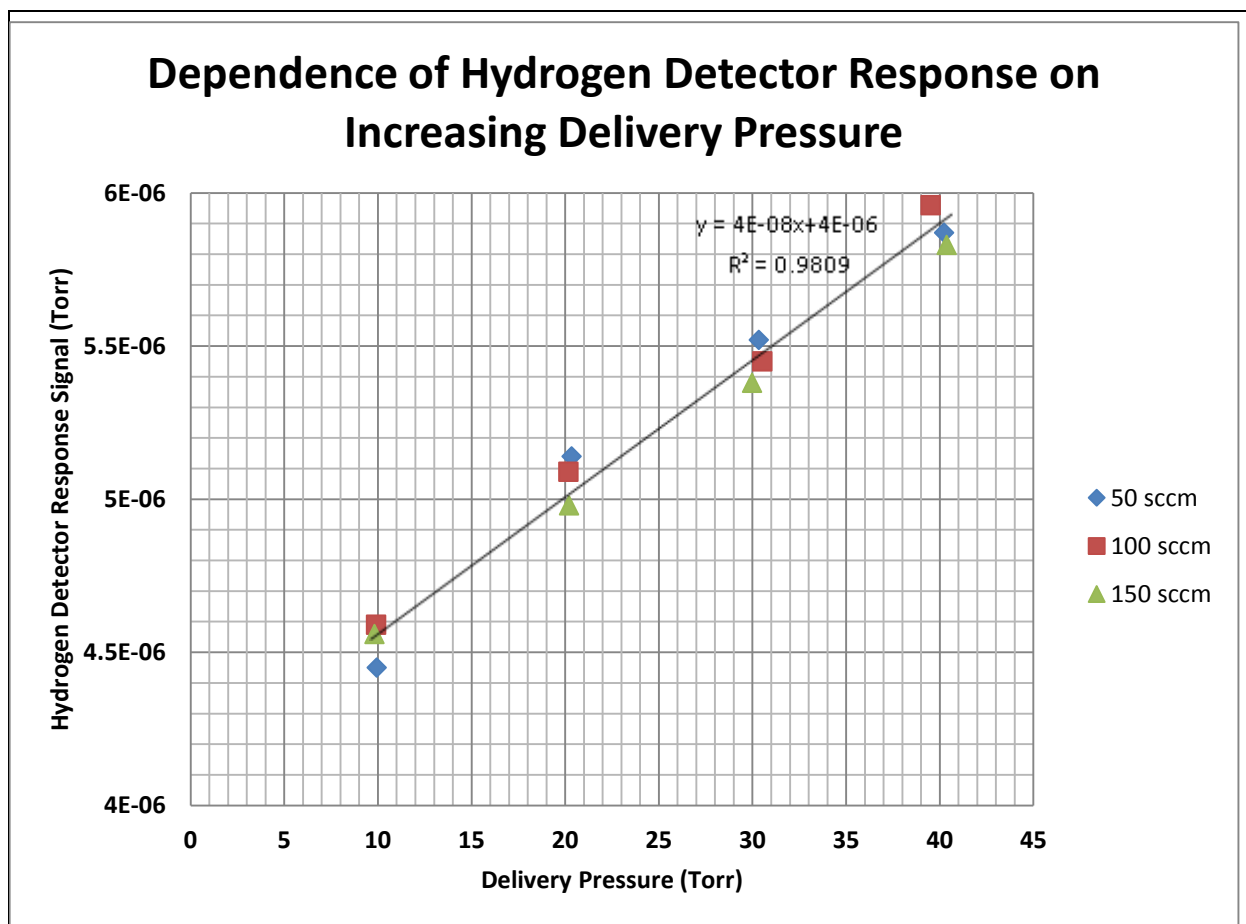


Figure 3. The dependence of the hydrogen detector response signal on increasing delivery pressure. The gas flow was 1% H₂ in He. The delivery pressure was measured by ion gauge P₁, and the detector response was measured by the RGA for flow rates from 50 to 150 sccm. Increasing the flow rate had no significant effect on detector response, so the different flow rates were given the same least-squares regression line.

He Flow rate (sccm)	Hydrogen Partial Pressure (Torr)
50	1.0E-06
100	5.2E-07
150	3.5E-07

Table 1. The hydrogen partial pressures detected by the RGA when only helium was flown in the sample stream. These pressures were slightly affected by changes in helium flow rate. Hydrogen partial pressures were independent of delivery pressure, hence the exclusion of delivery pressures from the table.

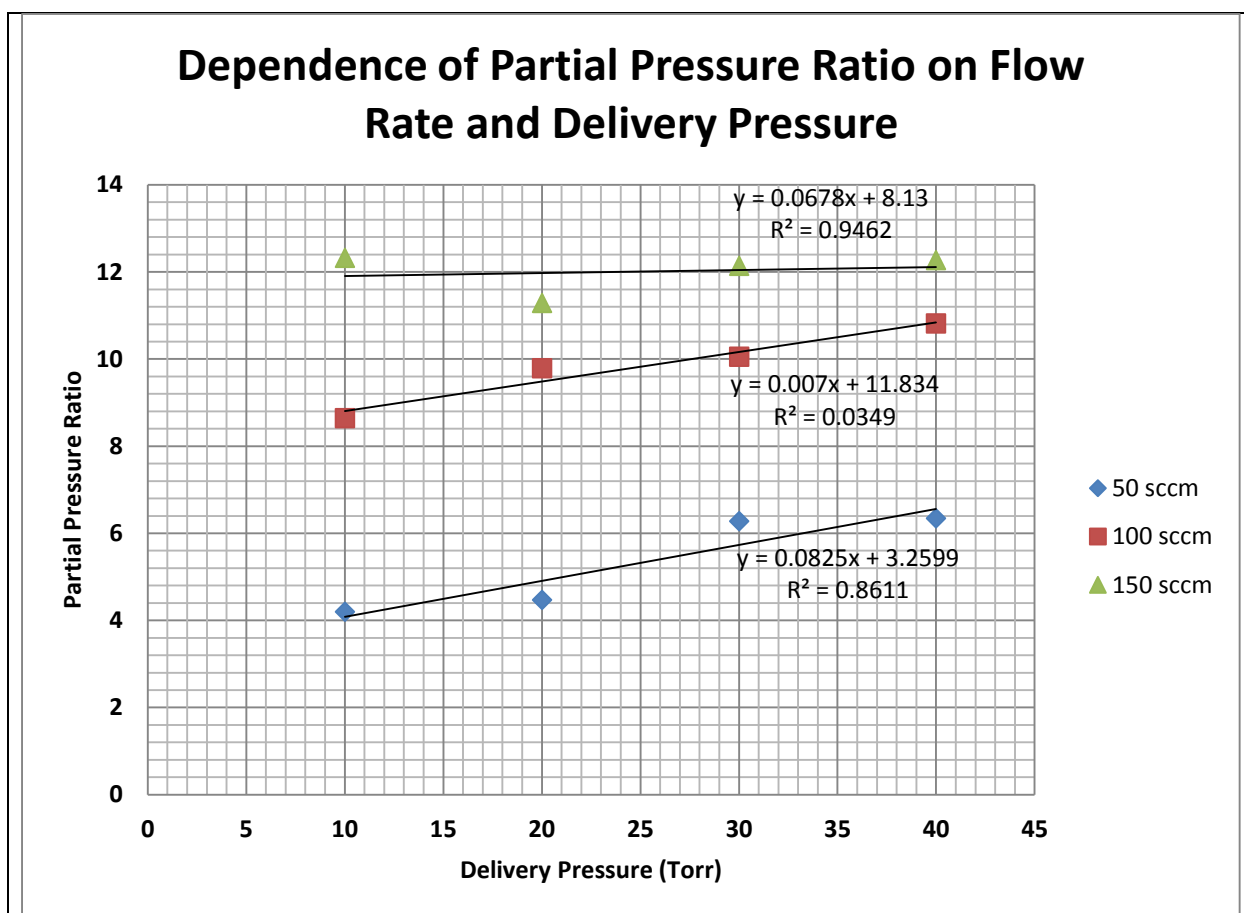


Figure 4. The dependence of the partial pressure ratio on flow rate and delivery pressure. The delivery pressure was measured by P_1 . Partial pressure ratios are obtained by dividing figure 3 hydrogen partial pressures by table 1 hydrogen partial pressures of the same flow rate.

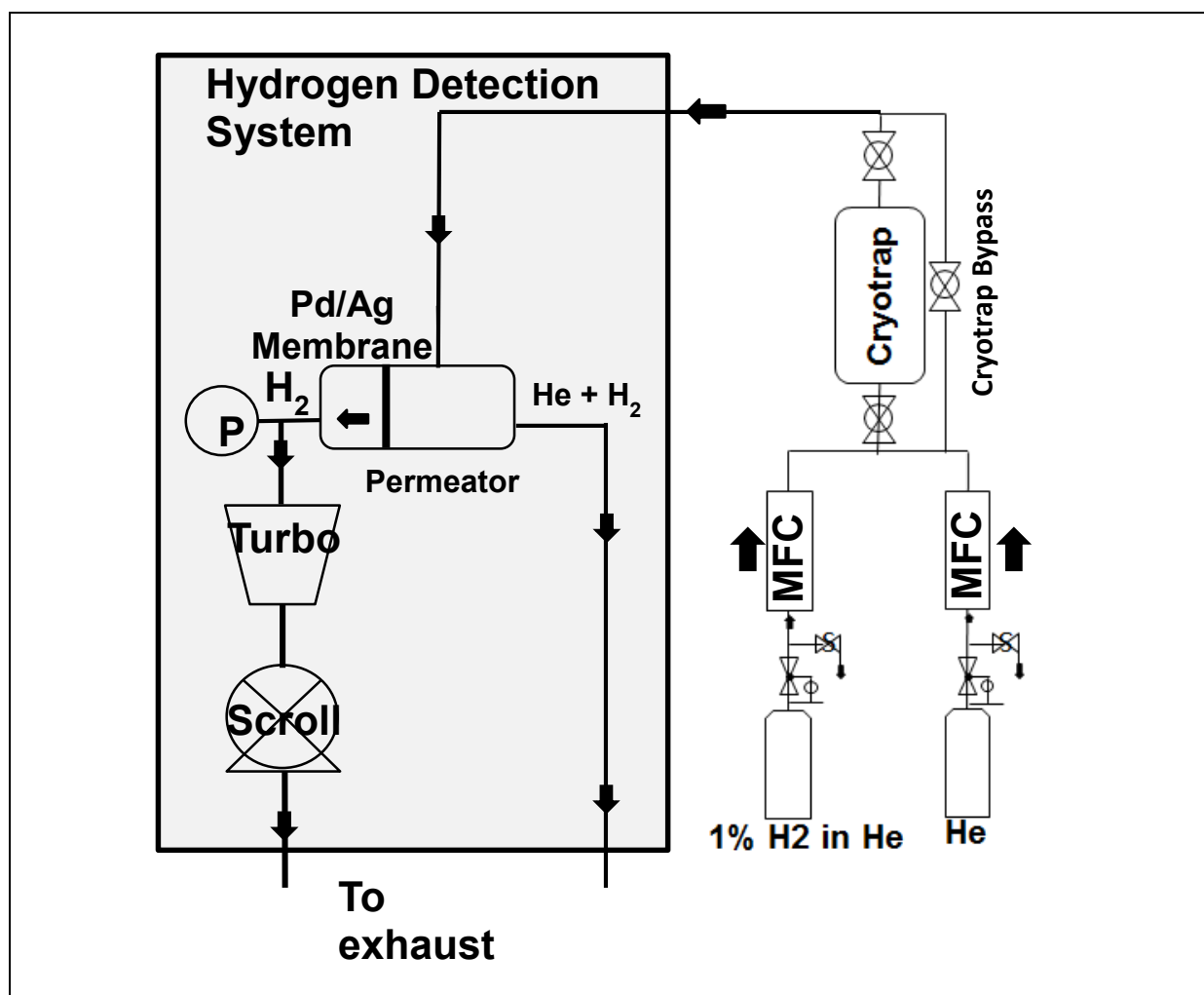


Figure 5. Schematic of the permeation sampling system. Most hydrogen permeated through the Pd/Ag membrane, while some hydrogen and all helium was immediately released as exhaust. The hydrogen that did permeate was detected by ion gauge P and pumped out by the turbomolecular pump backed by a scroll pump.

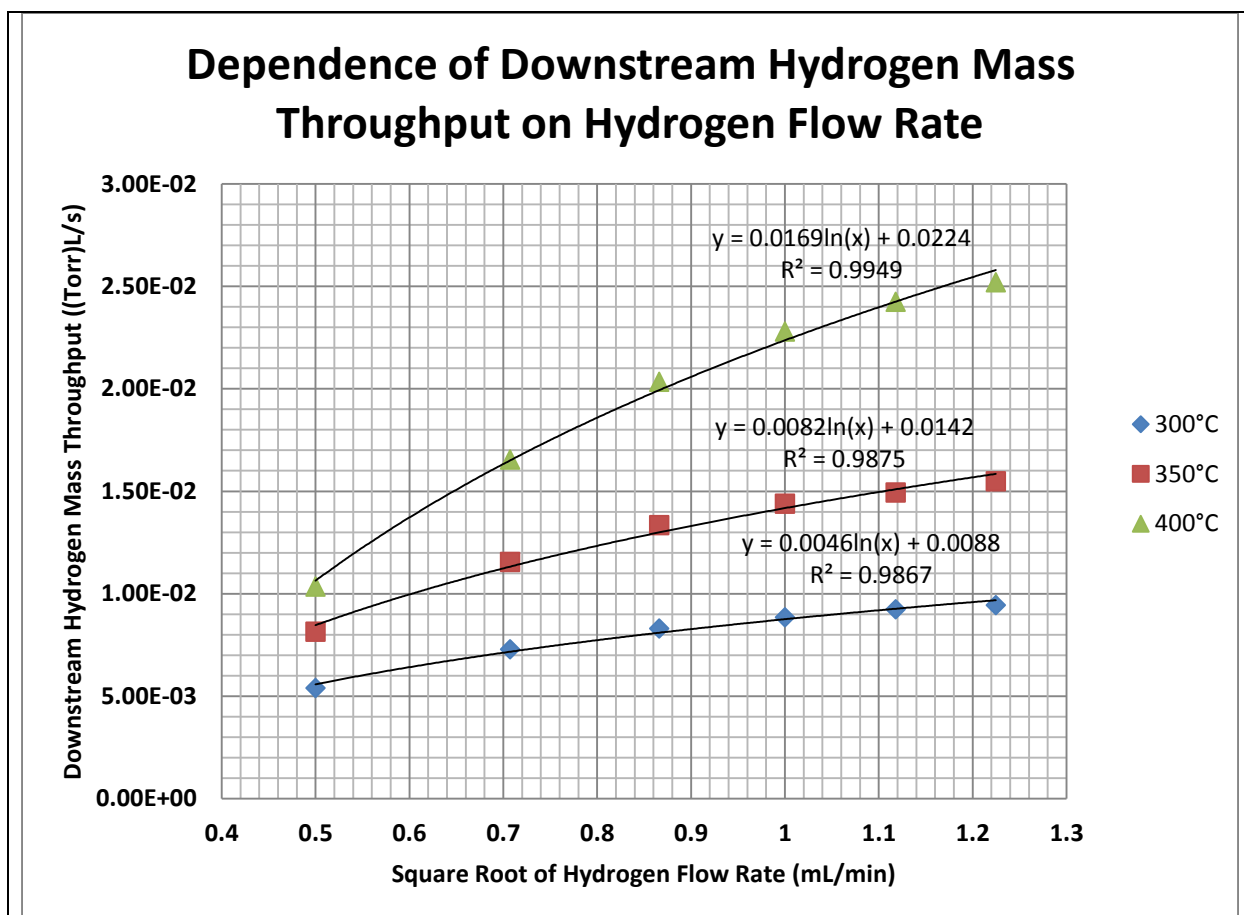


Figure 6. The dependence of downstream hydrogen mass throughput on the flow rate of hydrogen. Hydrogen mass throughput was calculated by multiplying the detected hydrogen partial pressure by the 50 L/s conductance.

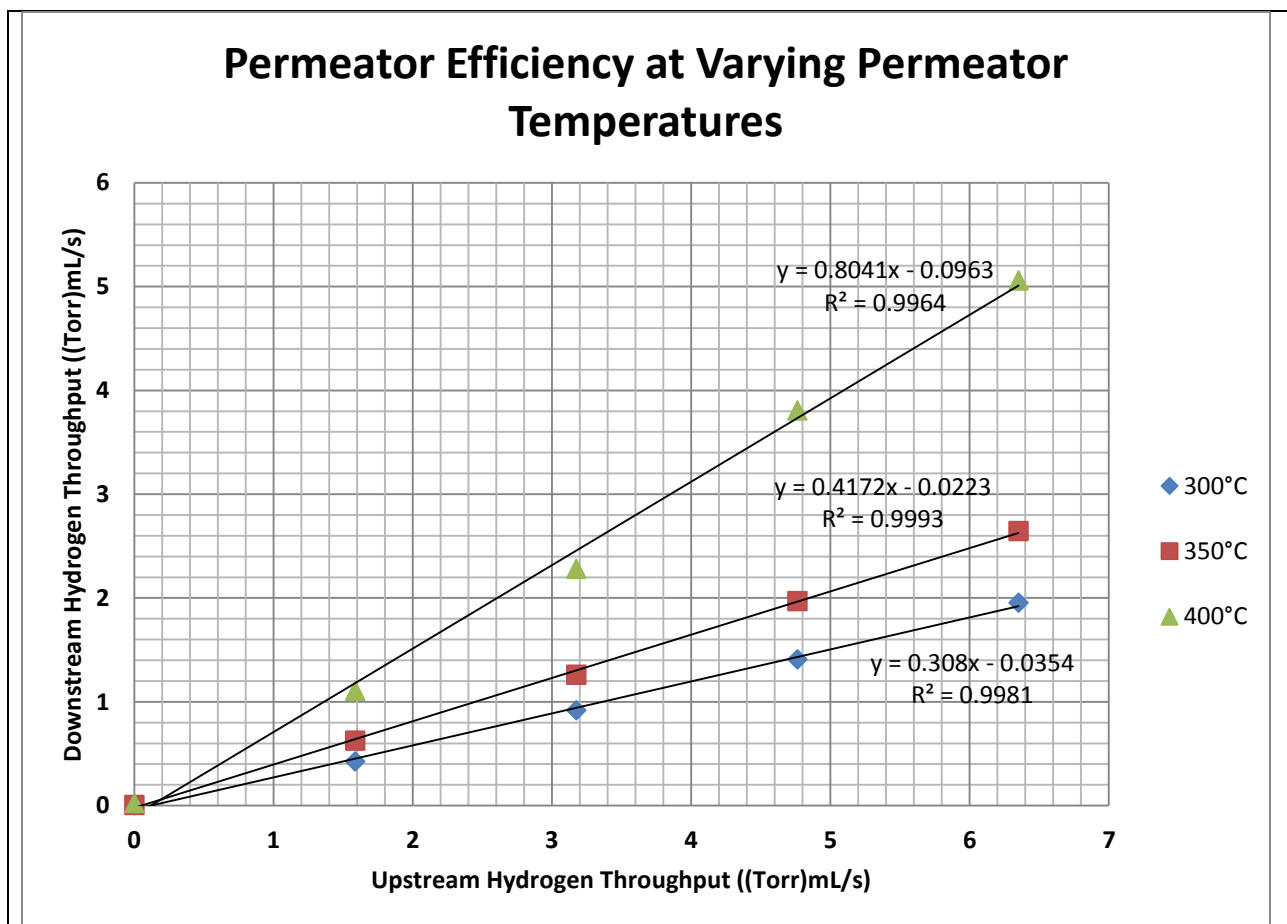


Figure 7. The downstream throughput of hydrogen relative to the upstream throughput at various temperatures. Permeator efficiency (the slope of the graph) is highest at higher membrane temperatures. He/H₂ carrier stream flows at 50 sccm. The hydrogen flow is controlled by a MFC, and hydrogen throughput (the rate at which hydrogen permeates into the vacuum chamber) is calculated based on measurements from the mass spectrometer.

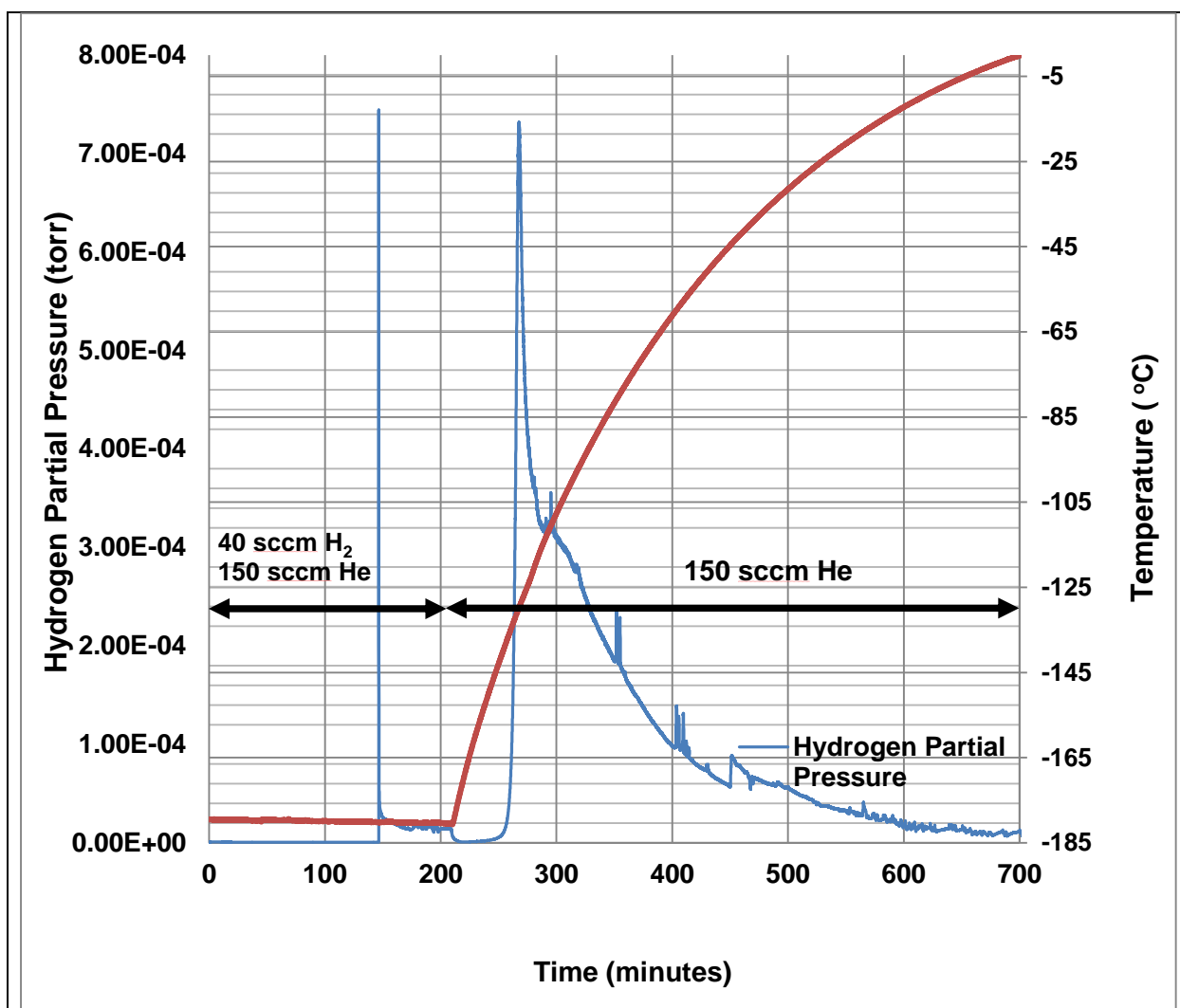


Figure 8. Partial pressure of hydrogen measured downstream of the permeator (the blue curve) as a function of time, illustrating a typical loading and unloading cycle for the cryotrap. The cryotrap reached its maximum hydrogen capacity at 146 minutes. The liquid nitrogen was valved off at 210 minutes. The permeator membrane was operated at 300° C for this experiment. Hydrogen charging the column was shut off at 209 minutes, and hydrogen stopped breaking through shortly after. Baseline partial pressure of 7E-7 torr. The red curve gives the temperature of the cryotrap as a function of time.

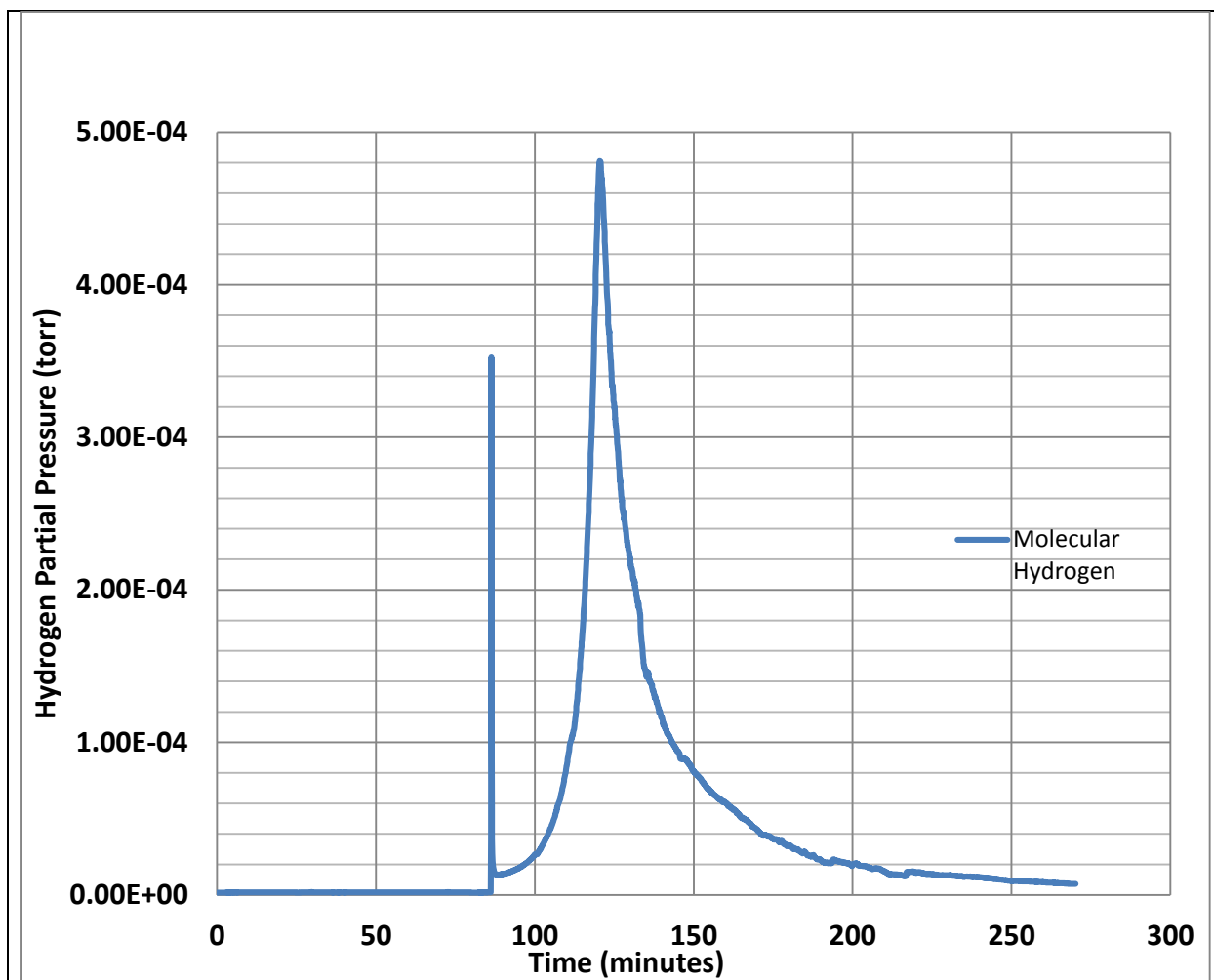


Figure 9. The same conditions as figure 8, but with the the 40 sccm hydrogen flow and liquid nitrogen flow stopped at 85 minutes. At this time, the molecular sieve was filled to half of its capacity. The permeator membrane was operated at 300°C.

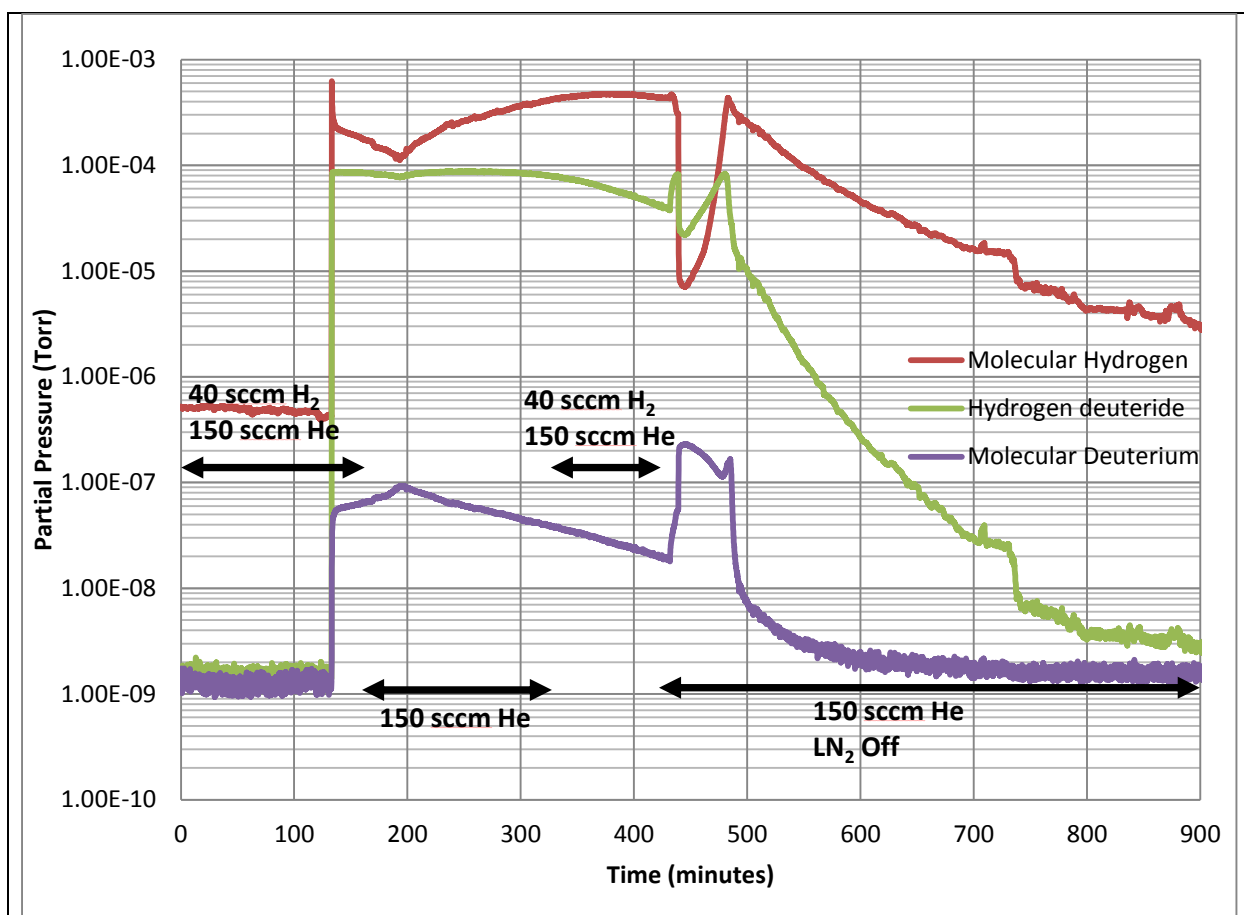


Figure 10. Partial pressures of molecular hydrogen, hydrogen-deuteride, and molecular deuterium measured as a function of time by an RGA in the vacuum chamber. The RGA detects all the hydrogen isotopes: mass 2 is hydrogen, mass 3 is hydrogen deuteride, and mass 4 is deuterium. Only hydrogen and its isotopes can permeate through the membrane, so the particles of masses 3 and 4 are unlikely to be contaminants of the same mass. Baseline hydrogen partial pressure is about 4.7×10^{-7} torr. H_2 was turned off at 166 minutes and on again at 319 minutes, before being turned off for the final time at 428 minutes. Temperature increased at the same rate as in figure 8 once liquid N_2 was turned off at 428 minutes.

Emulating Laser Facility Operations through a Real-time Collaborative Network

Michael Hartman

Pittsford Sutherland High School

Pittsford, NY

Advisor: Rick Kidder

Laboratory for Laser Energetics

University of Rochester

Rochester, New York

November 2013

1. Abstract

Research has been done to support large-scale laser facility operations through the use of semantic data integration, real-time collaborative networking, three-dimensional graphics, and web-based services. Various technologies were utilized in establishing methods of setting up experimental configurations in a visually intuitive manner for experiments that use the Omega lasers. Current technologies have been identified that support scalable tools development to aid in the creation of experimental configuration designs. Virtual environments can be used to examine and collaborate on new or existing configuration requests and provide real-time communication between scientists using the tools. A virtual environment is a simulation of an environment, in this case the OMEGA Target Chamber, on a computer. Users can perform actions such as adding diagnostics in real-time, so researchers may be in different places but interact as if they are in the same room. A three-dimensional virtual model of the OMEGA Target Chamber was created as a platform for user interaction. This interactive model can be used to easily display experimental configurations, and to create campaign proposals from scratch.

2. Introduction

The nature of the Laboratory for Laser Energetics (LLE) is that many scientists collaborate on one project together. Each has a responsibility and carries it out while maintaining clear communication with other researchers. Researchers from around the world use the OMEGA and OMEGA-EP lasers. The idiosyncrasies of the facility and lasers along with the number of scientists involved in any given experiment create difficulties in communication. Furthermore, the compatibility of diagnostics with

experimental configurations, their availability at any given time, and their current working order is not information that researchers have readily available. A program SILOCON (Simulation of Laser Operations through Collaborative Networking) has been written in an attempt to solve this problem.

3. SILOCON

The program SILOCON is based on the creation of a three-dimensional model of the OMEGA target chamber. One feature that distinguishes it from a conventional graphics program is its use of an ontology. An ontology is used in order to find the relationships between researchers, diagnostics, and other items. Ontologies are composed of “subjects” and “predicates”; “subjects” are the objects themselves and “predicates” are the links between all of the subjects [1].

This creates a web of data that can be easily traversed and through which relationships between objects can be used. At LLE, there is an ontology containing information about the ports on the OMEGA laser. For example, for any given port there is a predicate “hasPortID” and “hasAzimuthalAngle.” As shown in Fig. 1, these two predicates link to two subjects, “H_10” and “306,” respectively.

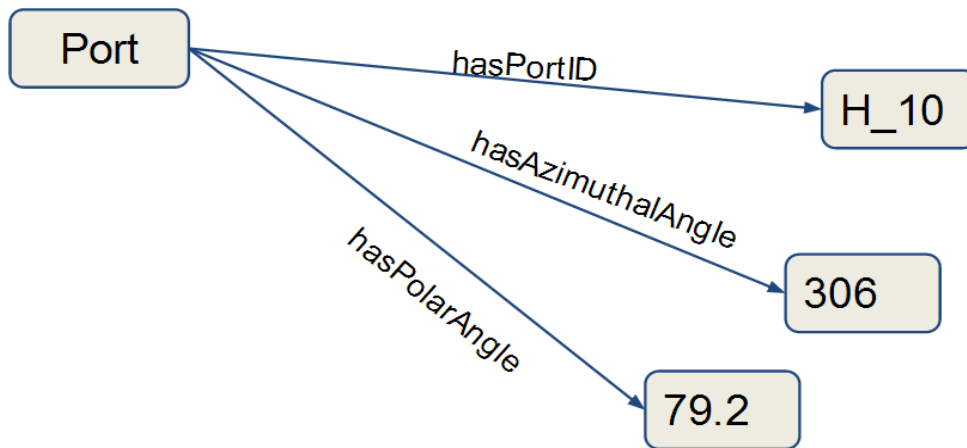


Figure 1: In the ontology, data is represented through connections with other objects. Here, the “port” object has the properties, hasPortID, hasAzimuthalAngle, and hasPolarAngle.

Real time updating and chat capability

SILOCON implements web technologies in order to provide real-time updating among users in a session as well as chat functionality. Researchers can log onto SILOCON and join a “session” with other users. A “session” is an online protocol that allows researchers to share information with each other securely. The session allows multiple different online connections to see update information immediately. For example, if one user in a session moves a diagnostic around the target chamber, the other users in that session will see it move in real-time.

A chat functionality was created in order to facilitate communications among researchers. A list of “contacts” is populated with relevant Principal Investigators (PIs) and facility specialists. Based on the selected experimental configuration, SILOCON searches the ontology to find people who work with the different parts. The “contacts” page then contains the necessary and relevant researchers who may be available to answer the PIs’ questions.

SILOCON creates an interactive environment the PIs can actively use. It differs from

previous attempts to facilitate communication among researchers in that it is not just a forum; its ability to show, create, and manipulate experimental configurations increases its interactivity and allows for clearer communication.

WebGL

WebGL is an integral part of SILOCON; it is used to power the 3D graphics. WebGL is a Javascript API (application programming interface) that uses a computer's graphics card in order to render three-dimensional scenes. WebGL is based on OpenGL, a cross-platform API that uses "shaders" to make 3D graphics. A "shader" is a program that tells the computer how to draw the graphics based on input values. This is where shading takes place in order to create the effect of lighting and shadows [2].

The WebGL rendering process takes several steps, beginning with the input of vertex data into the vertex shader (Fig. 2). The rasterization process then converts 3D points in space to two-dimensional screen locations. These locations are averaged together based on which pixel they are closest to, and they send the averaged color into the fragment shader. In the fragment shader, the color for each pixel is manipulated based on its screen coordinates, cursor location, time, and other variables.

The API "Three.js" was used to facilitate WebGL operations. Since WebGL deals

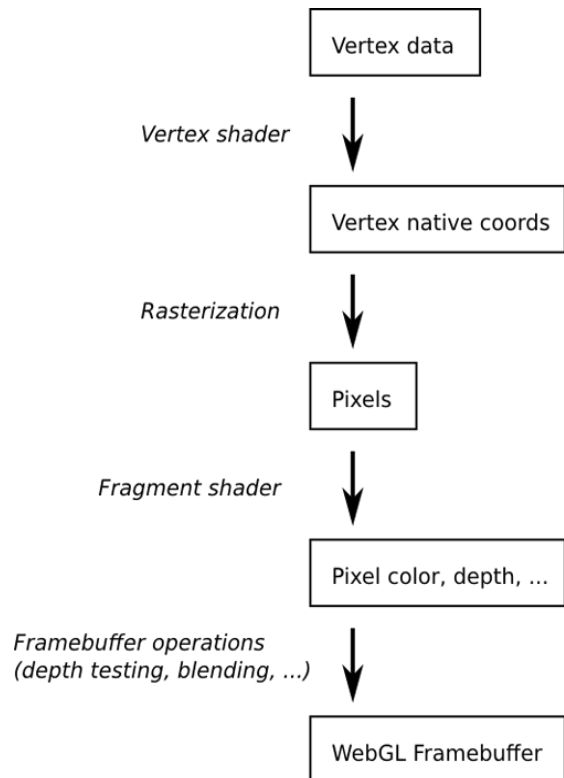


Figure 2: This is the process vertex data must go through in order to be displayed on a computer screen. This is known as the "graphics pipeline."

directly with the hardware of the computer the webpage is running on (the GPU), it lacks user-friendliness despite its robustness. Three.js provides some common functions to make WebGL processes easier. All of the three-dimensional graphics in SILOCON utilize Three.js functions in some way or another [3].

Capabilities of SILOCON

Fig. 3 shows a flattened, two-dimensional version of the OMEGA target chamber. This is currently one of the tools PI's use to plan their experimental configurations. With the model in SILOCON, a three-dimensional, virtual target chamber is projected onto the computer screen and provides an intuitive look at the OMEGA Laser.

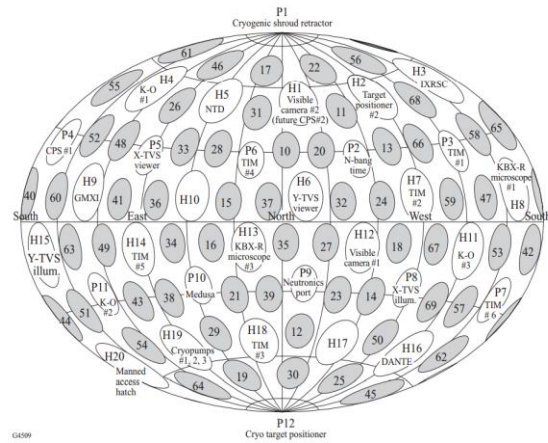


Figure 3: A two-dimensional view of the target chamber.

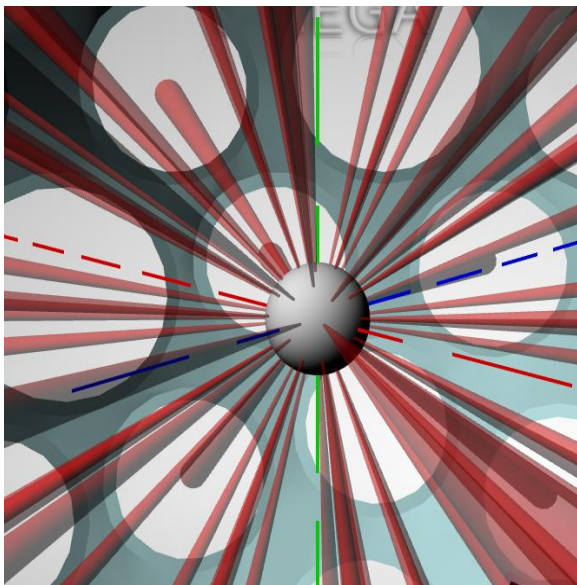


Figure 4: Laser beams converging on a center target (sphere).

Another key feature in SILOCON is its ability to visualize laser projections. In Fig. 4, every laser port is projecting a cone onto the center of the target chamber. These cones' characteristics (such as starting and ending radius) can be manipulated so a realistic representation of the laser beams is shown. SILOCON also has the ability to display dashed lines from any given port to the center of the target chamber as illustrated in Fig. 5. This is helpful for PI's because they can see the lines normal to the ports they are

change their whole configurations late in the experimental planning process.

One of the key features of SILOCON is that it provides real-time feedback for errors it has detected. Because SILOCON utilizes an ontology that contains information about each diagnostic, it can find errors in experimental configurations immediately after the errors have been made. An example of a SILOCON error display is shown in Fig. 6.

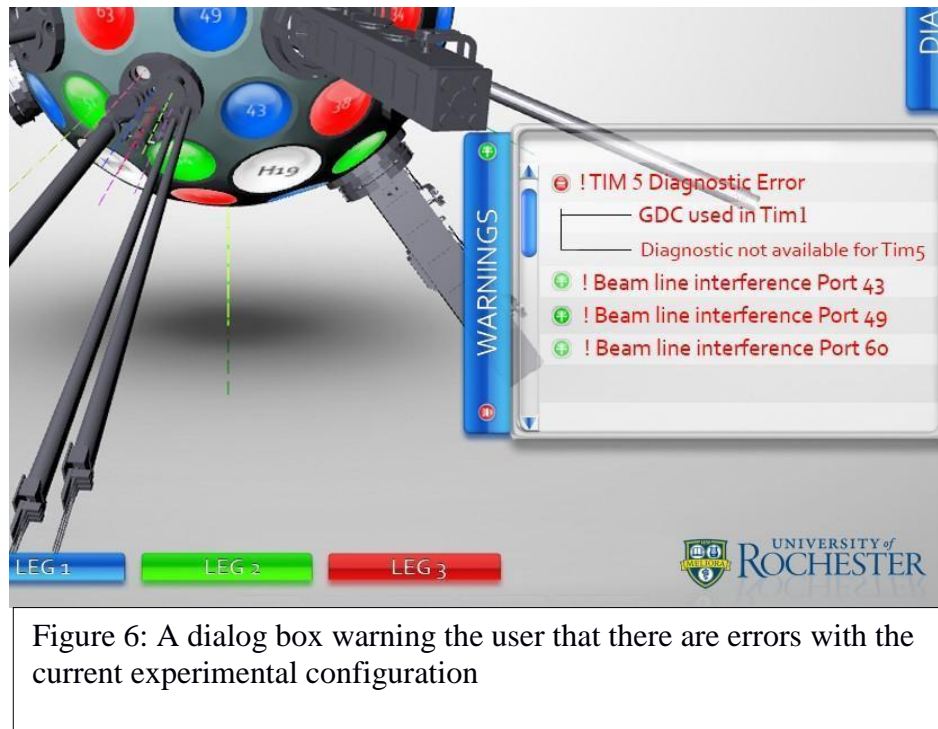


Figure 6: A dialog box warning the user that there are errors with the current experimental configuration

4. Future Work

SILOCON is still being added to and worked on. In order for it to become a full-fledged and useful tool for PI's, it needs to have functionality to load configurations from Shot Request Forms (SRFs) or PI Proposal Templates. This would be the first step in allowing PI's to visualize legacy experimental configurations. Also, the functionality to store information into the OMEGA database needs to be added to SILOCON. This is the database which currently stores all of the information on diagnostics, TIMs, etc.; the ontology is a relational mapping of this database.

This way, when a PI opens up the configuration into SILOCON, he or she may save it back in the database after manipulating data.

5. Conclusion

This research demonstrates that tools like SILOCON can be useful in the LLE work environment. The key differences between SILOCON and a typical, static, forum-based tool are its versatile functionality, three-dimensional capabilities, and dynamic error-detection functionality. A forum-based tool, or a website with a strict, question-and-answer layout, lacks the versatility and communication options SILOCON provides. Future work will make SILOCON an extremely useful and integral part of the LLE facility.

6. References

1. "W3C." Semantic Web - W3C. W3C, n.d. Web. July-Aug. 2012.

<<http://www.w3.org/standards/semanticweb/>>.

2. "OpenGL ES 2.0 for the Web." *Khronos Group*. Khronos, Inc, n.d. Web. Aug. 2013.

<http://www.khronos.org/webgl/>

3. "Three.js: JavaScript 3D library." *Three.js*. Mrdoob, n.d. Web. July-Aug. 2013.

<<http://threejs.org/>>.

7. Acknowledgments

This work couldn't have been possible without Dr. Stephen Craxton and Mr. Richard Kidder. Dr. Craxton paired me perfectly with Mr. Kidder; I love programming and was appropriately assigned a programming task. Mr. Kidder helped me learn my way around the

idiosyncrasies of the LLE facility, database, and ontology. He shared his vision of what he wanted by the end of the summer, but graciously left me room to experiment with my own ideas.

The Development and Testing of a Signal Processing Algorithm to Improve OMEGA Beam Timing

Eric Hwang

Penfield High School

Advisors: Robert Boni, William Donaldson

University of Rochester

Laboratory for Laser Energetics

Summer High School Research Program 2013

1. Abstract:

60-beam OMEGA coincidence timing at target chamber center (TCC) is achieved by adjusting individual beamline path lengths until $\sim 1\text{-}\mu\text{J}$, 1053-nm, 1-ns laser pulses propagated along each beamline arrive simultaneously at TCC. The final turning mirrors before the target chamber are coated for high reflectivity at 351 nm. Unfortunately, at 1053 nm, this creates a second delayed pulse from the back surface of the mirror. If the wedge angle of the mirror is small, then both the timing pulse and the delayed pulse reach the detector and oscilloscope. The detector records the sum of these pulses, resulting in a distorted timing signal. Distorted timing signals that were created using an offline test setup introduced 60-ps shifts in timing measurements when using the oscilloscope's built-in analysis routines. A new signal-processing algorithm has been developed that recovers the timing pulse from the distorted pulse shape. Using this algorithm, the recovered timing pulses introduced only a 6-ps timing shift, not 60 ps.

2. Introduction:

OMEGA is a 60-beam laser system capable of imploding $\sim 1\text{-mm}$ -diameter thin-wall spherical fuel pellets pressurized with isotopes of hydrogen gas. The 60 laser beams must arrive coincident at the fuel pellet to produce the pressure and temperature necessary to form helium from the hydrogen by a process known as thermonuclear fusion. Fusion is exothermic, releasing energy in the form of energetic free neutrons. OMEGA utilizes a beam timing system in advance of a 60-beam fusion experiment capable of verifying that all 60 beams will arrive simultaneously at the fuel pellet within ± 20 ps. The beam timing system propagates a low-energy, 1-ns, 1053-nm, laser pulse at 5 Hz down each of the 60 beamlines, one beamline at a time. Before propagating down a beamline, a sample of the pulse is sent to a reference photodiode, which connects directly to an

oscilloscope and is used as a baseline timing reference. Each beamline's path length varies in distance, which causes the pulse to arrive at the target at different times.

Figure 1 shows a schematic of the OMEGA Laser. The beam timing system positions a photodiode at the center of the target chamber; this is where all 60 beams will ultimately converge. The timing difference of a certain beamline can be calculated from the time the pulse reaches the reference photodiode to the time it arrives at the measurement photodiode. Using this, the timing differences of all 60 beamlines can be compared. For example, a pulse on beamline 1 may take 120 ns to arrive at the target, but a pulse on beamline 2 could take 121 ns if beamline 2 was longer in distance. In beam timing, the PLAS (Path Length Adjustment System) individually tests each beamline and shifts the distance of mirrors to adjust the path length of each beamline so that all of OMEGA's 60 beamlines will be co-timed at the target chamber center.

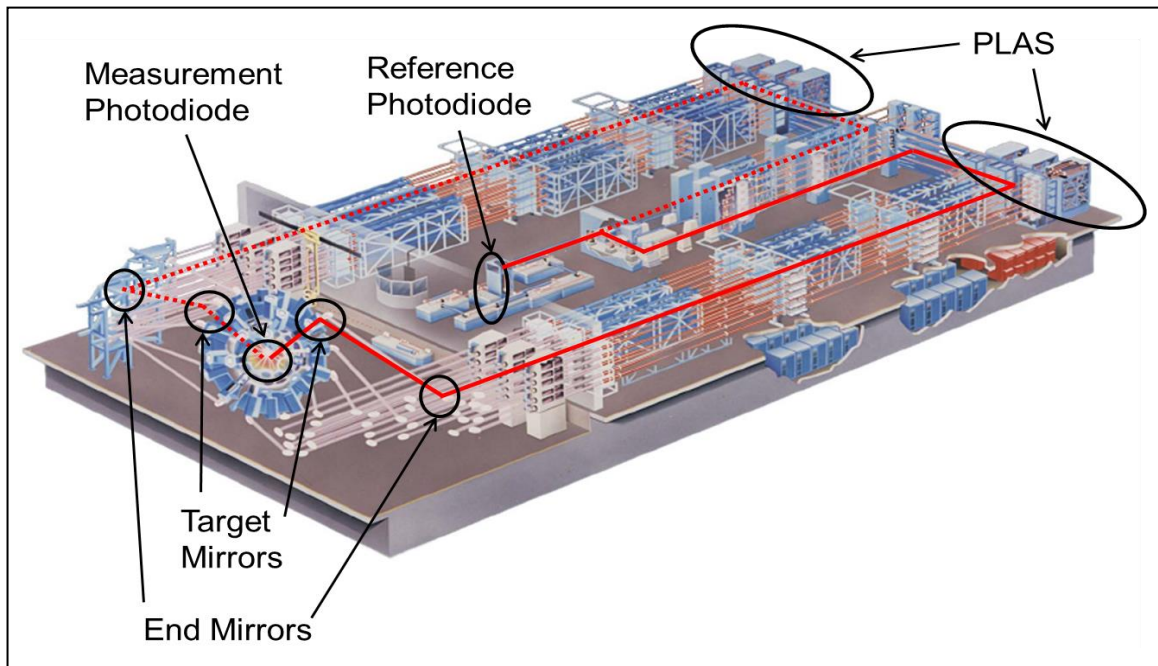


Figure 1: Diagram of beam timing on the OMEGA Laser – Shown are two separate beamlines, which travel different paths but center on the same target. In OMEGA, there are 60 beamlines. The beam timing system utilizes the PLAS (Path Length Adjustment System) to ensure all 60 beamlines are co-timed. This project investigates potential timing errors caused by back surface reflections from the final two turning mirrors, the end and target mirrors.

For a majority of beamlines, adjusting the path length with the PLAS reduces timing errors to as low as 10 ps [1]. However, timing errors as large as 30 ps still exist on some beamlines even after PLAS adjustments. One possible source of error is due to the fact that a 1053-nm laser is used during beam timing while a 351-nm laser is used in an actual shot. 1053-nm laser timing pulses can be propagated at 5 Hz with micro-Joule energy. This is not possible at 351 nm; therefore beam timing is performed at 1053 nm.

The target mirrors and end mirrors are coated for high reflectivity at 351 nm (at greater than 99% reflectivity); however, they transmit at 1053 nm, creating a delayed signal from the back surface [2]. As a result, four timing pulses are generated from a single timing pulse for each beamline at the turning mirrors [3]. Only the pulse that reflects off the front surfaces of both mirrors is the correct timing pulse. The other three are delayed pulses created from back surface reflections. For some beamlines, the wedge angle in one or both of the mirrors is small enough to allow this back surface reflection signal to reach the detector, creating a distorted pulse shape at the detector (figure 2).

The PLAS adjusts each beamline path length based on oscilloscope measurements. For beamlines whose back surface reflections do not overlap the original timing pulse, the oscilloscope measurement is correct. However, when they do, the composite pulse shape creates a distorted signal, giving an inaccurate measurement. This poses a problem for beam timing since the PLAS adjusts the path length based on inaccurate data. In this project, a post-processing algorithm is used to recover the original timing pulse from the distorted composite pulse so that more accurate timing measurements can be obtained.

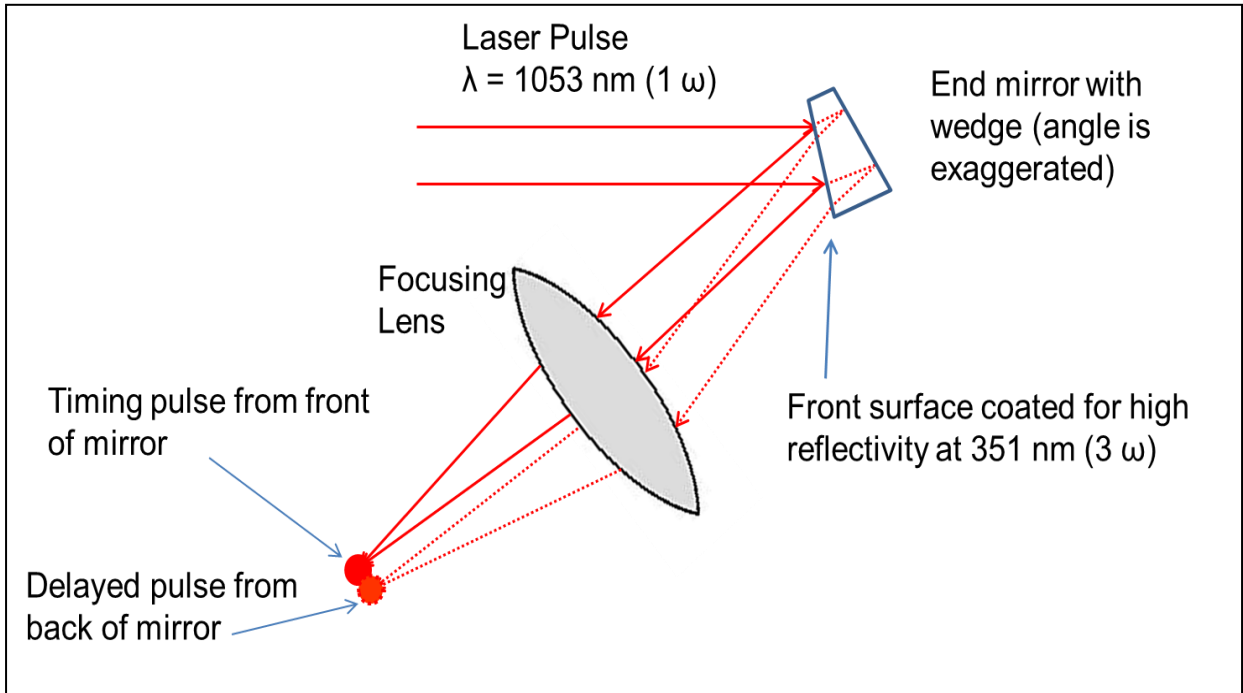
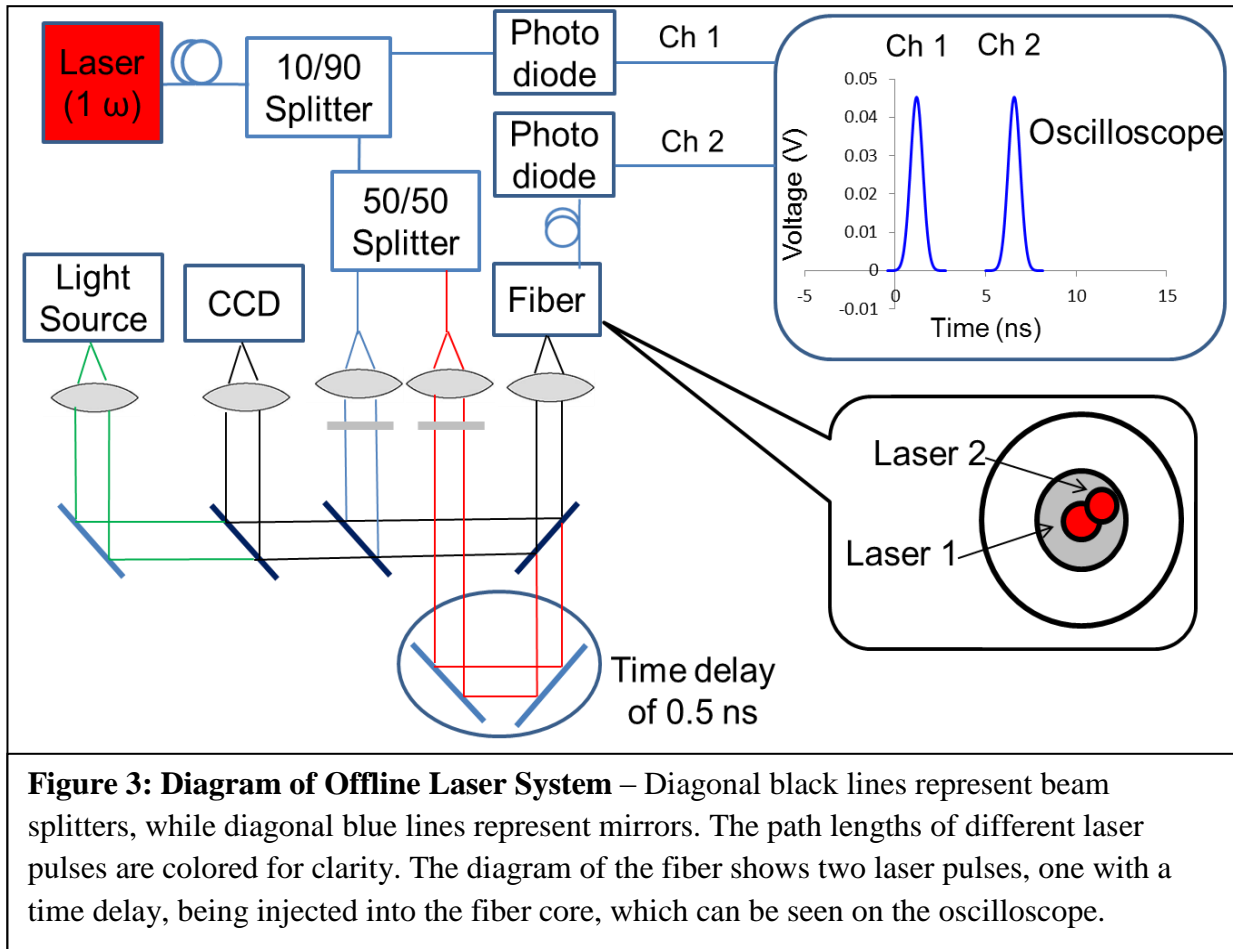


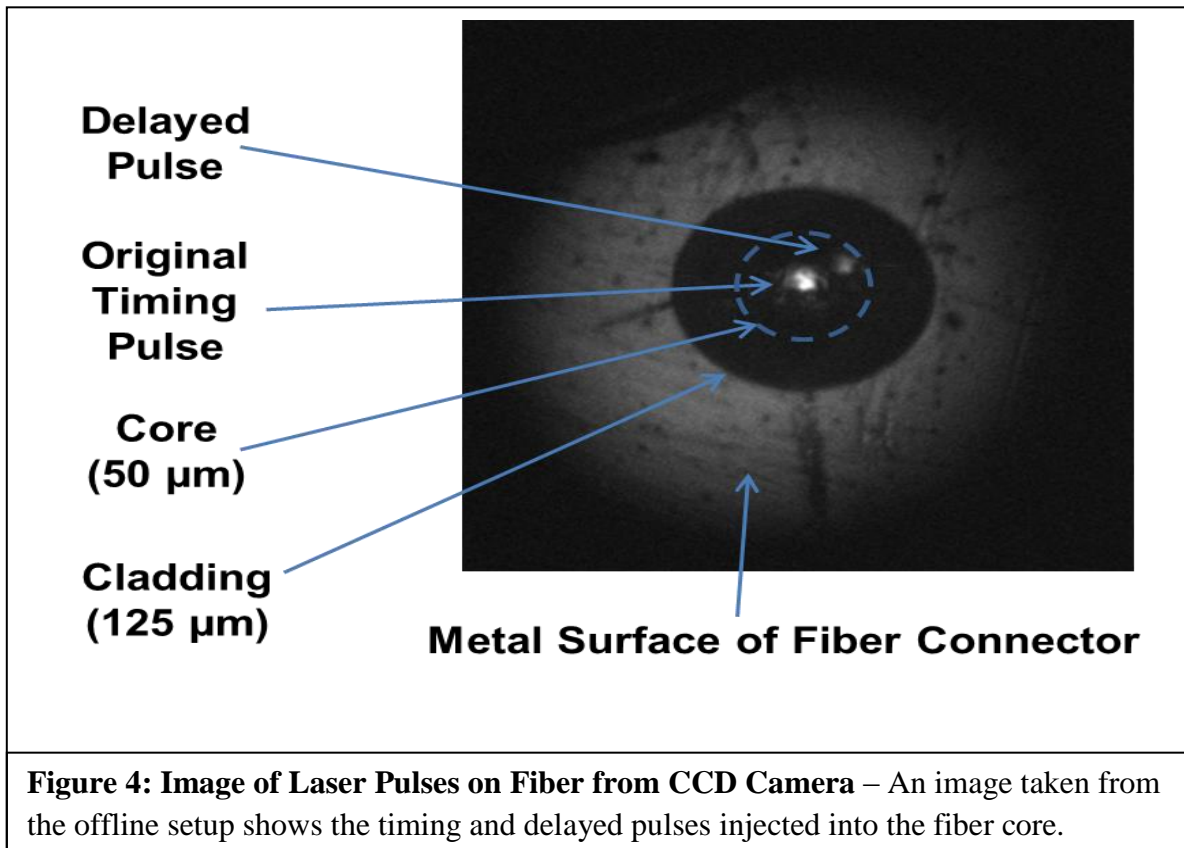
Figure 2: Diagram of Back Surface Reflection from Turning Mirror – A portion of a 1053-nm laser pulse transmits through a mirror coated for high reflectivity at 351 nm, creating a back surface reflection and a second spot when focused to the detector at TCC. The distance between the two spots varies based on the wedge angle of the mirror. When the spots overlap, they create a distorted signal at the detector. In the diagram, only one mirror is shown. In OMEGA, there are two mirrors, creating four spots.

3. Experimental Setup:

An optical setup was built to duplicate conditions seen on OMEGA’s beam timing system (figure 3). The system begins with a 1053-nm fiber-delivered laser pulse, which connects to a 10/90 splitter so that 10% of the laser is sent into a photodiode that connects directly to an oscilloscope on channel 1. This represents the reference signal on OMEGA. The other 90% of the laser travels through a 50/50 splitter and the resulting two pulses are injected into the optical setup. The timing pulse (highlighted in blue) takes a shorter path to the fiber while the delayed pulse (highlighted in red) travels a longer distance to reach the fiber. In OMEGA, the final turning mirrors have a thickness of 5 cm. Therefore, the light would take approximately 0.25 ns to travel through one



mirror when striking it at a roughly 45° angle with a speed of 2.0×10^8 m/s (3.0×10^8 m/s speed of light divided by 1.5 index of refraction in glass). Hence, it takes about 0.5 ns for the light to travel through both the end mirror and the target mirror. In the offline setup, the path length of the second pulse is extended using two mirrors to achieve a delay of 0.5 ns and replicate conditions on OMEGA. A viewing system composed of a CCD camera and a light source is used to view the timing and delayed pulses so that the two pulses can be adjusted and placed precisely at the desired positions on the fiber core (figure 4). The fiber then connects to a photodiode, which reads on channel 2 of the oscilloscope.



4. Oscilloscope Measurements:

Using the oscilloscope's current built-in routines, data was taken for two configurations, one with the distorted pulse and one with just the timing pulse. The latter was done by blocking the delayed pulse (red beam in figure 3) with a dark object. In the first configuration, the oscilloscope measured a 3.11-ns timing shift between the reference pulse and the distorted pulse (figure 5a). In the second configuration, the oscilloscope measured a 3.05-ns timing shift between the reference pulse and the timing pulse (figure 5b). Therefore, the oscilloscope measurement was skewed by 60 ps when presented with a distorted pulse. The offline setup using the oscilloscope's built-in routines confirmed that the oscilloscope routines did not compensate for timing shifts caused by distorted pulses.

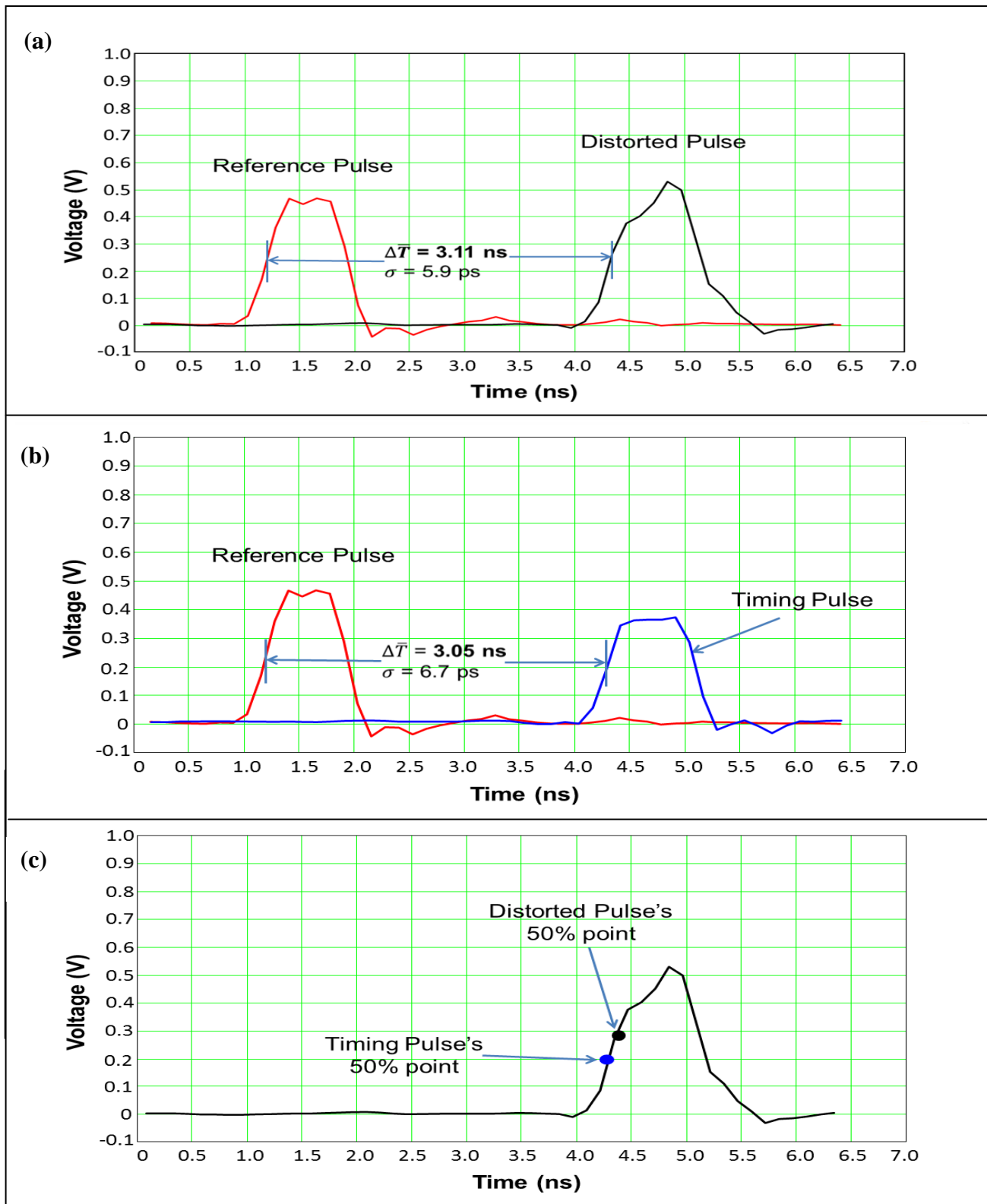


Figure 5: Oscilloscope Data Readings from Offline Optical Setup – The oscilloscope measured a 3.11-ns timing shift between the 50% points of the reference and distorted pulses (a) and a 3.05-ns timing shift between the reference and timing pulses (b). This discrepancy is caused by differences in the 50% points of the timing pulse and distorted pulse (c).

Current oscilloscope routines use a measurement technique called Full Width Half Max (FWHM), which finds the peaks of two pulses, goes down to their respective 50% points, and measures the difference in time between those 50% points (figure 5a). However, because the distorted pulse is the summation of the timing pulse and delayed pulse, its amplitude is larger and thus, its 50% point is higher than the 50% point of the timing pulse (figure 5c). This results in a timing shift in the oscilloscope measurement.

5. Algorithm:

A signal-processing algorithm was developed to correct for timing shifts caused by distorted pulses. The new signal-processing algorithm is designed to recover the timing pulse from the distorted pulse. An assumption made when creating the algorithm is that the reference and timing pulses are similar in shape. This is a valid assumption because both the reference and timing pulses originate from a single laser pulse. The algorithm takes two reference pulses and delays one in time to simulate the back surface reflection. It then scales the two pulses individually in amplitude, as the delayed pulse has lower intensity than the original timing pulse. Finally, the algorithm sums the two pulses to create a distorted pulse that is very similar in shape to the actual distorted pulse, as shown in figure 6.

A least-squares regression equation with a cubic spline interpolation served as the basis for the algorithm. The purpose of the least-squares regression equation is to fit the best curve along the oscilloscope's data points. The cubic spline interpolation first takes four consecutive data points and fits a cubic function through these points. It repeats this process on all possible sets of four consecutive data points. The two reference pulses are then placed on a time grid. The cubic spline interpolation combines the cubic functions and a least-squares regression equation is used to produce the best possible curve from the summation of the two reference pulses. The cubic spline is

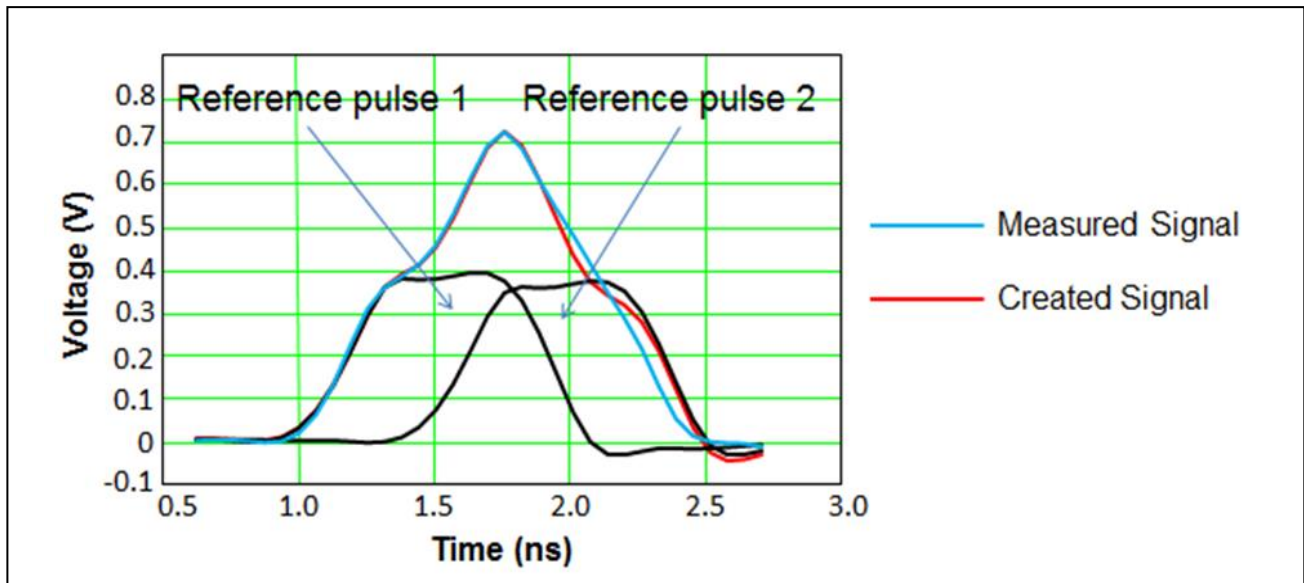


Figure 6: Mathcad Reconstruction of Distorted Pulse Shape – This graph shows two reference pulses, colored in black. One is measured on the oscilloscope and the other is copied and delayed in time, and both are individually scaled in amplitude. The new distorted signal, created from the summation of these two reference pulses, is in red, while the distorted pulse as seen in the offline setup is in blue. The two distorted pulses are nearly identical to each other.

needed because the oscilloscope’s sampling rate is one data point every 125 picoseconds (8 GHz), but since the algorithm needs to measure timing shifts to the single picoseconds, data points must be interpolated. The algorithm minimizes the quantity σ , where

$$\sigma^2 = \sum_k [A \cdot Ref[t_k] + B \cdot Ref[t_k - \Delta t_1] - Dist[t_k + \Delta t_2]]^2$$

A and B are the amplitudes of the two reference pulses and t_k is the point k on the time grid of the first reference pulse. The algorithm sums over k, where t_k ranges from the beginning of the first reference pulse to the end of the second reference pulse. Δt_1 is the time delay of the second reference pulse with respect to the first, and Δt_2 is the time delay of the distorted pulse with respect to the first reference pulse, or the correct timing shift.

Results using the algorithm for a case in which the timing shift, Δt_2 , was found to be 3.059 ns are shown in figure 7. Figure 7a shows the reference pulse and the newly created distorted pulse.

Blocking the delayed pulse so that only the timing pulse is injected, a 3.053-ns time difference was measured between the reference pulse and timing pulse (figure 7b). Therefore, the new algorithm only had a 6-ps timing shift when presented with a distorted pulse shape, an order of magnitude smaller than the 60 ps obtained above.

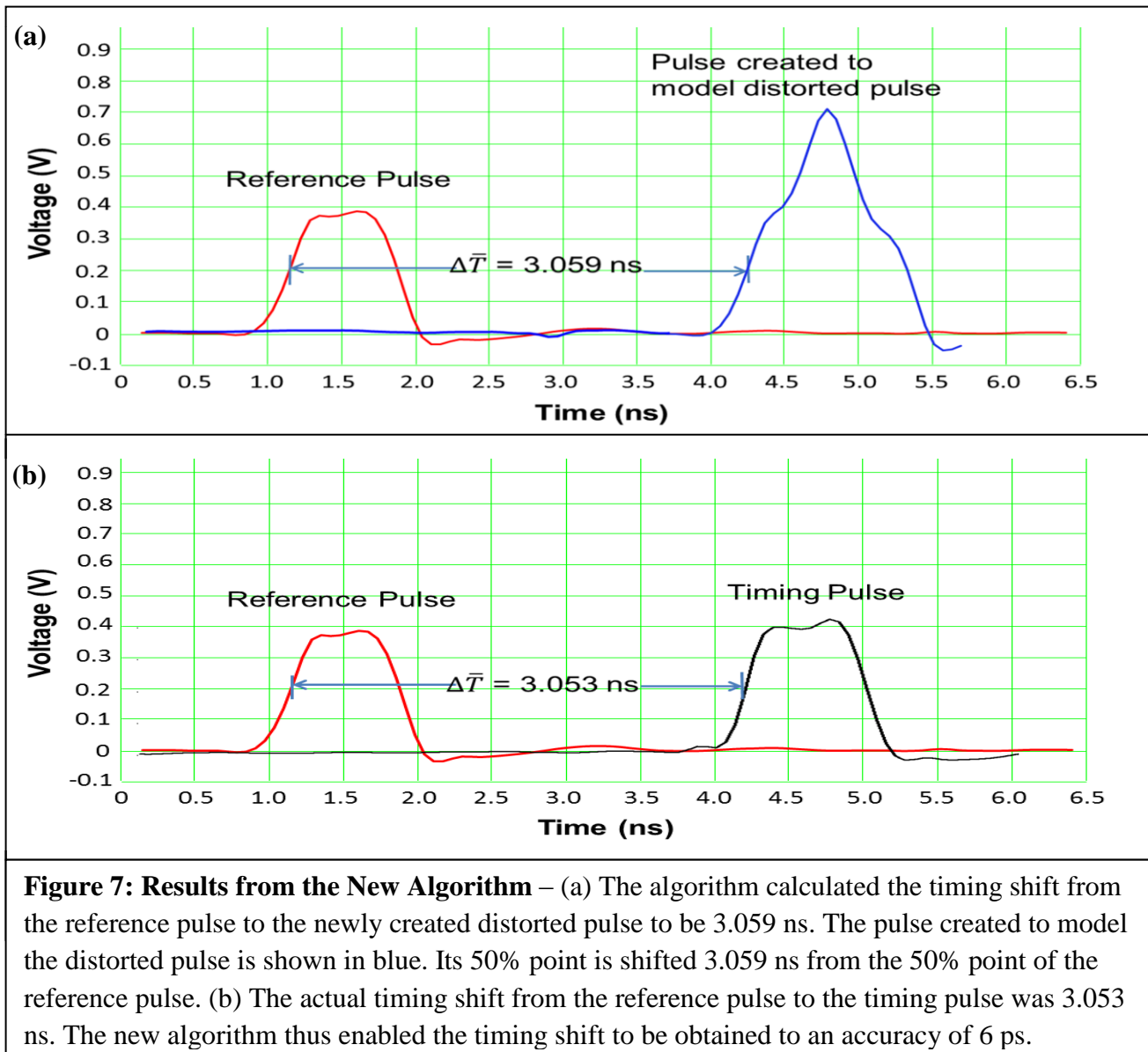


Figure 7: Results from the New Algorithm – (a) The algorithm calculated the timing shift from the reference pulse to the newly created distorted pulse to be 3.059 ns. The pulse created to model the distorted pulse is shown in blue. Its 50% point is shifted 3.059 ns from the 50% point of the reference pulse. (b) The actual timing shift from the reference pulse to the timing pulse was 3.053 ns. The new algorithm thus enabled the timing shift to be obtained to an accuracy of 6 ps.

6. Conclusion:

An offline setup has been built to test a new algorithm for the OMEGA laser timing system. Data obtained from the offline setup confirm that the oscilloscope's built-in measurement routine incorrectly predicts timing shifts by up to 60 ps when presented with distorted pulse shapes. A new signal processing routine recovers the correct timing offset from the distorted pulse shapes with only 6 ps of error. The offline setup used delayed pulses up to ten times larger in amplitude than the pulses from the back surfaces of the final turning mirrors to produce timing shifts that were large and unambiguous. However, since the signal processing algorithm places no restrictions on the amplitude of the distorting pulse, it can be used to predict the timing offset for any of the beamlines.

7. Future Work:

Results obtained using this algorithm show the algorithm's effectiveness, but the algorithm was only used on two sets of data: one set with a delayed pulse the same amplitude as the timing pulse (figure 7), and another set with a delayed pulse half the amplitude of the timing pulse (figure 5). In the experiment, these two amplitudes were used simply so that there would be large timing shifts that could be clearly measured. However, it is believed that timing errors by distorted pulses on OMEGA rarely exceed 30 ps, so the real delayed pulse is much smaller than those simulated in the offline setup. There was an attempt to take data for the delayed pulse at one-twentieth the amplitude of the timing pulse, but due to laser instability and possible shortcomings in the optics, the reference pulse and timing pulse did not have the same shape and violated the necessary assumption. In the future, data should be taken with the amplitude of the delayed pulse small enough to see what timing errors can be expected for conditions on OMEGA.

The next step would be to implement the algorithm on OMEGA's beamlines during beam timing. On August 2, 2013, a beam timing run was done and results from this run showed that

beamline 61 had a distorted pulse shape very similar to distorted pulse shapes created in the offline optical setup. By implementing this algorithm on OMEGA's next beam timing run, it can be verified if beamline 61 has been distorted by the delayed pulse and if its timing error can be reduced.

8. Acknowledgements:

I would like to thank my advisor, Mr. Robert Boni, for being not only a great advisor, but also an incredible teacher. Mr. Boni made sure I understood what I was doing and patiently taught me concepts that I did not fully understand. In addition, Mr. Boni went out of his way to make sure I got the best experience from this program, taking me through the successes and failures that every scientist must face while doing an experiment. Furthermore, I would like to give thanks to my advisor Dr. William Donaldson for teaching me to use his laser and for helping me troubleshoot many computer and laser-related problems that I encountered. Without Dr. Donaldson's help, I would not have been able to complete such an extensive research project in my short time at the LLE. Finally, I owe gratitude to all the staff at the LLE and to Dr. Stephen Craxton for organizing this wonderful program and for having the far-reaching goal of educating the future generations of scientists. Programs such as the LLE's are the reason why the STEM fields are rapidly growing and reaching new heights.

9. References:

- [1] S. Morse, "Current Beam-Timing System Measures Relative On-Target Arrival Time of Each Beam to Plus or Minus 10 ps," June 1998.
- [2] T. Laurin, "Coatings," *The Photonics Handbook*, book 3, pp 256-257, 2008.
- [3] R. Boni, "Beam Timing System CDR," July 1994.

Rewriteable Photoalignment of Liquid Crystals as a Route to High-Laser-Damage-Threshold Active Beam Shapers

Katherine James

Honeoye Falls – Lima High School

LLE Advisor: Kenneth L. Marshall

University of Rochester

Laboratory for Laser Energetics

Summer High School Research Program 2013

Abstract

The fabrication of rewriteable liquid crystal (LC) cells using high-damage-threshold photoswitchable azobenzene materials has been investigated as a route to all-optical active beam shapers. Beam shapers are used to modulate the intensity profile of OMEGA EP's petawatt-peak-power laser beams. All-optical photoswitchable beam shapers would allow intensity profile tailoring to occur at higher-fluence locations in OMEGA EP's beam lines than is currently possible using electro-optical LC beam shapers. Photoswitchable LC cells were assembled using one substrate coated with a non-switchable buffed polyimide alignment layer and a second substrate coated with an azobenzene-based photoswitchable alignment layer. The cells were filled with nematic E7 LC. Irradiating the cell with polarized UV light induced an azobenzene trans-to-cis isomerization, facilitating in-plane switching of LC alignment. The irradiation time was optimized to produce high-quality LC alignment. Different transmission functions were obtained after multiple alignment write cycles. During the fabrication of these devices, limitations in the azobenzene material's ability to continually rewrite were discovered, but high-quality rewritable behavior was obtained by exposing the photoswitchable layer to UV light through various masks.

1. Introduction

Beam shaping is required in high-peak-power laser systems such as the 60-beam, 40-TW, 351-nm OMEGA laser and the 4-beam, 1-petawatt 1054-nm OMEGA EP laser in order to ensure that the beams fill the entire aperture of the large-scale laser amplifiers and to compensate for spatial variations in energy across the laser beam clear aperture.¹ A beam shaper is an optical element that can control the spatial beam energy profile, either passively (at one fixed profile) or actively in real-time. In order to compensate for the lack of uniformity created by the amplification process, an inverse of the intensity profile of the amplified beam is used. After passing through the beam shaper and undergoing amplification, the high-energy beam entering the laser system's target chamber has a uniform intensity profile.

Laser beam shapers currently used in OMEGA and OMEGA EP are made up of patterns of metal pixels deposited on a fused silica substrate.² These metal pixels do not transmit the incident laser light, while the areas where the metal pixels are not present allow full transmission. Macroscopically, this distribution of pixels creates a smooth energy gradient and can be used to produce a beam with a tailored intensity profile. Such metal-mask beam shapers have a 1054-nm laser damage threshold of 0.2 J/cm^2 at 1-ns pulse width, which is relatively low compared to the output of a high-powered laser.

Liquid crystals (LC's) have also been used in the fabrication of beam shapers.² Nematic LC's display orientational order and have useful optical properties. On a molecular level, LC's are anisotropic in shape, like a rod or a disc, which causes them to exhibit optical properties whose values can change depending on what direction light is incident on the molecular structure. The combination of anisotropy and orientational order results in birefringence, which

is defined as the difference between the refractive index measured along the LC material's long molecular axis and the index measured at an angle to the molecular axis. Birefringence allows the polarization or the phase of incident light to be altered.

To make use of the optical properties of LC materials in devices such as beam shapers, the alignment direction of the long molecular axis must be controlled. Molecular alignment on the surface of a substrate used for LC devices is accomplished by inducing a preferred alignment direction in a thin polymer layer deposited on the substrate surfaces by either mechanical buffing or irradiation with polarized UV light ("photoalignment"). Buffing requires a velvet cloth to be rubbed against the polymer alignment coating, and the LC molecules align along the buffing direction. This system of alignment is photo-stable, so the alignment direction will not change from its original orientation. Because the surface of the substrate comes into contact with the fabric, the buffing process induces scratches and particulate contamination in the coating surface, which lowers the device's laser damage threshold. In the photoalignment process, a photoactive polymer is exposed to polarized UV light, causing the material to dimerize either parallel or perpendicular to the direction of polarization, depending on the photochemistry of the alignment layer. The LC molecules align along the dimerization direction. Because the process is non-contacting, it is inherently clean, and photoaligned LC devices typically show significantly higher laser damage thresholds than do buffed LC devices.

Previously, passive LC beam shapers that function in a very similar manner to metal-mask beam shapers were fabricated at LLE using a coumarin photoalignment layer (Fig. 1). Such coumarin-based photoaligned beam shapers have 1054-nm laser damage thresholds upwards of 27 J/cm^2 (1-ns pulse) and show pixel resolution comparable to metal-mask beam shapers.³ The high laser damage threshold of LC beam shapers allows the optic to be placed in different, possibly more convenient places after the beam has undergone more amplification.

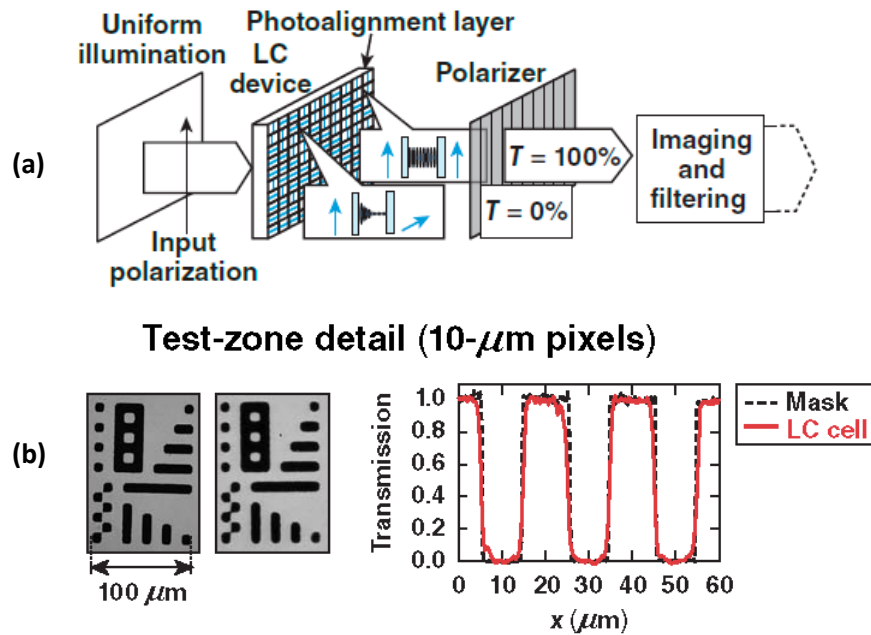


Fig. 1: (a) An illustration of the concept of the LC beam shaper. Polarized light passes through the LC device containing a distribution of pixels with parallel or twisted alignment states. The polarization of the light passing through each pixel changes accordingly and is either blocked by or transmitted through a second polarizer. (b) A test zone detail of a liquid crystal device on the right and a metal mask on the left along with the transmission graph comparing the two. The resolution and contrast of the liquid crystal device is on par with the metal masks currently in use.

Active laser beam shaping would allow the pattern of the pixels to be dynamically rewritten without replacing the optic. Currently, real-time, active beam shaping in OMEGA EP is conducted using electro-optical LC devices that contain a matrix of conductive-oxide electrodes deposited on the inner surfaces of the substrates, similar to what is used in LC displays in

computer monitors and flat-screen televisions.³ The requirement for these conductive-oxide electrodes results in laser damage thresholds for electro-optical LC devices comparable to those of metal-mask beam shapers ($< 1 \text{ J/cm}^2$ at 1054 nm, 1-ns pulse), limiting their use to low-fluence areas of the laser system. A photoaddressable, rewriteable alignment layer with sufficiently high laser damage threshold could be used to fabricate an optically addressed active LC beam shaper. Such materials are commercially available from Beam Engineering for Advanced Measurements

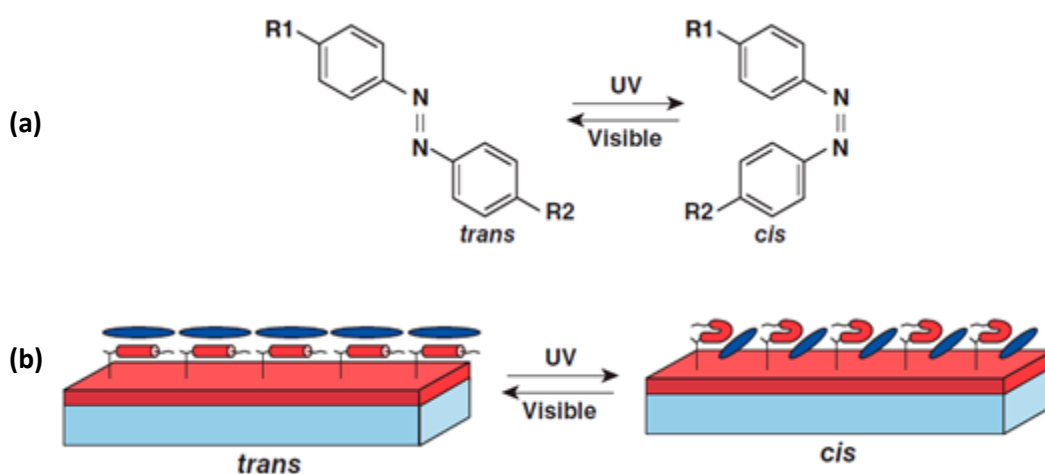


Fig. 2: (a) An illustration of the trans to cis isomerization of azobenzenes when exposed to UV light.(b) A representation of the in-plane switching of liquid crystal alignment when the azobenzenes undergo a trans to cis isomerization.

(BEAM) Company.⁴ These materials are azobenzene based, and can therefore undergo a reversible trans- to cis- isomerization when exposed to polarized UV light. This change in shape results in reversible, in-plane switching of LC alignment (Fig. 2).⁵ Recent work at LLE has shown that the BEAM Co PAAD photoswitchable azobenzene alignment layers have 1054-nm laser damage thresholds ranging from 28 to 67 J/cm^2 (1 ns pulse), depending on the alignment layer material composition.³ These materials provide a potential route to an all-optical active LC laser beam shaper.

In order to determine whether these PAAD materials could potentially be used in the fabrication of an active beam shaper, LC devices were fabricated with an azobenzene-based photoalignment layer and a buffed polyimide (PI) coating. The PAAD photoalignment layer was photopatterned using a photolithographic UV lamp. These devices were characterized macroscopically and microscopically and assessed on their contrast between different alignment areas and the resolution sharpness of the transitional boundary. This work showed that PAAD alignment layers can rewrite and that a similar, high quality material has the potential to be used in the development of an active LC laser beam shaper.

2. Experimental

2.1 Device Fabrication

Two 50-mm-diameter fused silica substrates were cleaned via an aqueous cleaning process during which they were scrubbed with 0.05- μm MasterPrep® polishing suspension using a synthetic wiper (2 minutes), rinsed with 2 megohm-cm deionized (DI) water and nanopure DI water (1 minute each), and ultrasonically cleaned at 69°C in a solution of Extran detergent for 1 hr. The substrates were then rinsed with 18.5 megohm-cm DI water for one minute, before being blown dry with nitrogen to remove any visible moisture and placed on a hotplate to dry at 130°C for 30 minutes.

In this process, two metrics were used to ensure substrate cleanliness. The first was a seven-second water break test. While rinsing a substrate after the scrubbing step, each surface is flooded with DI water, and the substrate is held at an angle. The water should remain a continuous sheet across the substrate for at least seven seconds; breaks in the sheet of water indicate that hydrophobic contaminants are present, and the substrate should be scrubbed again.

The second metric was a visual inspection of the cleaned and dried substrate performed by looking through the substrate towards a fiber optic lamp. The substrate should appear clear (cloudiness is indicative of polishing abrasive dried on the surface) with no apparent particles on the surface. Substrates that do not pass this check must go through the entire cleaning process again. Additionally, substrates with obvious surface damage (e.g., scratches or pit marks), are discarded.

After the substrates were cool, one was coated with Nissan Sunever polyimide (PI) and buffed to provide UV-stable LC alignment and the other was coated with a photoalignment material (in this case PAAD-22). The first substrate was placed on a spin coater and flooded with the PI solution filtered through a 0.2 μm PTFE syringe filter. The solution was allowed to sit on the substrate for one minute before being spun off at 2000 rpm for 40 seconds. The coating was soft-baked on a hot plate at 80°C for 10 minutes, followed by hard-baking at 230°C for one hour.

A commercial buffing machine was used to buff the PI coating. The buffing wheel and motorized stage were vacuumed to remove loose fibers. Then, the PI coated substrate was placed on the stage near the buffing wheel, and the height of the wheel was adjusted to just graze the substrate. The wheel was turned on, and the substrate was held in place by vacuum. The substrate passed under the buffing wheel 8 times. After it was removed from the stage, the substrate was rinsed with 8.5 megohm-cm DI water and blown dry with nitrogen to remove any buffing fibers. This rinsing and drying were repeated until all fibers were removed. The substrate was then allowed to dry on a hot plate at 130°C for half an hour.

To deposit the PAAD-22 photoalignment material, the second substrate was first conditioned by placing it on the spin coater and flooding the surface with isopropanol, which was spun off immediately at 2000 rpm for 30 seconds. The substrate was then flooded with PAAD-22

filtered through a 0.2- μm PTFE syringe filter. The solution was spun off immediately with the same spin parameters. The coated substrate was placed in a clean hood to air dry for 10 minutes at room temperature.

The LC cell was then assembled with the coated substrates. Glass microspheres (8 μm dia.) were dispersed into Epotek UV curing epoxy and the mixture deposited as small spots onto the PI coated side of the substrate in three locations 120° apart using a syringe needle. The PAAD coated substrate was placed, coated side down, on top of the PI coated substrate, and the epoxy cured under a UV lamp for 10 minutes. The empty cell was placed on a hot plate along with a surface thermometer and the hotplate temperature was raised to at least 70°C (past the clearing point of the LC). The inter-substrate gap was filled by capillary action with the LC mixture, E7 containing 0.07 weight-percent of the chiral twisting agent CB15 in its isotropic phase. The filled cell was cooled at a rate of 10°C per hour to ambient temperature.

2.2 Device photopatterning

To complete the device, the fluid-filled cell was irradiated with polarized UV light in a photolithography setup as shown in Fig. 3.

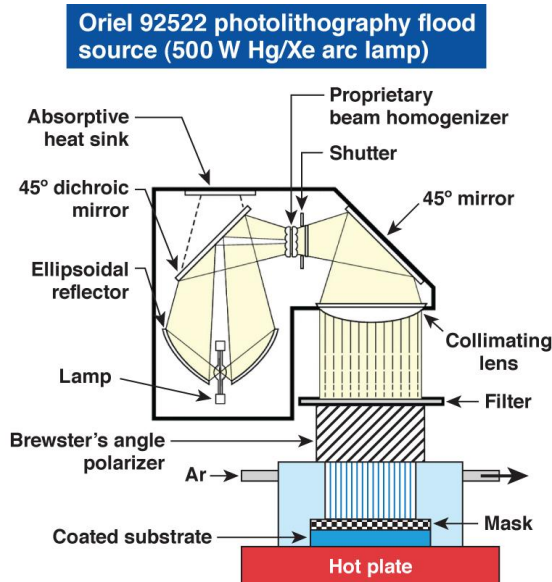


Fig. 3: The photolithography setup used to pattern and expose photoalignment layers for the LC beam-shaper device. Pictured at the bottom is a coated substrate that is exposed to the filtered, polarized light coming from the 500 watt lamp.

The cell was placed in the irradiation chamber with the buffing direction of the polyimide-coated substrate either parallel or perpendicular to the UV polarization direction and with the top substrate having the photoalignment layer. To create a patterned device, the cell was exposed to UV light, then rotated 90° and irradiated again through a mask. This action resulted in a rewritten portion of alignment in the unmasked area. The cell was continually rewritten by changing the orientation of the substrates with respect to the polarization direction and using different masks.

2.3 Device characterization

Devices were characterized both macroscopically and microscopically (Figure 4). Macroscopic characterization was conducted by viewing the devices between crossed and parallel polarizers to evaluate the overall alignment quality. High quality alignment was indicated by high contrast between different alignment areas and by sharp resolution in transition areas. The boundary resolution between adjacent alignment zones and the level of coating contamination were determined by examination of the devices in transmission with a polarizing microscope at 100 x magnification.

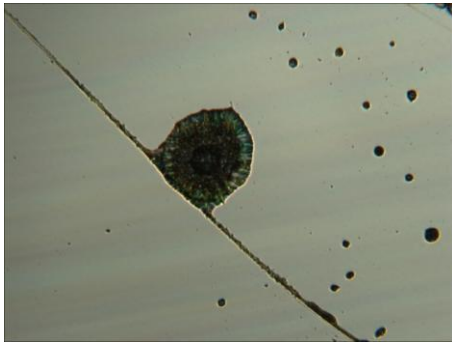


Figure 4a: A microscopic view of phase separation. This concentration of dye in the coatings is detrimental to the alignment quality of LC devices

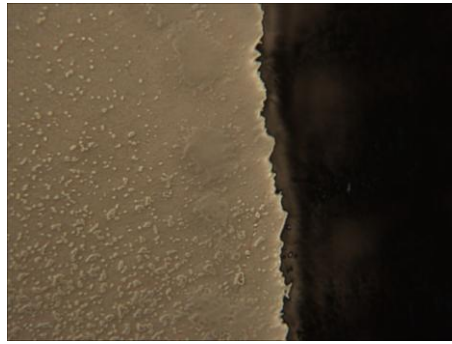


Figure 4b: A microscopic view between crossed polarizers of the boundary between two alignment areas. The resolution of this boundary is quite good, but is not on par with metal mask beam shapers.

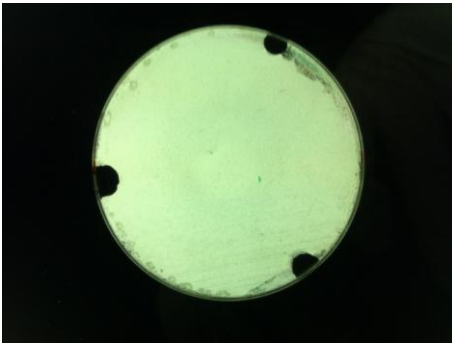


Figure 4c: A macroscopic view of a device with twisted alignment between crossed polarizers. This example shows good alignment and very few features.



Figure 4d: A microscopic view between crossed polarizers showing the texture of the coating. There are few features and the texture is mostly smooth, which shows good coating quality.

3. Results and discussion

An initial experiment determined that the PAAD-22 produced LC alignment perpendicular to the direction of the polarized light used to irradiate the device. In this experiment a device was irradiated, keeping track of the buffing direction, and then viewed between crossed and parallel polarizers. When the buffing direction was aligned with the direction of polarization of the UV light, a twisted cell was produced. Twisted cells look bright between crossed polarizers, and dark between parallel polarizers.

The quality of LC alignment varied with irradiation time. In order to determine the optimal irradiation time, a bracketed exposure experiment was conducted where a device was exposed to UV light for 30 seconds at a time. The device was first irradiated to give a twisted cell. One half of the device was rewritten to a parallel aligned configuration. For every 30 seconds of irradiation in the parallel aligned orientation, the device was characterized macroscopically to see if the quality of alignment improved. It was discovered that the contrast between two sections of alignment continued to improve until 4 minutes of irradiation had gone by. After that amount of time, the quality no longer showed any substantial changes. From here on, exposure time was set to 4 minutes.

The patterned device produced as shown in Fig. 5 demonstrated the ability to write and rewrite a pattern. First, the device was written with twisted alignment, then rotated and masked to produce the first pattern. That pattern was rewritten by irradiating in the same orientation without the mask. The second pattern was written by turning the device 90°, masking it, and irradiating it. Each irradiation lasted 4 minutes. Although the first pattern was sharp, rewriting proved to be tricky and the resulting device was of a lower quality.

A memory effect was also observed while using these materials. After rewriting a pattern, remnants of the original would sometimes be visible. Sometimes, this effect would appear immediately after the initial erasing or rewriting of the pattern (as in Fig. 5), while on other occasions, the original pattern would disappear and then reappear in later irradiations. To determine if the LC was *remembering* its original pattern, the cell was heated to the isotropic phase and then cooled at 10° C per hour. This treatment had no noticeable effect on the memory. This confirmed that the memory effect was rooted in the photoalignment layer. In an effort to mitigate memory effects, devices were irradiated for longer periods in order to more fully expose the azobenzenes. Unfortunately, this method also proved to be inadequate.

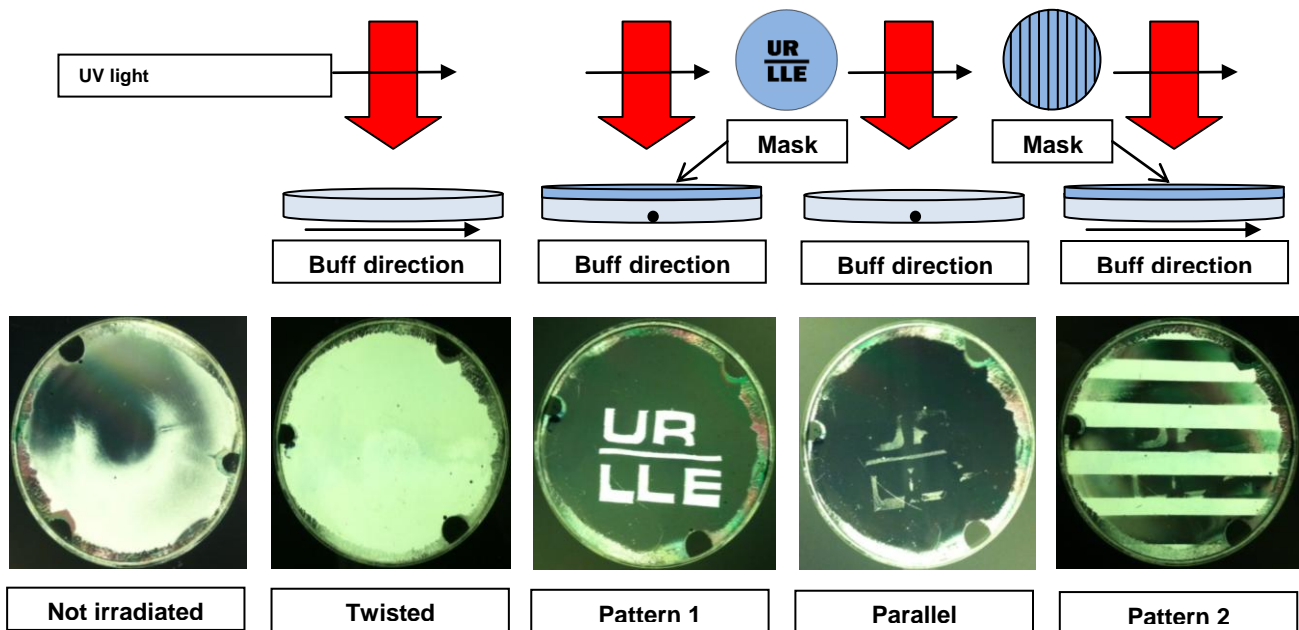
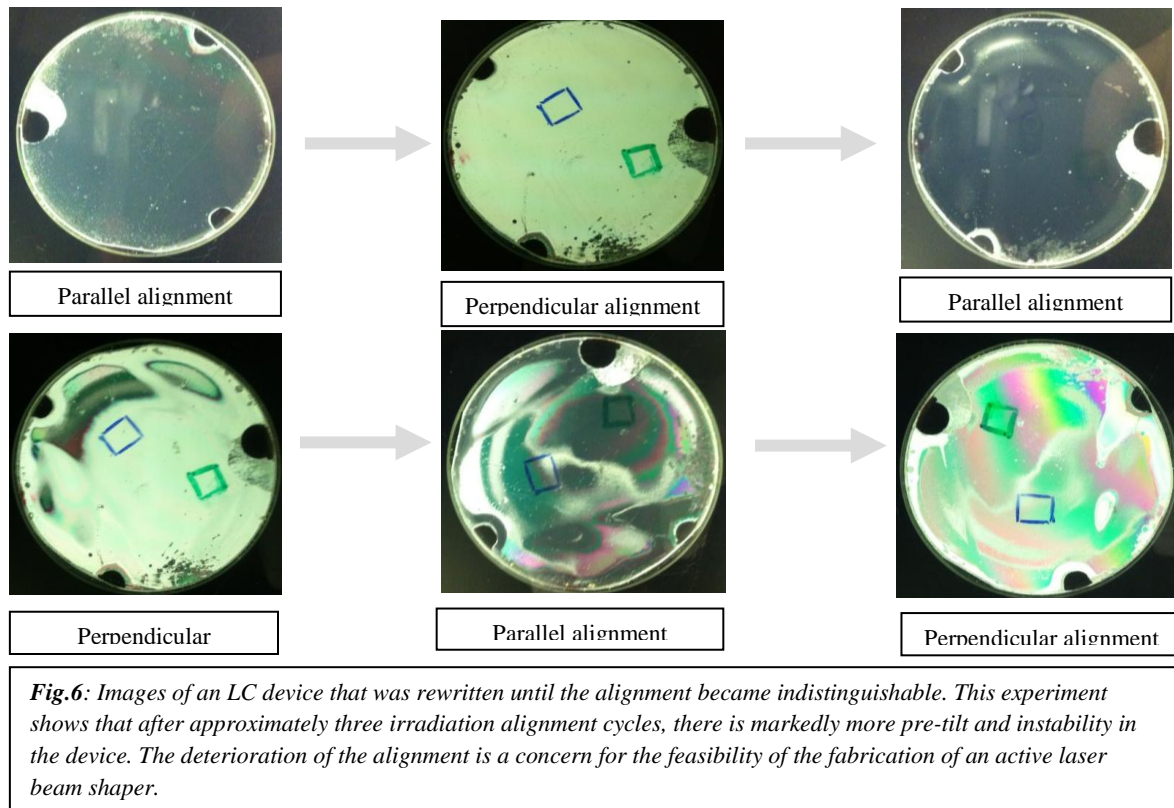


Fig.5: A schematic showing the irradiation procedure for rewriting an LC device. Each irradiation lasted 4 minutes and all images show the device through crossed polarizers. First, the device was written with twisted alignment, then rotated and masked to produce the first pattern. That pattern was rewritten by irradiating in the same orientation without the mask. The second pattern was written by twisting the device 90°, masking it and irradiating it.

Another device was tested to determine the maximum number of times the PAAD material can be rewritten (Fig. 6). The irradiation of this device did not utilize a mask – instead

the entire device was rewritten with each exposure by changing its orientation with respect to the polarization direction. Each irradiation lasted 4 minutes and was accompanied by a decreasing alignment quality and an increase in pretilt, where the LC molecules do not lay flat on the alignment layer. With each irradiation, the increased pretilt caused the response of the device to applied pressure to increase. This effect is seen as the alignment becomes less homogeneous and there are no longer two different alignment orientations, but many. One possible cause of the increased pretilt may have been residual dimethylformamide (DMF) escaping from the coating. Attempts to cure the coating either by air drying for a longer period of time before cell assembly or by gently heating the coated substrate (65°C) showed no improvement, but DMF has not been ruled out as a potential cause. Increased phase separation in the photoalignment coating was also seen in multiple devices after many irradiations had taken place. Phase separation was observed as the formation of orange droplets in the coating (Fig. 4a). Another source of phase separation was the spin-coating process. During the coatings when less than 2 mL of PAAD material was used, phase separation was immediately and macroscopically visible, while when 2 mL or more was used, even microscopically there was little or no phase separation.



4. Conclusions

Using PAAD-22, a photoalignment material, rewriteable LC devices were fabricated. These devices demonstrated that it is possible to rewrite patterned liquid crystal cells. An optimal irradiation time of four minutes was discovered alongside various rewriteability limitations. Procedural improvements were also made in order to reduce the amount of phase separation in the PAAD coating. Although these materials were shown to be rewriteable, the quality of the alignment is simply not yet good enough for fabrication of laser beam shapers. Future work will look into improving the quality of the coating and minimizing the memory effects. Ultimately, a new photoalignment material will mostly likely need to be developed in order to make an active laser beam shaper feasible. The concept of rewriteability has been proven possible and will see valuable applications if improved upon in the future.

5. Acknowledgements

I thank Dr. Stephen Craxton for the time and effort he put in to make the Summer High School Intern Program such a wonderful opportunity. I thank Mr. Kenneth Marshall, my advisor, and Debbie Saulnier for their help and guidance. I also thank Dr. Christophe Dorrer for his helpful advice and suggestions in preparation for my presentation at the 2013 LLE Summer High School Research Symposium. Additionally, I thank all of the Materials Lab staff and students, especially Christa Caggiano and Michael Statt, for teaching me about liquid crystals and helping me with the experiments.

6. References

- [1] Van Wonterghem, B. M. et al., "Performance of a prototype for a large-aperture multipass Nd:glass laser for inertial confinement fusion," *Appl. Opt.* 36(21), 4932-4953 (1997).
- [2] Marshall, K. L. et al., "Liquid crystal beam-shaping devices employing patterned photoalignment layers for high-peak-power laser applications," *Proc. SPIE* 8114, Paper 81140P (2011).
- [3] Marshall, K. L. et al., "Liquid crystal near-IR laser beam shapers employing photoaddressable alignment layers for high-peak-power applications," *Proc. SPIE* 8828, Paper 88280N (2013).
- [4] Beam Engineering for Advanced Measurements Company, Winter Park, FL 32789.
- [5] Ichimura, K., "Photoalignment of liquid-crystal systems," *Chem. Rev.* 100(5), 1847-1873 (2000).

**Modeling the Effects of Deformable Mirror Location in the
OMEGA EP Pulse Compression System**

John Jamieson

Allendale Columbia School
Pittsford, NY

Advisor: Mark Guardalben

Laboratory for Laser Energetics
University of Rochester
Rochester, NY

Modeling the Effects of Deformable Mirror Location in the OMEGA EP Pulse Compression System

Abstract:

The wavefront of the OMEGA EP laser beam within the pulse compression system is corrected using a deformable mirror (DM) located after the last grating of the pulse compressor. A spatio-temporal numerical model (EPCOMP) was used to investigate whether the DM could be moved to a location before the first grating of the compressor. This would reduce the peak power incident on the DM by a factor of 1000. In the model, measured surface deformations were applied to the seven mirrors that transport the beam from the output of the compressor to the target chamber and a DM correction was applied to produce a focal spot size of 2.4 microns at 80% encircled energy (R80) and a pulse width close to its transform-limited value of 0.52 ps for both DM locations. A two-grating analytical model was used to confirm that the spectral phase distortion at the output of the compressor was indeed negligible for the expected wavefront error introduced by DM pre-correction.

1. Introduction

The two short-pulse beamlines of the OMEGA EP laser system use chirped-pulse amplification (CPA) [1] to achieve on-target intensities that exceed 10^{24} Watts per square meter in a picosecond pulse. The CPA technique, shown in Figure 1, is used to reduce the risk of laser damage to optics in the beamlines by first stretching a pulse in time, amplifying it through flashlamp-pumped Nd-doped glass disks, and then compressing it using a four-grating pulse compressor before propagating it to the target. Each of the four diffraction gratings used in the OMEGA EP pulse compressor comprises three smaller, tiled gratings because of the cost and technical challenges involved in implementing larger, meter-size gratings [2].

After pulse compression, the laser beam is transported through a series of mirrors to the target chamber. Because the compressor gratings and transport mirrors are not perfectly flat, each will introduce a wavefront error onto the beam that will degrade its focal spot quality if left uncorrected. The deformable mirror (DM), currently located after the last grating of the compressor, is used to correct the wavefront errors. The DM has 39 pistons behind it that can push and pull the glass of the DM and physically “mold” it to be the optimal shape for wavefront correction. The purpose of this project was to determine whether or not the DM could be moved to before the compressor without introducing excessive spectral phase errors that could degrade the compressed pulse, leading to reduced on-target intensities. Doing so would reduce the power on the mirror by a factor of 1000, substantially reducing the risk of further laser-induced damage on the DM.

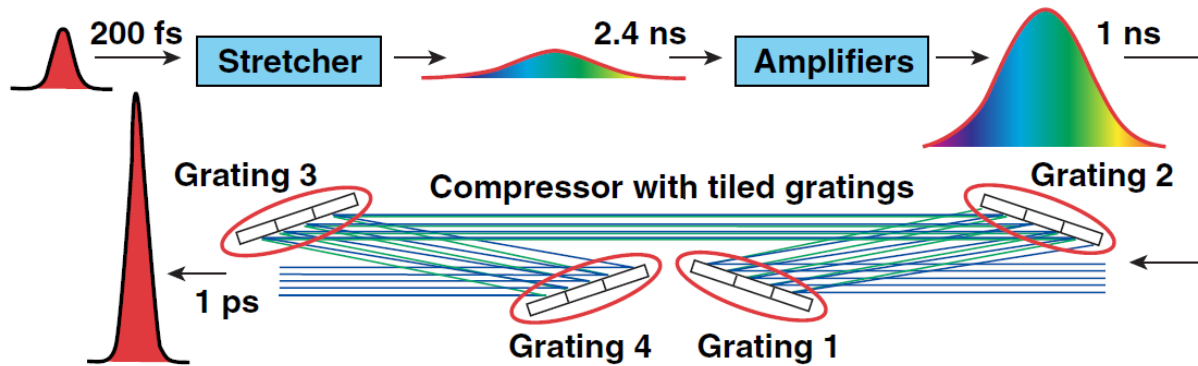


Figure 1 – **Chirped Pulse Amplification (CPA)** – Block diagram of the CPA technique used in OMEGA EP. The laser pulse is first stretched in time, amplified, and then compressed using a four-grating pulse compressor. The pulse stretcher stretches the pulse by delaying each color of the pulse spectrum by a different amount. The compressor produces a short pulse by bringing these colors back together in time.

2. EPCOMP Numerical Model

EPCOMP is a three-dimensional beam propagation code that is used to model the OMEGA EP tiled-grating pulse compressor. It uses the commercial software package FRED [3] as a non-sequential ray-tracing engine and performs coherent propagation using the Gaussian beamlet method [4]. The OMEGA EP pulse spectrum was assigned to each spatial point in the EPCOMP source grid and each spectral slice of the beam was propagated through the compressor and transport sections of OMEGA EP. The electric field of each spectral slice was coherently sampled on a rectilinear grid that was placed in two different locations. The near-field beam was sampled between the last transport mirror and the off-axis parabola (OAP) focusing element, and the far-field beam was sampled at the center of the OMEGA EP target chamber. A MATLAB [5] post-processor was used to calculate the temporal pulse from the pulse spectrum at each grid point, and can provide detailed predictions of the temporally resolved near-field and far-field beams.

The wavefront error incurred through the transport section was sampled at the central wavelength of the pulse spectrum just prior to the OAP. The DM surface height distribution necessary to correct this wavefront error was determined using an experimentally calibrated DM influence function model [6] and then applied to the deformable mirror surface in the FRED model as a bicubic mesh.

Figure 2 shows the FRED model that was used. The figure four at the input to the compressor does not currently exist in the actual laser system, but is a proposed configuration for the DM that would be located there.

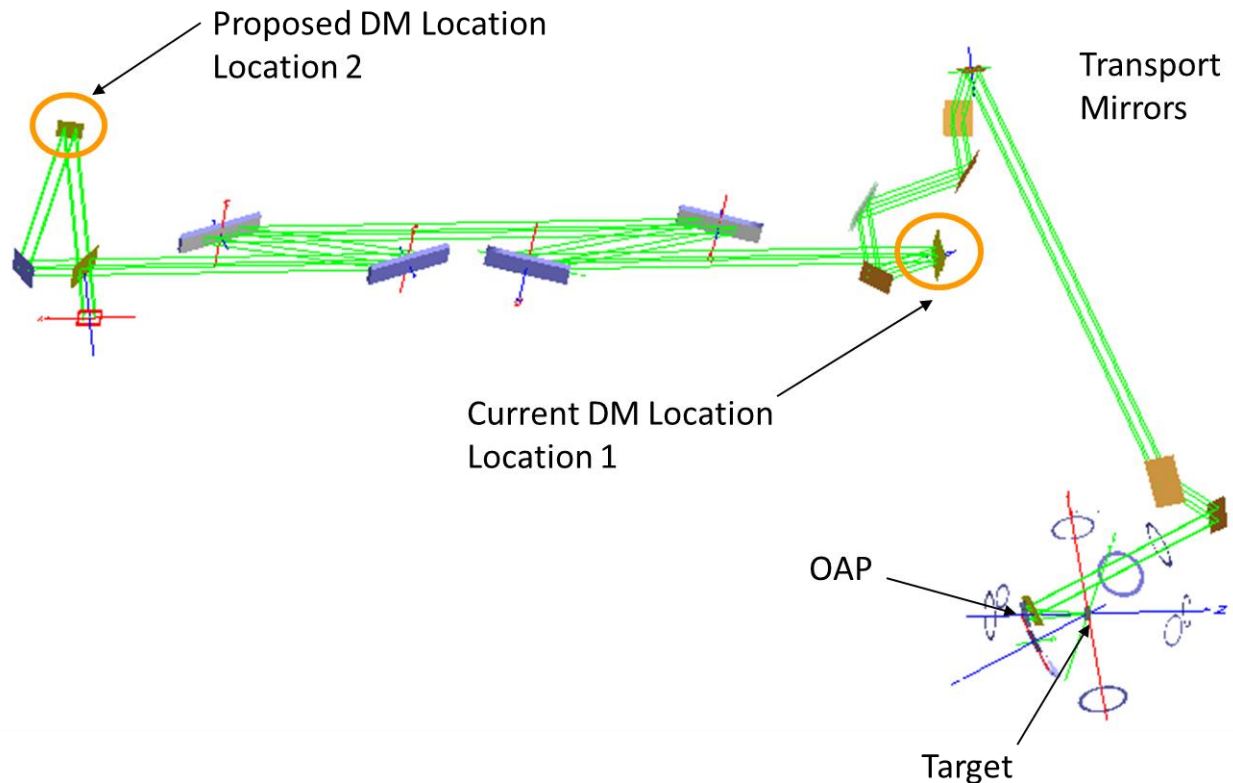


Figure 2 – **The FRED Model** - The beam was propagated through two mirrors arranged in a figure four, the four-grating compressor, and the transport section, and was focused onto the target using the off-axis parabola mirror (OAP). Location 1 is where the DM currently is located. Location 2 at the input to the compressor is the proposed DM location. The first mirror after the source was 100% reflecting when the DM was in Location 1, but 100% transmitting when the DM was in Location 2.

The temporally integrated focal spot was characterized using the 80% encircled energy radius (R80), which is the minimum radius of a circle that contains 80% of the energy in the focused beam. A smaller R80 is more desirable because it means that higher on-target intensities can be achieved. The spatially integrated pulse was characterized by its full width at half of its maximum value (FWHM). The transform-limited FWHM was 521 fs using a Gaussian spectrum with spectral width close to that of the amplified, on-shot OMEGA EP spectrum.

The spectral phase of the pulse represents how spread out the pulse spectrum is (see Figure 1). The spectral phase of the pulse entering the compressor for a perfectly matched stretcher and compressor was obtained by propagating the spectral pulse that had a uniform spectral phase profile through the compressor and transport system with no alignment or wavefront errors. The conjugate of the accumulated spectral phase of the output pulse was then assigned to the input pulse for subsequent modeling runs. The beam was modeled using a 36.9-cm square aperture source grid of 30x30 uniformly weighted rays.

3. Results

3.1 The Perfect System

The perfect system with no wavefront error or DM correction was modeled first to provide a baseline against which to compare subsequent modeling runs. These results are shown in Figure 3. With no wavefront error on the beam, the focal spot R80 was 2.4 microns, and the compressed pulse FWHM was 0.52 ps.

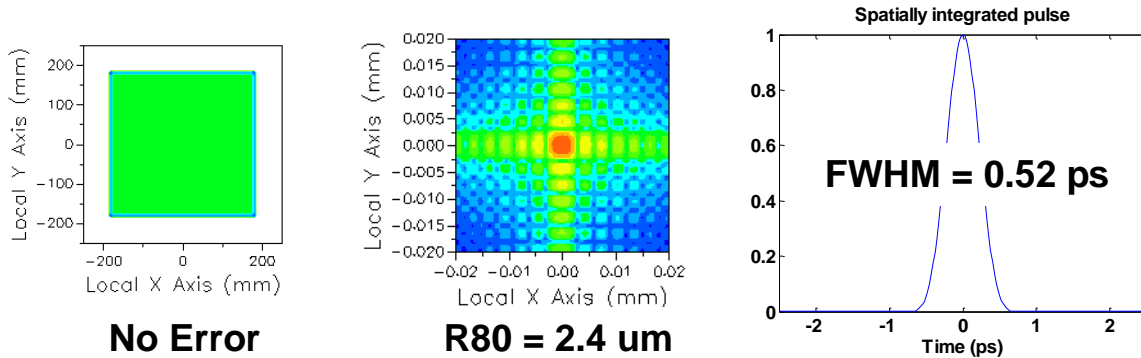


Figure 3 – **The Perfect System** The left plot displays the wavefront after the last mirror. The central plot is a log plot of the irradiance at the target, with 6 orders of magnitude represented by the color map used. Red regions in the central plot are areas of highest light intensity and blue regions are areas of lowest light intensity. The right plot is the spatially integrated pulse at the target. There is no error on the wavefront, the R80=2.4 microns, and the FWHM of the pulse is 0.52 ps.

3.2 Transport Mirror Error with No DM Correction

Measured surface errors were applied to the transport mirrors in the FRED model as third-order x, y polynomials with no DM correction for this run. Figure 4 shows that the peak-to-valley wavefront and R80 increased to 0.63 waves and 3.7 microns, respectively, but there was no difference in the FWHM pulse width compared to the perfect system.

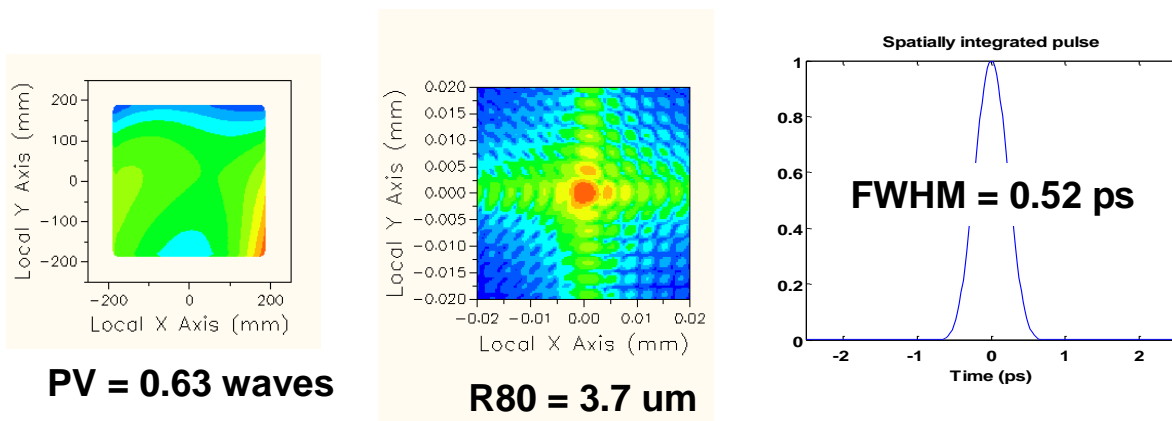


Figure 4 – **Transport Error with No DM Correction** –Measured surface deformations from the transport mirrors were applied to the perfect system. The left plot displays the wavefront after the last mirror. The central plot is a log plot of the irradiance at the target. The right plot is the spatially integrated pulse at the target. There is a peak-to-valley error of 0.63 waves on the wavefront, the R80 is increased to 3.7 microns, and the FWHM=0.52 ps.

3.3 DM Correction at Compressor Output

In this run, the influence function model was used to generate a DM correction for the wavefront error of section 3.2 that was applied to the DM at the output of the compressor. The DM was able to correct the focal spot R80 from 3.7 microns back down to the level of the perfect case, 2.4 microns, as shown in Figure 5. The left plot in Fig. 5 shows that the residual wavefront error had a peak-to-valley of 0.08 waves, with a spatial pattern arising from the finite distance between DM pistons, each piston being modeled by the influence function. The pulse width was not affected by the DM after the compressor.

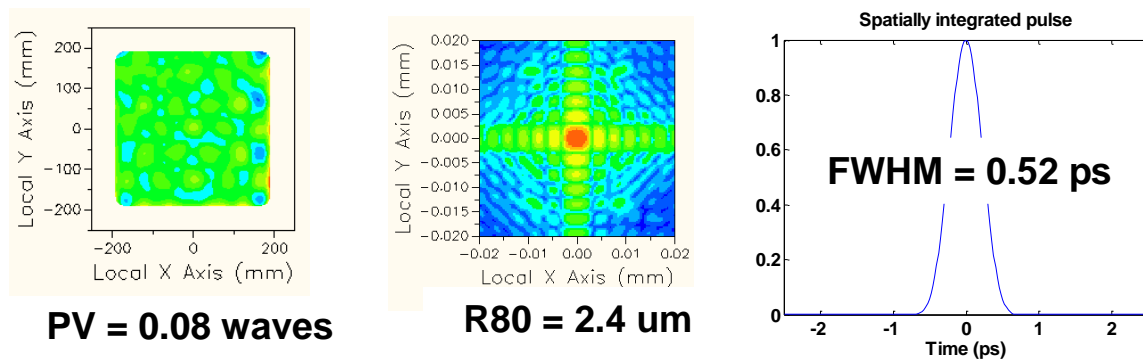


Figure 5 – **DM Correction After Compressor** – The DM correction was applied after the compressor. The left plot shows that there is a peak-to-valley residual wavefront error of 0.08 waves. The central and right plots respectively show that the R80=2.4 microns, and the compressed pulse FWHM=0.52 ps.

3.4 DM Correction at Compressor Input

In this run, the influence function model was used to generate a DM correction for the wavefront error of section 3.2 that was applied to the DM at the input of the compressor. The R80, peak-to-valley residual wavefront error, and compressed pulse FWHM were the same as for DM correction at the output of the compressor. These results are summarized in Figure 6.

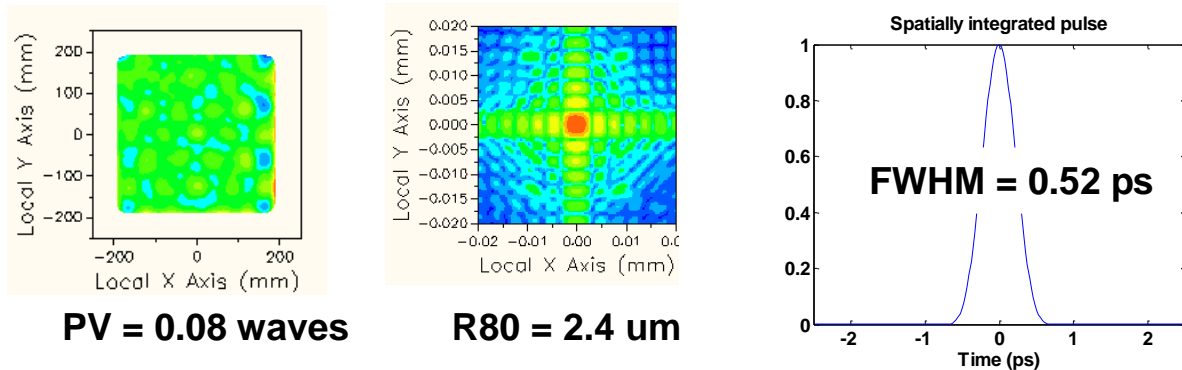


Figure 6 – **DM Correction Before Compressor** – The DM correction was applied before the compressor. There is a peak-to-valley residual wavefront error of 0.08 waves, the R80=2.4 microns, and the FWHM=0.52 ps.

4. Model of DM-Corrected Rays

One concern with placement of the DM before the grating compressor was that the compressed pulse might be distorted due to the different paths of the DM-corrected rays through the compressor. This is illustrated in Figure 7, where the dashed path represents a DM-corrected ray through a grating pair. The deviation of the DM-corrected ray (of order 10 microradians for the largest seen in Section 3) is greatly exaggerated in the figure. This effect was calculated for a two-grating system by working out the exact ray paths as shown in Figure 7, for each frequency in the pulse spectrum, and integrating over the spectrum using the method described in reference [7].

The delay for wavefront gradient errors (i.e., ray direction errors) is shown in the right plot of Figure 8. The delay is less than 8 as ($1 \text{ as} = 10^{-18} \text{ s}$). The left plot of Figure 8 shows that the temporal pulses calculated with and without the wavefront gradient errors are virtually identical.

The results of Figure 8 confirm that a DM that pre-corrects errors in front of the pulse compressor will lead to negligible pulse broadening in the OMEGA EP laser system.

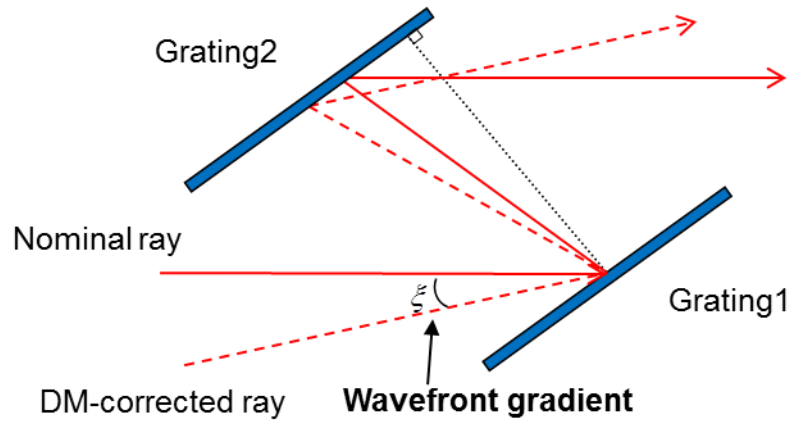


Figure 7 – **Two-Grating Model** – The paths of a nominal ray and a DM-corrected ray with the same frequency are shown.

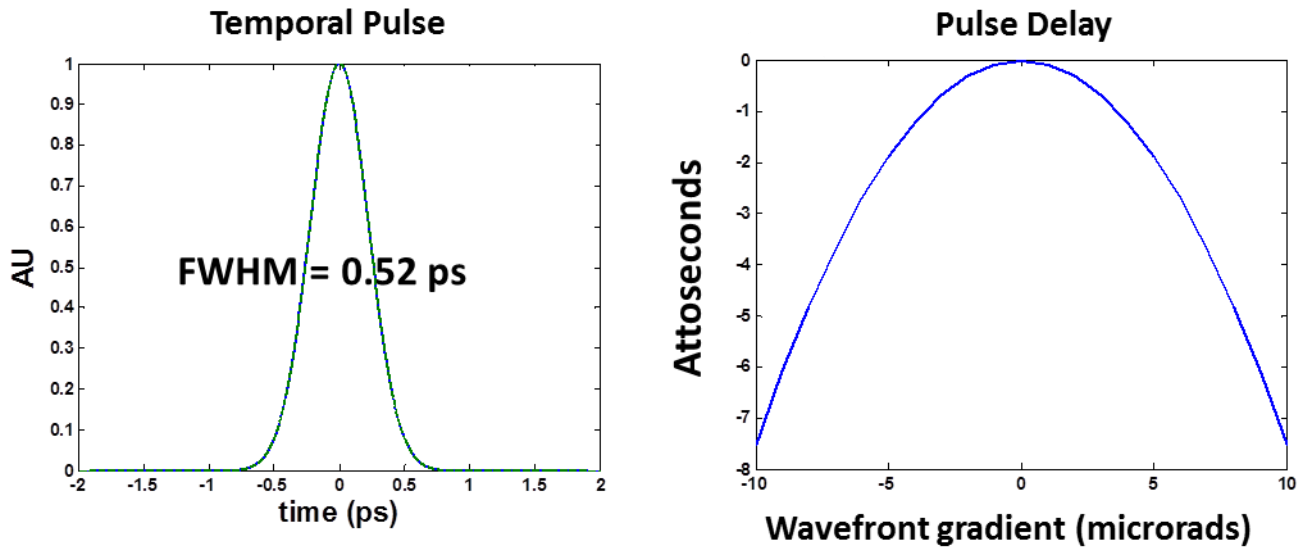


Figure 8 – **Temporal Pulse and the Pulse Delay**–The graph on the left is a spatially integrated pulse, showing virtually identical results with and without a 10 microradian change in wavefront direction due to DM corrections (solid and dotted lines are with and without DM correction, respectively). The plot on the right shows the relationship between the deviation in incoming wavefront direction (in microradians) and the pulse delay in as. This displays that a 10 microradian error would give less than 8 as delay.

5. Conclusion/Further Work

The spatio-temporal numerical model showed that a DM can correct for expected errors in the wavefront just as well when placed before the compressor as after the compressor. Both deformable mirrors corrected the wavefront errors sufficiently to recover the perfect-system focal spot R80 of 2.4 microns, while keeping the compressed pulse FWHM at its transform-limited value of 0.52 ps. A two-grating analytical model was used to confirm that the spectral phase distortion was indeed negligible.

To improve the simulation, the model will be expanded to include errors from the main beamline and the diffraction gratings. The effect of DM pre-correction on pulse contrast will also be explored. Finally, engineering considerations for moving the DM, such as opto-mechanical constraints of the system, implications for compressor alignment, and cost will also be investigated.

6. Acknowledgements

I would like to thank Dr. R. Stephen Craxton and the Laboratory for Laser Energetics for providing me with the opportunity to spend a summer doing research. I would like to thank my advisor M. Guardalben for advice, knowledge, and guidance throughout the process. I would also like to thank B. Kruschwitz for creating the DM model used to create the bicubic meshes.

7. References

1. D. Strickland and G. Mourou, "Compression of amplified chirped optical pulses," *Opt. Commun.* **56**(3), 219–221 (1985).

2. J. Qiao, A. Kalb, M. J. Guardalben, G. King, D. Canning, and J. H. Kelly, "Large-aperture grating tiling by interferometry for petawatt chirped-pulse–amplification systems," *Opt. Express* **15**, 9562-9574 (2007)
<http://www.opticsinfobase.org/oe/abstract.cfm?URI=oe-15-15-9562>
3. Photon Engineering, LLC, Tucson, AZ 85751.
4. J. Arnaud, "Representation of Gaussian beams by complex rays," *Applied Optics*, **24**(4), 538-543 (1985).
5. MathWorks, Natick, MA 01760.
6. MATLAB DM influence function model provided courtesy of Brian Kruschwitz.
7. Z. Wang, Zh. Xu, and Zh. Zhang, "A new theory for the treatment of a pulsed beam propagating through a grating pair," *IEEE J. Quantum. Electron.* **QE-37**(1), 1-11(2001).

Beam-Pointing Optimization for Proton Backlighting on the NIF

Yifan Kong

Webster Schroeder High School

Advisor: **Dr. R. S. Craxton**

Laboratory for Laser Energetics

University of Rochester

Rochester, New York

November 2013

1. Abstract

Optimized designs have been developed for proton backlighting on the National Ignition Facility (NIF) using the hydrodynamics simulation code *SAGE*. In proton backlighting, the deflections of a short pulse of protons are used to measure the electric and magnetic fields in a primary laser-irradiated target. It is proposed to use twenty-four of the NIF's 192 beams (providing 20 kJ of energy) to implode a thin D^3He -filled glass shell 210 μm in radius, generating protons from the reaction $D + {}^3He \rightarrow \alpha + p$. The remaining beams irradiate the primary target. The optimized design for the selection and aiming of the backlighter drive beams yields an energy deposition uniformity of 9.6% rms, a large improvement upon the 76% of an initial design. A simulation using the hydrodynamics code *DRACO* of a design similar to – but not as uniform as – the optimized design predicted a yield of 2.3×10^{10} protons, well above the required minimum of 10^9 . The design calls for the NIF's standard phase plates (which increase the beam spot size) to be removed. An additional design using the phase plates provides more uniformity (7.1% rms); while this design produces a slower implosion, it may still provide an adequate proton source.

2. Introduction

Nuclear fusion has the capacity to supply the future with clean, renewable energy. A virtually inexhaustible source of power, fusion does not harm the environment or contribute toward global warming and relies on fuel found readily in water rather than on oil or gas. One method to achieve nuclear fusion is to use high-powered lasers to irradiate a small (1 to 3 mm in diameter) target consisting of a glass or plastic shell typically surrounding a layer of cryogenic deuterium (D) and tritium (T).¹ When irradiated, the shell's exterior ablates outward, which causes an opposing force to implode the inner portion of the target. The implosion compresses the cryogenic DT layer to an extremely high density and ensures a large number of fusion reactions before the target explodes. The implosion simultaneously heats the fuel to temperatures around 100 million degrees Celsius, which provides the relative kinetic energy needed for the positively charged D and T nuclei to overcome the Coulomb barrier and fuse together. This fusion reaction results in a helium nucleus and an energetic neutron with the neutron accounting for most of the energy released. The energy of the helium nucleus is deposited in the fuel in a process known as ignition. Ignition makes breakeven possible, which is the point at which energy output equals energy input. Still larger targets will produce one hundred times the amount of energy put in, which would offer laser fusion as a plausible energy source.²

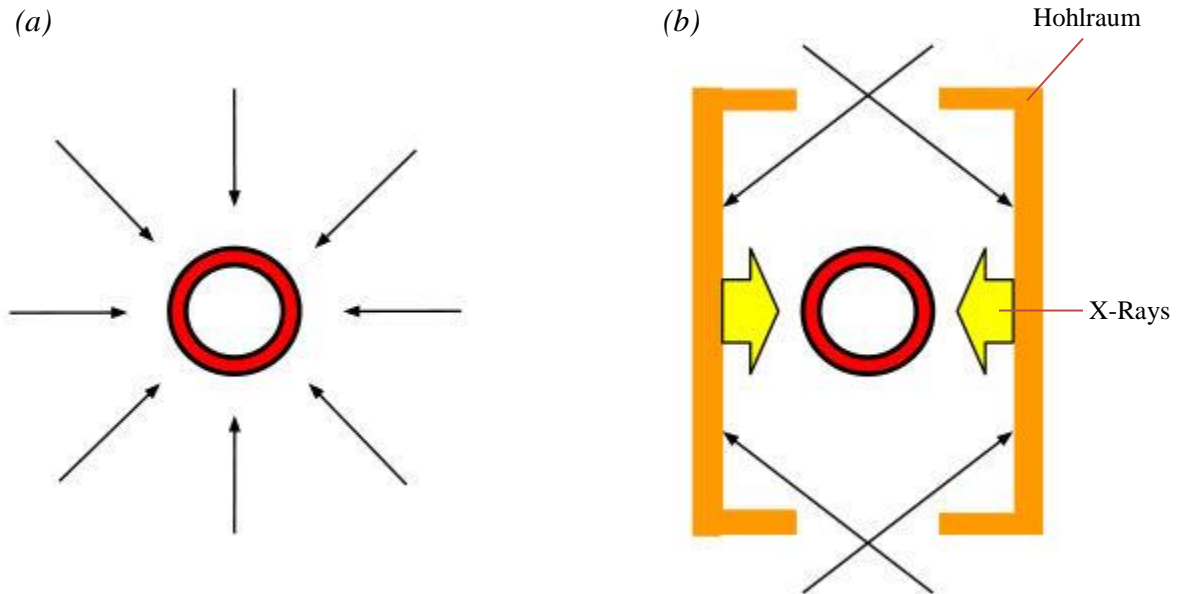


Figure 1: The two main approaches to inertial confinement fusion (ICF). (a) Direct drive calls for laser beams that are aimed directly at the target. (b) Indirect drive calls for beams that strike the inner walls of a cylindrical hohlraum, thereby generating X-rays that then irradiate the target. (Based on Figure 1 of Ref. 3)

Laser fusion can be executed through two chief approaches: direct drive and indirect drive. Direct drive involves positioning each beam around the target to strike the shell directly, usually at normal incidence [Figure 1(a)]; indirect drive involves directing beams through the openings of a metallic hohlraum [Figure 1(b)] to strike the cylinder's inner walls. Once struck, the walls (typically made of gold) emit X-rays that bathe over the target. Proponents of this method argue that indirect drive offers greater uniformity than direct drive. However, there is a significant loss of deposited energy; only 20% of the X-rays are absorbed by the target because the majority of the energy is lost either in the hohlraum walls or through the openings at the ends of the hohlraum.

The National Ignition Facility (NIF) at the Lawrence Livermore National Laboratory is configured for indirect drive and is currently the most powerful laser in the world; with 192 beams bundled in forty-eight quads of four, the NIF can deliver a total energy of 1.8 MJ to a

target. The laser beam ports are arranged into eight equally spaced rings of quads around the target (four quads each in the two rows closest to the north and south poles and eight each in the two rows above and below the equator, shown as black squares in Figure 4 below) and are divided between the northern and southern hemispheres at polar angles (Θ) of 23.5° , 30.0° , 44.5° , and 50.0° to the vertical. To allow for direct drive experiments to be conducted on the NIF, polar drive is used. Polar drive [Figure 2] is a method in which the beams are repositioned away from the poles and toward the equatorial region to compensate for the lack of ports near the equator.^{4, 5}

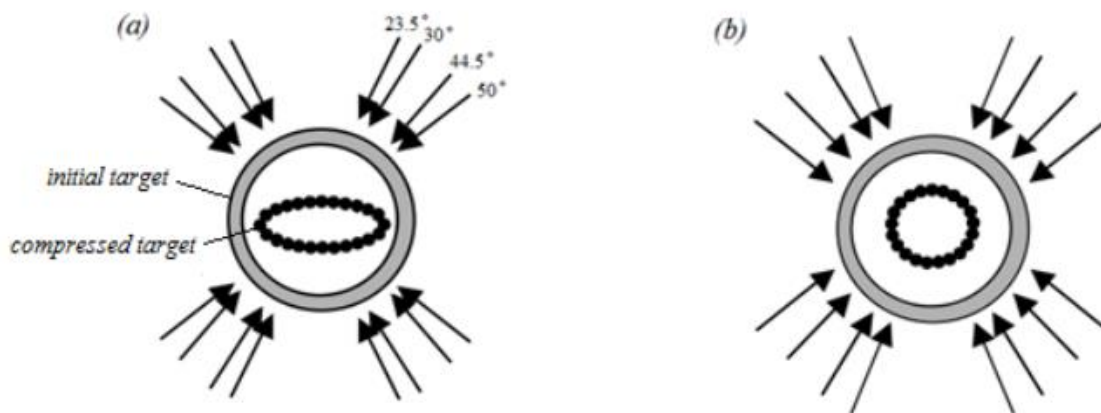


Figure 2: Direct drive without repointings versus polar drive on the NIF (Figure 3 of Ref 3). (a) Pointing the laser beams directly at the center of the target results in very poor uniformity of the compressed target. (b) Using polar drive, shifting the beams towards the equator allows for maximum implosion uniformity.

Another use for direct drive implosions is proton backlighting.⁶ Proton backlighting uses protons generated by a backlighter target to probe a primary target. Figure 3 shows the setup, which involves a backlighter and a primary target. Because there are two targets, two different sets of beams must individually irradiate each target. Protons are released through the implosion of the backlighter from the reaction $D + {}^3\text{He} \rightarrow \alpha + p$. They have an energy of 14.7 MeV and pass through a mesh that organizes the protons into separate beamlets. An image is projected

onto a surface (in Figure 3's case, a piece of CR-39 plastic, shown in green) after the backlighter protons are deflected as they pass through the plasma produced by the main target implosion. An image can also be produced through proton absorption rather than proton deflection in which areas of higher density in the main target absorb more protons so that the excess protons strike the screen and outline the shape of the implosion.

Dr. Chikang Li of the Massachusetts Institute of Technology's Plasma Science and Fusion Center has proposed a larger-scale monoenergetic proton backlighting experiment for the NIF using proton deflection to measure the electric and magnetic fields in laser-produced plasmas. In the proposed experiment, the backlighter is a target measuring 210 μm in radius filled with $D^3\text{He}$ fuel encapsulated by a thin (2 μm thick) glass shell. This experiment calls for a direct drive implosion of the proton backlighter using polar drive. However, because the experiment only allows six of the possible forty-eight quads to be reserved as backlighter drive beams, polar drive is made considerably more difficult. The best combination of six among the possible forty-eight quads must therefore be determined.

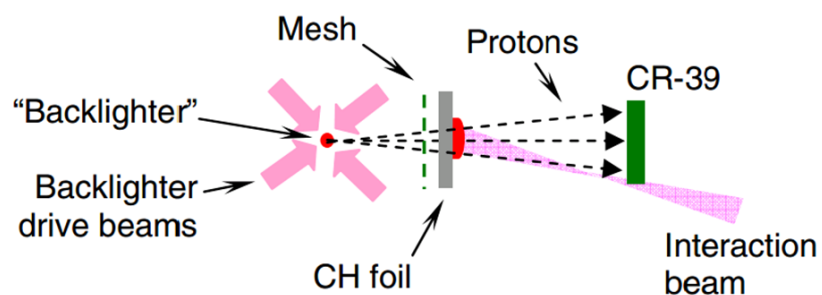


Figure 3: Setup for a proton backlighting experiment conducted by Dr. Chikang Li on the OMEGA Laser at the University of Rochester's Laboratory for Laser Energetics (Ref 6). The setup involves a backlighter and a primary target (in this case, a CH foil), which prompts the use of two different sets of beams to individually irradiate each target. An image is projected onto a piece of CR-39 plastic (shown in green) after the backlighter protons are deflected as they pass through the plasma produced at the interaction beam-CH foil interface.

The proposed experiment begins with the interaction beams irradiating the main target. The backlighter drive beams (consisting of 24 of the possible 192 NIF beams delivering 20 kJ in combined laser energy at a steady rate over 400 ps) then use polar drive to implode the proton backlighter, causing a short burst of protons. To produce a clear image, at least 10^9 protons must be produced by the implosion. These protons pass through a mesh and are (depending on the imaging technique) either deflected by electric and magnetic fields or absorbed by the main target before striking a screen to produce an image.⁷

The present work involves the selection of six quads and the optimization of the pointings of the 24 selected beams to implode the proton backlighter as uniformly as possible. There were three main stages of design, the first being the examination of an initial design⁸ which proved to yield poor uniformity. The second stage involved designs based on geometric solids. These produced an improved uniformity, but were not optimum. The third stage was the final development of an optimized design. Once the optimization process was complete, another optimized design was developed that kept the NIF's phase plates in place (rather than remove them for the experiment). However, because of the resultant decrease in energy deposited on the target surface, the phase plate design may not produce enough protons to clearly image an imploding target. One application of proton backlighting to diagnose polar drive implosions was also considered.

3. Initial Design

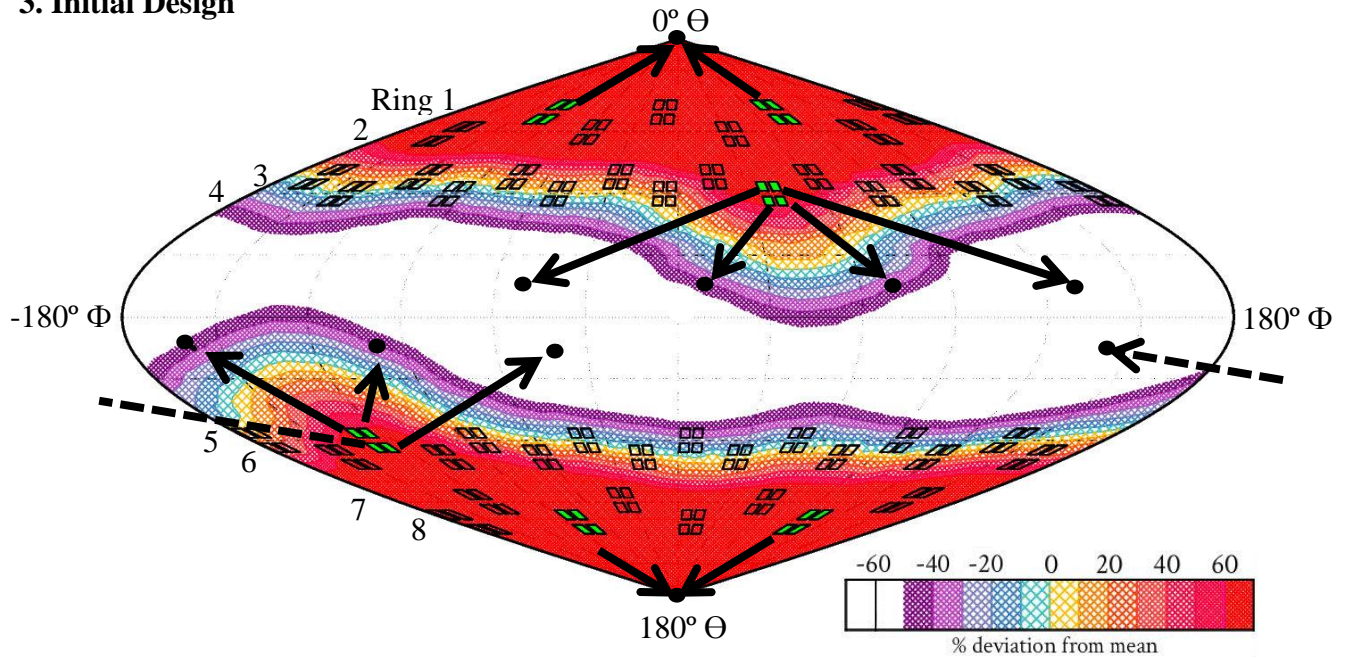


Figure 4: Energy deposition contours on a sinusoidal projection for the initial design 200 ps after the backlighter drive beams were turned on. The groups of four black squares (beams) indicate where the quads are positioned in the target chamber in relation to the target; quads highlighted in green are the ones selected for the design. The beam repointings are indicated by the arrows pointing to black dots, eight of which fall in the equatorial region, eight on the south pole, and eight on the north pole (the pointings clustered at the poles overlap, so only a single dot is shown). The rings (rows of quads) are numbered down the left-hand side

As shown in Figure 4, the initial design's quads were arranged so that four of the six quads chosen lay in the rings closest to the poles (ring 1 in the north and ring 8 in the south) with all four beams in each of these quads pointed at the closest pole. This left only two quads in rings 4 and 5 to spread their beams along the equator.

The colors of the contours used in Figure 4 indicate the percent deviation from the average amount of energy deposited on the surface calculated using the two-dimensional hydrodynamics code *SAGE*. Colorless areas denote portions of the target that received minimal amounts of energy (less than 50% of the average) while red areas connote portions that received maximum amounts of energy (over 60% of the average). The initial design yielded an rms (root mean square) energy deposition value of 75.5%. Rms is a measure of deviation; thus, to ensure a

uniform implosion, the value of the rms needs to be as low as possible. The lack of uniformity is due mostly to the poor choice of quads and beam pointings, which caused a large disconnect between the maximum and minimum amounts of energy deposited.

Because the NIF is designed for indirect drive experiments, the energy deposited by the beams is concentrated at the poles by default. Thus, the primary goal should be to redirect the energy to the equator. However, the initial design called for the majority of the quads and beams to be located on and around the poles, which explains why the poles receive most of the deposited energy (the maximum amount of energy deposited being 170% of the mean) and the equator was left strongly underdriven (the minimum being 94% under the mean).

The poles are propelled toward the center of the target with a greater velocity than the equator due to the disproportionate amount of energy concentrated at the top and bottom. This will cause the poles to collide first at ~ 200 ps [Figure 5(a)] before the equator collides at ~ 400 ps [Figure 5(b)]. Such an implosion is not desired because uniformity is needed to maximize the proton yield and to ensure that the protons are produced in the shortest time interval possible.

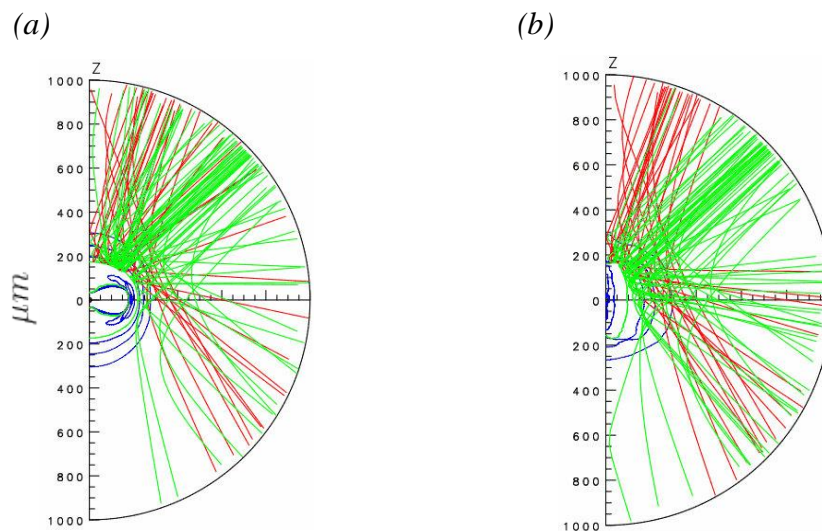


Figure 5: Ray-trace diagrams of the initial design with two incoming beams shown in red and green. The blue lines indicate the density contours of the target. (a) At ~ 200 ps, the poles collide while the equator has moved little from its initial radius of $210 \mu\text{m}$. (b) At ~ 400 ps, the equator collides as the poles are already exploding back outwards.

To improve the initial design, *SAGE* was used to optimize three main experimental parameters: quad selection, beam pointing, and defocus. Individual beams were able to be repointed to new polar (Θ) and azimuthal (Φ) angles and were set to beam-specific defocus distances [Figure 6]. By adjusting the

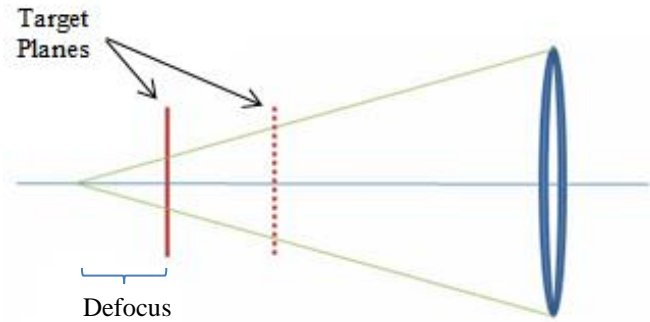


Figure 6: Defocus is the distance between the target plane and the point of best focus (where the rays converge). Increasing the defocus increases the size of the beam spot on the target plane; for example, the dotted target plane is covered by more of the rays than the solid target plane because its defocus is larger.

pointings of each of the twenty-four beams prescribed for the experiment, more or less energy can be distributed to certain points on the target surface, enabling the shape of the imploding target to be manipulated. In order to compare different designs, different facets of each run needed to be taken into account (i.e., the rms energy deposition just before implosion and the total energy absorbed). Energy absorption is an important consideration in that enough of the 20 kJ of incident energy provided by the twenty-four backlighter drive beams needs to be deposited and absorbed by the target in order to yield a fast implosion, a high temperature during implosion, and a high proton yield.

4. Designs Based on Geometric Solids

Having noted the problems with the initial design, new designs were produced. The first designs in the optimization process were based on geometric solids with equally spaced vertices. The first configuration was derived from an inscribed octahedron in that each of the six quads chosen for the design was pointed at one of six equidistant vertices. This design [Figure 7] produced an rms of 24.7%. It imploded at 250 ps, which occurred later than the initial design's

implosion because the improved uniformity ensured that the poles would not collide with a much greater velocity than the equator. Although each quad consists of four beams with independent repointing capabilities, the first design kept each quad bundled to a single aim point in order to produce a result that would indicate where energy needed to be mitigated.

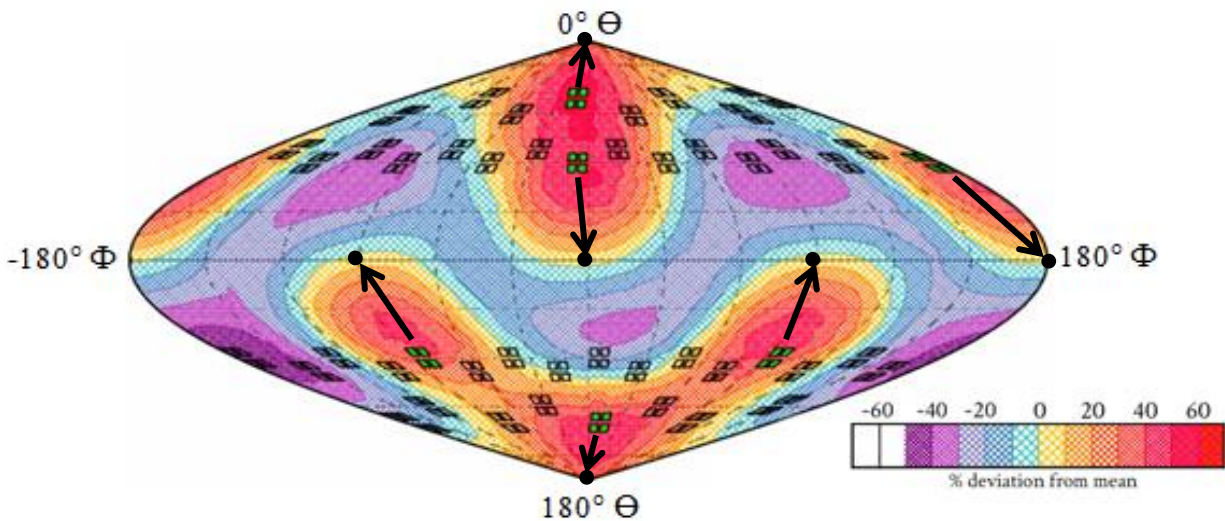


Figure 7: Energy deposition profile for an octahedral design 250 ps after the drive beams were turned on. Each quad in green is pointed at one vertex of an octahedron.

As can be seen in Figure 7, the areas of high deposition coincide with the quad selection. Essentially, the energy a quad deposits is concentrated around its place of origin in an “area of influence,” and repointing beams only serves to shift the entire area toward a certain direction while the area is still anchored to the placement of its original quad. For example, quad [R5, 7], the quad in Ring 5 (see Figure 4) and 7 quads to the right of $\Phi = 0^\circ$ (3 quads to the right of $\Phi = -180^\circ$), is pointed at $(0, 270^\circ)$, but the majority of its deposited energy lies not even halfway between the location of the quad and its aim point. The problem with quads’ areas of influence is a major issue in that as much energy as possible needs to be funneled toward the equator, but large repointings lower the amount of energy deposited and do not redirect energy far enough from the quad of origin. Another problem is the inherent asymmetry of the design. Because the

design calls for six quads, three quads must be arranged in a symmetrical fashion in each of the northern and southern hemispheres. Furthermore, the chosen quads should lie as close to the equator as possible in order to concentrate as much energy as possible in that region.

The second design was based on an inscribed rhombicuboctahedron (RCO), which has twenty-four equidistant vertices, but with all aim points shifted toward the equator in order to divert more energy along the central band.

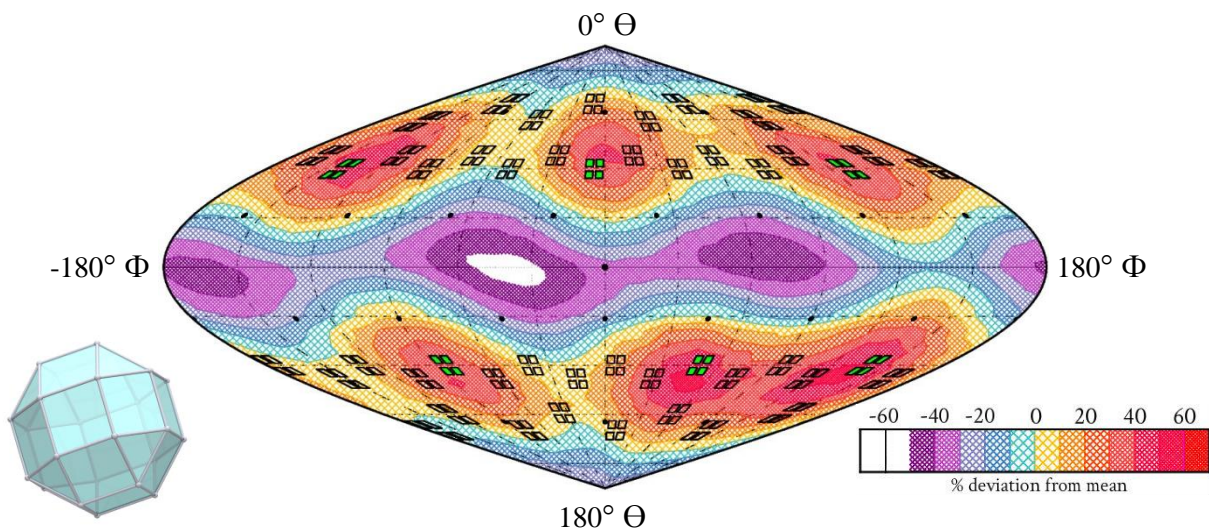


Figure 8: Energy deposition profile for a rhombicuboctahedral design 250 ps after the drive beams were turned on. The blue image is of a rhombicuboctahedron (Ref 9).

Each of the twenty-four beams allotted for this experiment was pointed near a vertex of an RCO and all quads used were chosen from rings 4 and 5. However, because these rings each contain eight equally spaced quads, it is impossible to choose three of the possible eight and maintain perfect symmetry. As a result, no matter the quad set-up chosen, there will always be abnormalities in a few sections (e.g., the white spot along the equator in Figure 8). The increased beam dispersion aided the spreading of energy and improved the uniformity of the implosion to an rms of 25.4%.

5. Optimized Design

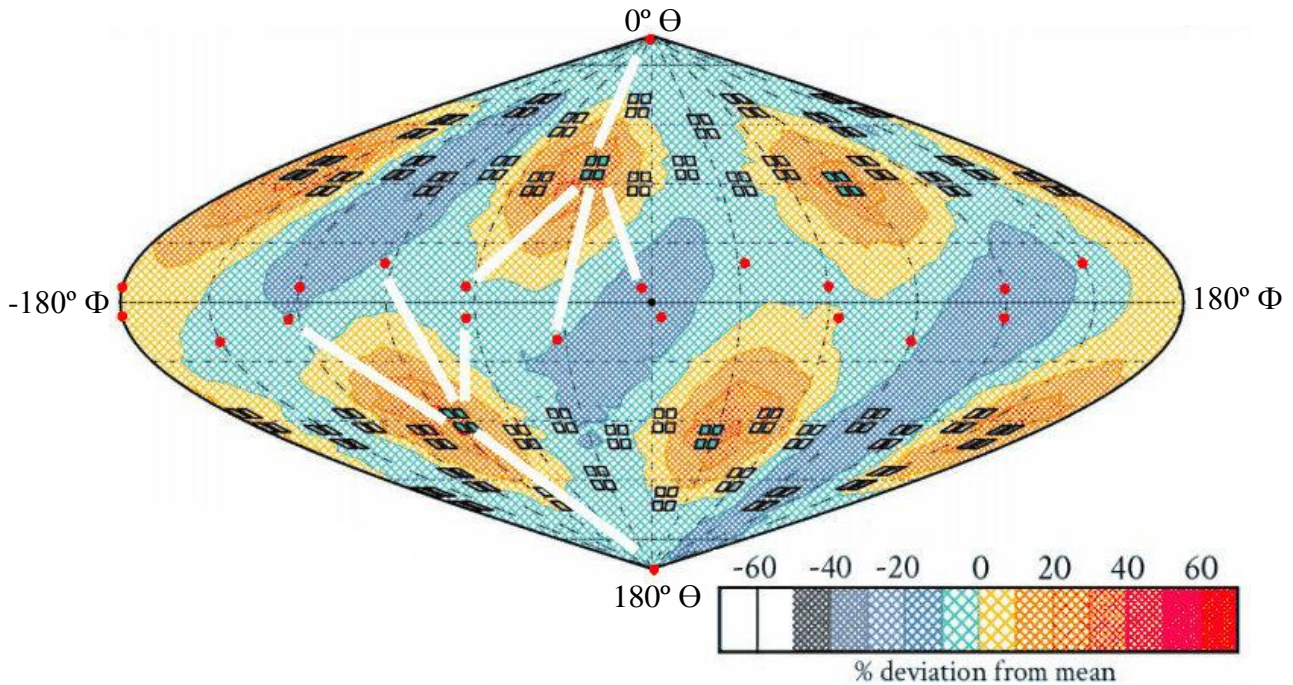


Figure 9: Optimized design. For each quad, three beams were pointed toward the equator and one toward the pole. Red spots indicate aim points; the poles each have three beams redirected there and are indicated by a single red dot. The white lines indicate beam repointings. Because the repointing pattern repeats at regular intervals, only two quads are shown with repointings.

The optimized design is illustrated in Figure 9. All quads were selected from the rings closest to the equator and for each quad, three beams were pointed toward the equator and one toward the closest pole. The design yielded a 9.6% rms, decreasing the original 75.5% by a factor of about seven. Based on a similar design with an 11.1% rms that was modeled using the two-dimensional hydrodynamics code *DRACO*,⁸ it can be assumed that the optimized design will produce at least 2.3×10^{10} protons, comfortably exceeding the 10^9 goal.

In reducing the rms to obtain the most uniform implosion possible, a few glaring problems needed to be addressed. First, the defocus (the distance between the target plane and the point of best focus, see Figure 6) and amount of deposited energy are inversely related. For

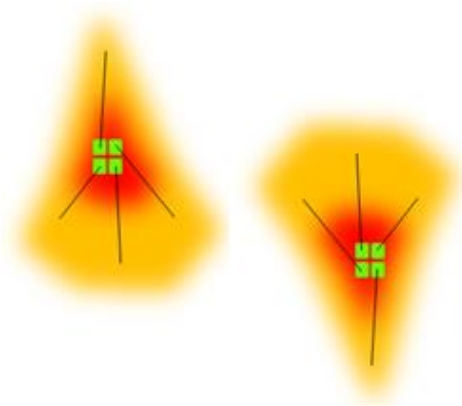


Figure 10: Three-to-1 separation of beams in a quad (a grouping of four green rectangles). The black lines show where each beam (one green rectangle) has been repointed to and areas in red show more energy deposition than orange areas. This method proved most effective in directing as much energy as possible toward the equator without completely neglecting the pole. It also diffused the concentrated deposition of energy centered around each quad in use, which increased uniformity.

this reason, there is a point where increasing the defocus lowers the energy deposited by an excessive amount (the amount of energy deposited should remain high in order to ensure a larger proton yield). Second, beam repointing can only fine-tune the areas of deposited energy decided by quad selection. To maximize the benefits of beam pointing, a 3:1 ratio was used in separating a quad's four beams into two subsets directed at different regions of the target [Figure 10]. Using this method, one beam was sent to its hemispherical pole while the remaining three were sent toward the equator with the middle beam repointed a bit further than the others. This method allowed the majority of a quad's energy to be shifted toward the equator without neglecting the pole entirely.

To reduce the effects of asymmetry, the three quads used in each hemisphere were staggered between the two rows closest to the equator. This allowed the three chosen quads to be spaced at more even intervals. With this method, however, it was extremely important to mirror the northern and southern hemispherical quad placements. For example, since quad [R3, 8] was selected, quad [R6, 1] was also chosen because they are equidistant from the equator and are reflections across the $\Phi = 0^\circ$ axis. This also created a staggering effect in that between any two used quads in one hemisphere, there would be a used quad in the other hemisphere. In so doing, areas of high energy deposition were staggered north-south-north-south of the equator, which

aided the symmetry of the design as well as the uniformity. Furthermore, quads were chosen only from the four rows closest to the equator, which focused more energy around the equator.

In Table 1, the main parameters for optimization were the quad choice, the Θ and Φ of each beam's aim point on the initial target, and the defocus of each beam.

Quad	NIF Beam No.	Θ (deg)	Φ (deg)	Defocus (cm)	Quad	NIF Beam No.	Θ (deg)	Φ (deg)	Defocus (cm)
R3, 5	41	85.0	180.0	0.70	R5, 7	109	77.0	267.0	0.82
	42	0.0	0.0	0.70		110	95.0	297.0	0.82
	57	103.0	210.0	0.82		125	95.0	237.0	0.70
	58	85.0	240.0	0.82		126	180.0	0.0	0.70
R3, 8	47	85.0	297.0	0.70	R6, 1	129	95.0	3.0	0.82
	48	0.0	0.0	0.70		130	77.0	33.0	0.82
	63	103.0	327.0	0.82		145	180.0	0.0	0.70
	64	85.0	357.0	0.82		146	95.0	63.0	0.70
R4, 2	67	0.0	0.0	0.82	R6, 4	135	95.0	120.0	0.82
	68	85.0	120.0	0.82		136	77.0	150.0	0.82
	83	85.0	60.0	0.82		151	180.0	0.0	0.82
	84	103.0	90.0	0.82		152	95.0	180.0	0.82

Table 1: Beam parameter specifications for the six quads used in the optimized design. [R3,5] denotes Ring 3 (Ring 1 being the topmost ring), 5 quads to the right of $\Phi = 0^\circ$. Beams are numbered by rings of constant latitude counting from the top and increasing with Φ within each ring.

6. Optimized Design Using Phase Plates

Phase plates are large optics installed on the NIF that spread the energy deposited by beams over a larger area [Figure 11(a)]. They consist of a glass substrate with small random nonuniformities polished onto one surface to deflect incoming laser rays. The NIF uses these optics to avoid excessive intensity when the beams are focused at a laser entrance hole in the hohlraum [Figure 1(b)].

Because they are inconvenient to remove, a natural question to ask is whether or not a design can be developed without having to remove the NIF's phase plates. The major hurdle is

the fact that phase plates cause the beam spot size to become much larger than the target [Figure 11(b)].

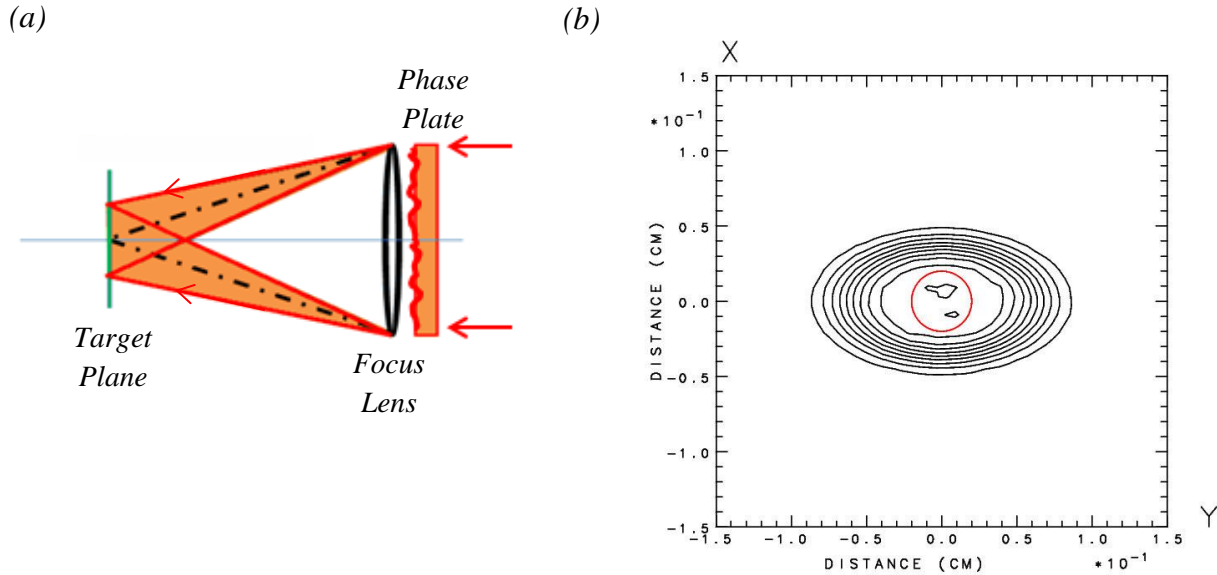


Figure 11: The effect of a phase plate on beam spot size. (a) Beam rays passing through a phase plate. With the phase plates, the original laser rays (the dotted black lines) are dispersed (the orange area around the dotted black lines) and cover more area on the target plane. (b) Intensity contours in the target plane for a typical phase plate. The red circle denotes the size of the target ($210 \mu\text{m}$ in radius) in relation to the beam spot. Thus, the majority of the beam energy completely misses the target.

The phase plates used on the NIF cause the beam spots to become elliptical in shape; for example, the (a,b) for the ellipse in rows 3 and 6 are $(635, 367) \mu\text{m}$ and rows 4 and 5 have an (a,b) of $(593, 343) \mu\text{m}$. The more uniform dispersal resulting from the large phase plate spots lowers the rms to 7.1%, but it also means that a large portion of energy misses the target completely [Figure 11(b)]. Because less energy is being provided to the target, the target implodes at a slower speed. This can be seen in Figure 12, a plot of electron number density n_e vs. radius at a time of 350 ps, when n_e reaches its peak value at a radius near zero. This implosion takes ~ 100 ps longer to occur than the optimized design of Section 5. This slowed implosion results from lower temperatures in the target and is expected to produce less protons in

a longer period of time. However, the yield of protons may still be sufficient to produce a clear image.

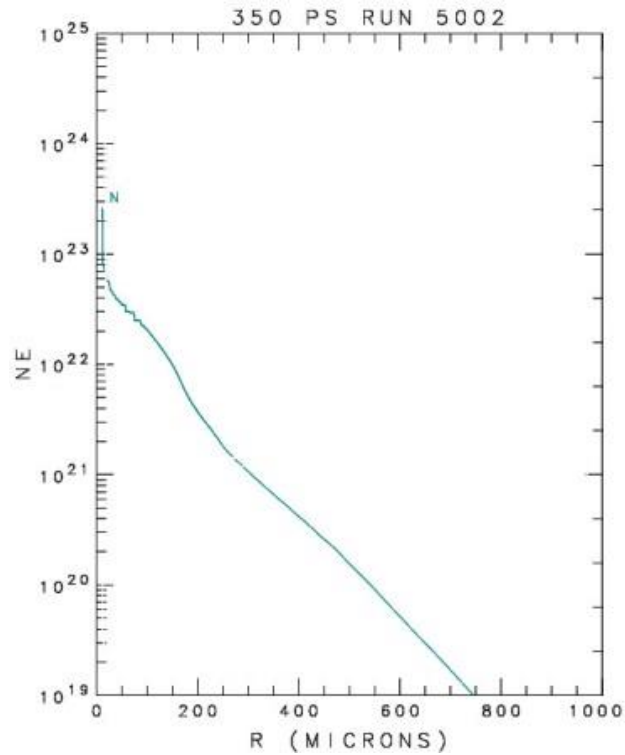


Figure 12: Plot of target electron number density (n_e in units of cm^{-3}) over a period of 350 ps with a phase plate. The implosion occurs at this time as n_e reaches its peak as the radius nears zero.

7. Future Applications

Proton backlighting on the NIF has a number of potential applications. The main target can be a flat target as in Figure 3, a hohlraum, or a polar drive target. Tucker¹⁰ and Olson³ have developed an optimized polar-drive design using 24 quads. As shown in Figure 13, this design could be used to irradiate the direct-drive capsule with drive beams while the design presented in this paper could be used to generate the protons from the backlighter. Furthermore, if more quads were allotted as backlighter drive beams and phase plates were used, uniformity and the amount of energy absorbed by the backlighter would increase.

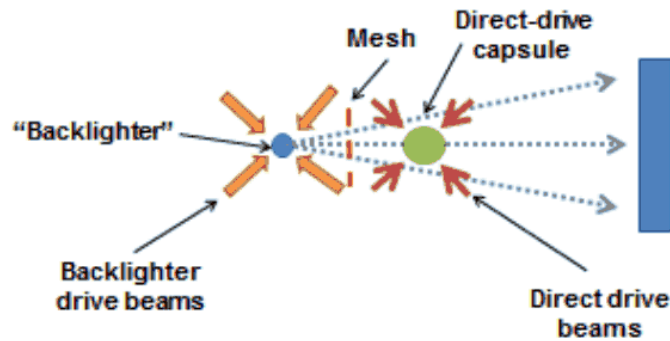


Figure 13: A possible proton backlighting set up to image a direct-drive capsule. As the capsule implodes, areas of higher density will absorb more protons and thus produce an image that can determine how uniform the implosion was based on its shape.

8. Conclusion

Designs have been developed for proton backlighting on the National Ignition Facility (NIF) using the hydrodynamics simulation code *SAGE*. The optimized design for irradiating a proton backlighter using 24 beams yields an energy deposition uniformity of 9.6% rms and over 2.3×10^{10} protons, well above the required minimum of 10^9 . Because the design calls for the NIF's standard phase plates to be removed, an additional design using the phase plates was developed to avoid the task of removing the large optics. The phase plate design yields an energy deposition uniformity of 7.1% rms, but less absorption and a slower implosion lead to a lower proton yield. More simulations need to be run in order to determine whether the optimized phase plate design provides a sufficient amount of protons.

9. Acknowledgments

This project could not have been completed without Dr. Craxton, whose consistent advice, feedback, and ready support served as an unwavering guide throughout the entire process. I would also like to thank Tricia Olson for answering my questions and getting me

acquainted with *SAGE*, Dr. Enck for being the first to kindle my interest in physics and in encouraging me to apply for this internship, Dr. Chikang Li for helpful discussions, and Dr. Pat McKenty for the *DRACO* simulation. Lastly, I would like to thank the Laboratory for Laser Energetics for running the summer high school program; it has been an invaluable learning and growing experience.

References

- ¹ J. Nuckolls et al., “*Laser Compression of Matter to Super-High Densities: Thermonuclear (CTR) Applications*,” *Nature* **239**, 139 (1972).
- ² Stefano Atzeni and Jürgen Meyer-ter-vehn, “*The Physics of Inertial Fusion: Beam Plasma Interaction, Hydrodynamics, Hot Dense Matter*.” Oxford: Oxford UP, 2004.
- ³ Patricia Olson, “*Optimization of Beam Configurations for Shock Ignition Experiments on the NIF and OMEGA*,” Laboratory for Laser Energetics High School Summer Research Program (2011).
- ⁴ S. Skupsky et al., “*Polar Direct Drive on the National Ignition Facility*,” *Phys. Plasmas* **11**, 2763 (2004).
- ⁵ A. M. Cok et al., “*Polar-Drive Designs for Optimizing Proton Neutron Yields on the National Ignition Facility*,” *Phys. Plasmas* **15**, 082705 (2008).
- ⁶ C. K. Li et al., “*Measuring E and B Fields in Laser-Produced Plasmas with Monoenergetic Proton Radiography*,” *PRL* **97**, 135003 (2006).

⁷ C. K. Li, et al., “*Mononoenergetic-Proton Radiography Measurements of Implosion Dynamics in Direct-Drive Inertial-Confinement Fusion*,” PRL **100**, 225001 (2008).

⁸ Dr. P. McKenty, unpublished

⁹ Rhombicuboctahedron [Digital Image]. (2007). Retrieved November 5, 2013, from:
http://simplydifferently.org/Geodesic_Polyhedra?page=7

¹⁰ L. Tucker, “A Design for a Shock Ignition Experiment on the NIF Including 3-D Effects,”
Laboratory for Laser Energetics High School Summer Research Program (2010).

A Radiation and Cryogenic Tolerant Encoder

Nathaniel Rogalskyj

McQuaid Jesuit

LLE Advisors: Gregory Brent, Dave Lonobile

Laboratory for Laser Energetics

University of Rochester

Summer High School Research Program

2013

Abstract:

A cryogenic and radiation tolerant encoder was designed and constructed to measure linear displacements with a resolution of 0.1 μm . A coil of wire was fashioned such that the insertion or retraction of an iron rod would result in a change in inductance. An analog circuit, incorporating this variable inductance, generates a ringing signal whose period is analyzed with reference to a 200-MHz counter. Resolution proved to be a function of displacement, smaller displacements yielding higher resolution. Exposure to cryogenic temperatures, although requiring calibration, proved to increase the resolution. Miniaturization of the inductor to a scale useful in laser-fusion target positioning systems is only possible at cryogenic temperatures. A Mathcad document was created to accurately calculate the optimal resolution, capacitance, and the number of turns of the inductor given certain physical input parameters such as temperature, cross-sectional area, length, and gauge.

Introduction:

Nuclear fusion is a possible source for large-scale, clean, virtually limitless energy production. One possible approach for fusion is the irradiation of an implosion target with high power lasers to create the necessary high temperatures and densities. On OMEGA, the implosion target must be held at low, cryogenic temperatures near 20 K. At these temperatures, there is a need for highly sensitive and accurate linear displacement measurements in positioning the capsule into the center of the target chamber. The current solution is centered on the use of a potentiometer, which correlates a measured voltage ratio to a given displacement. The resolution of the potentiometer solution is 0.39 μm . The primary goal of this project was to develop a new encoder that improves upon the current solution. Furthermore there are a number of other applications for an encoder at LLE, with varying physical constraints. A secondary goal of this project was to explore the encoder's design tradeoffs in the context of these other physical

constraints. Table 1 lists some of the desired characteristics of the new encoder. Most of them were explored in this work.

Table 1. Desired Characteristics of New Encoder	
<u>Engineering Desirable:</u>	<u>Goal:</u>
High sensitivity	The applications for the encoder require highly accurate measurements. In the case of the target positioning system, the goal was to attain a resolution on a level with or better than 0.39 μm .
Cryogenic Tolerance	The applications for the encoder require the above high resolution under extremely cold temperatures, near 20 K.
Physical Adaptability	The applications of the encoder require variable throws, and physical constraints
Radiation Tolerance	Due to use of tritium in the implosion target, and in the lab, the materials of the encoder need to be resistant to tritium corrosion.
Temperature Independence	It is highly desirable for the encoder to not need recalibration

Outline of Design

The goal of the encoder is to detect linear displacements. The system (Figure 1) is composed of a number of different subunits: an RLC circuit incorporating the variable inductance of a set of coils with a magnetic core, an operational amplifier, a voltage offset system and a Field Programmable Gate Array (FPGA).

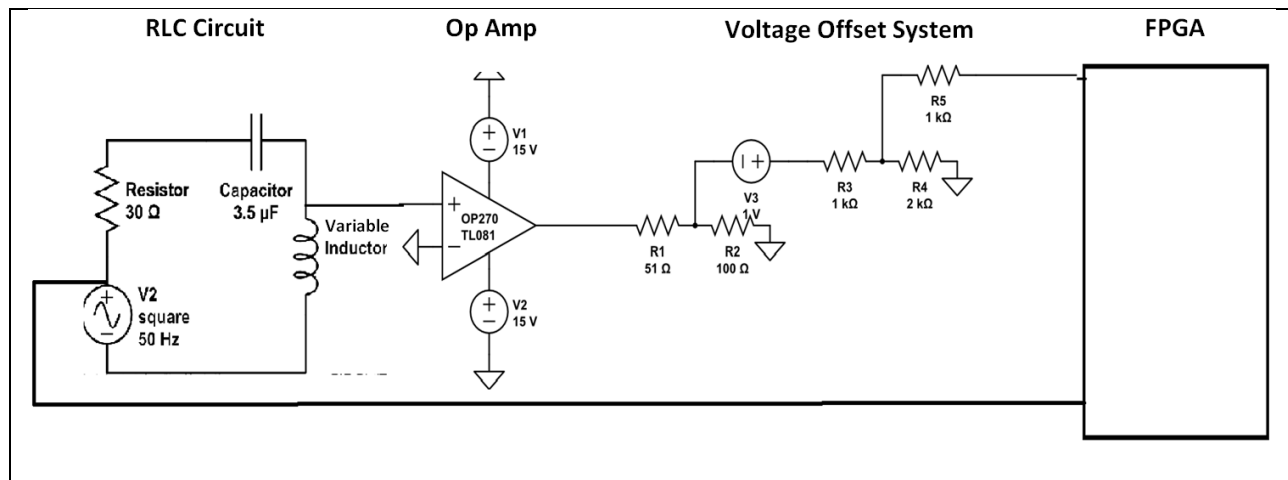


Figure 1. Diagram of the encoder circuitry. The system is composed of an RLC circuit incorporating a variable inductor, an operational amplifier, a voltage offset system, and a FPGA.

The RLC circuit generates a ringing signal. The ringing signal is amplified and squared by the operational amplifier. In the voltage offset system, a DC battery and two voltage dividers scale the signal to the specifications of the FPGA. The FPGA counts the duration that the signal is high with reference to a 200-MHz counter.

Variable Inductor:

A method was required to translate a linear displacement into an electrical property. A linear variable inductor was constructed such that the insertion of a magnetic permeable rod would cause an increase in the inductance. The formula for the inductance, L , of the coil is [1]:

$$L(x) = \frac{\mu * f(x)N^2\pi r^2}{l} \quad (\text{Eq. 1})$$

where N is the number of turns, r is the radius of the coil, l is the length of the coil, x is the distance the core has been inserted, and $f(x)$ is a dimensionless function that gives the variation of the inductance with x ; $f(x)=1$ at full insertion. The absolute magnetic permeability is [1]

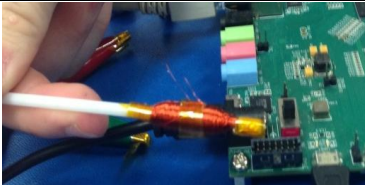
$$\mu = \mu_0 * \mu_{rel} \quad (\text{Eq. 2})$$

where μ_0 is the magnetic permeability of free space and μ_{rel} is the relative magnetic permeability. Factors such as magnetic shielding, the external magnetic permeability, the movement of the iron rod insert in warping the magnetic field lines, possible non-linearity between the magnetizing force and the induced magnetic field, and variable frequencies all change the overall measured inductance. The measured value of μ_{rel} from the coil setup is:

$$\mu_{rel} = \frac{Lin}{Lout} \quad (\text{Eq. 3})$$

where Lin is the inductance of the coil with the rod inserted, and $Lout$ is the inductance of the coil with the rod not inserted. The measured values of μ_{rel} of the coil setup were much lower than the literature values. Inductor construction materials proved to be minor contributors to this

discrepancy. Five inductor designs, listed in Table 2, together with some of their properties, were investigated.

Design Number	Coil Number N	Length (mm)	Radius (mm)	Inductance Not inserted L_{out}	Inductance Fully Inserted L_{in}	Picture
One	1500	300	9.525	2.89 μ H	6.5 μ H	
Two	92	239	9.100	3.87 μ H	11.39 μ H	
Three	1200	63.21	8.563	5.7896mH	32.901mH	
Four	1800	67.61	8.983	8.009mH	88.981mH	
Five	3600	21.79	2.63	12.706mH	70.787mH	
Table 2. Parameters of the five inductors tested with corresponding pictures.						

The materials for the first two inductor designs were 36 gauge wire, McMaster Carr stainless steel tube, and McMaster Carr High-Speed M2 Iron rod insert. The 36 gauge wire was wrapped around the stainless steel tube. The measurements were done with calipers and the

inductance was taken with an Agilent RLC meter running at 1 kHz frequency. The measured inductance range from not inserted to fully inserted was too small to gain the resolution that was the goal. For inductor 2, the u_{rel} was equal to 2.98.

Improving upon the above material choices for inductor 3, the stainless steel mold for the wires was replaced with a plastic tube. The plastic tube, unlike the stainless steel, did not interfere with the magnetizing force produced by the coils; the u_{rel} value was 5.68. Similar construction yielded even higher u_{rel} values. Inductor 4's u_{rel} value was 11.11. Inductor five's was 5.57.

The higher u_{rel} values allowed for a workable resolution, even though the literature values for the u_{rel} values of iron are near 5000. Similar results occurred when a Metglas core whose literature u_{rel} value is near 1,000,000 was tested in inductor 5 and had a measured u_{rel} value of 30.

Inductor Behavior:

In order to determine the functionality of the device, a number of tests were run on the inductors. With the third design, a measurement was conducted using calipers and the Agilent RLC meter running at 1 kHz frequency. The iron rod was stepped through the coil, and each corresponding inductance measurement was recorded as shown in figure 2. There is a linear portion of the graph, which can be used for the encoder as the operating range along the coil. In the final encoder, a mechanical block would limit the throw of the iron rod to this linear range and thereby ensure predictability.

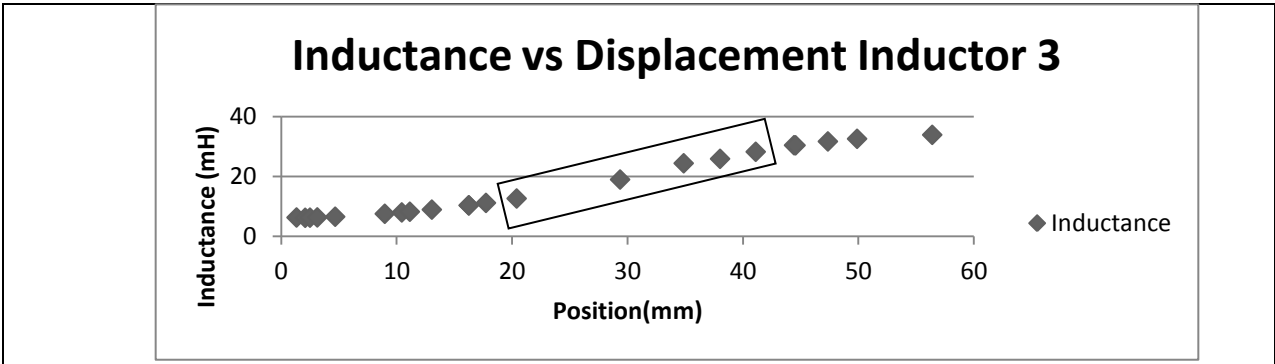


Figure 2. Inductance versus position of the iron rod insert into the inductor. The rectangular box highlights the existence of a portion that is linear. The linearity and the tailing off indicate how the magnetic flux acts as the iron rod is inserted.

The fourth inductor tested had a much more uniform coil density than the third inductor.

For inductor 4, the iron rod was stepped through a 20 mm portion of the coil, within the linear range as predicted by figure 2, using a Keyence laser displacement measuring system with an accuracy of one micron. The results are shown below in Figure 3:

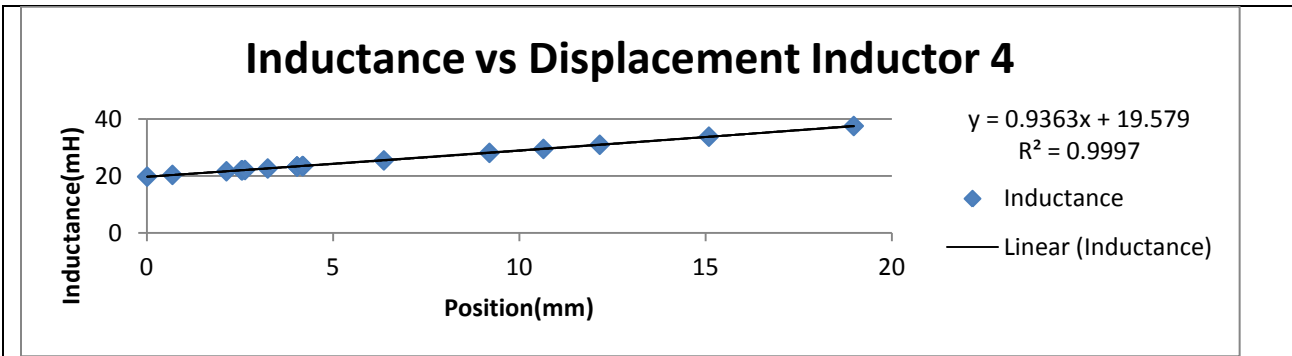


Figure 3. Inductance versus position of the iron rod for inductor 4 over a 20 mm range, centered well in the linear range of the inductor.

RLC Circuit, Operational Amplifier and the FPGA

To determine the position of the rod, a 50 Hz 3V square wave charges a capacitor as shown in yellow in Figure 4. When the power supply square wave drops to the trough, the capacitor discharges and there is an oscillatory voltage signal over the inductor seen in blue, which is fed into the operational amplifier whose output is seen in purple. The op amp output,

adjusted by the voltage offset system, is fed into the FPGA with a 200 MHz clock. The FPGA then counts the number of clock cycles that the purple wave has a high voltage. The count is then correlated to a position of the rod in the inductor.

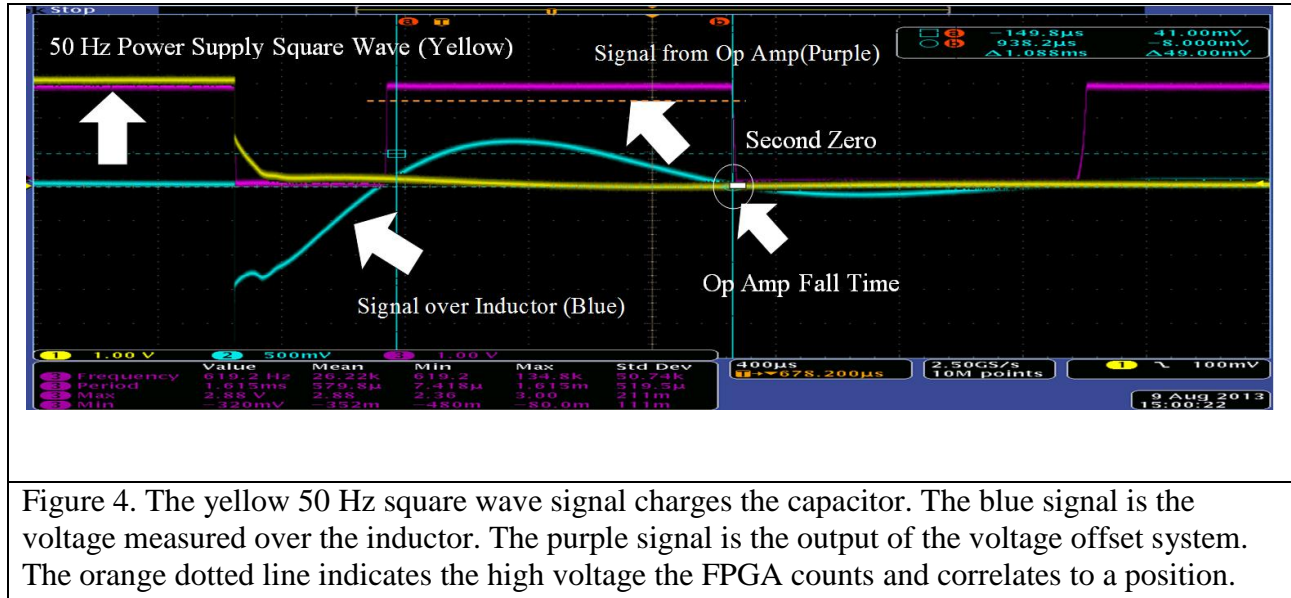


Figure 4. The yellow 50 Hz square wave signal charges the capacitor. The blue signal is the voltage measured over the inductor. The purple signal is the output of the voltage offset system. The orange dotted line indicates the high voltage the FPGA counts and correlates to a position.

The above system works well when the inductance, resistance and capacitance of the circuit for the full range of the rod insertion cause the blue signal to have well defined oscillations. If the blue signal does not oscillate, there can be no period reading by the FPGA. Furthermore, if the slope of the blue signal through its second zero is too shallow, then the op amp fall time increases asymptotically, as presented in figure 5. A longer fall time for the purple signal causes a non-linear correlation between the period of the blue signal and the FPGA count. In addition, the fluctuations of the FPGA count due to noise are greater for higher op amp fall times.

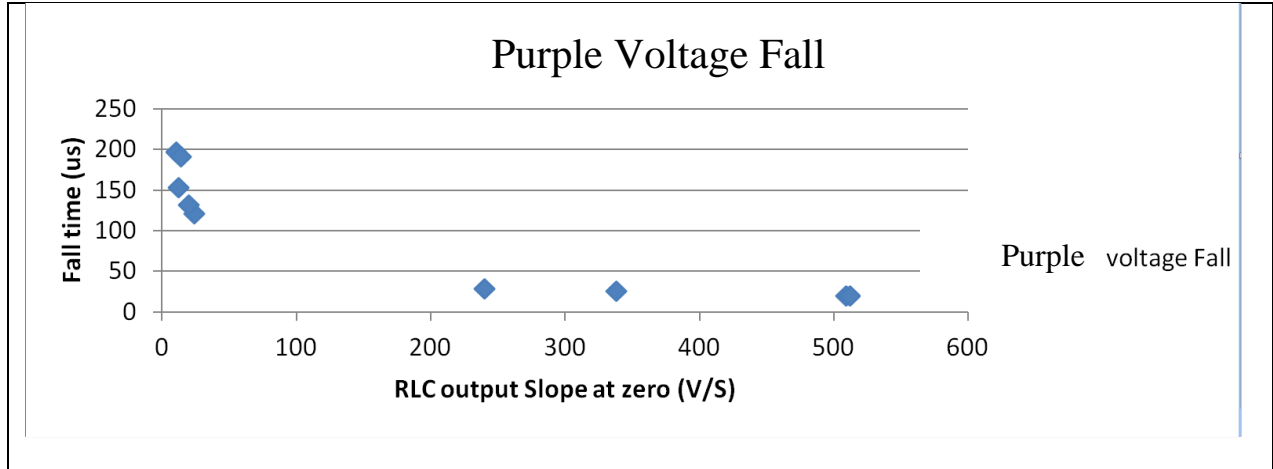


Figure 5. Fall time of the purple voltage signal of figure 4 against the magnitude of the RLC output's slope through the second zero of the period. Lower slope magnitudes cause asymptotically greater fall times, and non-linearity in the FPGA count.

To ensure that the signal over the inductor oscillates and that the fall times are kept under 50 μs , the inductance, resistance and capacitance of the circuit should be bounded such that the magnitude of the slope of the inductor signal at its second zero is greater than 200 V/s. It is therefore important to understand how the inductance, resistance and capacitance correlate to the inductor signal's slope at its second zero, the period of oscillation, and the exponential decay of the voltage.

First, the voltage across the capacitor in an RLC series circuit is [1]:

$$V_c(t) = V_c(\infty) + e^{-\alpha t} * (D_1 \cos w_d t + D_2 \sin w_d t) \quad (\text{Eq. 4})$$

$$D_1 = V_c(0) - V_c(\infty) \quad (\text{Eq. 5})$$

$$\alpha = \frac{R}{2L} \quad (\text{Eq. 6})$$

$$w_0 = \frac{1}{\sqrt{L * C}} \quad (\text{Eq. 7})$$

$$D_2 = \frac{V_c'(0) + \alpha * D_1}{w_d} \quad (\text{Eq. 8})$$

$$w_d = \sqrt{w_0^2 - \alpha^2} \text{ (Eq. 9)}$$

where $V_c(\infty)$ is the voltage at $t=\infty$, α is the attenuation coefficient, D_1 is the initial voltage, D_2 is given by the initial current, w_0 is the natural frequency of oscillation, and w_d is the damped frequency. The current through the circuit is [1]:

$$i(t) = C * \frac{dV_c}{dt} \text{ (Eq. 10)}$$

The voltage across the inductor in terms of current is [1]:

$$V_L = L * \frac{di}{dt} \text{ (Eq. 11)}$$

Performing two differentiations with respect to time:

$$V_L(t) = L * C * e^{-\alpha t} * \{[(\alpha^2 - w_d^2)D_1 - 2\alpha w_d D_2] * \cos(w_d t) + [(\alpha^2 - w_d^2)D_2 + 2\alpha w_d D_1] * \sin(w_d * t)\} \text{ (Eq. 12)}$$

Given that $\alpha \ll w_0$, i.e. the attenuation must be small for the method to be effective, Eq.9 shows that $w_d \approx w_0$, so the period of oscillation is:

$$T = \frac{2\pi}{w_0} = 2\pi * \sqrt{L * C} \text{ (Eq. 13)}$$

The time constant $\tau = 1/\alpha$, or the time it takes for the voltage to decrease by a factor of $1/e$ is:

$$\tau = \frac{2L}{R} \text{ (Eq. 14)}$$

As the magnetic rod slides through the coil, the inductance as shown in figure 3 increases linearly. Therefore, for greater amounts of rod insertion, the ratio of the time constant τ to the period T becomes greater:

$$\frac{\tau}{T} = \frac{\sqrt{L}}{\pi * R * \sqrt{C}} \text{ (Eq. 15)}$$

This results in a greater magnitude of the signal's slope at the second zero. The values of inductance, resistance and capacitance are then selected using the lowest values of the inductance corresponding to the magnetic rod being fully retracted. This condition was confirmed with testing as issues with non-linear fall times and lack of oscillations only occurred with no core inserted. The restrictive inductance is then taken from Eq.1, when $x=0$.

Because resistance only adds to damping, there is no need to add a resistor to the circuit. The only resistance then is the internal resistance of the inductor. The internal resistance of the inductor is:

$$R = 2\pi r * N * \theta \quad (\text{Eq. 16})$$

where θ is the resistance per unit length, dependent upon temperature and gauge of wire.

By taking the derivative of $V_L(t)$ and substituting in the time of the second zero, an inequality can be created that links the minimum 200 V/s slope to the construction characteristics of the inductor and the choice of capacitor. A good approximation to the derivative of $V_L(t)$ can be obtained from Eq. 12 for the usual case where $\alpha \ll \omega_0$ keeping just the terms in w_d^2 :

$$V_L(t) = -w_d^2 * L * C * e^{-\alpha t} * [D_1 \cos(w_d * t) + D_2 \sin(w_d * t)] \quad (\text{Eq. 17})$$

Differentiating,

$$V_L'(t) = -w_d^3 * L * C * e^{-\alpha t} * [-D_1 \sin(w_d * t) + D_2 \cos(w_d * t)] \quad (\text{Eq. 18})$$

The time of the second zero, $V_L = 0$ is:

$$t_0 = \frac{\text{atan}\left(\frac{-D_1}{D_2}\right) + \pi}{w_d} \quad (\text{Eq. 19})$$

Therefore the capacitance, inductance and resistance must satisfy the inequality:

$$200 \frac{V}{s} < |V_L'(t_0)| = w_d^3 * L * C * e^{-\alpha t_0} * [-D_1 \sin(w_d t_0) + D_2 \cos(w_d t_0)] \quad (\text{Eq. 20})$$

The requirement that the damping be small in comparison with the oscillation frequency can be expressed in terms of the damping coefficient $\delta = \alpha / \omega_d$:

$$\delta = \frac{R}{2} * \sqrt{\frac{C}{L}} \quad (\text{Eq. 21})$$

It was found that circuits that had damping coefficients under 0.2 and sufficiently large D_1 and D_2 had the necessary slopes to maintain a well defined oscillation, and avoid non-linearity with op amp fall times.

The values of capacitance, inductance and resistance also determine the resolution of the system. The goal then in the construction of the inductor and the circuit is to maximize the resolution while maintaining the inequality stated in Eq.20 above. The resolution is equivalent to how much of a movement of the iron rod there is per clock cycle. The resolution is:

$$\text{Resolution} = \frac{\Delta X}{\Delta T} * \frac{1}{\text{Clockspeed}} \quad (\text{Eq. 22})$$

$$\Delta T = \frac{2\pi}{\omega_{in}} - \frac{2\pi}{\omega_{out}} \quad (\text{Eq. 23})$$

where ω_{in} and ω_{out} are the oscillation frequencies with the rod in and out, respectively.

Furthermore,

$$\text{Resolution} = \frac{l}{2\pi \sqrt{\frac{\pi * r^2 * N^2}{l} * C * (\sqrt{u_0 * u_{rel}} - \sqrt{u_0})}} * \frac{1}{\text{Clockspeed}} \quad (\text{Eq. 24})$$

A Mathcad document was created to calculate the optimal capacitance and inductor construction that maximizes resolution while maintaining the necessary magnitude of the signal slope at the second zero.

Cryogenic Behavior:

Circuit exposure to colder temperatures affects the circuit in two major ways: first, it reduces the resistivity of the copper wire significantly, and thereby the resistance per unit length,

θ , and second, it causes a small change in the period given a certain amount of insertion. The resistivity of a wire as a function of temperature is:

$$\rho(T) = \rho_0[1 + K^{-1}(T - T_0)] \text{ (Eq. 25)}$$

where ρ_0 is the initial resistivity, K^{-1} is the temperature coefficient, T_0 is the initial temperature in Kelvin, and T is the current temperature in Kelvin. From Eq. 25 the resistivity of copper wire at 20 K is 2.28% of its resistivity at room temperature, 273 K. Testing showed that the resistance drop was close to 10% from room temperature to 77 K. The major reduction in resistance results in less damping, and a more defined waveform. Therefore, an encoder operable only at lower temperatures can be constructed with more turns and a higher gauge wire while maintaining the same resolution. Inductor 5 was constructed near the size specifications needed for use in the laser-fusion target positioning system. Such construction requires the use of a higher gauge, smaller diameter wire, which has much higher resistance. In addition, the encoder required a smaller radius coil. To attain around the same period change and resolution the encoder required a greater number of turns. At room temperature the inductor signal did not oscillate due to a higher resistance and thus excessive damping. When tested in liquid nitrogen near 77 K, the resistance decreased, and the signal oscillated, yielding a resolution near 0.1 μm .

Exposure to cryogenic temperatures also changes the period given a certain amount of rod insertion. One of the desirables for the encoder was temperature independence, or the need not to recalibrate the encoder for each new operating temperature. An encoder whose change in period results in a difference in measurement readings greater than the stated resolution would require recalibration or a reevaluation of its resolution. The resistance change in addition to the decrease in inductance displayed in Figure 6 causes about a 0.5 mm error between cold and warm readings.

Inductor Number	Warm (mH) Retracted	Cold (mH) Retracted	$\frac{\Delta L}{L_{warm}}$	Warm (mH) Inserted	Cold (mH) Inserted	$\frac{\Delta L}{L_{warm}}$
5	12.706	12.102	-0.0475	70.787	69.4	-0.0196
3 at 120Hz	5.5671	5.5620	0.0000	50.804	48.813	-0.0392
3 at 1 KHz	5.789	5.6465	-0.0246	32.9036	28.612	-0.1304

Figure 6. The inductances of different inductors with the rod inserted and retracted at room temperature and 77 K. Generally, there is a decrease in inductance between warm and cold temperatures.

Therefore, the encoder cannot have high resolution at both room and cryogenic temperatures as currently configured. The encoder construction results in higher resolution at warmer temperatures and lower resolution at colder temperatures. An encoder that is temperature independent must include a method for manual or sensor temperature input and a two-variable function that correlates the period input and temperature input to a certain amount of rod insertion. If temperature independence is not a requirement, the encoder can be constructed and calibrated to provide good resolution at a certain temperature.

Overall Device Functionality:

For each encoder, the time the op amp signal is high is correlated to the position of the magnetic rod. Data points correlating the position of the iron rod with the corresponding period of oscillation are shown in Figure 7 for inductor 4 by stepping the iron rod through the beginning 20 mm portion of the coil using a Keyence laser displacement measuring system.

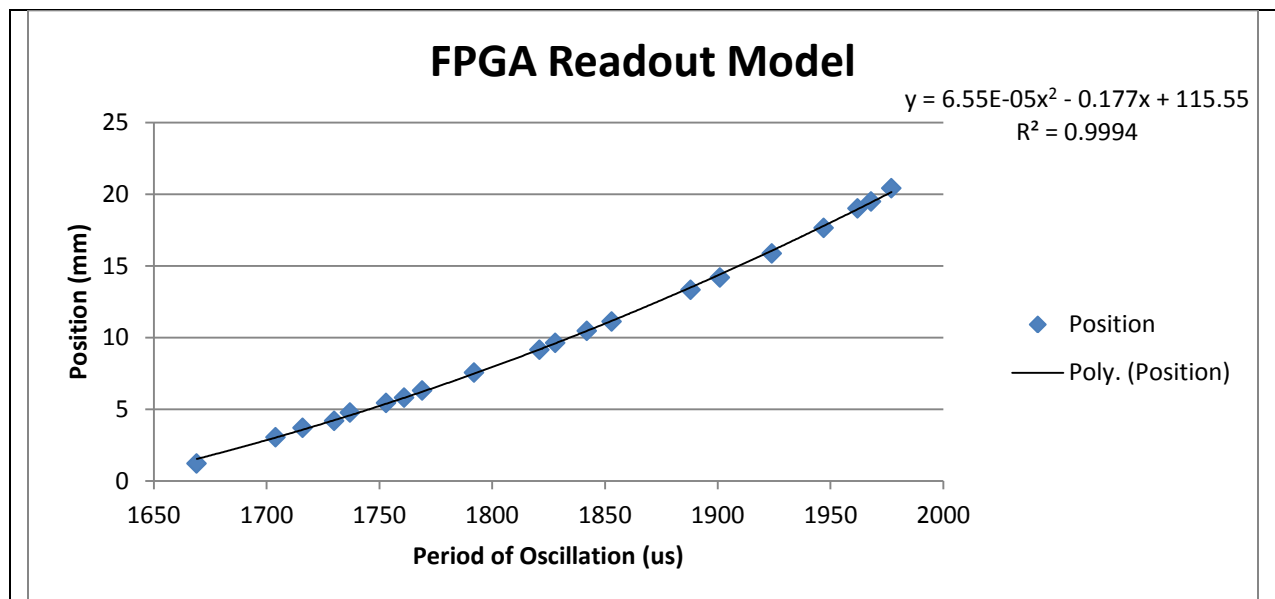


Figure 7. Correlation between the time the op amp signal is high and the position of the iron rod within the coil. For example, the FPGA would read a value such as 1873 μ s, run it through the trend line formula and display a distance of 13.8 mm.

With the number of data points taken, the accuracy of the readout model for any position within the 20 mm inductor range tested was about 1 mm. More data points and a greater resolution would improve accuracy greatly. For a temperature-independent encoder, trend lines would have to be created for each new operating temperature. The trend lines could be modeled knowing the resistivity and inductance as a function of temperature. The resistivity as a function of temperature is provided in Eq. 25 above. The inductance as a function of temperature seems to depend on the permeability of the iron rod and the contraction of the coils to a smaller radius. Experiments have shown that the magnetic permeability of soft annealed Swedish iron decreases with decreasing temperature. For a magnetic force of 1.77 CGS tested, the permeability decreased linearly with decreasing temperature. The overall decrease from room temperature to 77 K was -17.7%. Though the annealed Swedish iron most accurately represents the manufacturing methods used for the M2 steel iron insert, it is also found that soft unannealed

Swedish iron had the opposite dependence on temperature, the permeability increasing with decreasing temperature. It was also found that the percentage change in permeability from cold to warm was dependent upon the amount of magnetic flux through the sample [3]. Similarly, Metglas shows temperature dependence decreasing from a μ_{rel} value of 1,000,000 permeability at room temperature to 60,000 at 4.2 K. The contribution due to the copper coil contraction is orders of magnitudes smaller than the change seen in permeability. Thermal expansion data indicates that the percent change in length, which directly corresponds to the maximum possible percent change in radius, is -0.324%. The maximum coil contraction percentage contribution to the inductance percentage change is -0.649%. [4]

Conclusion:

An encoder concept was developed that combined a variable inductor, a ringing RLC circuit, an operational amplifier, and an FPGA. The insertion or retraction of a magnetically permeable rod into and out of a coil caused a change in inductance. This resulted in a change in the period of an oscillating RLC signal. The signal was converted into a square wave by way of an operational amplifier and a voltage offset system. An FPGA counted the time the signal was high, and correlated the count to a distance.

A relationship between inductor characteristics and circuit parameters was developed. The behavior of the RLC signal and the operational amplifier was characterized. It was found that the inductor's slope at the second zero and the op amp's fall time correlated. A Mathcad document was created to accurately calculate the optimal resolution, capacitance, and number of turns of the inductor given certain physical input parameters such as temperature, cross sectional area, length, and gauge.

With further improvement steps, the encoder has the potential to be a viable alternative to the currently used potentiometer solution. With the reduction of noise and more data points, the accuracy of a readout model could reach the measured resolution of 0.1 μm of the fifth inductor. Such accuracy would serve as an improvement over the current solution. With a more careful inductor construction, and sufficient calibration at the given operating temperature, an encoder can be constructed to replace the potentiometer solution.

References

[1]: Fawwaz T. Ulaby and Michel M. Maharbiz. *Circuits*. Allendale, NJ: National Technology & Science, 2009. Print.

[2]: Richard Palmer Reed and A. F. Clark. *Materials at Low Temperatures*. University of Michigan: American Society for Metals, 1983. Print.

[3]: J. Flemming and J. Dewar. "On the Magnetic Permeability and Hysteresis of Iron at Low Temperatures." *Proceedings of the Royal Society of London* 60 (1896): 81-95. Web.
<<http://archive.org/details/philtrans02805971>>.

[4]: Hung P. Quach and Talso Chui. "Low Temperature Magnetic Properties of Metglas 2714A and Its Potential Use as Core Material for EM1 Filters." Jet Propulsion Laboratory, California Institute of Technology Print.

Acknowledgements:

I would like to give my thanks to my advisors Mr. Gregory Brent and Mr. David Lonobile, and Mr. Dustin Axman for their guidance and support. In addition, I would like to thank Dr. Craxton for organizing the LLE High School Research Program, and providing an exhilarating and unique experience. Finally, I would like to thank my fellow interns for a tremendous summer.

Determining Plasma Temperature Using K-line Shifts in Rapidly Heated Matter

Ben Saltzman

Brighton High School

Rochester, New York

Advisor: Dr. Philip M. Nilson

Laboratory for Laser Energetics

University of Rochester

Rochester, New York

January 2014

1. Abstract

High-intensity infrared lasers focused above 10^{18} W/cm² accelerate electrons to relativistic energies. These high-energy electrons heat solid matter to hundreds of eV over picosecond timescales. K-shell emission is generated by collisional ionization and can be used to study the heating process. Copper targets were irradiated with picosecond pulses from the MTW laser and the K-shell emission spectra were measured. The program *CASK* was written in *MATLAB* to compare the experimental spectra and synthetic spectra generated by the collisional-radiative code *PrismSPECT*. The experimental spectra and the measured K-line shifts are consistent with an updated version of *PrismSPECT* based on first-principles calculations. These results show that K-line shifts can be used to infer plasma temperature.

2. Introduction

Lasers are coherent, collimated pulses of electromagnetic radiation. The coherence of the radiation allows a large amount of energy to be contained within a short pulse. High-energy lasers can deliver kilojoules of energy in picosecond (10^{-12} sec) pulses, achieving intensities above 10^{18} W/cm². At these short pulse lengths and high intensities, laser pulses interact with solid targets before any significant hydrodynamic expansion can occur, resulting in the creation of high-temperature, solid-density plasmas [1]. Such plasmas have an inertial disassembly time of approximately ten picoseconds [2]. Over greater timescales the hot dense plasma expands and decompresses below its initial solid density state.

When a high-intensity laser interacts with a solid target, large numbers of thermal electrons are accelerated to relativistic velocities. These fast electrons couple energy to solid matter over temporal scales longer than the laser-pulse duration and spatial scales larger than the laser focal spot [3]. Energy coupling to the target occurs through direct collisions and Ohmic dissipation of the induced return current of collisional background electrons [1]. In small-mass targets, the fastest electrons escape, charging the target, but most fast electrons are electrostatically confined to the target material (Fig. 1), rapidly heating it to tens or hundreds of electron volts (1 electron volt (eV) equals 11600 Kelvin) over picosecond timescales [3]. The heating process is isochoric (i.e. at constant volume) and creates extreme conditions that are inaccessible to conventional shock-wave techniques.

At temperatures approaching 1 keV, conditions in the solid-density plasma

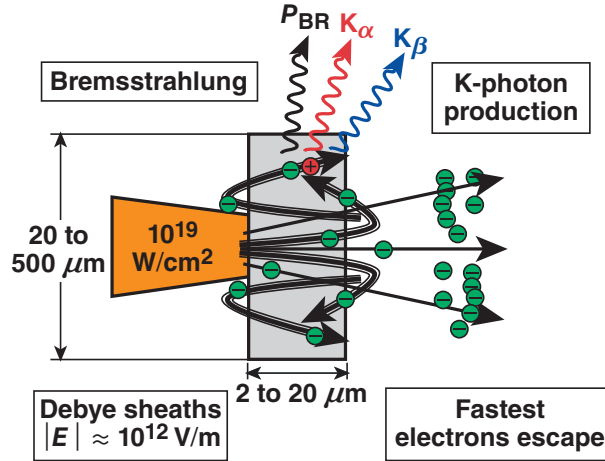


Figure 1: Schematic of the interaction between a high intensity laser (orange) and a thin solid metal target. Electron refluxing (recirculation) rapidly heats the solid material, creating bremsstrahlung radiation (P_{BR}) and $K\alpha$ and $K\beta$ emissions.

are similar to those in the core of a star. Generating and measuring these extreme plasma conditions through the analysis of X-ray emission spectra fosters an improved understanding of the rapid heating process. This is important for developing high-power X-ray sources for dense-matter probing.

In this report, experimental X-ray emission spectra from high-intensity laser-solid interaction experiments are analyzed. The experiments were carried out at the University of Rochester's Multi Terawatt Laser Facility (MTW) [4]. Thin copper foil targets were irradiated with picosecond laser pulses at focused intensities above 10^{18} W/cm^2 . Fast electrons accelerated by the laser pulse were electrostatically confined inside the targets due to target charging, enabling energy to be coupled to solid-density material over picosecond timescales (Fig. 1). This electron refluxing (recirculation) generates bremsstrahlung radiation due to electron accelerations [7]. During electron refluxing, a relativistic electron may collide with an electron of a copper ion, removing it from its orbital (Fig. 2). An electron in a higher energy level

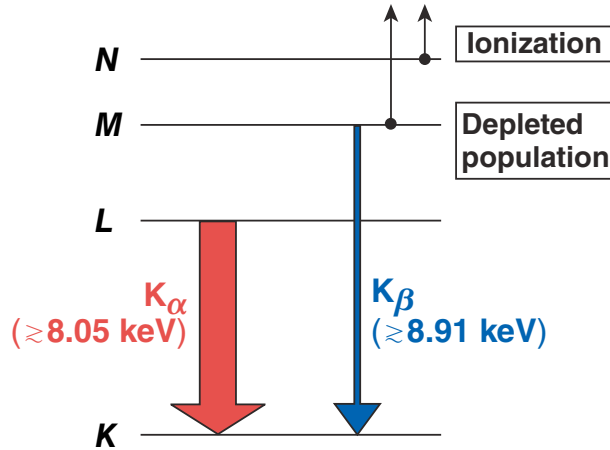


Figure 2: Copper energy levels showing $L \rightarrow K$ and $M \rightarrow K$ electronic transitions that generate K_{α} and K_{β} photons. Collisional ionization from the thermal background plasma depletes the outer lying shells, altering the K-shell ionization potential and reducing the K_{α} and K_{β} photon yields.

can transition down to fill the gap, releasing the excess energy as a photon [4]. When the gap occurs in the K shell of a copper ion, the emitted photon is a part of the K-line emission spectrum (Fig. 2).

The K-line emissions of copper are in the X-ray range. A transition from the L shell to the K shell produces K_{α} emission and a transition from the M shell to the K shell produces K_{β} emission (Fig. 2). Changes in plasma temperature affect the energy difference between shells, with higher plasma temperatures resulting in larger energy differences. K-line photons emitted from a copper ion will have a higher frequency and thus higher energy as the temperature of the plasma increases. This increase in energy causes the K-line emission spectrum to be shifted toward higher energies if plotted with the energy of detected photons as the independent variable and signal strength as the dependent variable. Measuring the energy shifts of K-spectra and comparing them to atomic physics calculations allows the plasma temperature to be inferred.

An X-ray spectrometer measured the copper $K\alpha$ and $K\beta$ emission spectra from the heated material. Analysis of the time-integrated copper $K\alpha$ and $K\beta$ emission lines allowed the plasma temperature to be inferred by comparing the spectra to theoretical predictions from the atomic physics code *PrismSPECT* [5]. The K-shell emission spectra predicted by *PrismSPECT* were used to understand how the $K\alpha$ and $K\beta$ spectral lines shift with increasing plasma temperature. The *PrismSpect* model predictions based on first-principles (Hartree-Fock) calculations [6] reproduced the experimental $K\alpha$ and $K\beta$ emission spectra when the plasma temperature was assumed to increase as a linear function of time.

The report is organized as follows: Sec. 3 describes the atomic physics code *PrismSPECT*, Sec. 4 presents the data analysis, Sec. 5 shows the data comparison with *PrismSPECT* model predictions, and Sec. 6 provides a summary and conclusions.

3. PrismSPECT

PrismSPECT is an atomic physics (collisional-radiative) code used to simulate the atomic level populations of plasmas over a range of conditions represented by specified parameters, such as plasma density and temperature [5]. *PrismSPECT* generates the spectra that result from these plasmas. *PrismSPECT* can run both steady-state simulations and time-dependent simulations over a timescale defined by the user. In a steady-state simulation, the temperature of the plasma remains constant over an identified time period. Time-dependent simulations vary the plasma temperature as specified by the user (e.g., as a linear increase with time).

These spectra can be combined to produce a time-integrated emission spectrum for a particular simulation.

PrismSPECT predictions, calibrated against experimental measurements made by Tanis *et al* [5], accurately reproduce copper $K\alpha$ emission spectra. In contrast, *PrismSPECT* has shown insufficient accuracy for reproducing copper $K\beta$ emission spectra [2]. Prism Computational Sciences, Inc., has recently developed a new model for $K\beta$ emission based on first-principles (Hartree-Fock) calculations [6]. These new model calculations aim to correctly predict the $K\alpha$ and $K\beta$ emission spectra from hot dense copper plasmas. They predict the same copper $K\alpha$ energy shift as the original *PrismSPECT* model, but a much larger $K\beta$ energy shift. However, these shifts have not been tested against experimental data. This report compares experimental emission spectra from high-intensity laser-solid interactions with the synthetic spectra generated by these new model predictions.

4. Data Analysis

X-ray spectroscopy with a highly oriented pyrolytic graphite (HOPG) crystal spectrometer was used to record K-line emission spectra from rapidly heated copper targets [8]. An example of a raw x-ray emission spectrum is shown in Figure 3. This emission spectrum was measured from a copper target irradiated with a 1-J, 1-ps pulse on the MTW Laser Facility. The x-ray signal was measured with an X-ray charge coupled device (CCD) and is time integrated. The data is spectrally resolved in the vertical direction. The copper $K\alpha_{1,2}$, $He\alpha$, and $K\beta$ lines are shown (the Cu $He\alpha$

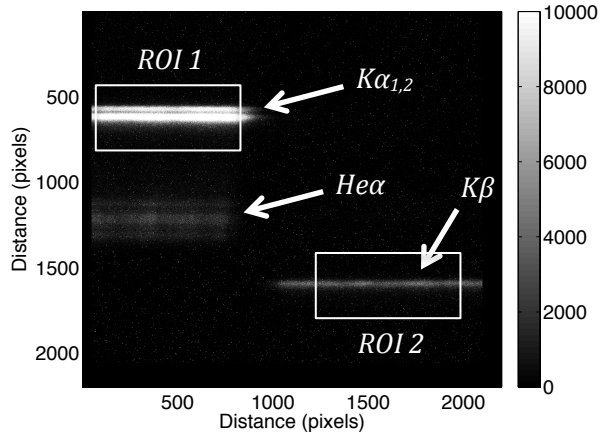


Figure 3. Example two-dimensional X-ray emission spectrum from a copper target measured with a crystal spectrometer coupled to an X-ray charge coupled device (CCD). The copper $K\alpha_{1,2}$, $He\alpha$, and $K\beta$ lines are shown. Regions of interest (ROIs) are shown. The $He\alpha$ and $K\beta$ lines have a low signal and do not reproduce well in the image.

line emission is not considered in this study). A hard x-ray photon background generated during the laser-target interaction created the white speckle pattern in the data.

To analyze the data, a program called *CASK* was written in *MATLAB*. *CASK* carries out three procedures. First, the copper $K\alpha$ and $K\beta$ lines are identified and isolated into regions of interest (ROIs). Second, each ROI is given a small rotation to correct for CCD misalignment [see Figs. 4(a) and 4(c)]. Third, one-dimensional spectra are obtained from the two-dimensional ROIs by summing the signal along each row, improving the signal-to-background ratio. Figures 4(b) and 4(d) show example raw copper $K\alpha$ and $K\beta$ emission spectra plotted as a function of distance (in CCD pixels) generated by *CASK*.

In this work, two MTW shots were analyzed: shot numbers 3204 and 3189. Shot 3204 is an example of a low energy density shot with laser energy (J)/target volume (mm^3) of $2 \times 10^3 \text{ J}/\text{mm}^3$. Shot 3189 has two orders of magnitude higher

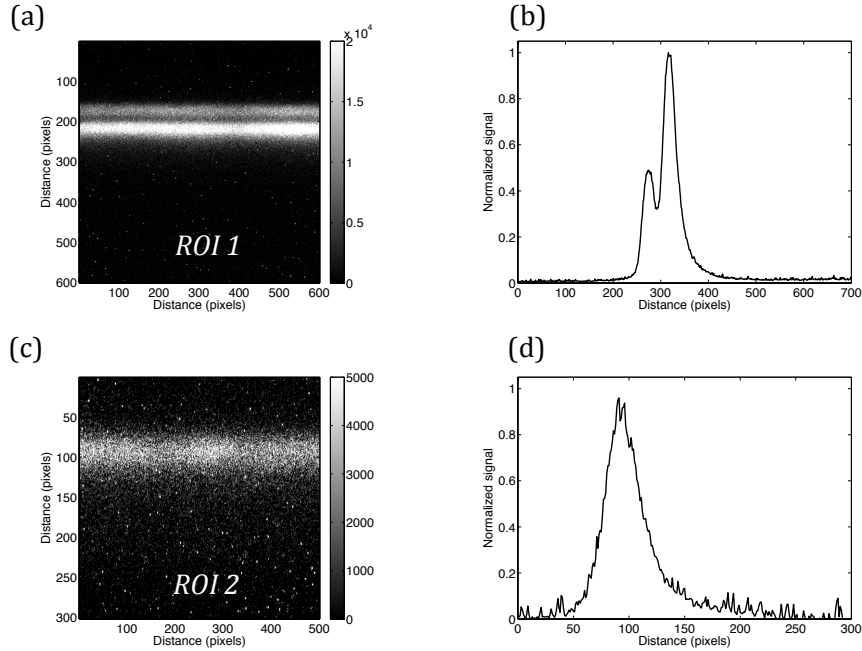


Figure 4: (a, c) Regions of interest (ROIs) identified from the X-ray CCD data shown in Figure 3. (b, d) Raw copper $K\alpha_{1,2}$ and $K\beta$ emission spectra, respectively, calculated from the ROIs in (a, c). This data analysis was carried out with the CASK program.

energy density ($2 \times 10^5 \text{ J/mm}^3$). Figure 5 shows calibrated $K\alpha$ and $K\beta$ emission spectra for these shots. The spectra were calibrated by converting distance in pixels to photon energy in eV based on the known spectral separation between copper $K\alpha_{1,2}$ in cold material (20 eV). The data shows that the $K\alpha$ and $K\beta$ lines are shifted in the higher energy density target compared to the lower energy density target. Higher plasma temperatures generated this spectral shift.

5. Data Comparison with *PrismSPECT*

Using trial and error, the data from each shot was matched to synthetic spectra generated from one steady-state and one time-dependent *PrismSPECT* simulation. The time-dependent simulations used a linear temperature temporal gradient to model conditions in the solid-density plasma, each beginning at the same

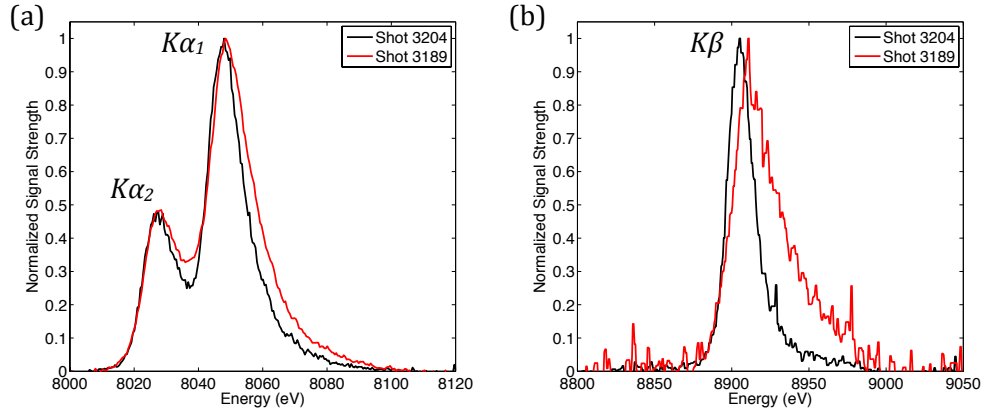


Figure 5: Copper $K\alpha_{1,2}$ (a) and $K\beta$ (b) emission spectra for Shots 3204 and 3189. Shot 3189 shows spectral shifts consistent with higher temperature plasma.

temperature of 1 eV and increasing linearly over a 10-ps timescale to a specified final temperature that was varied between simulations, ranging from 10 eV to 350 eV. The data showed better agreement with the synthetic spectra generated from time-dependent simulations than steady-state simulations.

Figure 6 shows the measured K-shell emission spectra from Shots 3204 and 3189 and compares them with time-dependent *PrismSPECT* calculations. Good agreement between the measured and calculated emission spectra is found assuming peak temperatures of 10 eV (Shot 3204) and 120 eV (Shot 3189). The new *PrismSPECT* model reproduces to a good approximation the emission peaks and the falling and rising edges of the measured $K\alpha$ and $K\beta$ emission spectra. This was not the case in the original *PrismSPECT* model and provides confidence that plasma temperature can be inferred from both the $K\alpha$ and $K\beta$ emission lines. Based on the assumptions implemented, the new *PrismSPECT* model reproduces the dominant features in the K-line emission spectra of these hot dense copper plasmas.

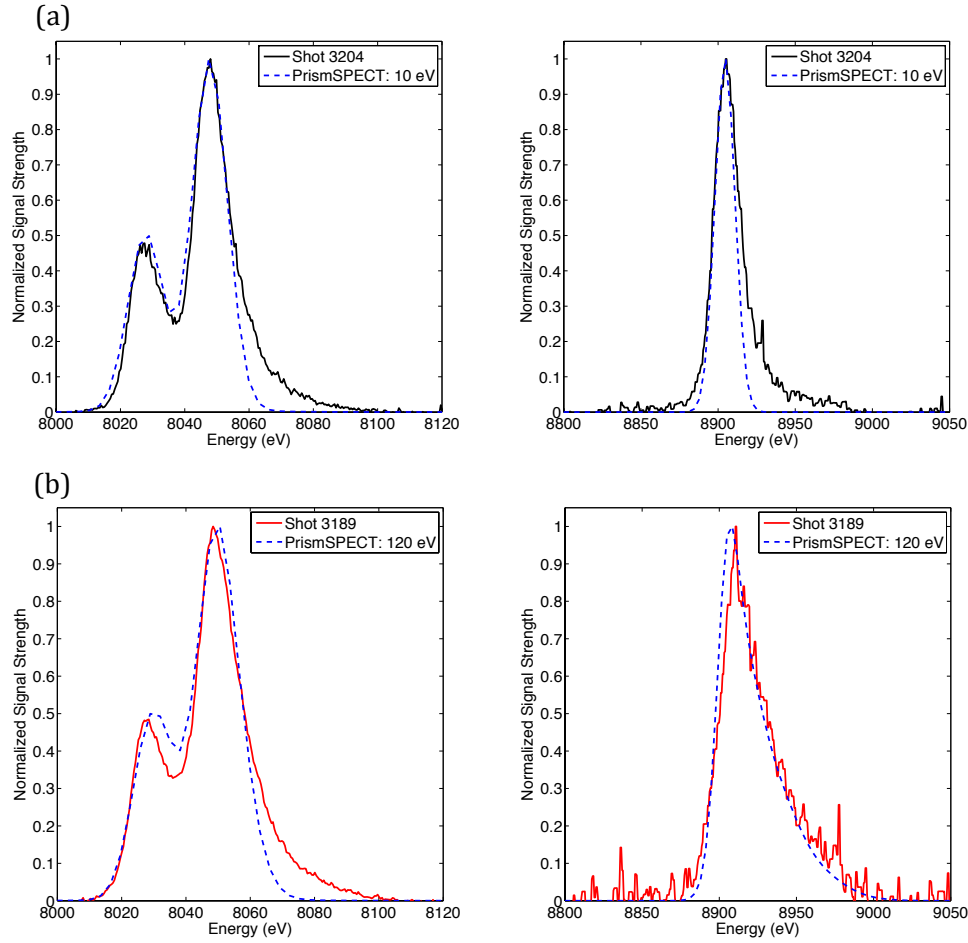


Figure 6: Copper $K\alpha$ and $K\beta$ emission spectra for Shots 3204 (a, black) and 3189 (b, red). Emission spectra calculated by PrismSPECT (blue) for peak temperatures of 10 eV (a) and 120 eV (b).

6. Summary and Conclusions

Experimental X-ray emission spectra were analyzed from high-intensity laser-solid interaction experiments in which thin copper foil targets were irradiated with picosecond laser pulses at focused intensities above 10^{18} W/cm² [4]. Fast electrons accelerated by the laser pulse refluxed inside the targets and caused K-shell emission spectra to be radiated. An X-ray spectrometer measured the copper $K\alpha$ and $K\beta$ emission spectra from the heated material. Theoretical predictions from the collisional-radiative code *PrismSPECT* [5], in the form of synthetic spectra, were

obtained. *PrismSPECT* model predictions based on first-principles calculations reproduced the experimental $K\alpha$ and $K\beta$ emission spectra assuming a linear temperature temporal gradient [6]. Comparisons between the simulated and experimental spectra enabled the plasma temperature to be inferred. The *MATLAB* program *CASK* analyzed the experimental data and reduced the emission spectra for comparison with *PrismSPECT* model predictions. This work shows good agreement between the new theoretical model of K-line emission spectra for copper and the experimental results from X-ray spectroscopy measurements on MTW. An accurate model for K-line emission spectra will lead to a more precise understanding of rapid material heating at high energy densities. This work is important for the development of many applications from flash X-ray generation and laboratory astrophysics to dense-matter probing.

Acknowledgements

I would like to thank Dr. Philip M. Nilson for his guidance and insight. I would also like to thank Dr. R. Stephen Craxton and the Laboratory for Laser Energetics for creating and running the high school internship program, and my parents, Daniel and Risa Saltzman, for their love and support.

References

- [1] S. D. Baton, *et al.* “*Relativistic electron transport and confinement within charge-insulated, mass-limited targets.*” High Energy Density Physics 3, 358-364 (2007).
- [2] P. M. Nilson, private communication (2014).
- [3] A. R. Bell, *et al.* “*Fast-electron transport in high-intensity short-pulse laser-solid interactions.*” Plasma Phys. Control. Fusion 39, 653-659 (1997).
- [4] P. M. Nilson. “*High-Intensity Laser-Plasma Interactions in the Refluxing Limit.*” 49th Annual Meeting of the American Physical Society Division of Plasma Physics (2007).
- [5] J. J. MacFarlane, I. E. Golovkin, and P. R. Woodruff. “*Modeling of Inner-Shell ($K\alpha$, $K\beta$) Line Emission from Cu Targets Heated by Short Pulse Lasers*”. Prism Computational Sciences, Inc., Madison, WI (2010).
- [6] J. J. MacFarlane, I. E. Golovkin, and P. R. Woodruff. “*Modeling of Inner-Shell ($K\alpha$, $K\beta$) Line Emission from Cu Targets Heated by Short Pulse Lasers ($K\beta$ Modeling Revisions; July 2013)*”. Prism Computational Sciences, Inc., Madison, WI (2013).
- [7] P. M. Nilson *et al.* “*Scaling Hot-Electron Generation to High-Power, Kilojoule-Class Laser-Solid Interactions*”. Physical Review Letters 105, 235001 (2010).
- [8] P. M. Nilson *et al.* “*Scaling hot-electron generation to long-pulse, high-intensity laser-solid interactions*”. Physics of Plasmas 18, 056703 (2011).

Controlling Laser Beam Speckle with Optimized Illumination of Zooming Phase Plates

Adeeb Sheikh

Advisor: Dr. Reuben Epstein

*Laboratory for Laser Energetics, University of Rochester
Rochester, New York 14623-1299*

1. ABSTRACT

Energy deposition by the laser during inertial confinement fusion implosion experiments [J. Nuckolls et al., *Nature (London)* 239, 139 (1972); S. Atzeni and J. Meyer-ter-Vehn, *The Physics of Inertial Fusion*, (Clarendon Press, Oxford, 2004).] is reduced by the shrinking surface area of the target with respect to the constant area of illumination of the laser. It has been proposed to reduce this energy loss by implementing a method called “two-state focal zooming,” [D. H. Froula et al., *Phys. Plasmas* **20**, 082704 (2013).] wherein the illumination area of the laser is changed from a large initial area to a smaller area as the target implodes. The zooming is accomplished by utilizing a specialized distributed phase plate (DPP) [Y. Kato and K. Mima, *Appl. Phys. B* **29**, 186 (1982); Laboratory for Laser Energetics LLE Review 33, NTIS Document No. DOE/DP/40200-65, 1987 (unpublished), p. 1.] that has two sets of regions, each creating a different-sized focal spot where the beam is focused on-target. Different configurations of these “zooming phase plates” (ZPPs) produce speckle with unique spectra of spatial frequencies. To model these spectra, statistical models for discrete DPPs were generalized and implemented in a computer program that was applied to various ZPP configurations to find specific arrangements that reduce the speckle at lower spatial frequencies. Good agreement was obtained between the measured and predicted spectra for an experiment in which certain portions of a standard DPP were illuminated.

2. INTRODUCTION

Successful laser-driven fusion requires uniform target implosions. In order to accomplish this using the direct-drive method for inertial confinement fusion (ICF),¹ the spherical target must be uniformly irradiated. However, spatial aberrations in the wavefront of the laser cause intensity variations in the illumination incident on the target,² causing uneven energy deposition

and implosion asymmetry, and reduce the implosion performance. One method for smoothing the intensity profile of a laser beam is to utilize a distributed phase plate (DPP).³

DPPs are diffractive elements built with a varying thickness that breaks up the laser into spatially incoherent beamlets. The purpose is two-fold: to smooth the laser profile in the far-field by breaking the laser coherence and diminishing the effect of wave aberrations on illumination uniformity, and to increase the size of the focal spot in the far-field on-target to match that of the target. The superposition of each of these beamlets creates a fine-scale intensity pattern, or “speckle,” that is much finer and smoother, relative to the original non-uniform intensity of the laser beam without the DPP. The speckle pattern arises because of the interference between the beamlets diffracted through the DPP. This speckle can be modeled as the product of an envelope function representing the smoothed beam shape and a modulation function, which adds “noise” to the envelope as a result of the random element in DPP diffraction and interference.

There are two types of DPPs: discrete and continuous. Discrete DPPs are constructed from a uniform honeycomb pattern of hexagonal area elements, with one of two different thicknesses, selected randomly, such that any one element will shift the phase of the light wave by 0 or π radians [Fig. 1].³ In discrete DPP's, the light passing through each element is referred to here as a beamlet. Because of the random relative phase between the area elements of the DPP, the beamlets have properties of beams that propagate independently. The focal spots of all the beamlets are superimposed at the same focal spot on-target. Because of the diffractive properties of the discrete DPPs, energy is lost to the edges of the focal spot, coupling only 78% of the incoming energy onto the target. Thus, continuous DPPs replaced discrete DPPs. Their thickness varies continuously reducing the energy lost to the focal spot edge and increasing the energy focused onto the target to about 99%.⁴ While the two types of DPPs are structurally different, they produce similar effects and have similar properties.⁵ This would seem to allow the use of discrete DPP statistics in the context of modern continuous DPPs.

Two issues with the DPPs arise when considering the static size of the focal spot in the far-field. The first occurs because the target shrinks during implosion, causing light near the edge of the far-field to miss the target as implosion continues; naturally, this reduces the energy deposition onto the target. The second problem is a result of the first; errant light, which we visualize as rays, near the edge of the beam causes a phenomenon known as Cross-Beam Energy

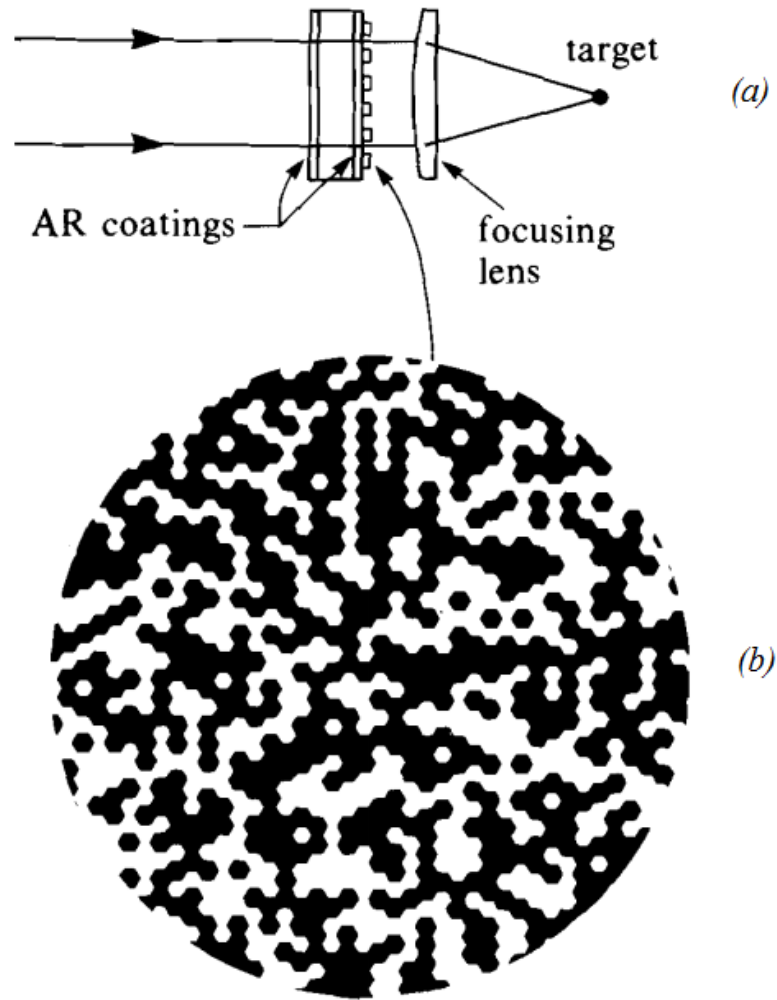


Fig. 1. (a) Principle of a distributed phase plate (DPP). The laser illumination that passes through each element of the DPP irradiates the whole target when focused by the lens. (b) A discrete DPP. This is binary in nature, with randomly distributed elements of two different thicknesses (shown as black and white) in order to evenly break the coherence of incoming laser light. [Figure from Ref. 3]

Transfer (CBET),⁶ a multiple-beam laser-plasma interaction instability that further reduces the energy deposition of incoming light. CBET is a consequence of stimulated Brillouin scattering (SBS).⁷ SBS occurs when intense laser light drives ion acoustic waves in a medium, causing the medium to act as a diffraction grating that scatters incoming light. CBET occurs when incoming laser light (the center-beam ray of Fig. 2) scatters into the outgoing off-center laser illumination

(the edge-beam ray of Fig. 2). This keeps much of the incoming light from reaching its innermost turning point where it would be most efficiently absorbed, thus reducing the energy deposition onto the target [Fig. 2].

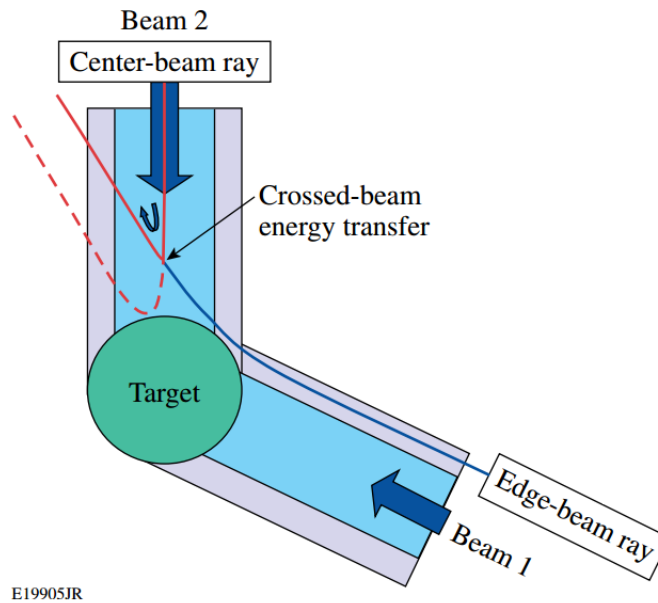


Fig. 2 Schematic of cross-beam energy transfer. Edge-beam rays miss the target completely and intersect the paths of incoming rays. The plasma-beam SBS interaction transfers incoming laser energy of the center-beam rays [such as the ray shown in red] to outgoing edge-beam rays [such as the solid blue ray], thus reducing the incoming energy that reaches the target surface. [Figure from Ref. 6]

3. TWO-STATE FOCAL ZOOMING

One proposed method for mitigating CBET involves dynamically changing the diameter of the focal spot of the laser in the far-field. This can be accomplished through a process known as two-state focal zooming,⁸ wherein an initial picket pulse⁹ is incident upon the target with a wide diameter focal spot, while the main pulse irradiates the target with a smaller focal spot. Two-state focal zooming has the benefit of mitigating CBET through a dynamic focal diameter, while still maintaining relative uniformity of implosion, by matching the illumination spot size to the target size, both early and late in the implosion.

The process itself involves illuminating specific parts of a specially designed DPP -- a Zooming Phase Plate (ZPP), such that the picket pulse will produce a wide diameter illumination

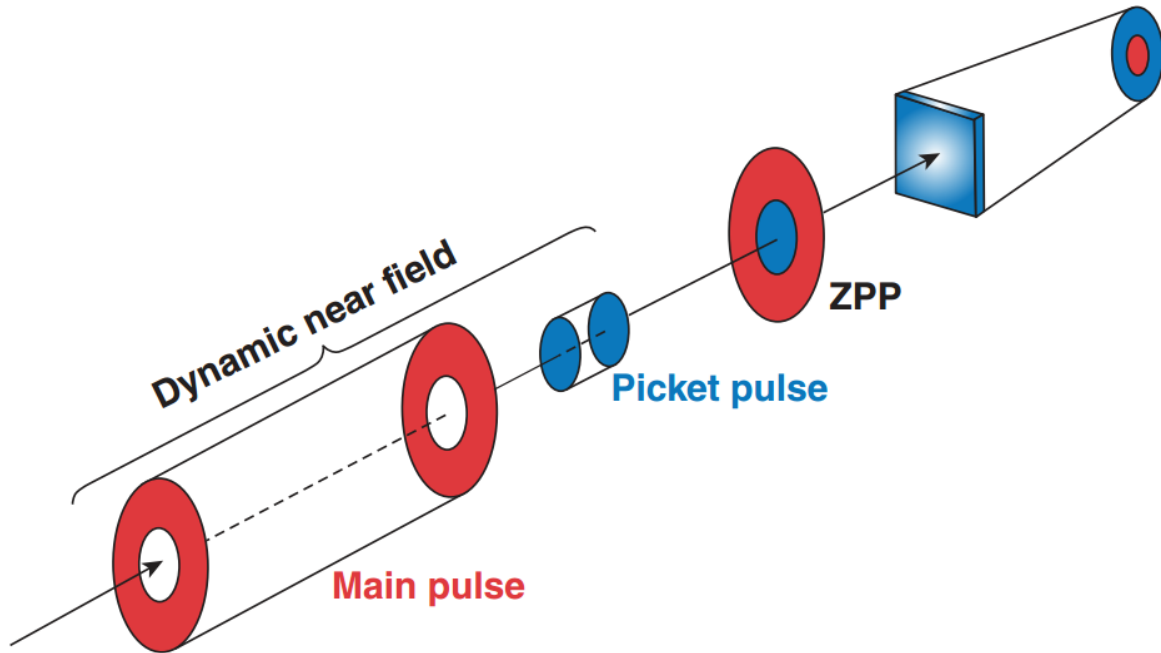


Fig. 3 Principle of a zooming phase plate (ZPP). The picket pulse is fired first, passing through a specific region of the ZPP with smaller “elements” (i.e. denser structure variations), creating a wide focal spot. Then the main pulse is fired through the rest of the ZPP with larger “elements,” creating a focal spot with a reduced diameter. [Figure from Ref. 9]

in the far-field and the main pulse will produce a smaller diameter illumination [Fig. 3].⁹ The ZPP functions because it consists of two types of regions: one which is illuminated by the picket pulse and one which is illuminated by the main pulse. The nature of these regions is such that their illumination yields different size focal spots. This is accomplished by exploiting the properties of DPPs. Consider a continuous DPP with shorter-scale or “dense” variations in thickness -- the equivalent of smaller elements in a discrete DPP. Illuminating this DPP, the focal spot would be larger than that of a continuous DPP with larger-scale or “sparse” variations in thickness. We can apply this principle to a ZPP by having regions of dense variations for the picket pulse and sparse variations for the main pulse [Fig. 4].⁹ However, different ZPP designs produce different speckle spectra, depending on which regions of the ZPP are illuminated at any given time. To this end, it is necessary to identify an optimal configuration, where the most harmful spatial frequencies, the low frequencies, are minimized, in order to optimize the

uniformity of the energy deposition.

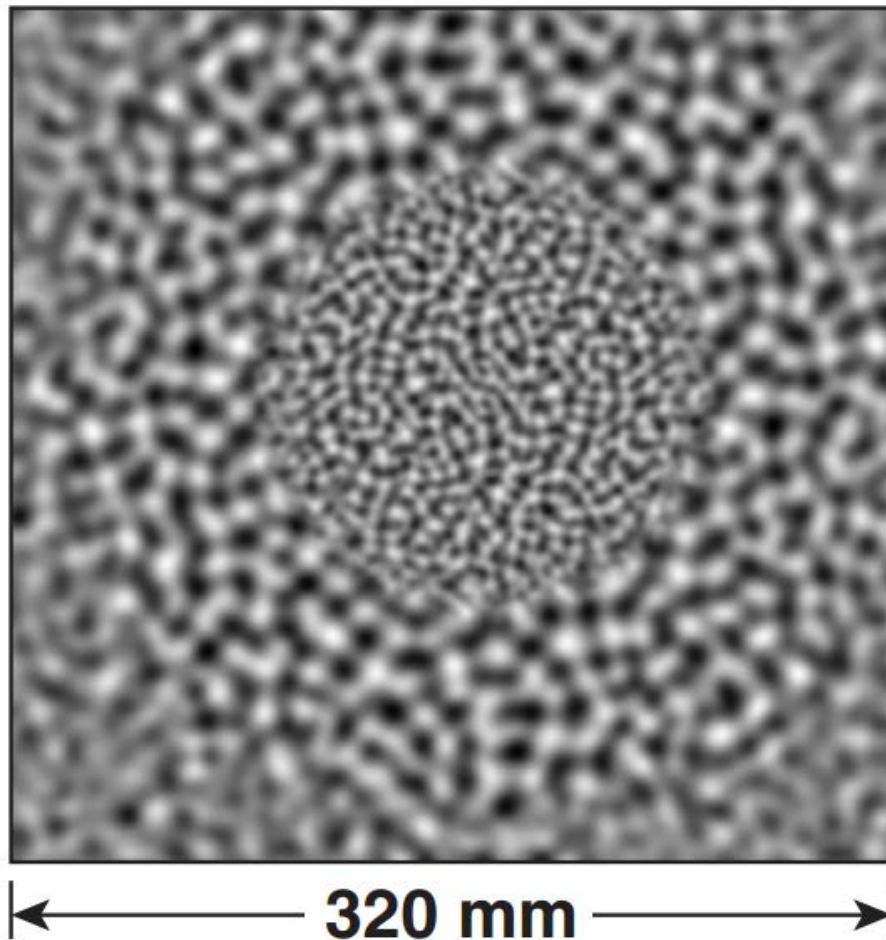


Fig. 4 A phase-contrast photograph of a continuous DPP with the phase contrast represented by shading. This is a ZPP, with a central and surrounding regions constructed with patterns characterized by different overall structure scale lengths selected for zooming from larger to smaller focal spots at the early and late stages of an implosion. [Figure provided by D. H. Froula]

4. DEVELOPING THE STATISTICAL MODEL AND SIMULATION

In order to determine the effectiveness of different ZPP configurations, it was first necessary to model the speckle spectrum and express it in terms of spectral density. This would show which spatial frequencies are most prominent in the far-field. Before developing such a model, however, it was important to lay down some assumptions: (1) the DPP in question is discrete, with a number of elements N , each of an area, a , resulting in a total illuminated area

$A=aN$; (2) the light is focused with focal length, z_0 , wavelength, λ (or wave number, $k = 2\pi/\lambda$); and (3) the phase aberrations along the wavefront are negligible. The first assumption allows us to approximate the properties of continuous DPPs with those of discrete DPPs, which are much easier to calculate; the second assumption is simply a statement of the constants associated with the laser and optics; and the third assumption serves to simplify calculations, by avoiding the inherent problems of a real-world laser -- namely, the deformed wavefront.

The speckle of the intensity profile of the focused laser beams is expressed in our model as a modulation function. This modulation function represents the variations in the intensity of the laser projection on the target that arise because of the interference of beamlets after they have passed through the diffractive elements of a discrete DPP. The relationship between the intensity profile and the modulation function is expressed by

$$I(\vec{x}) = I_{env}(\vec{x})G(\vec{x}), \quad (1)$$

where $I(\vec{x})$ represents the actual intensity profile of laser as a function of position on the target surface, \vec{x} , where $I_{env}(\vec{x})$ represents the smooth envelope of the intensity distribution, and $G(\vec{x})$ represents the modulation function [Fig. 5].¹⁰ For the purposes of modeling speckle

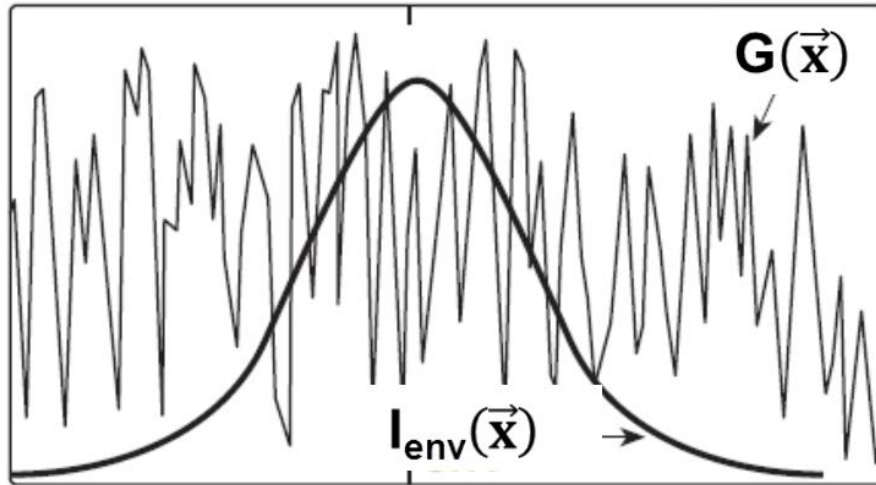


Fig. 5. A visual representation of the modulation function $G(\vec{x})$ and the intensity envelope $I_{env}(\vec{x})$ overlaid on the same set of axes. In expressing the intensity profile of a discrete DPP with Eq. (1), the envelope is the ideal smooth, “average” intensity profile that would be obtained with an individual beamlet, and the modulation function represents the speckle produced by the interference among all the superimposed beamlets. [Figure from Ref. 10]

spectra, the modulation function is expressed in terms of a phase correlation function $C(\vec{q})$, as

$$G(\vec{x}) = 1 + \sum_{\{\vec{q}\}} C(\vec{q}) e^{-i\vec{K} \cdot \vec{x}}, \quad (2)$$

such that the modulation function varies from unity by the sum of all products of the mean phase correlation function, $C(\vec{q})$, and the exponential of the dot product of the wave vector \vec{K} and \vec{x} , summed over the set of all distinct element pair separations \vec{q} .¹¹ Each distinct \vec{q} in the near-field plane corresponds to a spatial frequency component of frequency \vec{K} in the far field. The specific relationship between \vec{q} and \vec{K} is

$$\vec{K} = \frac{k}{z_0} \vec{q}. \quad (3)$$

Because of the discrete nature of discrete phase plates, the DPP elements shift the phase of the incoming beamlets passing through element k at position \vec{z}_k by $\phi(\vec{z}_k) = 0$ or π . Thus the phase difference between two elements will always be either 0 or π (modulo 2π) selected at random with equal probability. The mean phase difference between pairs of all illuminated phase plate elements of spatial separation \vec{q} for a particular DPP is given by the spatial correlation function $C(\vec{q})$ expressed as the sum

$$C(\vec{q}) = \frac{1}{N} \sum_{k=1}^{N_{\vec{q}}} e^{i(\phi(\vec{z}_k + \vec{q}) - \phi(\vec{z}_k))} \quad (4)$$

over all $N_{\vec{q}}$ illuminated element pairs with the spatial separation \vec{q} . In this expression, the exponentials of the phase differences, ϕ , between each two-element pair, k , with displacement \vec{q} between them are summed and then divided by the total number of illuminated elements, N . The exponential expression, itself, equals -1 or 1 with equal probability. Formally, the mean value of $C(\vec{q})$ for each possible \vec{q} and across all possible random phase differences, averaged over all possible different random DPP's, is 0, a result that is not helpful to our purposes. The typical value, however, is the square root of the mean square of $C(\vec{q})$ (or the “root mean square” or RMS). This value is non-zero and can be related to the area of intersection $A \cap A'$ between the

illumination area A and an exact copy of that illumination area A' displaced by the distance \vec{q} as described in detail in Ref. 11, and expressed as

$$N^2 \langle |C(\vec{q})|^2 \rangle = N_{\vec{q}}, \quad (5)$$

where

$$aN_{\vec{q}} = A \cap A' . \quad (6)$$

Equation (5) is based on the statistics of the random walk where the length of a walk of n steps either forward or backward in a line, selected at random, is \sqrt{n} steps, averaged over many walks. Just as no two random walks are identical, the speckle modulations of no two independently designed random DPP's are identical. Nevertheless, when they are constructed following the same rules, the same RMS statistical results apply to them all. The total RMS speckle modulation σ_{RMS}^2 from any set of element separations $\{\vec{q}\}$ or, through Eq. (3), spatial frequencies $\{\vec{K}\}$ is the sum

$$\sigma_{RMS}^2 = \sum_{\{\vec{q}\}} \langle C^2(\vec{q}) \rangle. \quad (7)$$

In the limit of a DPP with a large number of small elements, this discrete sum can be expressed as an integral. The contribution to the total RMS speckle modulation by all \vec{K} whose absolute values are within an infinitesimal interval dK of $K = (k/z_0)q$ is given by the spectral power density

$$\frac{d\sigma_{RMS}^2}{dK} = \frac{z_0}{k} \int_0^{2\pi} \langle C^2(\vec{q}) \rangle \frac{q}{a} d\theta. \quad (8)$$

Using Eqs. (5) and (6) to substitute the area of intersection $A \cap A'$ for the mean square of the correlation function $C(\vec{q})$ in its relationship with spectral density of the speckle spectra, we obtain, continuing to follow the development in Ref. 11, the expression,

$$\frac{d\sigma_{RMS}^2}{dK} = \frac{z_0}{k} \int_0^{2\pi} \frac{(A \cap A')_{\vec{q}}}{A^2} q d\theta. \quad (9)$$

The integral over the angle θ in Eqs. (8) and (9) represents the sum over all \vec{q} of the same length

to obtain the spectral power density with respect to the scalar separation $q = |\vec{q}|$ or the spatial frequency $K = |\vec{K}|$ for all directions.

While Eq. (9) contains in principle exactly what we need, there are some alterations to be made for our convenience. Namely, we want to express the spectral power density in terms of the normalized spatial frequency K / K_{\max} and use the square root of the spectral power density given by Eq. (9) to express the amplitude of the spatial frequency terms of Eq. (2). Next, we must construct a discrete approximation of the integral appropriate for a numerical evaluation. Equation (9) provides the basis for developing the key algorithm of the computer program for the speckle simulation, henceforth referred to by its name: SPQL.

The first task in programming SPQL was to find the area of intersection between an arbitrary illumination area and that same illumination area displaced by \vec{q} . This was accomplished by representing the entire DPP surface with a square array of square array elements, each assigned the value with 1's and 0's as selected by a user, where a 1 or 0 indicates an illuminated or unilluminated area element of the DPP, respectively. These array elements are created as a discrete representation of an arbitrary illuminated area of the DPP surface; they are not to be confused with either the area elements of the phase-delay pattern of the DPP or their phase. The program then copies the illumination array and displaces it by \vec{q} . The number of intersecting illuminated area elements is then calculated by multiplying the assigned value of each element of the original illumination array by the value of the overlying element of the displaced illumination array, thus forming a product array, and then summing the values of all the numbers of this product array. The area of intersection is equal to the product of the number of intersecting area elements and the area of a single area element. This works because the only elements of the product array with a value of 1 are those where *both* factor array elements at the original and displaced position have a value of 1. These areas of intersection are then stored in a separate array, tabulated with respect to their associated displacements, so that it is possible to refer to them later and sum them as

$$\frac{d\sigma_{RMS}^2}{dK} = \sum_{(q-\Delta q/2 < |\vec{q}| < q+\Delta q/2)} \frac{(A \cap A')_{\vec{q}} z_0}{aN^2 \Delta q k}, \quad (10)$$

which is the discrete sum, corresponding to Eq. (9), forming the spectral power density of the

speckle, where Δq represents the element interval of the spacing of the discrete representation of the speckle spectrum or, through Eq. (3), the spatial frequency interval ΔK . Once we have tabulated the spectral power density function, we can obtain

$$\sqrt{d \frac{d\sigma_{RMS}^2}{K_{max}}} = \sqrt{\frac{\sum_{(q-\Delta q/2 < |\bar{q}| < q+\Delta q/2)} \frac{(A \cap A')_{\bar{q}} z_0}{aN^2 \Delta q k}}{\frac{k}{z_0} q_{max}}}, \quad (11)$$

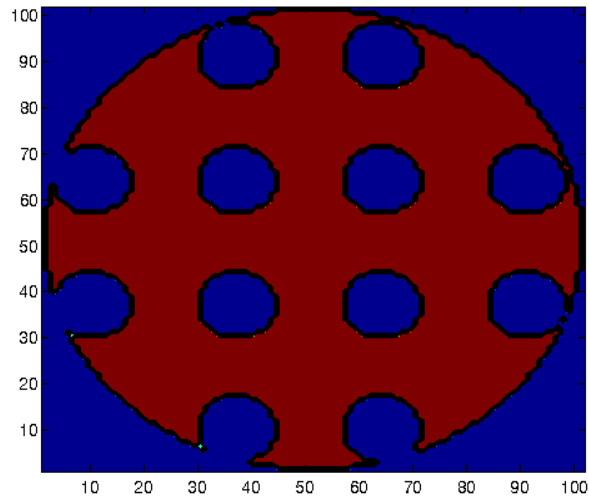
the RMS amplitude spectrum of the DPP model speckle spectrum.

5. EVALUATING THE ACCURACY OF THE SIMULATION

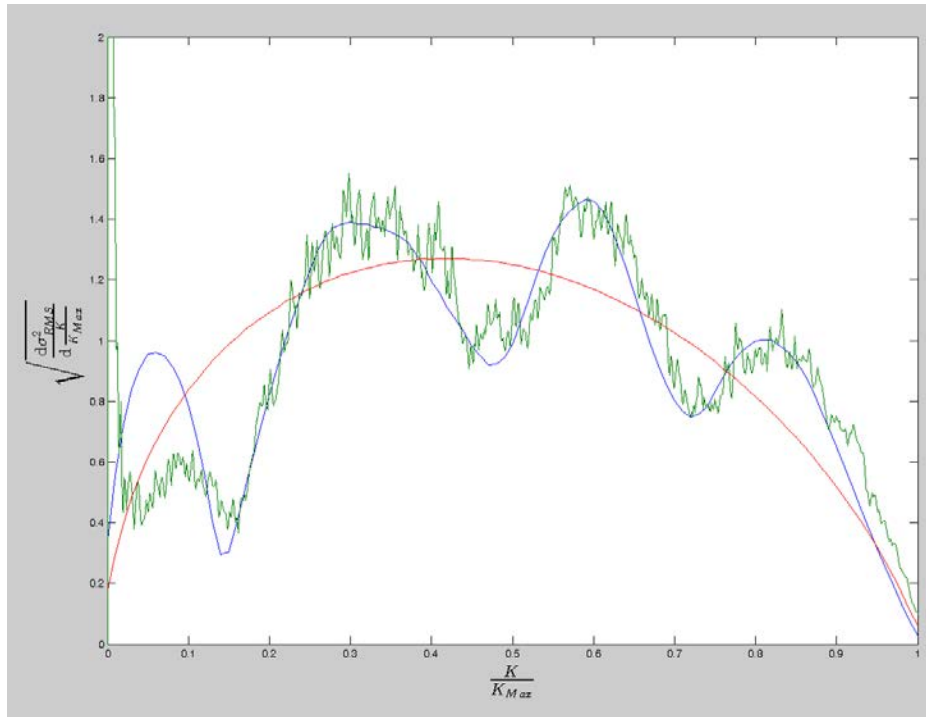
It has been noted before that the simulation and corresponding model were developed specifically with the statistics of the discrete DPPs in mind. However, modern lasers such as OMEGA and the NIF use continuous DPPs. Thus, testing the accuracy of the discrete DPP simulation by comparing its results with continuous DPP laboratory measurements is especially important. Similarities between the two sets of results support the notion of the general similarity between discrete and continuous DPPs.⁵

We compared the modeled modulation spectrum with the measured modulation spectrum obtained by Mr. Terrence Kessler and Dr. Hu Huang for a ZPP configuration they selected.¹² The configuration they proposed involved the illumination of twelve circular areas distributed along a square lattice within the full circular aperture [Fig. 6(a)]. Visually, the modeled and measured amplitude spectra matched very well over all but the first small peak at the low end of the spatial frequency spectrum [Fig. 6(b)]. The spectral effects of the focal spot envelope and perhaps other characteristics unique to continuous DPP's are present in the measured spectrum at the low end. The modeled spectrum is of the speckle modulation function alone, while the speckle and the envelope of the measured spatial-frequency spectrum cannot be separated in a similarly well-defined way.

Nevertheless, for our purposes, a matched-pair t-distribution hypothesis test and the associated confidence intervals effectively demonstrate the model's predictive powers. The conditions for applying this test are met: the sample is random, as previously mentioned; the



(a)



(b)

Fig. 6. (a) The 12-circle configuration of the ZPP. (b) The corresponding modeled amplitude spectrum in blue, the measured power spectrum in green, and the full-aperture power spectrum in red for comparison.

standard deviations of the error are unknown; internal independence is assured, as points in either the data set or the model are individually calculated and do not interfere with each other; the model and the data set are dependent, because they vary non-randomly and operate off a similar set of principles; and a sample size of 100 data points is large enough to assume a

normal-like distribution of the mean difference values.

The null hypothesis for the test is that the difference between the model and the data is zero, or insignificant; naturally, the alternative hypothesis is that they are not equal. The calculated sample mean difference and associated sample standard deviation are 0.01694 and 0.1788 respectively. From this we attain a P-value of 0.9247 for a t-distribution of sample size 100, which allows us to fail to reject the null hypothesis at a significance level of 0.05. Based on this test, we can say with 95% confidence that the true mean difference lies between -0.03378 and 0.03717. Performing similar operations for the mean percent difference, we calculated the sample mean percent difference, 2.928; the sample standard deviation, 24.71; the P-value, 0.2411; and a 95% confidence interval for the true mean percent difference between -1.999 and 7.856. Once again, we fail to reject the null hypothesis. Thus, there is significant evidence indicating that the model suitably predicts the behavior of continuous DPPs.

6. OPTIMIZING THE CONFIGURATION

With the verified model, it is possible to move towards the ultimate goal: optimizing ZPP configurations to reduce harmful spatial frequencies. Initial attempts consisted of simple trial-and-error designs, with new configurations based on intuition and basic calculations. Generally, we looked for configurations where elements of picket illumination are as far apart as possible, because if the q 's between elements are generally made larger, the smaller, most harmful K frequencies are present to a reduced degree. Beyond that, there were no other criteria. Next, we implemented a different method of optimization known as “simulated annealing.”¹³ The idea behind the method is to make a small change to the configuration, then evaluate the resulting change in the power spectrum, and then decide whether or not to keep or reject the change. A subtlety of this standard method is that there is an adjustable probability, rather than a certainty, that favorable changes are accepted and unfavorable changes are rejected. This process is iterated many hundreds of times. The purpose of having a probability, rather than a certainty, of keeping or rejecting favorable or unfavorable changes, respectively, is to allow the annealing process to escape from so-called “local peaks” -- where harmful frequencies are minimized with respect to any immediate small change, but where continuing the search slightly further afield would find a more favorable minimization of the harmful frequencies.

Although the results of this calculation were very preliminary, we did learn something interesting and not altogether surprising: the most ideal configurations tended to have the picket pulse illuminate small, circular, radially distributed areas. More investigation is necessary, but this at least provides a starting point.

7. CONCLUSION

The discrete DPP models appear to satisfactorily predict the behavior of continuous DPPs used on OMEGA and the NIF. This can be particularly helpful in the study of two-state focal zooming and the search for an optimal picket pulse illumination. By distributing the illumination in an optimum fashion, harmful spatial frequencies can be reduced, and the energy lost due to CBET as a result of plasma perturbations can be minimized. The optimization process itself can be automated through “simulated annealing,” which has already shown favorable preliminary results, even if the idea has not been thoroughly developed. Ultimately, this leaves another avenue of exploration for increased energy deposition -- a necessary development to achieve ignition.

8. ACKNOWLEDGEMENTS

I would like to thank my advisor Dr. Reuben Epstein, who was invaluable in my research and simulation development. Without him and his guidance, nothing could have come out as cleanly as it did, and my understanding of the project as a whole would not be possible. I would also like to thank Dr. Stephen Craxton, the director of the Summer High School Internship Program, as well as the whole of the Laboratory for Laser Energetics and the University of Rochester, for the opportunity to conduct research and experience work in science. For their contributions to my work, I would like to thank Dr. Dustin Froula, Mr. Terrence Kessler, and Dr. Hu Huang, who shared their DPP speckle spectrum measurements with me and who helped my work come together, particularly in the final weeks. Additionally, I would like to thank my fellow summer interns, who provided a network of support for those times when my progress was slow and who gave feedback on my work and presentation skills. Finally, I would be remiss if I didn't thank the entire staff of the Laboratory for Laser Energetics, who provided their help in less direct, but no less invaluable ways.

REFERENCES

1. J. Nuckolls, L. Wood, A. Theissen, and G. Zimmerman, *Nature (London)* **239**, 139 (1972); S. Atzeni and J. Meyer-ter-Vehn, *The Physics of Inertial Fusion*, (Clarendon Press, Oxford, 2004).
2. Y. Kato and K. Mima, *Appl. Phys. B* **29**, 186 (1982).
3. Laboratory for Laser Energetics LLE Review 33, NTIS Document No. DOE/DP/40200-65, 1987 (unpublished), p. 1.
4. Laboratory for Laser Energetics LLE Review 63, NTIS Document No. DOE/SF/19460-91, 1995 (unpublished), p. 126.
5. J. Kandlikar, 1999 Summer Research Program for High School Juniors at the University of Rochester's Laboratory for Laser Energetics—Student Research Reports, 1996 (unpublished).
6. I. V. Igumenshchev et al. *Phys. Plasmas* **19**, 056314 (2012); C. J. Randall, J. R. Albritton, and J. J. Thompson, *Phys. Fluids* **24**, 1474 (1981).
7. I. V. Igumenshchev, D. H. Edgell, V. N. Goncharov, J. A. Delettrez, A. V. Maximov, J. F. Myatt, W. Seka, A. Shvydky, S. Skupsky, and C. Stoeckl, *Phys. Plasmas* **17**, 122708 (2010); W. L. Kruer, *The Physics of Laser Plasma Interactions* (Addison-Wesley, Redwood City, CA, 1988).
8. I. V. Igumenshchev et al. *Phys. Rev. Lett.* **110**, 145001 (2013).
9. D. H. Froula, T. J. Kessler, I. V. Igumenshchev, R. Betti, V. N. Goncharov, H. Huang, S. X. Hu, E. Hill, J. H. Kelly, D. D. Meyerhofer, A. Shvydky, and J. D. Zuegel, *Phys. Plasmas* **20**, 082704 (2013).
10. Y. Kato, K. Mima, N. Miyanaga, S. Arinaga, Y. Kitagawa, M. Nakatsuka, and C. Yamanaka, *Phys. Rev. Lett.* **53**, 1057 (1984).
11. R. Epstein, *J. Appl. Phys.* **82**, 2123-2139 (1997).
12. T. Kessler and H. Huang, private communication.
13. W. H. Press et al., *Numerical Recipes*, (Cambridge University Press, Cambridge, 1986), §10.9.

Modeling and Controlling Electron Movement in a Ballistic Deflection Transistor

Logan Toops

Webster Thomas High School

Webster, New York

Advisors: Roman Sobolewski, Yunus Akbas

Laboratory for Laser Energetics

University of Rochester

Rochester, New York

November 2013

1. Abstract

In the ideal Ballistic Deflection Transistor (BDT), electrons bounce off the walls of the transistor in a ballistic fashion, like bullets, uninterrupted by a transport medium. The BDT, operating at terahertz frequencies, is expected to far surpass the conventional transistor in speed, while utilizing very little power and generating almost no heat. Unlike the conventional transistor, where computing is achieved by starting and stopping the flow of electrons, the BDT uses inertia and an applied voltage on its walls to control the output voltages by directing electrons to their proper pathways. The MATLAB program, MEME (Modeling and Etching the Movement of Electrons), was created to simulate the motion of electrons in the ideal BDT when different voltages are applied to the walls. After the user inputs values such as channel width, number of electrons, and voltage applied to the walls into a Graphical User Interface (GUI), the program calculates the electrons' trajectories and outputs the number of electrons that entered each drain (Left, Right, North, or South). MEME can also simulate the electrons bouncing in the BDT for visual purposes.

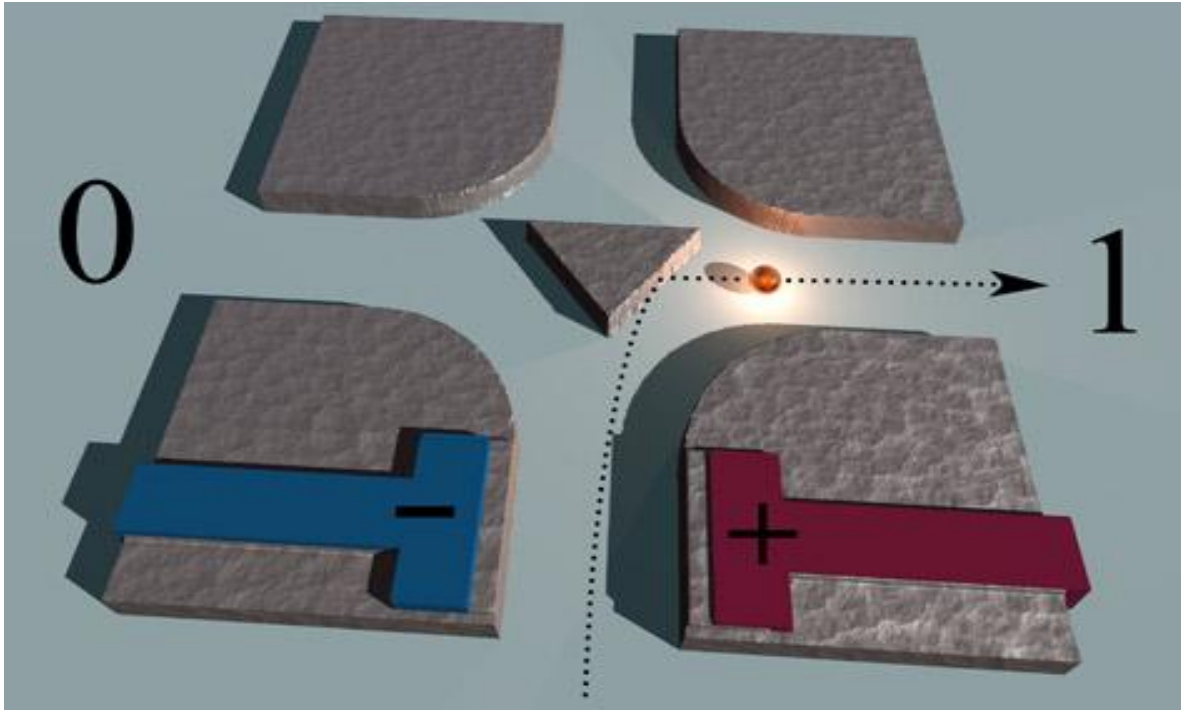


Figure 1: Simple depiction of a Ballistic Deflection Transistor

2. Introduction

Transistors are the basis of all modern day electronics. By starting and stopping the flow of electrons, transistors are able to output a 1 for the “on” state and a 0 for the “off” state. Transistors can be manufactured in the nano-scale, allowing billions of them to be placed on microchips. Computers operate by using the transistors on these microchips to complete many simple Boolean calculations with the 0 and 1 binary states. Because of the vast amount of transistors on these microchips, computers can complete very complex calculations by piecing together billions of simple calculations. Modern day transistors are made out of a semiconducting material (most often silicon) and operate at gigahertz frequencies. Despite their high reliability and small size, a fundamental flaw of modern day transistors is their inefficient use of energy, which is lost in the form of heat.

A ballistic deflection transistor (BDT, Figure 1) [1, 2] is a new type of transistor that not only uses less power and reduces the energy lost in the form of heat, but also operates at terahertz frequencies. This means that this transistor is more than 1000 times faster than conventional transistors. Also, the BDT is much more resistant to electrical noise. The BDT achieves high speeds and efficiency due to the way it uses the inertia of electrons to bounce them like billiards, as opposed to conventional transistors, which use energy to forcibly start and stop the flow of electrons. Electrons in the BDT are attracted by an upwards voltage pull as shown in Figure 1. Their trajectories are then altered by an electrical field, which is applied in the horizontal direction by the red and blue gates in Figure 1 and increases in strength as the electrons travel closer to the gates. A triangular reflector is also present in the middle of the BDT to help guide the electrons to their appropriate destination. In order for this transistor to output a 1 for the “on” state and a 0 for the “off” state, the electrons will have to enter the right drain and left drain, respectively. There are also very small chances that electrons might enter the north drain or even the south drain; however, those electrons are simply ignored (transistor loss).

In an ideal BDT, there are no scattering points in the transport medium that randomly change the electrons’ trajectories. In a realistic BDT, scattering points exist due to the atoms of the semiconductor material. However, due to the extremely small size of the BDT, scattering has relatively little effect since the mean free path of the electrons is still greater than the size of the BDT. A program called MEME (Modeling and Etching the Movement of Electrons) was created in MATLAB to model the electron trajectories in an ideal BDT and record which drain each electron passes through, ultimately aiding future researchers to test new configurations on the BDT.

3. MEME

The program MEME consists of the MATLAB files named **draw**, **geometry**, **calculate**, **plot_e**, **many_electrons**, and **random_electron**. The **draw** file allows the user to enter the starting and ending coordinates for the lines representing the BDT to be drawn. The **geometry** file uses these coordinates to plot the outline of the BDT on a grid. Solid lines are used to mark the walls and triangular reflector; dotted lines are used to mark the electric field that alters the electrons' trajectories. After the **geometry** file draws the BDT model, the **calculate** file calculates the x and y coordinates that an electron will travel in the BDT. The **calculate** file accepts the initial angle of the electron, the starting x and y coordinates of the electron, the charges placed on the gates of Figure 1, and the initial channel wall width as parameters. The **plot_e** file plots one electron on the grid, **many_electrons** plots many electrons on the grid, and **random_electron** plots an electron with a random starting point near the south drain at a random launch angle between 45 and 135 degrees relative to the horizontal axis.

4. MEME Graphical User Interface (GUI)

A GUI was created to allow for easier interaction with MEME.

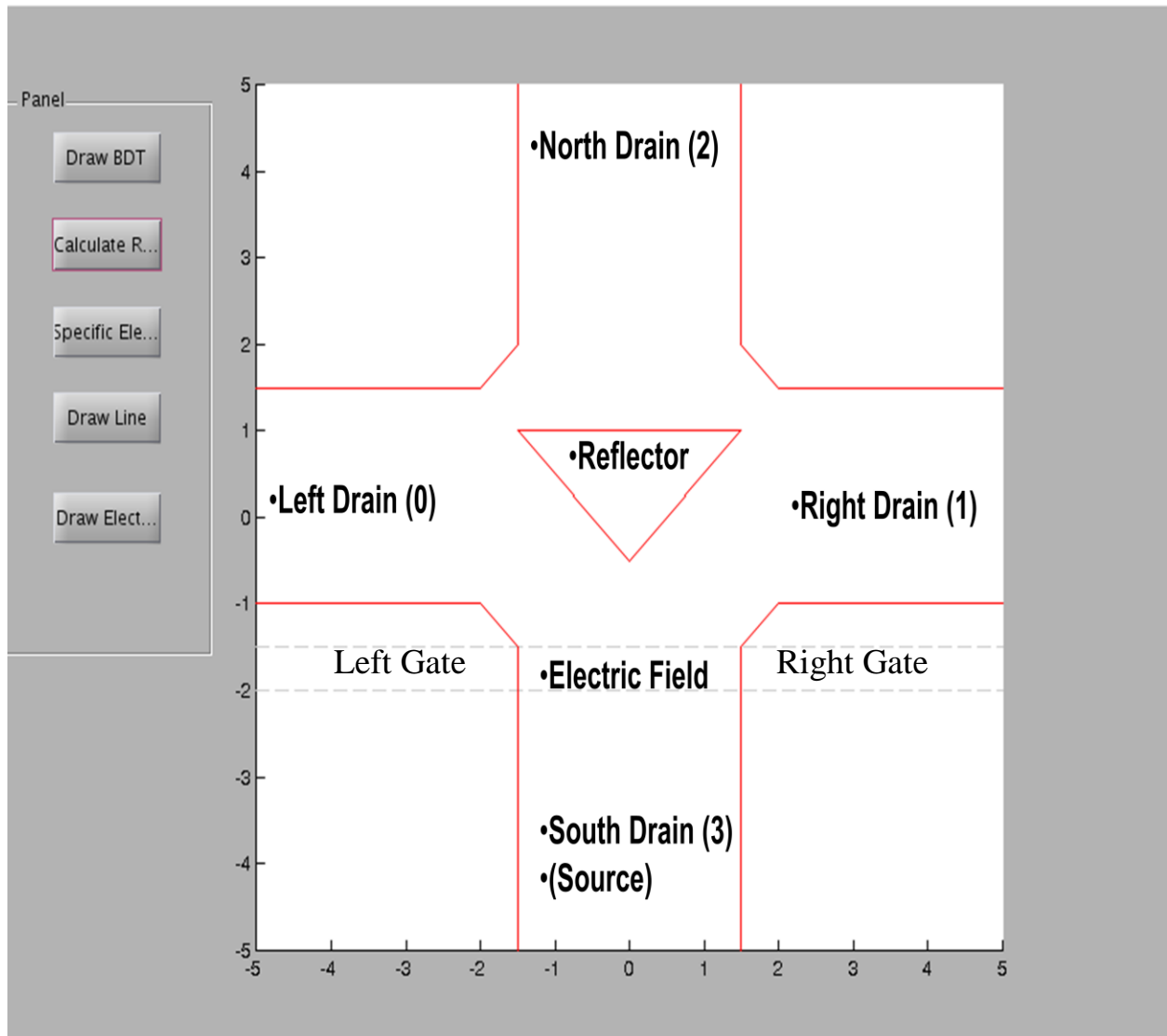


Figure 2: MEME GUI with BDT labeled (each interval represents 150 nm for the x and y axes)

The MEME GUI (Figure 3) draws a model of the BDT when the user hits the Draw BDT button. The solid red lines represent the walls of the BDT. The light gray dotted lines

represent the electric field that alters the trajectory of the electrons only when they are between the two dotted lines. Electrons are launched from the bottom, known as the source. They are then pulled upwards by a voltage as they travel through the BDT. The number representing the drain that each electron travels through is recorded and then outputted after the electron trajectories are calculated.

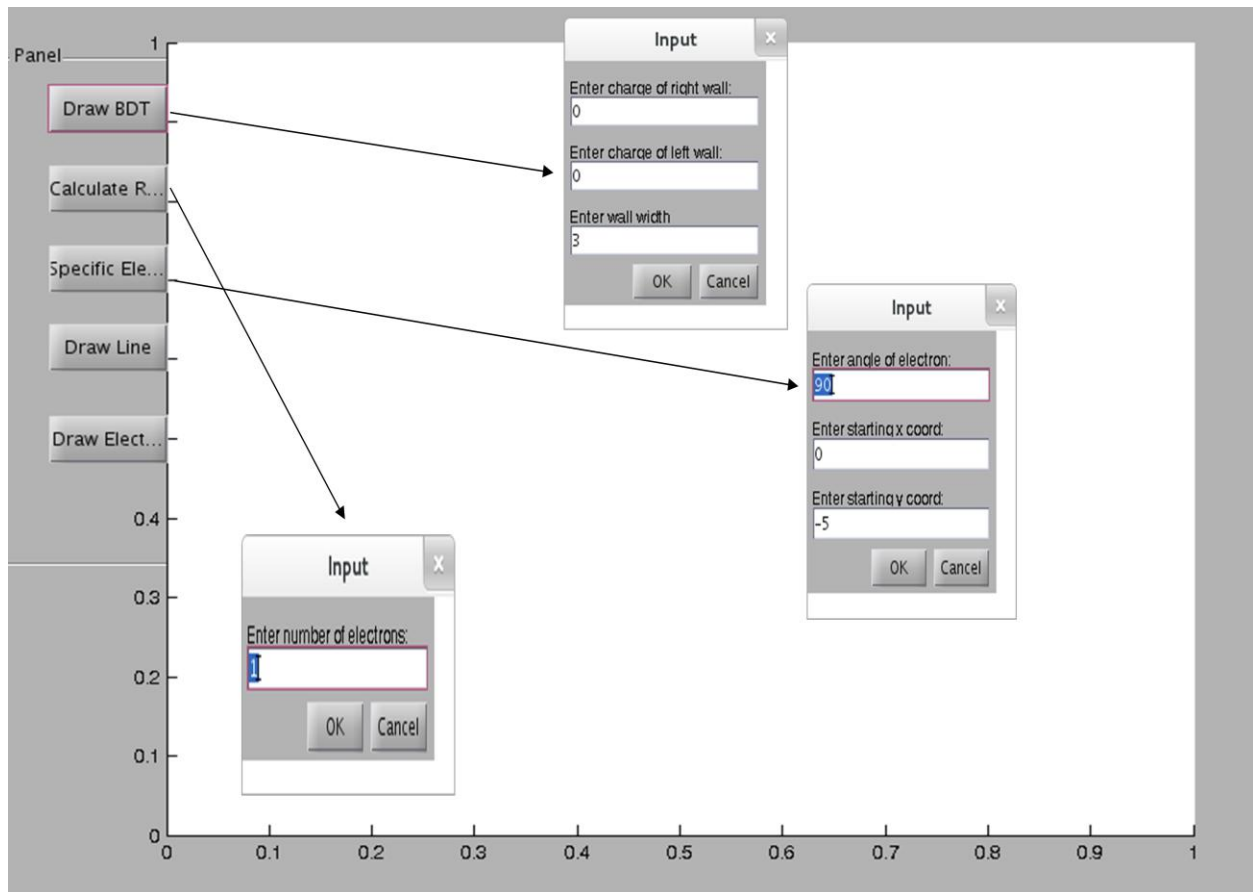


Figure 3: Popup Dialogue Boxes of the GUI

The *Draw BDT*, *Calculate R*, and *Specific Ele* buttons generate popup dialogue boxes (Figure 3) when clicked. These boxes accept the necessary parameters that the files require in order to function. The *Draw BDT* button requires the charge of the right and left walls of the electric field and the source channel wall width to be entered. The *Calculate R* button

requires the user to enter the number of randomly launched electrons to be calculated. The *Specific Ele* button requires the starting x and y coordinates as well as the launch angle of the electron. Large tests of random electrons can be run over night with the *Calculate R* button, while specific tests can be launched individually with the *Specific Ele* button.

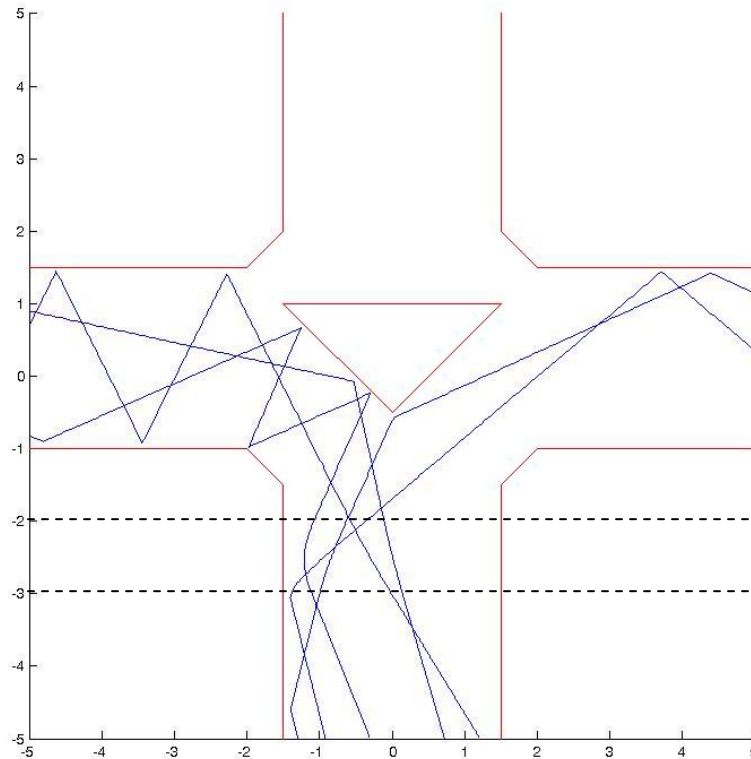


Figure 4: 5 random electrons launched with the Draw Line button (each interval represents 150 nm for the x and y axes)

Figure 4 shows a BDT that was drawn with a channel width of 3 (450 nm), a -2 charge on the left wall, and a +2 charge on the right wall using the *Draw BDT* button. The default upwards voltage was defaulted at 5. Then, 5 electrons were launched at a constant velocity of 350 nm/s and at random angles between 45 and 135 degrees using the *Calculate R* button. The *Draw Line* button was then clicked to draw blue lines representing the path that each

electron would take. The *Draw Elect* button can be clicked to animate small blue circles representing electrons bouncing in the BDT. Some of the blue electron trajectories do not exactly make contact with the walls because the electron trajectories were calculated in finite steps. Bounces were calculated when an electron was detected within a certain distance of a wall. This was done to ensure that the electrons did not skip over a wall during an iteration and tunnel through the BDT. Thus, some electrons might bounce a little before the wall, but none actually go through.

5. Sample Experiment

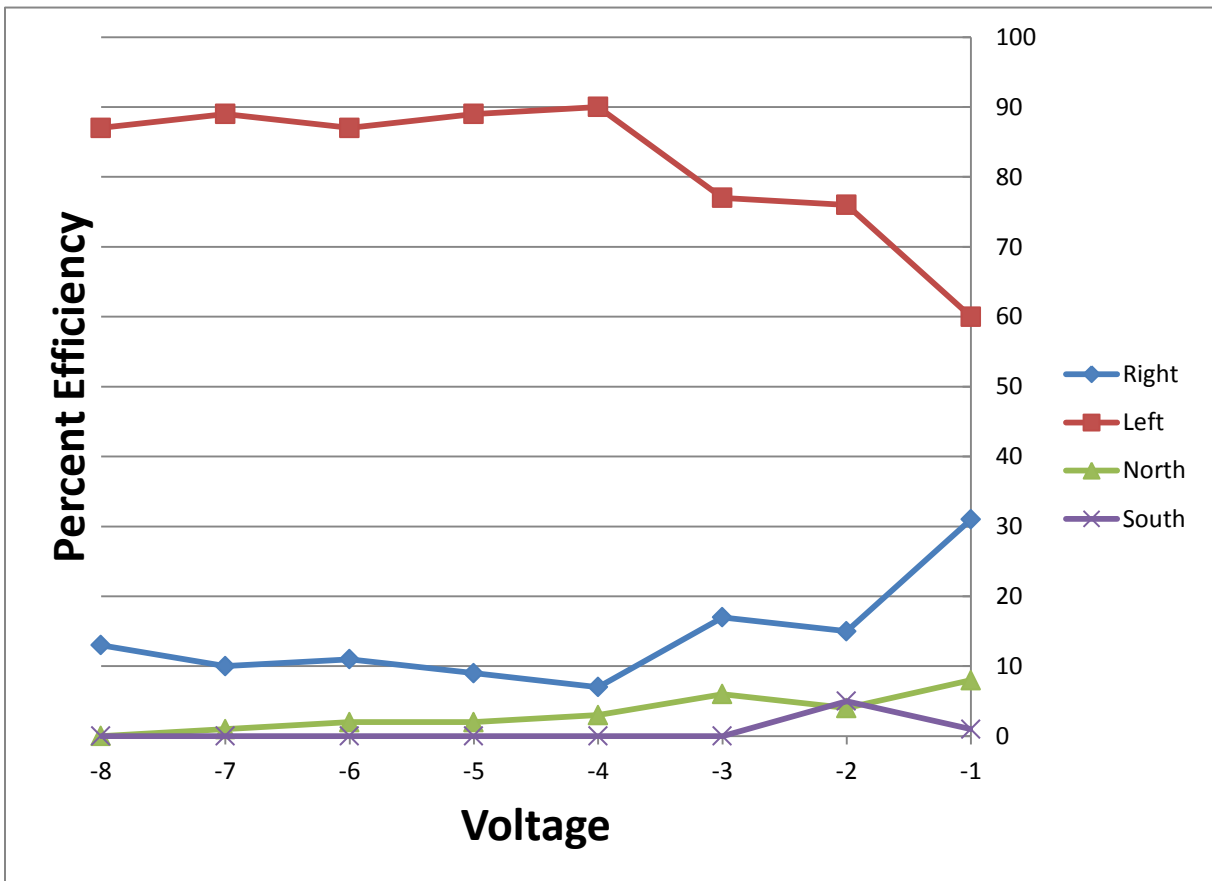


Figure 5: Percentages of electrons leaving through the right, left, north and south drains as a function of the voltage difference between the right and left gates. Samples of 100 electrons were launched in the same manner as Figure 4 with a negative voltage applied on the right gate and a positive voltage on the left gate (a voltage of -8 means that -8 volts

were applied to the right gate and +4 volts were applied on the left gate to shift the electrons to the left)

Figure 5 shows results from a sample experiment that was done to find the voltage that would produce the greatest efficiency, defined as the percentage of the electrons launched that entered the drain in the direction of the applied voltage. In Figure 5, negative voltages are applied to shift the electrons' trajectories to the left, so the efficiency is the percentage of electrons that enter the left drain (0). According to Figure 5, starting from the left, the efficiency remains relatively high until the voltage reaches -4. The efficiency then decreases because the voltage is not strong enough to shift enough of the electrons' trajectories to the designated drain.

6. Conclusion

The BDT holds many advantages over the conventional transistor. By using the electrons' inertia to bounce them through the BDT, the BDT is able to operate at terahertz frequencies and generate much less heat than the conventional transistor. The MATLAB program MEME was written to model electrons bouncing in the BDT and allow a user to change the shape of the BDT, gate size, and electric field strength as necessary. MEME will help future researchers working on the BDT to run experiments to determine what effects new configurations will have on the BDT's performance.

7. Acknowledgments

I would like to thank Dr. Stephen Craxton, the Laboratory for Laser Energetics, and the University of Rochester for giving me the opportunity to experience cutting edge research in high school. Without the invaluable work of Dr. Craxton, the high school program that I participated in would not exist. I would also like to thank my mentors, Dr. Roman

Sobolewski and Yunus Akbas, for the project they gave me and for their guidance. In addition, I would like to thank my fellow intern and research partner, Aaron Appelle, for the many weeks he devoted to working on our program, MEME. Finally, I would like to thank Ian Gabalski for his notable contribution to MEME, the other high school interns for providing a great environment to work in, and the US Army Research Office High School Apprenticeship Program for providing financial support.

8. References

1. Irie, Hiroshi. *Ballistic Electron Transport in Nanoscale Three-Branch Junctions*. Thesis. University of Rochester, 2010. N.p.: n.p., n.d. Print.
2. Sherwood, Jonathan. "Radical 'Ballistic Computing' Chip Bounces Electrons Like Billiards." *Radical 'Ballistic Computing' Chip Bounces Electrons Like Billiards : Rochester News*. University of Rochester, 16 Aug. 2006. Web. 02 Mar. 2014.

Thermodynamics of the Solid-Liquid Phase Boundary of Deuterium

Erin Wang

Brighton High School
Rochester, NY

Advisor: Dr. David Harding

Laboratory for Laser Energetics
University of Rochester
Rochester, NY
November 2013

Abstract

Cryogenic targets used for inertial confinement fusion experiments contain a deuterium-tritium (DT) ice layer that begins to melt when the protective shroud is removed to implode the target. Heat (from ambient radiation) absorbed in the plastic shell creates a “slush” (partially melted) region at the plastic/ice interface that expands with time to encompass the entire DT fuel layer. The increasing fraction of the lower-density liquid in this slush region generates a volumetric expansion that buckles the surface of the ice layer making it less hydrodynamically stable when imploded. Little is known of the early-time response of the target to this heat load and whether this behavior is important for the brief time lapses used for current and future ICF targets (0.1 s and up to 5 s, respectively).

The experiments performed here applied a controlled heat load to deuterium ice inside a calorimetry cell and measured how the energy was partitioned between melting the ice and raising the temperature of the liquid fraction in the region. A 0.62 mg sample of deuterium ice (equivalent to a 270 μm thick ice layer in an ignition target) at a temperature marginally below the triple point of D_2 (18.733 K) was heated at different rates. It was determined that ~ 20 μm of the 270 μm ice layer would melt with 5 seconds of exposure to a blackbody radiation load that a NIF target would see. Most (90 to 95%) of the heat was expended melting the ice; the remainder was used to raise the temperature of the liquid. These data quantify the importance of minimizing the time the target is exposed to ambient radiation.

1. Introduction

Inertial confinement fusion (ICF) target designs for fusion experiments are shown in Fig.1 for three different laser drivers. The targets for OMEGA and the National Ignition Facility (NIF) consist of a hard plastic shell, an inner shell of solid deuterium-tritium (DT), and a central core of DT gas. The NIF target is larger and contains more DT fuel than the OMEGA target, in proportion to the relative power of the lasers. This target is designed to achieve ignition at the NIF. The third type of target is proposed for inertial fusion energy (IFE) and adds a low-density foam layer filled with solid DT.

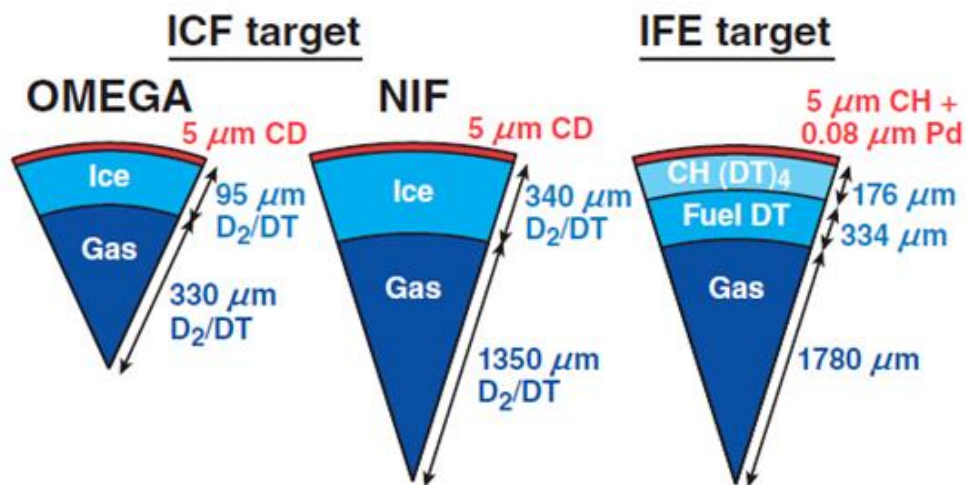


Fig. 1. Design of cryogenic targets for use at OMEGA and the NIF, and a possible future IFE target.

Cryogenic targets for OMEGA and NIF ICF experiments contain a DT ice layer that will rapidly warm up when the targets are exposed to ambient blackbody radiation before the implosion. The radiant energy is absorbed in the outer plastic capsule causing the temperature of the D_2 ice closest to the plastic to rise faster than the inner surface of the ice layer. (For reference, the temperature of a DT target rises at a rate of ~ 0.077 K/s based on the heat capacity

of the solid and volumetric heating from tritium decay, without any radiative heating, and the target fully melts in 250 s.) Once the temperature reaches the triple point value for deuterium the ice begins to melt. Importantly, over the time period that is relevant to ICF targets (0.1 s and 5 s for OMEGA and NIF targets, respectively), only the ice nearest to the plastic melts before the target is imploded.¹ However, because the heat that continues to be deposited in the plastic during that period will both flow to the cooler inner surface of the ice layer and also be consumed melting the ice (and raising the temperature of the liquid), it is unclear how much ice will melt.

An example of this phenomenon is shown in Fig. 2 for an IFE target that will experience a sizeable heat load during the 0.05 s it is inside a fusion reactor before it is imploded.² The lower density of the liquid (0.18 gm/cm³ for liquid D₂ compared to 0.2 gm/cm³ for the solid D₂ used in these experiments; DT liquid and solid used in fusion targets have proportionally higher densities) generates a volumetric expansion stress that will buckle the inner surface of the ice layer rather than the plastic (which is significantly stiffer than the ice and better resists the applied stress). The magnitude of buckling will be proportional to the extent of melting.

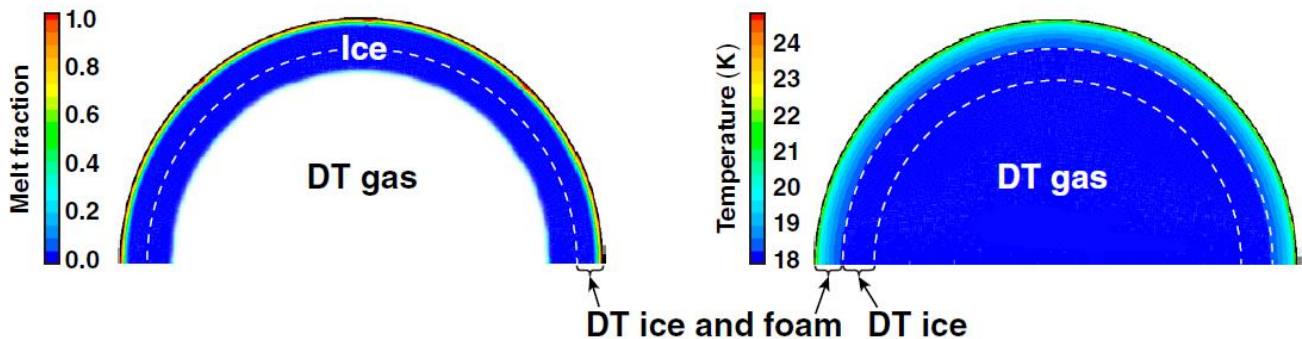


Fig. 2. The melt fraction (a) and temperature (b) of an IFE target calculated for a heat load of 50 kW/m² at the surface of the target. The diameter of the target is 4.5 mm and the thickness of the ice layer is 0.35 mm. After 0.05 s the outer portion of the ice layer has completely melted while the temperature of the inner ice surface is unchanged.

The calculated effects of ambient radiation on an OMEGA target (5- μm plastic ablator and a 100- μm D_2 ice layer)¹ are shown in Fig. 3. The temperature of the ice at the outer surface rose from an initial value of 17.0 K to the triple point value in 0.05 s (Fig. 3a). After 0.1 s, 2.4% of the ice closest to the plastic wall has melted. (Fig. 3b) The limitation with this calculation is the uncertainty of how to partition the available energy between melting the ice and flowing to the internal surface of the ice layer where it sublimates the ice.

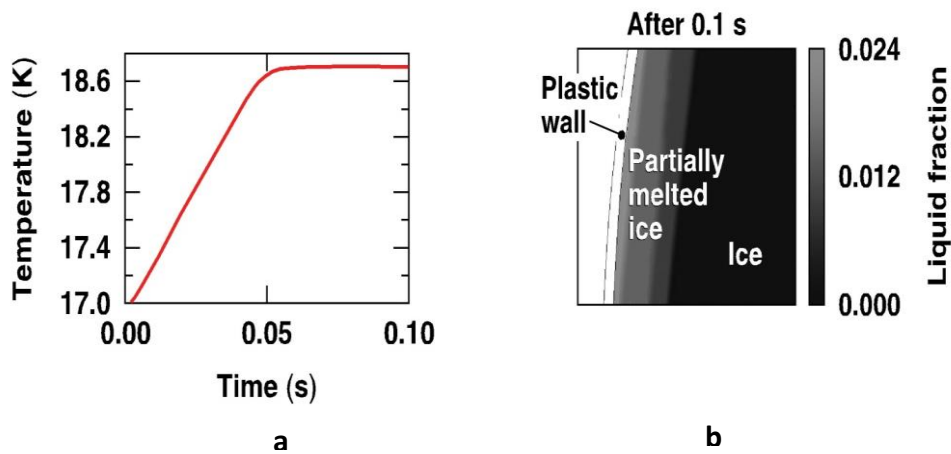


Figure 3. (a) Time-dependent temperature of the outer surface of the ice layer and the (b) liquid fraction in the ice layer after 0.1 s.

The roughness of the target's DT ice surface is measured prior to retracting the protective shroud, but not after the shroud is retracted: no diagnostic is available that can evaluate the target's roughness with sufficient resolution at the center of a 6-m diameter vacuum chamber in the brief time before it is exploded. The roughness that develops in that intervening period will create hydrodynamic instabilities that cause the target to break up and reduce the pressure in the hot spot. That roughness value needs to be inferred from experiments that can separately

quantify each of the possible causes for roughness. The data obtained here are a necessary first step to implement accurate experimental corrections to improve target uniformity.

2. Experimental Methods

2.1. The calorimetry cell

The goal of this experiment was to demonstrate that a calorimetry cell containing an amount of D_2 comparable to that found in an ICF target could be used to measure how rapidly the D_2 ice responded when heated above the melting temperature. A calorimetry cell works by applying a known amount of heat to a thermally isolated system and measuring the resulting change in temperature. The rate at which the temperature of an empty cell changes with time is determined by the heat capacity of the materials (which is well known) and the amount of heat applied. Adding D_2 to the cell slows the rate at which the temperature changes as additional heat is needed to compensate for the heat capacity (C_p) of D_2 . That rate slows further when the temperature reaches the ice's freezing temperature (18.73 K; heat of fusion is 199 J/mol). The feasibility of this concept was demonstrated in earlier experiments where the calorimetry cell had a heater and temperature sensor connected directly to the cell.³ However, that design lacked the ability to provide small heat loads needed to replicate the heating of a target and the sensitivity needed to measure small differences in the rate of temperature rise between a D_2 -filled and empty cell when a small quantity of D_2 (such as the amount present in an ICF target) was used.

The earlier calorimetry cell was redesigned for these experiments to be smaller (to lower the C_p of the cell) and to better control the small amount of heat that needed to be applied; heaters that are large enough to balance the multi-watt cooling power of the cold head lack the

precision to provide sub-milli-watt level control of the output; and applying too much heat will melt the ice too rapidly to diagnose the melting process.

Images of the cell are shown in Fig. 4 and the design concept is shown in Fig. 5. The cell consisted of a copper cube (1.22 cm³ volume; weighing 24.87 gm) with a cylindrical hole through the vertical axis. Sapphire windows (3.2 gm) on the top and bottom of the cell were attached to the copper cell with steel flanges (3.68 gm) to form a vacuum-tight seal. The cell was connected by a thin wire (10 cm x 1.6 mm diameter) to a copper mass that functioned as a thermal reservoir. D₂ gas was added to the cell through a thin-wall narrow diameter steel tube that was connected to a gas manifold. The steel tube was attached (via a copper wire) to the first stage of a cold head (35 K) to intercept heat flowing from the gas manifold (at room temperature) to the cell.

A heater connected to the reservoir controlled the temperature of the entire system; heat flowed from the cell to the reservoir down the single copper wire. The reservoir was connected to a cold head (CryoMech), which was maintained at 12 K and functioned as a heat sink for the calorimetry cell. One temperature sensor was attached to the cell and a second sensor was attached to the reservoir. The sensor was sensitive enough to detect 0.001 K changes in temperature. A test of the sensitivity of the cell to small temperature changes was to switch the room lights off, which (Fig. 6) registered a 0.001 K decrease in temperature, followed by a 0.001 K increase when the light were switched on. A more extreme test was to switch on a blue LED beneath the cell (set to 4 V), as a result of which the calorimetry cell recorded a 0.005 K change in temperature.

The entire cell was contained within a vacuum-sealed copper radiation shield and the viewing windows were insulated with 3-mm thick gold-coated infrared radiation absorbent glass.

The calorimetry cell was sufficiently isolated from ambient radiation that it could detect heat changes as small as 0.0002 J.

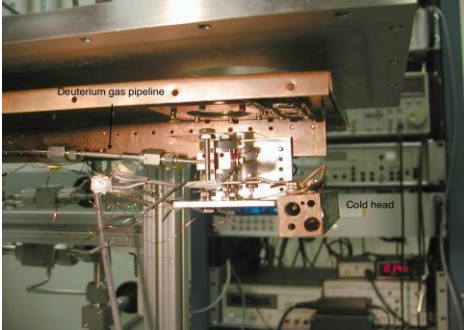


Fig. 4a. Side view of calorimetry cell. Deuterium is fed through a pipeline into the cell. The thermal reservoir is visible in this photo.

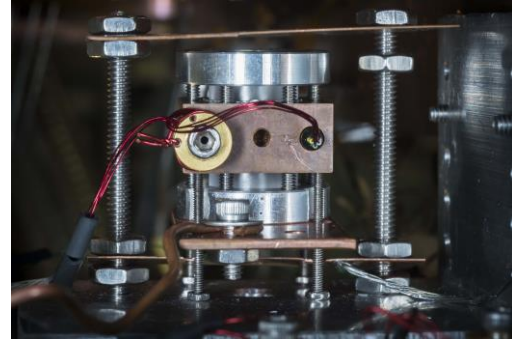


Fig. 4b. Front view of calorimetry cell. Deuterium contained within the chamber is heated by a wire running between the cell and heat reservoir.

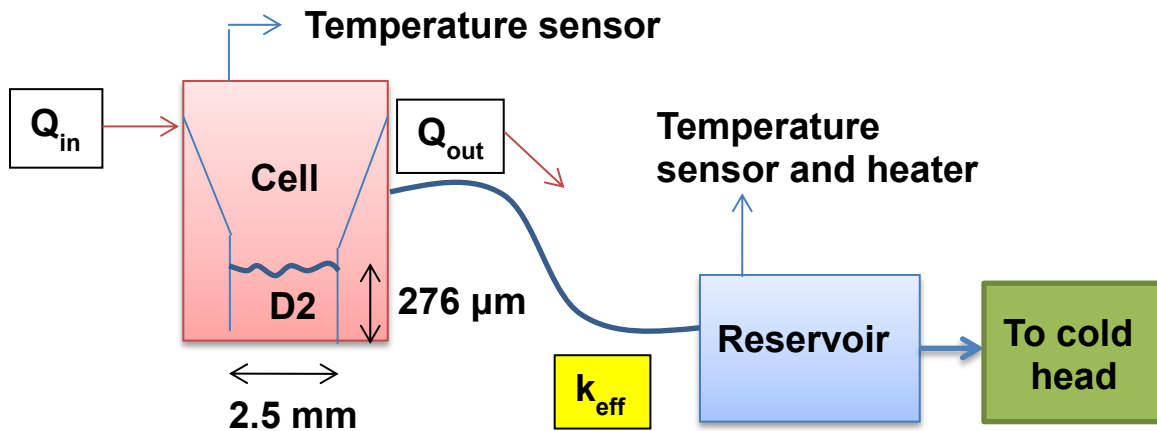


Fig. 5. Schematic diagram of calorimetry cell. Temperature sensors located in the cell and reservoir measure changes in temperature that allow the thermal conductivity (k) of the wire connecting the cell and reservoir to be calculated. Q_{in} represents the heat load into the cell from radiation and thermal conduction sources and, in steady state, balances the heat load Q_{out} conducted, through the wire, out of the cell.

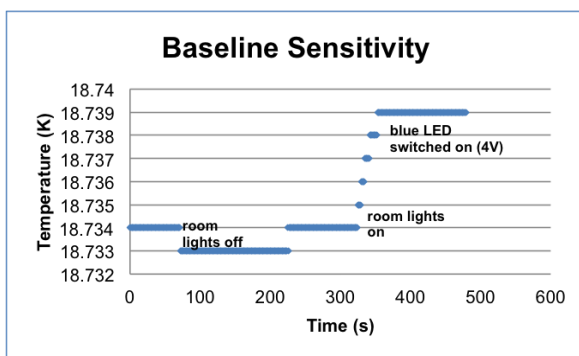


Fig. 6. The sensitivity of the calorimetry cell is demonstrated by switching the room lights on and off to produce a 0.001 K temperature change. Activating the blue LED that can be used to view the ice layer (but was not done in these experiments) increased the temperature by 0.005 K.

When the cell temperature was ~ 19 K the valve separating the gas manifold and cell was opened and a controlled amount of D_2 condensed inside the cell. The deuterium formed a 2.5-mm diameter and ~ 270 - μm high cylinder at the bottom of the cell. The base of the D_2 liquid cylinder contacted the sapphire window and the vertical sides contacted the copper cell. Importantly, copper and sapphire are both very thermally conductive ensuring that the cell and D_2 were isothermal to within 0.001 K. Heating the cell caused the outer surface of the D_2 cylinder contacting the copper and sapphire to heat first and the internal volume of the D_2 heated more slowly. In this way the cell approximates a target with the difference that the D_2 shape is cylindrical rather than spherical.

2.2. Experimental process

For each experiment the temperature of the cell was initially below the triple point temperature of D_2 (~ 18.73 K, the unique temperature where the liquid, solid and vapor phases co-exist). At steady state conditions the temperature of the reservoir was ~ 0.4 K lower than the

temperature of the cell, and the heat load into the cell from radiation and thermal conduction sources (Q_{in} , Watts) equaled the heat load out of the cell to the reservoir (Q_{out}). (Fig. 5)

Heat was added to the cell by raising the temperature of the reservoir by a controlled amount (0.02, 0.05, 0.1 and 0.3 K) using the heater attached to the reservoir. The time required for the reservoir to reach the higher temperature value ranged from <1 to 7 s, depending upon the size of the temperature step. It is important to note that increasing the temperature of the reservoir did not cause heat to flow from the reservoir to the cell; the reservoir temperature was lower than the temperature of the cell all times. Heat flowing into the cell (Q_{in}) from external sources remained constant at all times while heat flowing out of the cell to the reservoir (Q_{out}) decreased temporarily as the temperature gradient between the cell and reservoir decreased. During that period the additional heat flow ΔQ into the cell ($\Delta Q = Q_{in} - Q_{out}$, which increased as Q_{out} decreased) raised the cell temperature, which raised the temperature gradient and caused Q_{out} to rise and ΔQ to decrease. Ultimately, a higher and stable cell temperature was achieved and the temperature gradient between the cell and reservoir returned to the original value. The time required for the cell to converge to this new higher temperature ranged from 20 to 50 s and depended upon the net heat load available to the cell (ΔQ) and the heat capacity of the cell.

The rate of change of Q_{out} determined the duration and amount of surplus energy available to heat the cell and depended on the physical dimensions and thermal conductivity of the thin copper wire (as well as the thermal resistance of the connections between the copper wire and the cell and reservoir), and the temperatures of the cell and reservoir. Previous experiments tested different lengths and thicknesses of the copper wire to provide a suitably weak thermal link between the cell and reservoir that was strong enough to cool the cell from room temperature to 18.7 K in a reasonable duration (8 h), and weak enough that the time

required for the temperature of the cell to re-establish a steady-state value would be longer than that of the reservoir (> 20 s and < 3 s, respectively).³

The first step towards calculating the amount of heat flowing into the cell was to calculate the thermal conductivity of the copper wire connecting the cell and reservoir; D_2 was not present in the cell for these experiments. The temperature of the reservoir was raised by 0.02 K. The temperatures of the cell and reservoir were recorded every second and the temperature difference (ΔT_i) for each time step (i) of duration Δt was calculated for the duration of the temperature transient until thermal equilibrium was re-established. The corresponding heat flow out of the cell during that time step, $q_{out,i}$ depends on the temperature difference and the thermal conductivity (k) of the wire (which is constant) according to Fourier's Law.

$$q_{out,i} = k * \frac{A}{l} * \Delta T_i \quad (1)$$

where A and l are the cross-sectional area and length of the wire, respectively.

The resulting heat flow available ($q_i^{available}$) to raise the temperature of the cell varied with time:

$$q_i^{available} = Q_{in} - q_{out,i} \quad (2)$$

where Q_{in} , which does not change during the experiment, is given by Fourier's law under steady-state conditions.

$$Q_{in} = k * \frac{A}{l} * (T_{cell}^{steady-state} - T_{reservoir}^{steady-state}) \quad (3)$$

The total amount of energy needed to raise the temperature of the cell, equal to the product of the heat capacity of the cell ($C_p = 0.198$ J/K) and the change in temperature of the cell ($\Delta T = T_{cell, final} - T_{cell, initial}$), was equated to the total available energy:

$$C_p \cdot \Delta T = \sum_i^N q_i^{available} \cdot \Delta t \quad (4)$$

where N is the number of time steps during the temperature transient. The thermal conductivity was calculated from equations (1) - (4).

The calculation was repeated using the ΔT values measured for each of three temperature step changes to the reservoir (0.05, 0.1 and 0.3 K, and a repeat of the 0.1 K step change). The average thermal conductivity from these five measurements was 998 ± 35 W/m/K. This thermal conductivity value is realistic; it corresponds to high purity copper wire with a RRR (residual resistance ratio) of ~ 50 , which suggests that the thermal resistance at the wire connections is not a large contributor to the overall thermal resistance. Using this value for k , the steady state heat load to the cell from radiative and conductive heat loads (which accounts for the cell being 0.387 K warmer than the reservoir) was 0.0083 W.

Figure 7 shows the measured time-dependent response of the temperature of the cell (solid red line) and the reservoir (black dotted line) when the temperature of the reservoir was increased from 18.332 to 18.352 K. The cell temperature calculated using the average thermal conductivity value obtained from all the experiments (the dashed blue line) agreed closely with the measured value. The temperature of the reservoir re-established a steady state value within 3 s of the initial temperature change, while the temperature of the cell required ~ 30 s to stabilize.

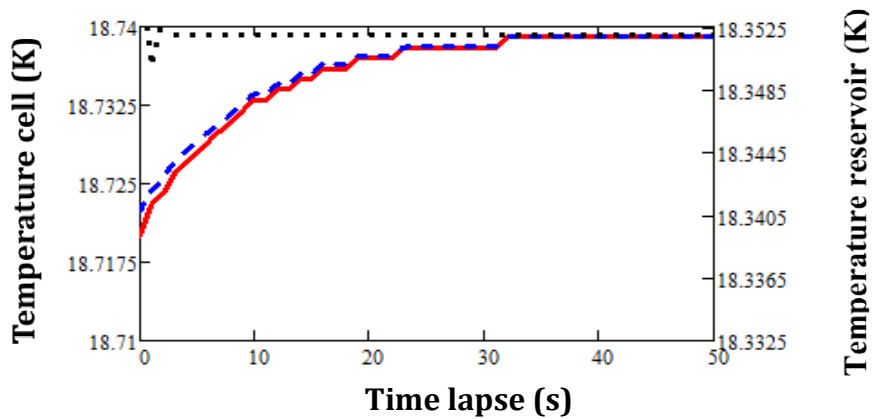


Fig. 7. Temperature profile for the cell (red solid line) and the reservoir (black dotted line) when heated by 0.02 K. The blue dashed line is the temperature of the cell calculated using the heat capacity value and the averaged thermal conductivity (derived above).

The amount of deuterium added to the cell was determined using the following protocol: D₂ gas was added to a calibrated volume (40 cm³) and gas manifold (12.7 cm³) that combined possessed a significantly larger volume than the cell (calculated to be 1.2 cm³ from the dimensions of the components). The pressure of the gas in the calibrated volume was recorded and the gas then expanded into the cell. The amount of D₂ in the cell was 0.0015 gm. The volume of the cell was calculated from the change in pressure to be 1.22 cm³, in good agreement with the value calculated from the cell's dimensions. The cell was isolated from the vacuum manifold and cooled to 18.72 K to first liquefy the gas in the cylindrical base of the cell and then solidify the liquid. The steady-state vapor pressure of the gas above the ice was calculated using the D₂ equation of state and the amount of D₂ in the gas phase was determined knowing the volume of the cell. The remaining mass was in the form of ice (0.0006 gm at 18.72 K). This mass is equivalent to the amount of fuel in a NIF direct drive ignition target with a 270 μm thick

ice layer. The surface area of the ice was calculated from the known D₂ ice mass and the dimensions of the cylindrical bore of the cell.

3. Results and Discussion

The experiments described above to measure the thermal conductivity of the copper wire were repeated with solid deuterium in the cell: the temperature of the reservoir was initially set to a value where the temperature of cell was stable at 18.72 K, and the temperature of the reservoir was then increased in 0.02, 0.05 and 0.1 K steps. The temperature of both the reservoir and cell were recorded every second. The 0.02 and 0.05 K increases did not produce a sufficiently large heat flux for long enough to melt a measurable fraction of the ice. Further, the heat load and flux were calculated to be much lower than a cryogenic target will experience before it is imploded and consequently were not of interest. The effect of a 0.1 K increase in temperature was clearer; the temperature of the deuterium-filled cell rose notably slower than it did when the cell was empty (Fig. 8) once the cell temperature reached 18.734 K, and the difference became more apparent at 18.742 K. It is important to note that the temperature of the cell was not constant while the deuterium ice was melting, rather the temperature of the copper cell and liquid continued to rise together while the remaining ice melted.

The heat flowing into the D₂ (q_i^{net}) at time step i was calculated from the difference in available heat flows between an empty cell and one filled with D₂, ($q_i^{net} = q_i^{D2_filled_cell} - q_i^{empty_cell}$). This was proportional to the temperature difference between the two cases according to Fourier's Law. (Fig. 9) The energy first raised the temperature of the solid to the melting temperature, then began to melt the ice, and finally raised the temperature of the liquid while simultaneously melting the remaining ice. Given the thinness of the ice layer (<300 μm), and the

high thermal conductivity of the ice and liquid (0.38 and 0.12 W/m/K, respectively), the temperature of the liquid was assumed to be the same as the temperature of the cell, whereas the temperature of the ice remained clamped at the triple point value.

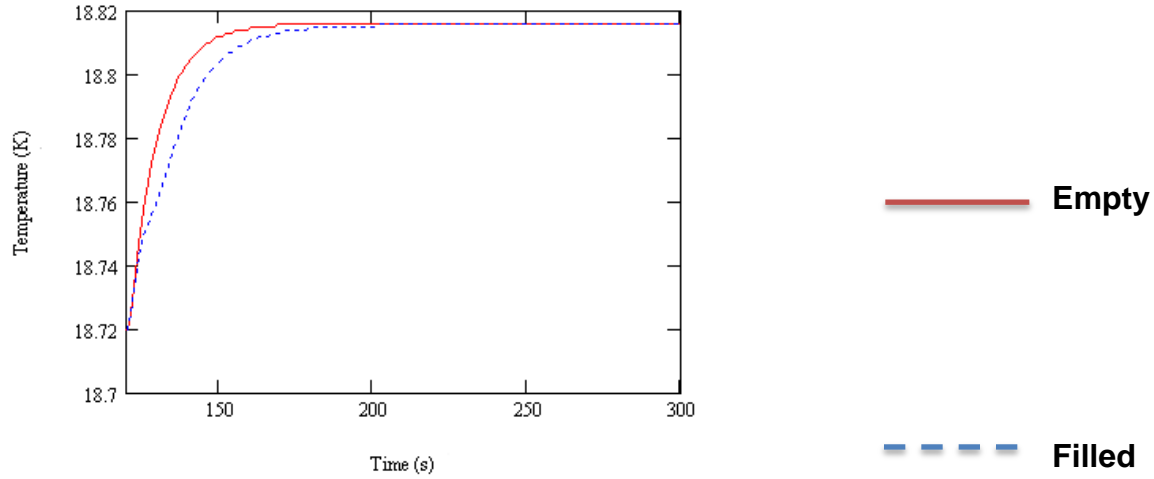


Figure 8. Temperature profiles of the cell containing D₂ (dotted blue line) and empty (red line) in response to a 0.1 K temperature increase.

Initially only ice was present in the cell so all the heat coupled into the D₂ was used to melt the ice. As liquid formed a portion of the heat was used to raise the temperature of the liquid to match the temperature of the cell. The partition of the available energy (q_i^{net}) between melting the ice ($q_i^{melting_ice}$) and heating the liquid ($q_i^{heating_liquid}$) in each time step (i) is defined by Eqn. 5.

$$q_i^{melting_ice} = q_i^{net} - C_{p_{liq}} * [(T_i^{D_2-filled} - T_{i-1}^{D_2-filled})] * m_{liq} / \Delta t \quad (5)$$

where $T_i^{D_2-filled}$ is the temperature of the D₂-filled cell at time increment i , $C_{p_{liq}}$ is the heat capacity of liquid D₂ (5472 J/kg/K), and m_{liq} is the total mass of the liquid. The mass of ice that melted ($mass_{ice_melted,i}$) in each time interval was calculated knowing the heat of fusion ($H_{fusion} = 49,500$ J/kg) from Eqn. 6.

$$mass_{ice_melted,i} = \frac{q_i^{melting_ice}}{H_{fusion}} * \Delta t \quad (6)$$

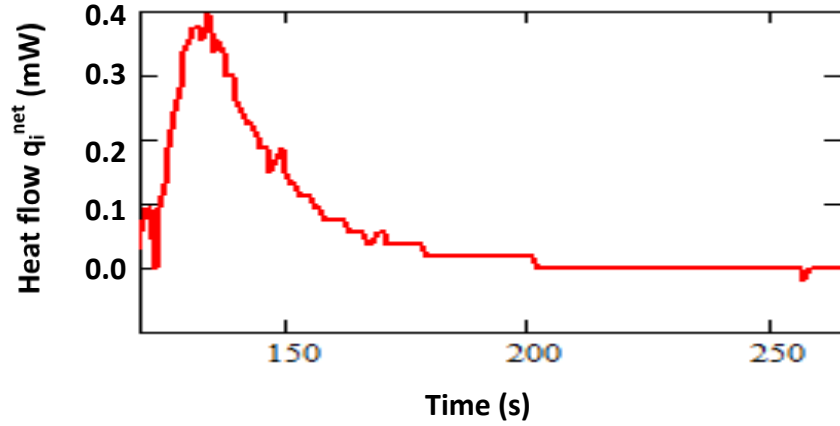


Fig. 9. The time-dependent flow of heat q_i^{net} into the cell that was available to melt the ice and heat the liquid, obtained from the temperature profiles of Fig. 8.

The greatest heat load (0.4 mW) into the D_2 ice occurred during the initial ~10 seconds after the temperature of the reservoir was raised by 0.10 K. The heat load plateaued for ~10 seconds and began to decrease as the temperature gradient between the cell and reservoir increased and the temperature of the cell stabilized. The decreasing heat load to the D_2 with time reduced the rate the ice melted: after 80 s an estimated 30% of the ice had melted and after 780 s 60% of the ice had melted. The most relevant information was obtained during the initial ~20 s when the heat load, and the corresponding heat flux (based on the surface area of the cell), were comparable to the conditions a direct drive NIF target with a reflective gold coating will experience when it is exposed to ambient radiation. The heat flux into the ice was determined by dividing q_i^{net} by the surface area of the cylinder of D_2 ice/liquid in contact with the cell walls. (Heat conduction through the vapor to the top surface of the ice cylinder that did not contact the

copper walls was neglected because the thermal conductivity of D₂ vapor is sufficiently small that heat conducted through this path will not affect the ice on the time scales studied here.) The depth and surface area of the ice/liquid were calculated from the known geometry of the cell, the amount of D₂ present, and the D₂ liquid density at 18.72 K. The heat loads into different ICF targets are displayed in Fig. 10 for comparison with the experimental values obtained for the calorimetry cell.

The fraction of heat used to melt the ice ($\frac{q_i^{melting_ice}}{q_i^{net}}$) and the resulting increase in the thickness of the liquid D₂ layer at each time increment are shown in Fig. 11. The liquid layer in this study is defined as consisting of only liquid, although in reality the liquid will exist in a much thicker ice/liquid “slush” layer, with the liquid fraction decreasing with increasing distance from the copper surface. (The amount of liquid present is reported as a 100% liquid layer because the experiment is unable to determine the thickness and composition of this “slush” region.) The data most relevant to an ICF target is the first ~20 s of the heating cycle when 90 to 95% of the incident heat load was used to melt the ice. From the maximum slope of the dotted blue line, ~4 μm of liquid D₂ is formed every second, or ~ 20 μm during a 5-s period. The conversion of a ~20-μm thick layer of ice into a liquid will increase the overall thickness of the cylindrical D₂ layer from 170 μm to 172 μm because of the lower density of the liquid. This effect in a spherical geometry will be more damaging as the difference in the radius of the outer and inner surfaces of the ice layer will cause the inner surface to buckle as well as expand, and the added roughness will affect the hydrodynamic stability of the implosion.

	Heat load (W)	Heat Flux (W/m^2)	Time exposed to the elements (s)
OMEGA	0.0006	260	0.1
NIF (no reflective coating)	0.023	670	5
NIF (gold reflective coating)	0.0003	9	5
Fusion Energy	0.3 – 1	7,000 – 25,000	0.05
This experiment	0.00045	42	15

Fig. 10. Comparison of heat load and heat fluxes experienced by the D_2 ice when the protective shrouds are removed and the target is exposed to ambient radiation. These values are compared with the values generated in this experiment.

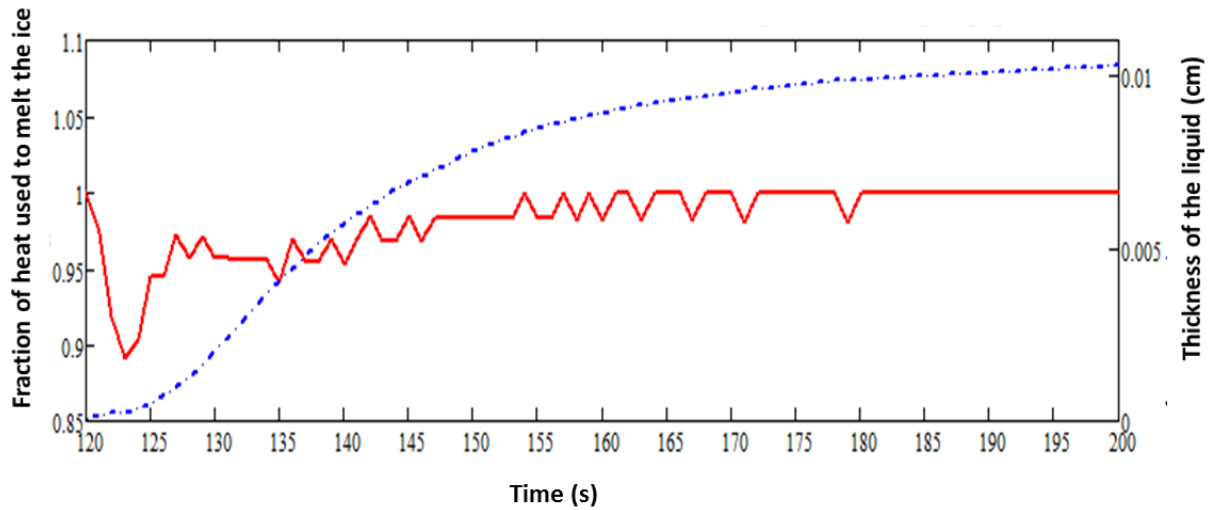


Fig. 11. The fraction of the instantaneous heat (solid red line) used to melt the ice in the experiments of figs. 8 and 9 and the corresponding equivalent thickness of the liquid layer (dotted blue line).

4. Conclusion

A cryogenic calorimetry cell was used to determine how rapidly a D₂ ice layer melts when a heat load that approximates the radiative load to a NIF target is applied to the cell. Extrapolating these results to a NIF target, it is estimated that a liquid layer, ~4- μ m thick, will form every second during the first 5 seconds of the target's exposure, and that 90 to 95% of the heat load will be used to melt the ice rather than heat the liquid or sublime the ice.

Two ways to reduce this heating effect are: (i) to decrease the length of time the target is exposed to ambient radiation, or (ii) to maintain the target at a lower initial temperature in the target chamber so that the DT ice does not melt when it warms up. The former approach will require a higher-speed shroud retraction mechanism at the NIF than is currently available, which will complicate the design of the cryogenic equipment. The second approach has more fundamental limitations as cooling the ice well below the triple point temperature compromises the quality of the ice layer, which doesn't recover when the ice subsequently warms.

Acknowledgements

I'd like to thank Dr. David Harding for guiding me through this project and making sure I not only understood what I was doing but also why it was important; Dr. R. Stephen Craxton for making this research opportunity possible; Kyle Areal-Raines for teaching me how to perform experiments with the calorimetry cell; and Eugene Kowaluk for shooting excellent photos of the calorimetry cell.

References

1. Harding, D., HAPL Meeting Atlanta GA, Feb 2004
<http://aries.ucsd.edu/HAPL/MEETINGS/0402-HAPL>
2. Bobeica, M. et. al., Fusion Engineering 2005, Twenty-First IEEE/NPS Symposium.
3. “ Heterogeneous crystal-growth seeds on interior surfaces of ICF capsule” Bernat, T.; Harding, D.; Contract # DE-NA0001369 November 1, 2013

Alignment of an Offner Triplet Radial Group Delay Compensator

Cameron Ziegler

Canandaigua Academy

Canandaigua, New York

Advisor: Seung-Whan Bahk

Laboratory for Laser Energetics

University of Rochester

Rochester, New York

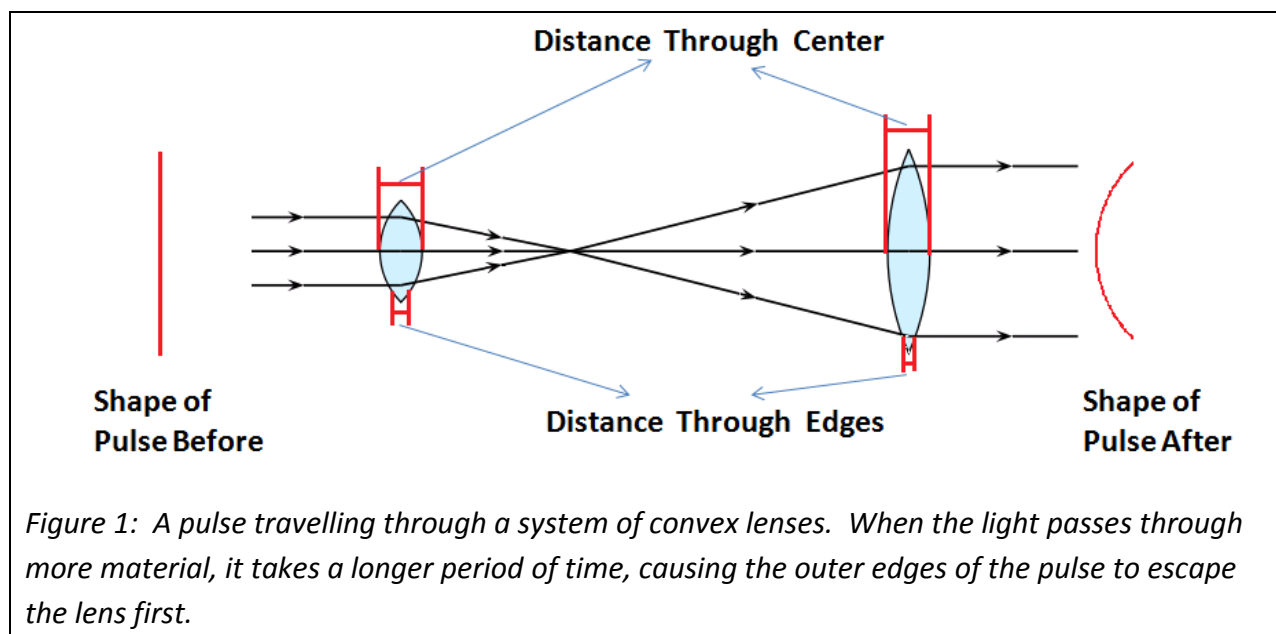
Abstract

In broadband lasers with short femtosecond pulses, radial group delay (RGD) is introduced when a laser pulse passes through traditional lens systems. With RGD, the center of the beam travels behind the edge of the beam. RGD can decrease the intensity at focus by orders of magnitude. An optical system made of an Offner triplet and a pair of negative lenses can compensate for the RGD. For cost effectiveness, the primary mirror of the Offner triplet is split into two smaller spherical mirrors. Using a ray tracing model, it was shown that these mirrors must be cophased within 4 mm. The spherical mirrors were co-phased by using a 100-nm bandwidth superluminescent laser diode with a coherence length of 4 μm . The alignment was near optimum when the light was temporally coherent and interference fringes appeared. By measuring the visibility of the fringes, it was found that the co-phasing error can be reduced to less than 3 μm , which is well within acceptable tolerances.

Introduction

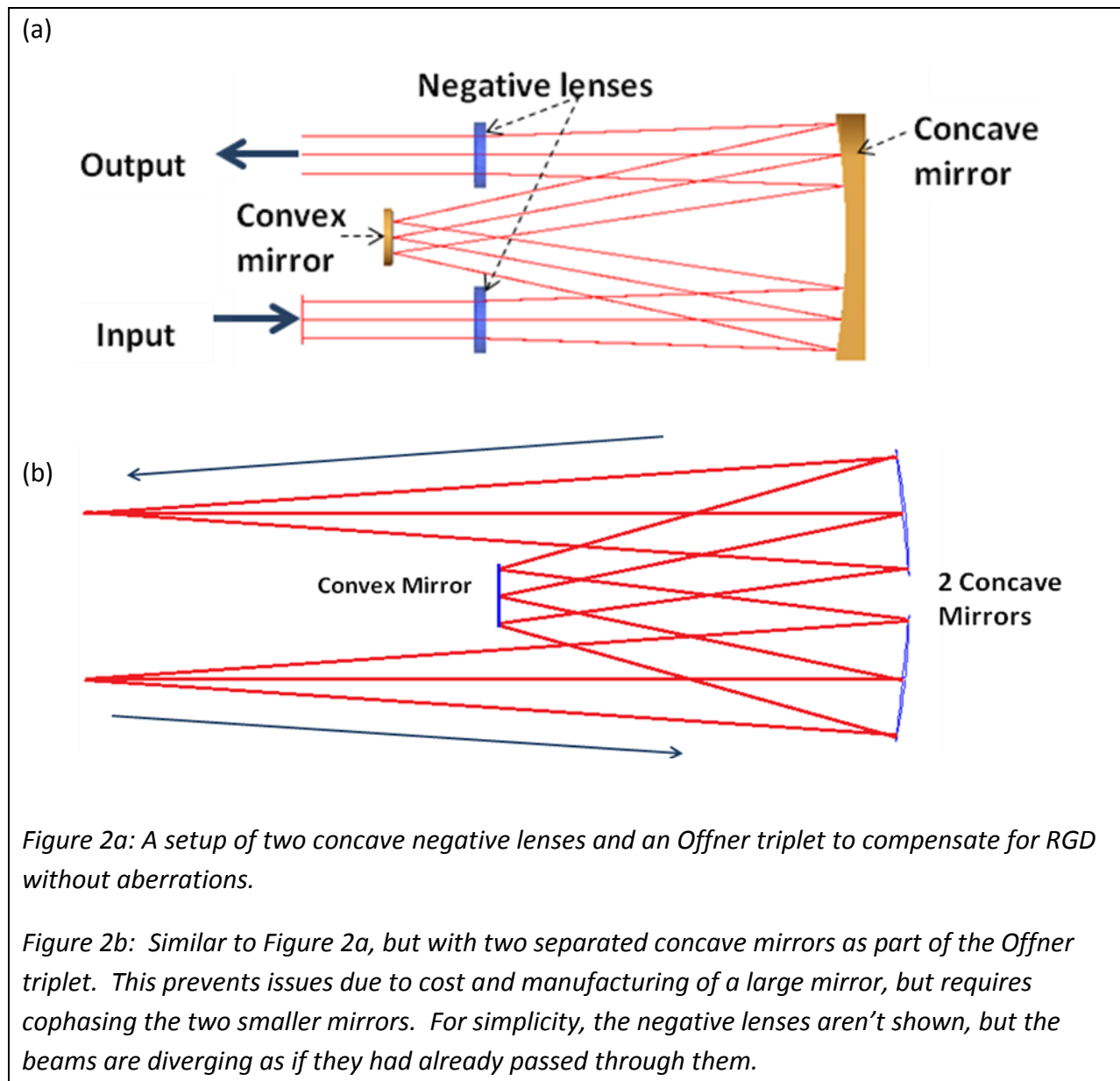
Radial group delay (RGD) is a phenomenon that occurs in optical systems that use convex lenses and pulses on the order of femtoseconds ($1 \text{ fs} = 10^{-15} \text{ s}$). RGD is illustrated in Figure 1, where a pulse of light passes through two lenses. The outer edges of the pulse travel through less material than the center of the pulse. The center of the pulse takes more time to pass through each lens, causing it to lag behind, resulting in the curved pulse shape seen in Figure 1 [1]. This time difference is small (on the order of femtoseconds), so in most optical systems, RGD is negligible. However, RGD is important when the pulse length is on the order of femtoseconds, and the effect becomes more noticeable with shorter pulses. RGD causes the

outside of the pulse to arrive on the target before the inside, reducing the intensity by orders of magnitude in some cases [2].



The MTW-OPAL laser, under construction at LLE, will use ultra-broadband pulses of lengths of only 15 fs, so RGD would impact it greatly. To compensate for RGD, a system could be constructed using an Offner triplet and two concave lenses, shown in Figure 2a. Just as convex lenses in conventional image relays cause the center of a pulse to lag behind, concave lenses, with more material near the edges, will cause the outer areas of the pulse to pass through slower, forcing the pulse back into its initial shape. However, once the collimated beam passes through a concave lens, it begins to diverge. To account for this divergence, an Offner triplet, composed of a large concave mirror and a small convex mirror, can be used to form a perfect image on another concave lens which recollimates the beam [3]. Due to the large beam size of the MTW-OPAL laser, if an Offner triplet were to be constructed, it would require a very large spherical mirror, both expensive and difficult to manufacture. Instead, two smaller spherical mirrors could be used in its place, as shown in Figure 2b. To do this requires cophasing the two

concave mirrors as if they were on the surface of the same sphere. It was assumed that the cophasing would need to be very precise to keep aberrations to a tolerable level. It was necessary to discover how much precision was required through modeling the Offner triplet and then to actually cophase the mirrors to learn how much precision could be reasonably obtained.



Set-up for Cophasing Concave Mirrors

The setup used in testing the precision of cophasing can be seen in Figure 3. In order for the two concave mirrors to be cophased properly, they must be cophased correctly in three dimensions: tip, tilt and translation, all of which can be adjusted for each mirror individually. The first two relate to the angle at which the mirror is directed while translation is simply forward or back. It is also important for the two mirrors to be at the same height; setting the height of two such mirrors is very simple. While aligning the mirrors for tip and tilt, the camera is hooked up to a monitor that displays the relative locations of the part of the beam that has been reflected off each mirror. Because of this, the mirrors can be aligned by hand for tip and tilt simply by adjusting the mirrors until the dots from each mirror overlap.

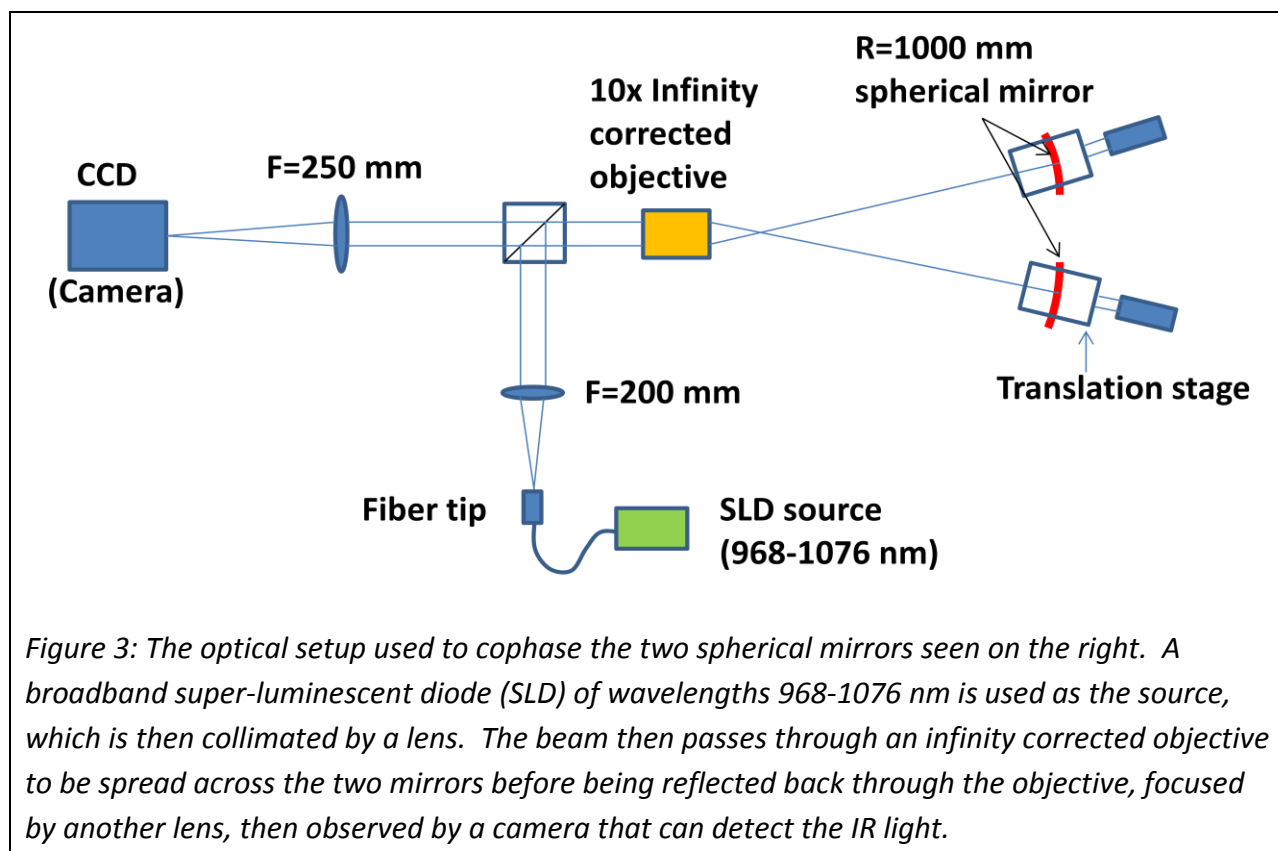


Figure 3: The optical setup used to cophase the two spherical mirrors seen on the right. A broadband super-luminescent diode (SLD) of wavelengths 968-1076 nm is used as the source, which is then collimated by a lens. The beam then passes through an infinity corrected objective to be spread across the two mirrors before being reflected back through the objective, focused by another lens, then observed by a camera that can detect the IR light.

Aligning the translation of the mirrors, however, is more difficult. It was assumed that the mirrors would have to be very precisely cophased. To achieve such precision, the beam source has a very short coherence length of only 4 μm . This means that the beam is only able to interfere with itself if the path difference between the beam reflected off one mirror and the beam reflected off the other is within only a few times the coherence length, with the most interference seen in only a 4 μm window centered around the mirrors being perfectly cophased. Therefore, the translation stages the mirrors are mounted on are adjustable to an accuracy close to a micron.

Simulation of the Offner Triplet

Using a ray tracing program in MATLAB, a model of the Offner triplet was constructed as seen in Figure 4. Because tip, tilt and height can be fairly easily adjusted for, the main goal of the simulation was to discover how far one mirror can be translated relative to the other without a significant aberration appearing in the beam. To do this, one mirror was moved out of perfect alignment a little at a time while the wavefront error was examined until the resulting wavefront error from max to min was about 0.1 waves, the acceptable tolerance. This acceptable translation of one concave mirror was found to be up to 4 mm away from perfect cophasing. The wavefront error from a perfectly aligned Offner triplet can be seen in Figure 5a, while the error in a triplet with a 4 mm translation in one concave mirror is shown in Figure 5b.

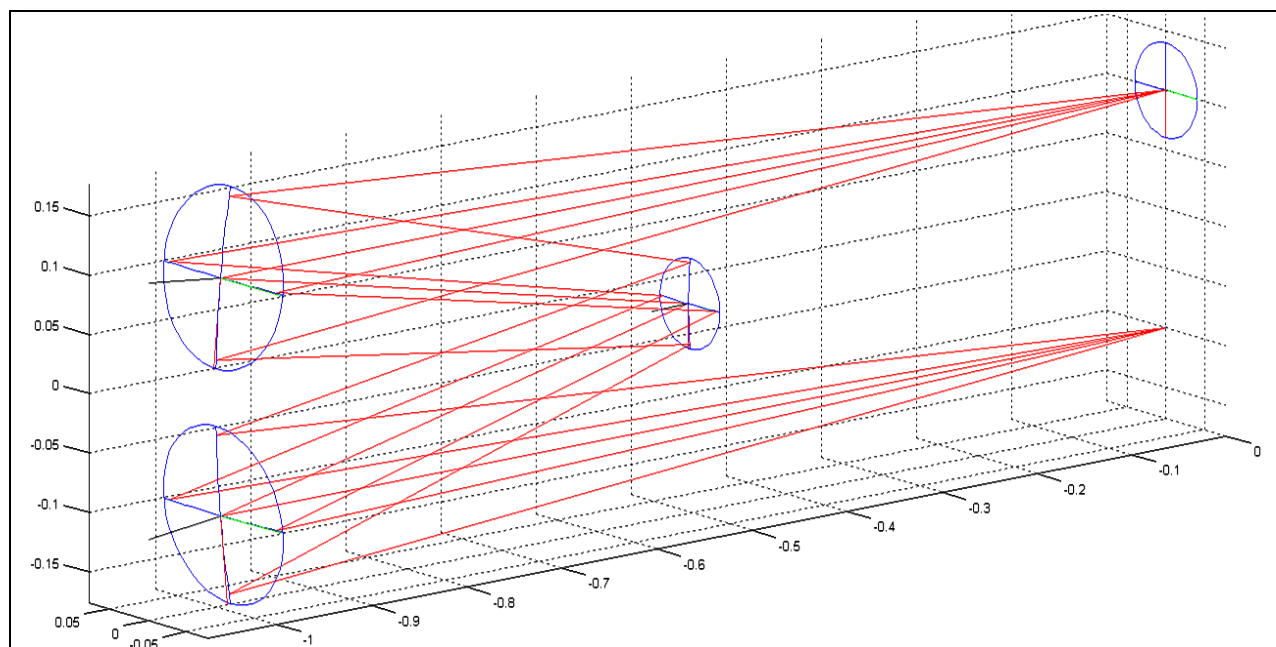


Figure 4: The model of an Offner triplet using a ray tracing program. The Offner triplet is comprised of the two concave mirrors on the left, which are initially perfectly cophased, and the center convex mirror. The detector plane is in the upper right, where the wavefront error is analyzed.

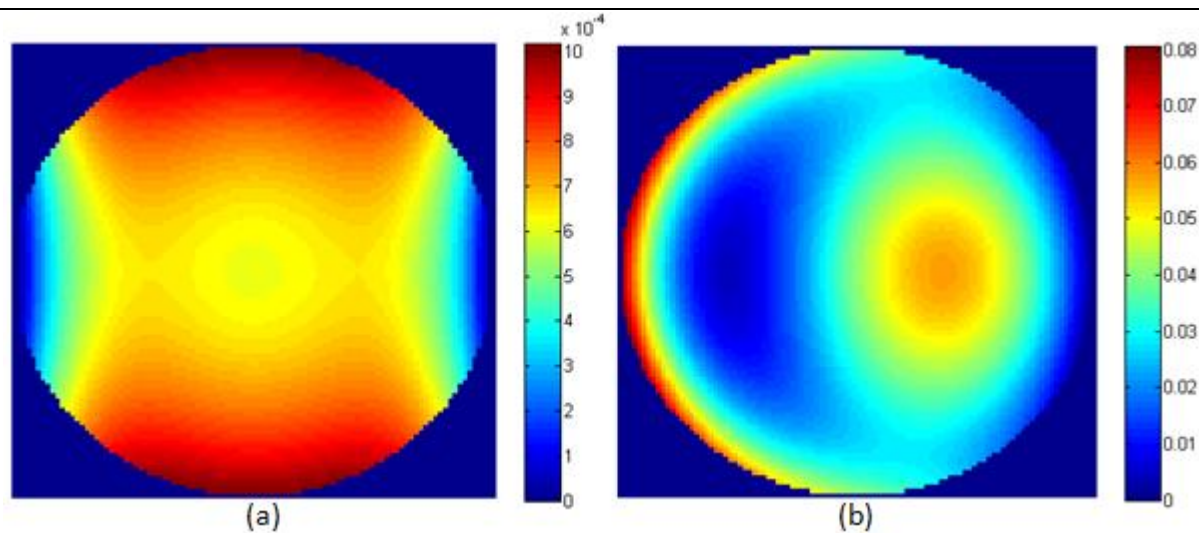


Figure 5a: The miniscule wavefront error when the concave mirrors are perfectly cophased. Note that the scale is $\times 10^{-4}$ and is measured in waves.

Figure 5b: The wavefront error when one concave mirror is translated 4 mm relative to the other, resulting in a peak to valley wavefront error of almost 0.1 waves, the acceptable tolerance.

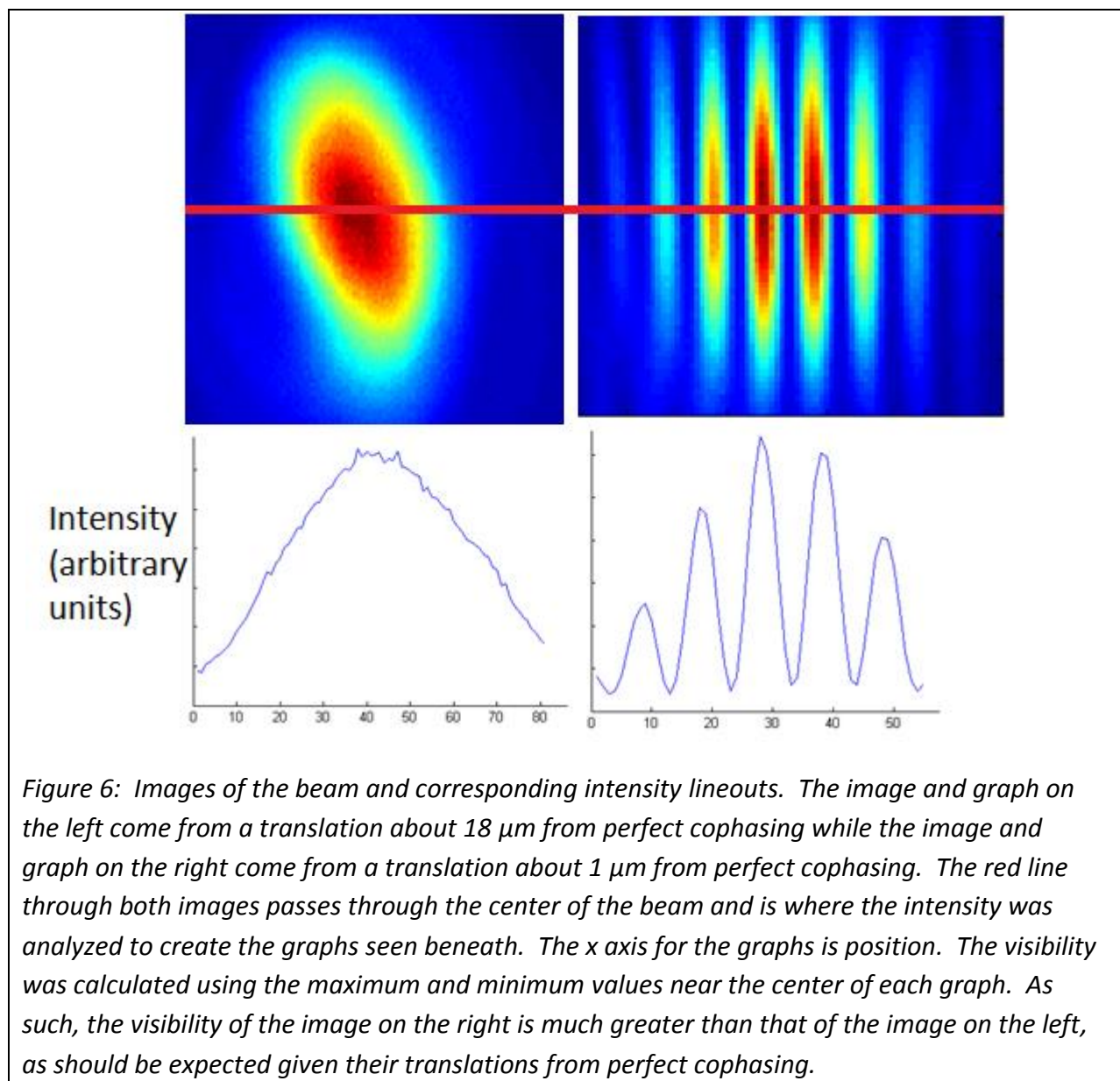
Testing the Precision of Cophasing

The setup seen in Figure 3 was constructed on an optical table. With the source turned on and using the display from the camera, the two spherical mirrors were cophased for tip and tilt by overlapping the two reflected dots onto the same point. From there, one mirror was slowly translated until an interference pattern was seen where the dots overlapped. Tip and tilt were adjusted whenever necessary to maintain beam overlap. After that, the mirror was translated 3 μm at a time from the point an interference pattern could be seen until it could not. 3 μm was about the smallest interval which the translation stage could move at a time while preserving significant accuracy. At each interval, ten pictures of the interference pattern were taken, a fraction of a second apart. This was because the air flow in the room caused the beams to vary slightly. Many pictures were taken so at least one would show the beams being nearly perfectly overlapped in each interval.

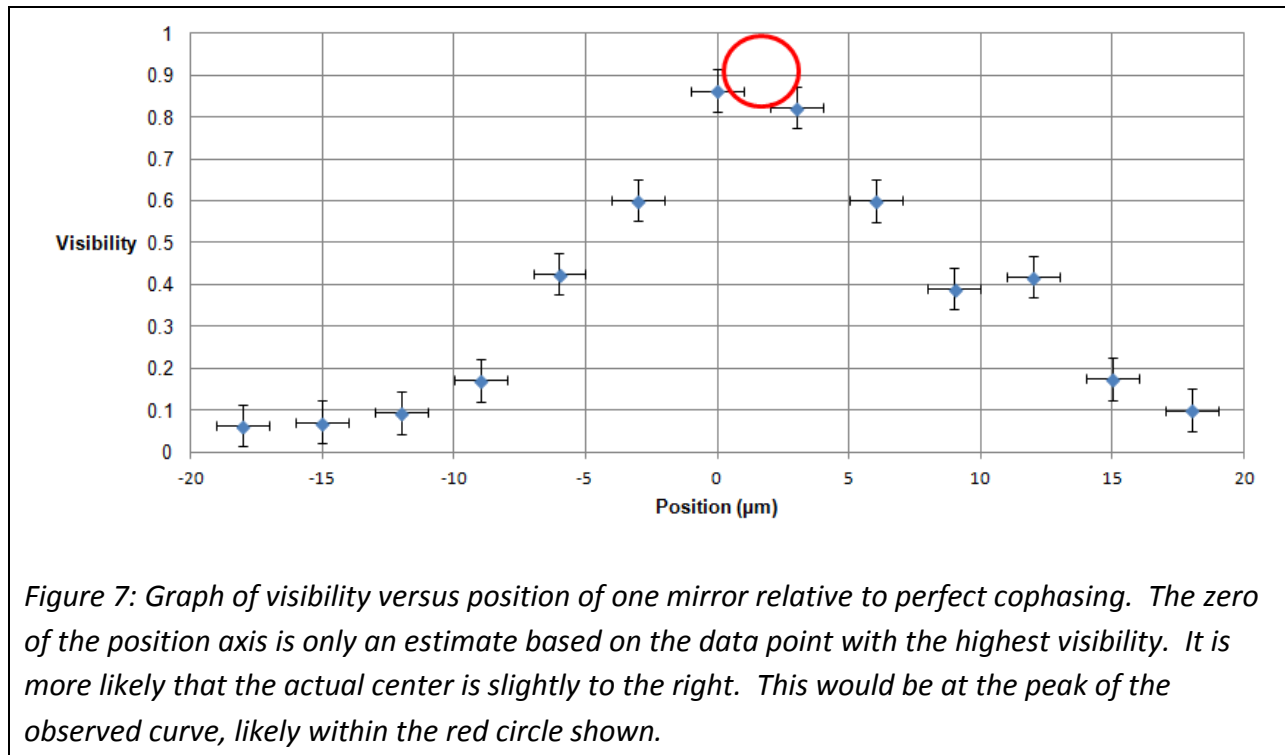
Another MATLAB program was used to sort out the best picture for each interval by finding which one had the smallest area with a relatively high beam intensity. The program then calculated the visibility of each of these images. The visibility, V , of an interference pattern is a quantifiable value for contrast between the fringes and can be calculated as

$$V = \frac{I_{\max} - I_{\min}}{I_{\max} + I_{\min}},$$

with I representing the beam intensity. Visibility is always a value between 0 and 1, with 1 being the greatest possible contrast between fringes. The min and max values were found by examining the intensity along a horizontal line passing through the center of where the beams overlapped, as seen in Figure 6.



The visibility for each translation was graphed, as seen in Figure 7. Due to the accuracy of the translation stages, there was a potential error of $\pm 1 \mu\text{m}$ in the translation. It was also deemed reasonable, given the method for selecting the optimal image for each interval and the calculation of visibility, that there was a potential error of ± 0.05 in visibility. From the data, it can be seen that there is a range of positions of about $3 \mu\text{m}$ in which maximum visibility is obtained. Cophasing the mirrors is then achieved within $3 \mu\text{m}$.



Conclusion

To compensate for radial group delay in the MTW-OPAL laser, a proposed solution uses concave lenses and an Offner triplet. However, to reduce the cost of manufacturing, the concave mirror of the triplet could be split into two that are cophased. It was found that the mirrors would be easy to cophase in all dimensions except for translation. A ray-tracing program was used to determine that the translation tolerance is 4 mm. An optical setup was then assembled to test the alignment of two such concave mirrors. This setup included a broadband laser with a coherence length of 4 μm and the mirrors mounted on translation stages. One mirror was translated until an interference pattern with high visibility was seen. It was found that the mirrors could be cophased to an accuracy of about 3 μm, well within the 4 mm tolerance. By demonstrating this, it was determined that the use of two smaller mirrors in the Offner triplet is feasible.

Acknowledgements

I would like to thank my adviser, Dr. Seung-Whan Bahk for allowing me to work with him on this project and the assistance that he's provided me. I would also like to thank Dr. R. S. Craxton for his patience, and for the opportunity he provided to me, as well as to my peers. Lastly, I would like to thank Mr. Paul Sedita for inspiring me in the field of physics, whose class I will never regret taking.

References

- [1] Z. Bor, J. Mod. Opt. **35**, 1907 (1988).
- [2] H.-M. Heuck, P. Neumayer, T. Köhl, and U. Wittrock, Appl. Phys. B **84**, 421 (2006).
- [3] R. L. Lucke, Opt. Eng. **46**, 073004 (2007).